PERFORMANCE OF POST-TENSIONED CONCRETE-FILLED GFRP TUBES FOR WIND TURBINE TOWERS IN REMOTE AREAS

By

AWS HASAK

Thesis submitted to the University of Ottawa

in partial Fulfillment of the requirements for the

Doctor of Philosophy in Civil Engineering

Department of Civil Engineering

Faculty of Engineering

University of Ottawa

Abstract

Providing sustainable energy infrastructure in remote areas of Canada presents significant challenges such as limited access to materials and skilled labour, large distances between neighbouring communities, and maintenance requirements. Wind turbines are a form of decentralized sustainable energy production that are well-suited for remote areas, though conventional tower structures made of steel or concrete are heavy (requiring large foundations), can be difficult to transport, and have relatively short service lives because of deterioration from corrosion and/or fatigue. Glass Fibre Reinforced Polymer (GFRP) tubes are increasingly used for utility poles because they are light in weight and easily connected on-site, thereby reducing transportation costs and emissions while simplifying erection and foundation requirements. Moreover, GFRP materials have a high tensile strength and improved durability to corrosion and fatigue compared to steel and concrete. In other applications (e.g., bridge piers), GFRP tubes have also been used as structural formwork and filled with concrete to produce a composite system with enhanced performance; the concrete adds strength and stiffness while the outer tube confines the concrete core and provides resistance to bending. Hence, concrete-filled FRP tubes (CFFTs) present a promising unexplored solution for wind turbine towers in northern remote areas.

The research presented in this thesis consists of two phases: experimental work and numerical modelling. Three hollow tapered CFFTs with different diameters were constructed and tested to assess their structural performance. Post-tensioned steel tendons were used to increase the stiffness of the tower and reduce the deflection caused by lateral loads. The towers were large scale, with heights of 5.8 m and base diameters between 460 mm and 535 mm and were tested as vertical cantilevers by fixing them to a large reusable foundation block. The outcomes of the experimental tests include: (I) understanding the response of CFFT wind turbine towers under static loads; (II) dynamic properties of prestressed CFFT towers for use as wind turbine towers; and (III) design recommendations and analysis of CFFT wind turbine towers for remote areas. Furthermore, in the second phase of the project, a finite element model was developed and validated using the experimental results to conduct parametric studies. The results confirmed that post-tensioned CFFT towers provide adequate stiffness, strength, and dynamic performance for wind turbine applications in remote areas. Failure mechanisms observed experimentally were well captured by

the models, supporting their use in design optimization. The parametric investigations further clarified the (I) effect of different prestress force levels on the lateral load–deflection behaviour, (II) influence of GFRP thickness on structural response, (III) impact of concrete confinement modelling on structural performance, and (IV) effect of different elastic moduli for the GFRP tube on the lateral load–deflection behaviour of the tower. Together, these results improve understanding of the structural behaviour of CFFT wind turbine towers and offer guidance for their practical application in remote northern energy infrastructure.

Acknowledgements

The journey to completing this PhD has been long and challenging, and it would not have been possible without the support, guidance, and encouragement of many individuals to whom I am deeply grateful.

First and foremost, I would like to express my sincere and heartfelt gratitude to my supervisor, Dr. Martin Noël, for his invaluable guidance, constant inspiration, and unwavering moral support throughout this research. His ability to motivate me to exceed his high expectations played a crucial role in my academic development. Beyond his academic distinction, his kindness and gentle manner were a significant source of reassurance during challenging moments. I hold him in the highest regard, both professionally and personally, and I am privileged to consider him not only a mentor but also a friend.

I would also like to extend my sincere gratitude to my co-supervisors, Dr. Mark Green and Dr. Amir Fam, for their insightful guidance, constructive feedback, and sustained encouragement throughout this research project. Their expertise and commitment were instrumental in shaping this work, and I am proud of the outcomes we achieved together.

Special thanks are extended to Dr. Muslim Majeed and Dr. Gamal Elnabelsya (University of Ottawa) for their valuable expertise and dedicated involvement during the laboratory testing and subsequent analysis.

My sincere thanks are also extended to Dr. Bessam Kadhom for his valuable assistance and the many enlightening discussions we shared on the response of structures under static and dynamic loading, which significantly contributed to my technical understanding.

I would also like to express my sincere appreciation to Yikai Gong (Kate) for her invaluable technical support and assistance with the development and verification of the finite element models used in this research. Our discussions and collaborative problem-solving significantly enhanced the quality of the finite element work presented in this thesis, and her support is gratefully acknowledged.

Finally, and most importantly, I am profoundly grateful to my family for their continuous support throughout my life. In particular, I owe my deepest thanks to my wife and best friend, Gufran, who

has been my greatest source of joy and strength. Her love, patience, encouragement, and unwavering support carried me through the many ups and downs of this journey and helped me maintain perspective on what truly matters in life. Without her support, understanding, and editing assistance, this thesis would not have been completed. For her belief in me and for giving me the freedom to pursue a research dream that has now become a reality, this thesis is dedicated to her.

Table of Contents

Abstract ii

Acknowledgements iv

Table of Contents vi

List of Figures xiii

List of Tables xxiii

Chapter 1 - Introduction 1

1.1. General 1

1.2. Research Significance 2

1.3. Research Objectives 3

1.4. Scope of Work 4

1.5. Thesis Organization 4

1.5.1. Chapter 2: Literature Review 4

1.5.2. Chapter 3: Experimental Program 5

1.5.3. Chapter 4: Analysis and Modeling 5

1.5.4. Chapter 5: Tower M4-1 5

1.5.5. Chapter 6: Tower M4-2 5

1.5.6. Chapter 7: Tower M5 6

1.5.7. Chapter 8: Discussion 6

1.5.8. Chapter 9: Conclusions and Recommendations 6

Chapter 2 - Literature review 7

2.1. Wind turbine towers 7

2.1.1. General 7

2.1.2. Wind turbine tower design limits 8
2.1.3. Wind turbine tower loads 9
2.2. Previous research on wind turbine towers 14
2.3. Concrete filled FRP tubes 21
2.3.1. Dynamic Behaviour of Concrete Filled FRP Tubes 21
2.3. 2. Flexural behaviour 24
2.3. 3. Torsional Behaviour 32
2.3.4. Foundation design 36
2.3.5. Analytical and Numerical Modelling 39
2.4. Summary and Research Gaps 46
2.4.1. Summary 46
2.4. 2. Research gaps 46
Chapter 3 - Experimental Program 48
3.1. Introduction 48
3.2. Material Properties 49
3.2.1. Glass Fibre Reinforced polymer (GFRP) 49
3.2.2. Concrete 52
3.3. Construction of towers 53
3.3.1. Reinforcing cages 53
3.3.2. Strain gauges 57
3.3.3. Sonotube 58
3.3.4. Concrete 61
3.3.5. Foundation units 65
3.4. Tower Testing 68

3.4.1. Test procedures 68
3.4.2. Instrumentation 75
Chapter 4- Analysis and Modeling 79
4.1. Introduction 79
4.2. Analytical Work 79
4.2.1. Natural frequency and damping ratio ζ 79
4.2.2. Moment resistance 80
4.2.3. Shear resistance 85
4.2.4. Deflections 86
4.2.5. Foundation 90
4.3. Finite Element Modeling 90
4.3. 1. Element Types and Material Models 90
4.3. 2. Concrete 91
4.3. 3. GFRP 93
4.3. 4. Damage Evolution 96
4.3. 5. Steel Reinforcement and Tendons 97
4.4. Mesh Sensitivity Analysis 98
4.5. Interaction 99
4.6. Boundary Conditions and Loading 100
4.7. Solver 104
4.8. Load 106
Chapter 5 - Tower M4-1: Experimental results and analysis 107
5.1. Overview 107
5.2. Stage 1: Free vibration test 107

5.3. Combined load–deflection results 110
5.4. Strain in internal longitudinal steel reinforcement bars 113
5.4.1. Strain response in rebars ‘A’ and ‘B’ under concentric flexural (CF) loading 114
5.4.2. Strain response in rebars ‘A’ and ‘B’ under small left eccentric (SLE) loading 114
5.4.3. Strain response in rebars ‘A’ and ‘B’ under big left eccentric (BLE) loading 115
5.4.4. Strain response in rebars ‘A’ and ‘B’ under big right eccentric (BRE) loading 116
5.4.5. Strain response in rebars ‘C’ and ‘D’ under concentric flexural (CF) loading 118
5.4.6. Strain response in rebars ‘C’ and ‘D’ under small left eccentric (SLE) loading 119
5.4.7. Strain response in rebars ‘C’ and ‘D’ under big left eccentric (BLE) loading 120
5.4.8. Strain response in rebars ‘C’ and ‘D’ under big right eccentric (BRE) loading 121
5.5. GFRP surface strain response under cyclic loading 123
5.5.1. Strain response in sides ‘A’ and ‘B’ under concentric flexural (CF) loading 123
5.5.2. Strains response in sides ‘A’ and ‘B’ under small left eccentric (SLE) loading 123
5.5.3. Strain response in sides ‘A’ and ‘B’ under big left eccentric (BLE) loading 124
5.5.4. Strain response in sides ‘A’ and ‘B’ under big right eccentric (BRE) loading 125
5.6. Test to failure 128
5.7. Numerical Model Verification 134
5.7.1. Stage 1. Free Vibration Test 134
5.7.2. Stage 2: Cyclic flexural testing under concentric loading 136
5.7.3. Stage 3A: Small left eccentric loading at 279.4 (mm) 142
5.7.4. Stage 3B: Big left eccentric loading at 559 (mm) 146
5.7.5. Stage 4: Test to failure 149
Chapter 6 - Tower M4-2: Experimental results and analysis 153
6.1. Overview 153

6.2. Free vibration test 153
6. 3. Combined Load–Deflection Results 155
6.4. Strain in internal longitudinal steel reinforcement bars 158
6.4.1. Strain response in rebars ‘A’ and ‘B’ under concentric flexural (CF) loading 158
6.4.2. Strain response in rebars ‘A’ and ‘B’ under big right eccentric (BRE) loading 159
6.4.3. Strain response in rebars ‘A’ and ‘B’ under big left eccentric (BLE) loading 160
6.4.4. Strain response in rebars ‘C’ and ‘D’ under concentric flexural (CF) loading 164
6.4.5. Strain response in rebars ‘C’ and ‘D’ under big right eccentric (BRE) loading 165
6.4.6. Strain response in rebars ‘C’ and ‘D’ under big left eccentric (BLE) loading 166
6.5. GFRP surface strain response under cyclic loading 168
6.5.1. Strain response in sides ‘A’ and ‘B’ under concentric flexural (CF) loading 168
6.5.2. Strain response in sides ‘A’ and ‘B’ under big right eccentric (BRE) loading 168
6.5.3. Strain response in sides ‘A’ and ‘B’ under big left eccentric (BLE) loading 169
6.6. Test to failure: Combined Flexural-Torsional and Monotonic Loading Tests 173
Chapter 7 - Tower M5: Experimental results and analysis 182
7.1. Overview: 182
7.2. Stage 1: Free vibration test 182
7.3. Combined load–deflection results 184
7.4. Strain in internal longitudinal steel reinforcement bars 188
7.4.1. Strain response in rebars ‘A’ and ‘B’ under concentric flexural (CF) loading 188
7.4.2. Strain response in rebars ‘A’ and ‘B’ under big right eccentric (BRE) loading 188
7.4.3. Strain response in rebars ‘A’ and ‘B’ under big left eccentric (BLE) loading 190
7.4.4. Strain response in rebars ‘C’ and ‘D’ under concentric flexural (CF) loading 194
7.4.5. Strain response in rebars ‘C’ and ‘D’ under big right eccentric (BRE) loading 195

7.4.6. Strain response in rebars ‘C’ and ‘D’ under big left eccentric (BLE) loading 196
7.5. GFRP surface strain response under cyclic loading 198
7.5.1. Strain response in sides ‘A’ and ‘B’ under concentric flexural (CF) loading 198
7.5.2. Strain response in sides ‘A’ and ‘B’ under big right eccentric (BRE) loading 198
7.5.3. Strain response in sides ‘A’ and ‘B’ under big left eccentric (BLE) loading 199
7.6. Test to failure 204
7.7. Numerical Model Verification 208
7.7.1. Stage 1. Free Vibration Test 208
7.7.2. Stage 2: Cyclic flexural testing under concentric loading (CF) 209
7.7.3. Stage 3B: Big left eccentric loading at 558.8 (mm) 212
7.7.4. Stage 4: Test to failure 215
Chapter 8 - Discussion 218
8.1. Introduction 218
8.2. Comparison of Tower Performance 218
8.2.1. Characterization of dynamic properties 218
8.2. 2. Comparative Analysis of Monotonic Load-Deflection Response 219
8.2.3. Influence of Prestress and Section Size on Stiffness and Strength 221
8.2.4. Comparative Cyclic Response under Concentric and Eccentric Loading 222
8.3. Parametric Study on the Influence of Design Variables 228
8.3.1. Effect of Prestressing on Load–Deflection Behaviour 229
8.3.2. GFRP Tube Thickness 230
8.3.3. Effect of concrete confinement 231
8.3.4. Effect of elastic modulus of the GFRP tube 232
8.4. Analytical Predictions 233

8.5. Critical Assumptions and Limitations 235
8.6. Unexpected Observations and Behaviour 236
Chapter 9 - Conclusions and Recommendations 238
9.1. Conclusions 238
9.2. Summary of Conclusions 238
9.3. Practical design recommendations 240
9.4. Recommendations for Future Work 241
References 244
Appendix A: 250
Appendix B: 251
Appendix C: 252
Appendix D: 255
Appendix E 258
Appendix F 258

List of Figures

Figure 2.1. (a) Steel tubular tower (Veljkovic et al., 2011), (b) Concrete tower (ACCIONA, n.d.), (c) Steel lattice tower (Veljkovic et al., 2011) 8

Figure 2.2. Different sizes of wind turbines (Rhoads-Weaver et al., 2013) 10

Figure 2.3. (3-D) forces at the top of the tower (Nicholson, 2011) 11

Figure 2.4. Load distribution on the wind turbine tower (Nicholson, 2011) 11

Figure 2.5. Single-cell cross-sectional details (Polyzois et al. 2009) 15

Figure 2.6. Phase I specimen after testing (Polyzois et al. 2009) 15

Figure 2.7. Sectional properties for the tested towers in Phase III (Polyzois et al. 2009) 16

Figure 2.8. Dynamic testing setup for Phase IV (Polyzois et al. 2009) 16

Figure 2.9. Top and mid height deflection for specimens in Phase III (Polyzois et al. 2009) 17

Figure 2.10. Damage on specimens at maximum load (Polyzois et al. 2009) 18

Figure 2.11. Comparison between load-tip deflection relationships computed using F.E.M with experimentally recorded results for Phase I (Polyzois et al. 2009) 19

Figure 2.12. Phase III comparison between load-tip deflection relationships computed using F.E.M with experimentally recorded results (Polyzois et al. 2009) 20

Figure 2.13. (a) photo of impact testing setup and (b) schematic of impact (Qasrawi et al. 2015) 22

Figure 2.14. Failures mechanisms of (a) monotonic specimens and (b) impact specimens (Qasrawi et al. 2015) 23

Figure 2.15. Measured and SDOF result displacements for specimens (Qasrawi et al. 2015). 24

Figure 2.16. Details of (a) Prestressed concrete pile; (b) Composite pile (Fam et al. 2003). 25

Figure 2.17. Moment- curvature responses of the composite and prestressed concrete piles (Fam et al. 2003). 26

Figure 2.18. Flexural tension failure of the composite pile (Fam et al. 2003). 26

Figure 2.19. Lateral load versus deflection response of piles (Fam et al. 2003). 27
Figure 2.20. (a) Side view (b) Schematic of test setup (Mohamed & Masmoudi, 2010). 30
Figure 2.21. Effect of the type of transverse reinforcement on load–deflection curves (Mohamed & Masmoudi, 2010). 31
Figure 2.22. Effect of the type of flexural reinforcement on load–deflection curves (Mohamed & Masmoudi, 2010). 32
Figure 2.23. Sample geometric of CFFT (dim. in mm) (St. Onge and Fam, 2021). 33
Figure 2.24. Conceptual illustration of the effect of concrete filling on the hollow tube (St. Onge and Fam, 2021). 34
Figure 2.25. Torque–twist response of hollow FRP tubes (St. Onge and Fam, 2021). 35
Figure 2.26. Torque–twist response of CFFTs (St. Onge and Fam, 2021)..... 35
Figure 2.27. Simplified CFFT torque mechanism: (a) pre-cracking; and (b) post- cracking (St. Onge and Fam, 2021). 36
Figure 2.28. Geometric configuration used for the model (Sadeghian and Fam, 2010) 37
Figure 2.29. Free body of the general model within the embedment length of the tube (Sadeghian and Fam, 2010) 38
Figure 2.30. Stress-Strain Model Proposed for Confined and Unconfined Concrete (Mandar et al. 1988)..... 39
Figure 2.31. Confining action of (b) FRP jacket to (a) Concrete (Lam and Teng, 2003) 41
Figure 2.32. Developed stress–strain model for FRP-confined concrete (Lam and Teng, 2003) 42
Figure 2.33. Finite element model of CFFT tower (Gong, 2021). 44
Figure 2.34. Cross-section of the two steel-prestressed CFFT models (Gong, 2021). 44
Figure 2.35. Load-deflection relationship of models with different diameter, concrete filling ratio, FRP tube thickness, taper ratio, steel reinforcement ratio, and prestressing ratio (Gong, 2021). 45

Figure 3.1. Tapered profile tubes ((a) FRP utility tower, (b) Size variations of FRP tube modules, (c) splice connection, (d) ease of transportation (R. S. Poles. (n.d.)) 49
Figure 3.2. Test setup of GFRP coupon (courtesy of Watfa, 2025) 50
Figure 3.3. Test setup of tension in hoop direction (courtesy of Watfa, 2025) 51
Figure 3.4. Slump flow test for self-consolidating concrete 52
Figure 3.5. Steel bar and strand layout 53
Figure 3.6. Tie bending jig and size template 54
Figure 3.7. Longitudinal steel bars and prestressing duct attached to ties and secured in the designated locations 55
Figure 3.8. Ties location for the tower specimens 55
Figure 3.9. Steel plates on top and bottom of the towers 56
Figure 3.10. Plastic spacers mounted along the longitudinal reinforcement bars 56
Figure 3.11. Galvanized wire wrapped around the end of the conduit 57
Figure 3.12. Strain gauges' location on steel bars 59
Figure 3.13. Preparation stages for Sonotubes 60
Figure 3.14. Extension wires attachment to the sonotube and passing through the hollow core to the top of the tower 61
Figure 3.15. Preparing tower specimens before casting 63
Figure 3.16. Tower specimens during casting 64
Figure 3.17. Octagon steel plates 64
Figure 3.18 - Foundation Design Details 66
Figure 3.19. Prestressing tendons extension 66
Figure 3.20. Steel cage in the formwork 67
Figure 3.21. Pouring the concrete in the formwork 67
Figure 3.22. Foundation with a hexagonal hole in the middle 67

Figure 3.23 (a) Lumber to secure the tower (b) Using plumbs in four cross positions to control verticality of the tower 68
Figure 3.24. Test setup and A-frame attached to the laboratory strong floor 69
Figure 3.25. Clamping system installed at the top of the column 70
Figure 3.26. Steel chain with high safe workload capacity to support the actuator 71
Figure 3.27. The actuator steel plate with actuator positions 72
Figure 3.28. CFFT tower segment prior to testing 73
Figure 3. 29. Notched rectangular steel plate 74
Figure 3.30. Cable transducer and strain gauge's locations 76
Figure 3.31. Strain gauges Locations on the GFRP surface 77

Figure 4.1. Steel stress-strain relationship 82
Figure 4.2. Flow chart of the layer by layer sectional analysis 84
Figure 4.3. Moment resistance of towers along the height for confined concrete model 85
Figure 4.4. Flow chart of tower's deflection calculation 88
Figure 4.5. Predicted deflection profiles of the M4 and M5 towers along their height at their respective peak loads, 132 kN and 182 kN, respectively 89
Figure 4.6. Comparison of experimental and theoretical load–deflection profiles at a height of 5 m for the M4 and M5 towers 89
Figure 4.7. Schematic of the numerical model showing fundamental parts 90
Figure 4.8.3D model and FE mesh of the M4 tower including foundation 93
Figure 4.9 Element types used for concrete and GFRP (Abaqus, 2014) 94
Figure 4.10. FE model of the reinforcement grid and post-tensioning tendons. 98
Figure 4.11. Lateral load–lateral deflection response from the mesh sensitivity analysis for different mesh sizes 99

Figure 4.12. Illustration of the finite element model showing the locations of embedded constraints and applied contact interactions. 100
Figure 4.13. FE mesh of the M4 tower 102
Figure 4.14.3D model and FE mesh of the M4 tower, including the clamping system and foundation 103
Figure 4.15. Reference points RP1 and RP6 on the tower model used for boundary conditions 104
Figure 4.16. Flowchart of quasi-static analysis procedure in Abaqus 105

Figure 5.1. Tower M4-1 free vibration response 109
Figure 5.2. Lateral load–lateral drift response under concentric, small left eccentric (279 mm), and big right and left eccentric (± 559 mm) cyclic loading conditions 112
Figure 5.3. Lateral load vs time response under (a) concentric, (b) small left eccentric (279 mm), (c) big left eccentric (559 mm), and (d) big right eccentric (559 mm) cyclic loading conditions 113
Figure 5.4. Strain readings recorded on rebars 'A' and ‘B’ under both push and pull loading phases for concentric, small left eccentricity (279 mm), big left and right eccentricity (559 mm) cyclic loading conditions. 117
Figure 5.5. Comparison of strain values on rebars ‘A’ and ‘B’ under CF loading, SLE, BLE, and BRE cyclic loading conditions (+42 kN and -38 kN applied loads) 118
Figure 5.6. Strain readings recorded on rebars 'C' and ‘D’ under both push and pull loading phases for concentric, small left eccentricity (279 mm), big left and right eccentricity (559 mm) cyclic loading conditions 122
Figure 5.7. Strain readings recorded on Side 'A' under both push and pull loading phases for concentric, small left eccentricity (279 mm), big left and right eccentricity (559 mm) cyclic loading conditions. 126
Figure 5.8. Strain readings recorded on Side 'B' under both push and pull loading phases for concentric, small left eccentricity (279 mm), big left and right eccentricity (559 mm) cyclic loading conditions. 127

Figure 5.9. Comparison of strain values on sides ‘A’ and ‘B’ under CF, SLE, BLE, and BRE cyclic loading conditions (+42 kN and -38 kN applied loads) 128
Figure 5.10. Lateral load vs lateral deflection response of tower M4-1 129
Figure 5.11. Lateral load vs longitudinal strain curves for tower M4-1 130
Figure 5.12. Strain readings recorded on the GFRP surface 130
Figure 5.13. Tower height vs GFRP strain reading 131
Figure 5.14. Tower’s curvature vs tower's height at maximum failure load of 132 kN 132
Figure 5.15. Failure mode of tower specimen M4-1 133
Figure 5.16. Flowchart structure for free vibration analysis 135
Figure 5.17. Comparison of displacement-time history for free vibration response of M4-1 – experimental and modeling results 135
Figure 5.18. Load–Displacement Response of M4-1 under Concentric Cyclic Flexural Loading: Experimental vs. Initial Model Result 136
Figure 5.19. Loading position for CF testing at the clamping system center. 137
Figure 5.20. Experimental early-stage load–displacement response of the tower during cyclic flexural testing under concentric loading 138
Figure 5.21. Load–displacement response of M4-1 under CF loading: Experimental vs. Model 140
Figure 5.22. FE simulation of the M4 tower under CF loading illustrating stress contours and damage distribution 141
Figure 5.23. Adjustment of boundary conditions and loading position for SLE loading at 279.4 mm eccentricity. 144
Figure 5.24. Load–Displacement Response of M4-1 under SLE Loading: Experimental vs. Model 144
Figure 5.25. FE simulation of the M4 tower under SLE loading illustrating stress contours and damage distribution 145

Figure 5.26. Adjustment of boundary conditions and loading position for BLE loading at 559 mm eccentricity. 147

Figure 5.27. Load–Displacement Response of M4-1 under BLE Loading: Experimental vs. Model..... 147

Figure 5.28. FE simulation of the M4 tower under BLE loading illustrating stress contours and damage distribution 148

Figure 5.29. Comparison of load- displacement response of M4-1 – experimental and modeling results 150

Figure 5.30. FE simulation of the M4 tower illustrating stress contours and damage distribution 151

Figure 5.31. Numerical simulation of the M4-1 tower showing fiber tensile damage (HSNFTCRT) and matrix tensile failure (HSNMTCRT) based on Hashin's damage criteria. 152

Figure 6.1. Tower M4-2 free vibration response 155

Figure 6.2. Lateral load–lateral drift response under concentric, and big right and left eccentric (± 559 mm) cyclic loading conditions 156

Figure 6.3. Cable transducer attached on the front side of the foundation 157

Figure 6.4. Strain readings recorded on rebars 'A' under both push and pull loading phases for concentric, and big left and right eccentricity (559 mm) cyclic loading conditions. 162

Figure 6.5. Strain readings recorded on rebar 'B' under both push and pull loading phases for concentric, and big left and right eccentricity (559 mm) cyclic loading conditions. 163

Figure 6.6. Comparison of strain values on rebars 'A' and 'B' under CF loading, BLE, and BRE cyclic loading conditions (+25 kN and -26 kN) 164

Figure 6.7. Strain readings recorded on rebars 'C' and 'D' under both push and pull loading phases for concentric, big left and right eccentricity (559 mm) cyclic loading conditions..... 167

Figure 6.8. Strain readings recorded on Side 'A' under both push and pull loading phases for concentric, big left and right eccentricity (559 mm) cyclic loading conditions. 171

Figure 6.9. Strain readings recorded on Side ‘B’ under both push and pull loading phases for concentric, small left eccentricity (279 mm), big left and right eccentricity (559 mm) cyclic loading conditions..... 172
Figure 6.10. Comparison of strain values on sides ‘A’ and ‘B’ under CF, BLE, and BRE cyclic loading conditions (+25 kN and -26 kN) 173
Figure 6.11. Lateral load verses lateral drift response of tower M4-2 under large eccentric loading and test to failure 176
Figure 6.12. Lateral load vs longitudinal strain response of tower M4_2 under BRE loading, with the peak load reaching 143 kN. 176
Figure 6.13. Strain readings recorded on the GFRP surface under BRE loading, with the peak load reaching 143 kN..... 177
Figure 6.14. Lateral load vs longitudinal strain curves under monotonic loading to failure 177
Figure 6.15. Strain readings recorded on the GFRP surface under monotonic loading to failure..... 177
Figure 6.16. Comparison of GFRP strain readings at different tower heights under monotonic loading to failure. 178
Figure 6.17. Tower’s curvature vs tower's height at maximum failure load of 125 kN 179
Figure 6.18. Failure mode of tower specimen M4-2 181

Figure 7.1. Tower M5 free vibration response 184
Figure 7.2. Lateral load–lateral drift response under concentric, and big right and left eccentric (± 559 mm) cyclic loading conditions 186
Figure 7.3. Lateral load vs time response under (a) concentric, (b) big right eccentric (559 mm), and (C) big left eccentric (559 mm) cyclic loading conditions 187
Figure 7.4. Strain readings recorded on reinforcing bar ‘A’ under both push and pull loading phases for concentric, and big left and right eccentricity (559 mm) cyclic loading conditions. 192

Figure 7.5. Strain readings recorded on reinforcing bar ‘B’ under both push and pull loading phases for concentric, and big left and right eccentricity (559 mm) cyclic loading conditions. 193
Figure 7.6. Comparison of rebar strain values rebars ‘A’ and ‘B’ under CF loading, BLE, and BRE cyclic loading conditions 194
Figure 7.7. Strain readings recorded on rebars 'C' and ‘D’ under both push and pull loading phases for concentric, big left and right eccentricity (559 mm) cyclic loading conditions 197
Figure 7.8. Strain readings recorded on Side ‘A’ under both push and pull loading phases for concentric, big left and right eccentricity (559 mm) cyclic loading conditions. 201
Figure 7.9. Strain readings recorded on Side ‘B’ under both push and pull loading phases for concentric, small left eccentricity (279 mm), big left and right eccentricity (559 mm) cyclic loading conditions. 202
Figure 7.10. Comparison of strain values on sides ‘A’ and ‘B’ under CF, BLE, and BRE cyclic loading conditions 203
Figure 7.11. Monotonic load-deflection response 205
Figure 7.12. Lateral load vs longitudinal strain curves for tower M5 205
Figure 7.13. Tower height vs rebars ‘A’ and ‘B’ strain reading 206
Figure 7.14. Tower’s curvature vs tower's height at maximum failure load of 182 kN 206
Figure 7.15. Strain readings recorded on the GFRP surface 206
Figure 7.16. Failure mode of tower specimen M5 207
Figure 7.17. Comparison of displacement-time history for free vibration response of M5 – experimental and modeling results 208
Figure 7.18. Load–Displacement Response of M5 under CF Loading: Experimental vs. Model 209
Figure 7.19. FE simulation of the M4 tower under CF loading illustrating stress contours and damage distribution 211
Figure 7.20. Load–Displacement Response of M5 under BLE Loading: Experimental vs. Model 212

Figure 7.21. FE simulation of the M5 tower under BLE loading illustrating stress contours and damage distribution 214
Figure 7.22. Comparison of load- displacement response of M5 – experimental and modeling results 216
Figure 7.23. FE simulation of the M5 tower illustrating stress contours and damage distribution 217

Figure 8.1. Load–deflection response under monotonic loading for specimens M4-1, M4-2, and M5 221
Figure 8.2. Lateral load–lateral drift response for M4-1 and M4-2 under concentric cyclic loading condition 223
Figure 8.3. Lateral load–lateral drift response for M4-1 and M5 under concentric cyclic loading condition. 224
Figure 8.4. Lateral load–lateral drift response for M4-1 and M2-2 under BRE loading condition 225
Figure 8.5. Lateral load–lateral drift response for M4-1 and M2-2 under BLE loading condition 225
Figure 8.6. Lateral load–lateral drift response for M4-1 and M5 under BRE loading condition 227
Figure 8.7. Lateral load–lateral drift response for M4-1 and M5 under BLE loading condition 227
Figure 8.8. Effect of prestress force on lateral load–drift response 229
Figure 8.9. Effect of GFRP tube thickness on lateral load–drift response 230
Figure 8.10. Effect of concrete confinement on the lateral load–deflection behaviour of the tower 231
Figure 8.11. Effect of elastic moduli for the GFRP tube on the lateral load–deflection behaviour of the tower M5 232

List of Tables

Table 2.1 Small wind turbines with different weights and sizes (Taisei Techno Co, 2025) 9

Table 2.2. Maximum load and deflection for Phase III (Polyzois et al.2009)..... 18

Table 2.3 The dynamic properties for the towers in Phase IV (Polyzois et al. 2009) 19

Table 2.4. Mechanical properties of composite GFRP tube (Fam et al. 2003). 25

Table 2.5 Dimension and mechanical properties of FRP tubes (Mohamed & Masmoudi, 2010). 29

Table 2.6. Details of specimens and summary of test results (Mohamed & Masmoudi, 2010). 30

Table 2.7. FRP tube structure (St. Onge and Fam, 2021)..... 33

Table 2.8. FRP tube properties (St. Onge and Fam, 2021)..... 33

Table 3.1. Tower specimen details 48

Table 3.2. GFRP properties 51

Table 3.3. Compressive strength of the tested cylinders 53

Table 4.1. Concrete properties..... 81

Table 4.2. Steel rebar sizes and material properties 81

Table 4.3. Prestressing strand properties 82

Table 4. 4. Prestress level and average microstrain (με) in towers 82

Table 4.5. GFRP properties 83

Table 4.6. Summary of confined concrete properties..... 83

Table 4.7. Maximum moment resistance (M_r) for each tower 85

Table 4.8. Summary of shear resistance calculation 86

Table 4. 9. Elastic properties of concrete 92

Table 4. 10. CDP parameters..... 92

Table 4. 11. Compressive behaviour and damage 92

Table 4. 12. Tensile behaviour and damage 92

Table 4.13. Material Parameters of GFRP 94

Table 4.14. Material parameters for steel reinforcement. 97

Table 4.15. Element Classification and Applications in the FE Model 101

Table 5.1. Damping values and frequency results of the tested tower 109

Table 6.1. Damping values and frequency results of the tested tower 154

Table 7.1. Damping values and frequency results of the tested tower 183

Table 8. 1. Summary of the natural frequency and damping ratio for M4 and M5 219

Table 8.2. Summary of Failure Loads and Corresponding Displacements of Tested Towers 221

Table 8.3. Maximum moment resistance (M_r) for each tower 234

Chapter 1 - Introduction

1.1. General

The global shift towards sustainable energy production has placed wind power to the forefront of renewable energy technologies. Wind energy systems, particularly wind turbines, have been implemented worldwide to limit use of fossil fuels and address the challenges of climate change. However, the utilization of wind energy infrastructure in remote areas presents significant technical and logistical barriers. Harsh climatic conditions, transportation difficulties, and limited access to specialized equipment complicate the construction, maintenance, and operation of wind turbines (Rodríguez, 2023).

A promising solution to these challenges involves the use of advanced materials and innovative structural designs. Concrete-filled fibre-reinforced polymer (FRP) tubes (CFFTs) have obtained increasing interest in civil engineering due to their unique combination of strength, corrosion resistance, and light weight. Previous research on CFFTs has demonstrated their suitability for members subjected to flexural and axial loading in applications such as bridges and other structures (Fam and Rizkalla, 2001; Fam et al., 2003; Fam and Mandal, 2006; Hadi et al., 2016; Mohamed and Masmoudi, 2010; Ozbakkaloglu and Vincent, 2013). They have also been used for utility poles (Mitchell and Fam, 2010) and have shown good performance under dynamic impact loading (Qasrawi et al., 2015). These characteristics suggest the potential extension of CFFT technology to wind turbine towers, where appropriate flexural stiffness is critical for limiting deflections.

Concrete towers for wind turbines are traditionally constructed using prestressed concrete. This involves introducing tensioned steel rods or strands into the structure to generate compressive stresses within the concrete that balance the tensile stresses caused by bending. Although prestressed concrete structures are more costly than conventional reinforced concrete structures due to additional tensioning elements, they offer higher load-bearing capacity and improved serviceability by reducing crack widths and deflections (Hau, 2006).

The incorporation of a glass fibre-reinforced polymer (GFRP) tube to form the outer circumference of wind turbine towers introduces an innovative parameter. This could significantly enhance the structural performance, durability, and constructability of the towers, particularly for small-scale turbines in remote locations where resources and maintenance access are limited.

Wind energy development in remote northern Canadian regions presents unique structural and logistical challenges. The harsh climate, characterized by extreme cold, ice, and high wind loads, demands materials and designs that can withstand severe environmental difficulties while minimizing costly maintenance. The limitations of conventional steel and reinforced concrete towers, specifically their susceptibility to corrosion and the expense of transporting large and heavy components, highlight the need for more innovative solutions. This study investigates post-tensioned CFFTs as a potential alternative, aiming to meet these essential requirements while enhancing the sustainability of wind energy projects in remote areas.

CFFTs offer significant advantages over conventional towers, including improved corrosion resistance, reduced maintenance needs, and lightweight properties. The lightweight nature of FRP simplifies transportation, and it can be shipped in segments of reasonable length that can be spliced together on site, making it particularly advantageous for construction in remote areas. This approach aligns with the concept of segmental construction, which allows for the assembly of towers of different heights by connecting prefabricated segments, as highlighted in the work by Watfa et al. (2025). Additionally, post-tensioned CFFTs have higher structural stiffness and load-bearing capacity, potentially extending their lifespan and lowering repair costs (Fam and Mandal, 2006). As wind energy is a key component of the Canadian government's renewable energy strategy, developments in wind turbine tower design are crucial for expanding infrastructure in remote areas. This research explores ways to optimize post-tensioned CFFTs for small-scale wind turbines, contributing to sustainable energy solutions and reducing reliance on non-renewable energy sources.

1.2. Research Significance

This research addresses a gap in the current knowledge regarding the application of CFFTs for wind turbine towers. While the use of CFFTs has been explored in other structural applications,

such as bridges, utility poles, and columns, their potential in wind turbine towers remains largely unexamined. This study is significant for several reasons:

1. The use of prestressed, hollow, tapered CFFT segments that can be spliced together on-site presents an innovative approach to improve the constructability and structural performance of wind turbine towers, especially in remote areas where traditional tower systems may not be ideal.
2. By optimizing wind turbine tower designs, this research could help to overcome logistical challenges in deploying wind energy infrastructure in northern Canada, where access to sustainable energy is limited.
3. The use of durable, low-maintenance materials in wind turbine towers has the potential to reduce maintenance costs and extend the lifespan of turbines, providing both environmental and economic advantages.
4. The findings of this research will provide practical design recommendations for engineers and local communities looking to develop wind energy systems in remote areas, contributing to the wider goal of making renewable energy more accessible.

1.3. Research Objectives

The aim of this research is to study the behaviour of post-tensioned hollow concrete-filled GFRP tubes for wind turbine towers, particularly for remote areas where construction and maintenance are challenging. These towers need to be strong, durable, and easy to transport and assemble. While CFFTs have shown promise in other structural applications, their performance in wind turbine towers, especially under cyclic and eccentric loading, is still not well understood.

To address this gap, the following objectives were set:

1. To evaluate how CFFT towers perform under lateral and dynamic loading, including both concentric flexural and flexural-torsional scenarios. The goal is to better understand their structural behaviour in real-world conditions.

2. To study the impact of post-tensioning and tower geometry on the overall structural behaviour of the towers.
3. To build and validate finite element models that replicate the experimental results. These models are then used to run parametric studies and identify ways to improve the tower design.
4. To develop design recommendations that can guide engineers who are looking to implement small-scale wind energy solutions in remote areas.

1.4. Scope of Work

The scope of this study focuses on the structural performance of hollow, tapered post-tensioned CFFTs for wind turbine towers. Specifically, the research is limited to small-scale wind turbines appropriate for use in remote northern Canadian areas. The study includes the following key areas:

1. Dynamic Testing: The study evaluates the dynamic properties of CFFT towers subjected to vibration testing at the top free end, with the goal of assessing their natural frequencies and damping characteristics.
2. Flexural Performance: The research investigates the flexural behaviour of CFFT towers under quasi-static cyclic lateral loading followed by monotonic loading to failure, with a focus on flexural stiffness, ultimate capacity, and the effects of eccentricity.
3. Numerical Modelling: A numerical model is developed to simulate the behaviour of the CFFT towers and predict their performance under various loading conditions.
4. Design Recommendations: Practical design recommendations are developed for the implementation of CFFT towers for small-scale wind turbines, focusing on optimizing their structural performance and adaptability to remote environments.

1.5. Thesis Organization

1.5.1. Chapter 2: Literature Review

This chapter provides a comprehensive review of existing research on wind turbine towers and CFFT technology. It discusses the necessity and advantages of using wind energy in remote areas,

the limitations of conventional steel and concrete towers, and the potential benefits of CFFTs. The chapter also explores previous experimental and numerical studies related to CFFTs, including their flexural, torsional, and dynamic behaviour.

1.5.2. Chapter 3: Experimental Program

This chapter details the experimental methodology used to assess the performance of post-tensioned CFFTs. It covers material properties, specimen preparation, testing setup, test procedures, and instrumentation.

1.5.3. Chapter 4: Analysis and Modeling

This chapter presents the analytical and numerical modelling work that supports the experimental findings. It begins by outlining the key analytical calculations used to estimate the moment capacity, shear resistance, required foundation depth, and expected deflection of the tapered post-tensioned hollow CFFT towers. It then describes the development of the ABAQUS finite element model, which was used to simulate both the dynamic response under vibration and the flexural behaviour under lateral loading. Together, these methods form the foundation of a parametric study investigating how critical design parameters influence overall tower behaviour.

1.5.4. Chapter 5: Tower M4-1

This chapter presents experimental and numerical findings for Tower M4-1. It includes findings from free vibration tests, cyclic flexural testing under concentric loading, cyclic flexural-torsional testing under eccentric loading at 558.8 mm and 279.4 mm, and failure tests. The results are compared with numerical simulations to validate the finite element models.

1.5.5. Chapter 6: Tower M4-2

Similar to Chapter 5, this section focuses on the structural assessment of Tower M4-2. The study evaluates the impact of design variations on the tower's vibration behaviour, cyclic flexural testing under concentric loading, cyclic flexural-torsional testing under eccentric loading at 279.4 mm, and failure mechanisms.

1.5.6. Chapter 7: Tower M5

This chapter investigates the behaviour of Tower M5, which had a larger diameter, under different loading scenarios such as free vibration tests, cyclic flexural testing under concentric loading, cyclic flexural-torsional testing under eccentric loading at 279.4 mm, and failure tests. Experimental and numerical results are presented to assess the tower's response to cyclic loading, torsional effects, and ultimate load capacity.

1.5.7. Chapter 8: Discussion

This chapter discusses the main outcomes of the tower tests and presents results from a numerical parametric study, focusing on how factors such as post-tensioning, eccentric loading, and material behaviour influenced the performance of the CFFT wind turbine towers. It also connects the findings back to the research objectives, compares them with existing literature, and outlines key design recommendations for practical applications in remote areas.

1.5.8. Chapter 9: Conclusions and Recommendations

This chapter presents the conclusions of results obtained in Chapter 5, 6, and 7 and recommendations for future work about CFFT wind turbine towers.

Chapter 2 - Literature review

2.1. Wind turbine towers

2.1.1. General

Conventional wind turbine towers are made of steel tubes or concrete as illustrated in Figure 2.1 (a) and (b), respectively. Lattice towers, as shown in Figure 2.1(c), are less suitable for remote areas since they require more regular maintenance. Steel tubular towers have excellent strength and ductility but have a short service life of only 20 years since they are susceptible to corrosion and are expensive to maintain. Concrete towers can have an extended life span of 40-60 years, and the cost of construction and transportation of these towers is lower than those of steel towers. Concrete towers are also more stable against buckling failure. However, concrete towers are heavier than steel tubular towers, requiring a larger footing, and require steel reinforcement as they are weak in tension. Drawbacks of conventional wind turbine towers include their high cost, transportation challenges, and long-term durability (de Lana et al., 2021; Veljkovic et al., 2011).

To avoid these weaknesses, CFFTs present a potential alternative that can be easily manufactured and transported to the site. In addition to acting as a permanent formwork for the concrete, the external FRP lightweight tube guarantees that CFFTs have high tensile strength and are appropriate for flexural loading. Furthermore, glass FRP (GFRP) tubes are light in weight and thus less energy is required to transport them to construction sites in remote areas. Moreover, the GFRP tubes are resistant to harsh weather conditions and corrosion attack, which means a reduction in maintenance costs and increased life span (de Lana et al., 2021; Veljkovic et al., 2011).

Figure 2.1. (a) Steel tubular tower (Veljkovic et al., 2011), (b) Concrete tower (ACCIONA, n.d.), (c) Steel lattice tower (Veljkovic et al., 2011)

2.1.2. Wind turbine tower design limits

There are a limited number of design guidelines available for wind turbine towers. The International Electrotechnical Commission (IEC) Wind Turbine Requirements document 61400-1 (2019) presents the wind conditions, loads, and load cases, and IEC 61400-2 is a simplified standard used for small wind turbines, typically rated from 0.1 kW to 100 kW, with tower heights generally ranging from 10 m to 40 m (IEA Wind TCP, 2021). These international standards were developed in 2001 for steel, concrete, or lattice towers.

ANSI/TIA 222-G (2005), established by the American National Standard Institute, is not specified for wind turbines but can be used for the design and analysis of latticed towers. The DNVGL-ST-0126 (2016) guidelines were developed by private companies in Norway and Germany for concrete and steel support structures for wind turbines.

Key design considerations for wind turbine towers include limits on the outer diameter and top deflection of the towers. The outer diameter relies fundamentally on the transportation restrictions, whereas the top lateral deflection is in some cases restricted by the manufacturer. According to

previous research, the outer diameter of turbine towers should be limited to 4.5 m, while the top lateral deflection should not exceed 1.25% of the tower height. Although no specific maximum tower height is prescribed, practical height limitations occur from serviceability, strength, dynamic, transportation, and constructability constraints (Nicholson, 2011; IEC 61400-1, 2005; DNV-ST-0126, 2013).

2.1.3. Wind turbine tower loads

Wind turbine towers are affected by different types of loads such as wind load, self-weight, internal fixtures loading, and loads from the wind turbine itself. Loads from the wind turbine are concentrated at the top of the tower and can be given by the wind turbine manufacturers.

Medium- and large-scale wind turbine are commonly used in commercial areas. With regards to off-grid or battery charging wind turbines, small-scale wind turbines under 5 kW are more efficient (Rhoads-Weaver et al., 2013). The weight and power rating of battery charging off-grid small wind turbines are illustrated in Table 2.1. Small wind turbines of varying height and rotor diameter are shown in Figure 2.2.

Table 2.1 Small wind turbines with different weights and sizes (Taisei Techno Co, 2025)

Size (Watt)	200	1000	5000	10000
Weight (kg)	20	60	620	1500

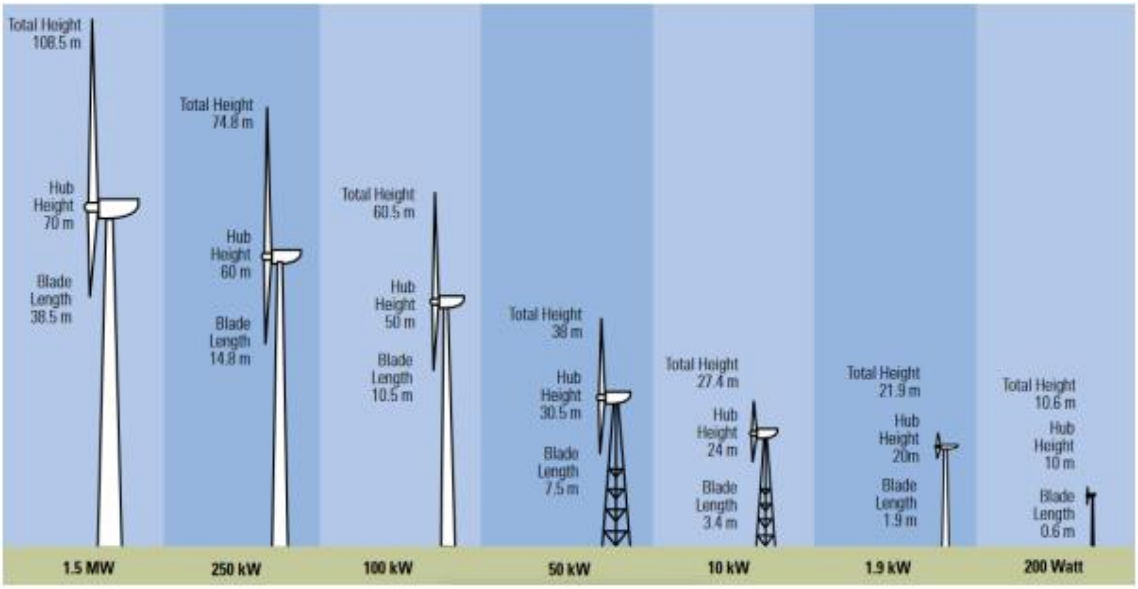

Figure 2.2. Different sizes of wind turbines (Rhoads-Weaver et al., 2013)

Figure 2.3 presents the forces at the top of the tower, where T_T and M_{RT} are the torsional and bending moments, respectively, and F_{vT} and F_{hT} are the vertical and horizontal forces. These loads are primarily induced by the turbine and are applied at the tower top. The corresponding force and moment values are taken from the structural load document provided by the turbine manufacturer, which accounts for the turbine self-weight, aerodynamic effects, and operational loading.

The 2-D force distribution along the height of the tower is illustrated in Figure 2.4, where w_h is the lateral wind load and w_v is the axial distributed load including self-weight and internal fixtures (Nicholson, 2011).

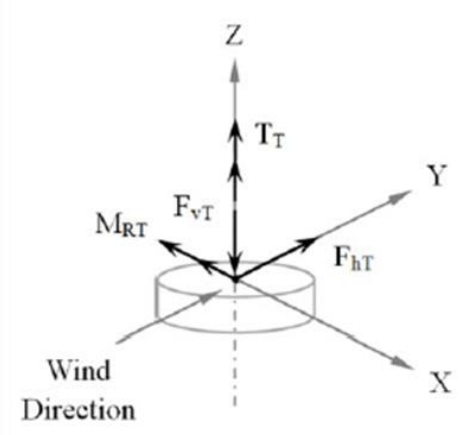

Figure 2.3. (3-D) forces at the top of the tower (Nicholson, 2011)

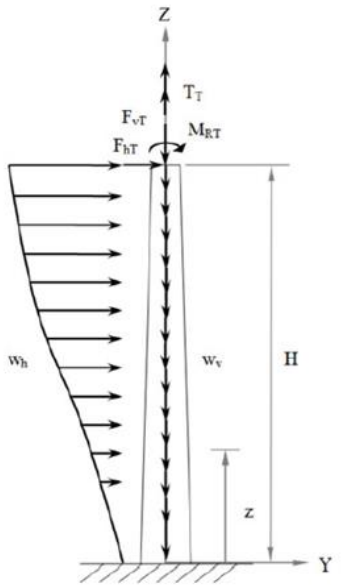

Figure 2.4. Load distribution on the wind turbine tower (Nicholson, 2011)

Loads on small wind turbines can be determined using a simple method given by IEC 61400-2. The method applies to small wind turbines fulfilling the following necessities: (I) having horizontal- axis wind turbine; (II) having 2 or more blades; (III) having a rigid hub (not teetering or hinged hub); and (iv) having cantilevered blades. Different boundaries like downwind or upwind rotor and variable or constant speed are not limited by this technique. Design loads are approximated using simple parameters such as the blade and shaft areas and the number of blades. However, multiple load cases should be considered for towers including: load case D (maximum

thrust), load case H (parked wind load), and load case I (parking wind loading, maximum exposure) (Gwon, 2011). The tower design is evaluated using a set of discrete load cases defined in IEC 61400-2, rather than combined loading scenarios. In Nicholson's study, each load case is assessed independently to identify the governing condition for structural demand. Load case D corresponds to the case of power production, while load case H is calculated when the parked wind turbine is idling or standstill. Likewise, load case I is related to parked wind turbine under fault conditions. Accordingly, only load case D and load case H are considered in this study.

For load case D, the ultimate shaft thrust load ($F_{x-shaft}$) is evaluated under an extreme wind condition according to Eq. 2.1. In accordance with IEC 61400-1, the design wind speed is taken as 2.5 times the annual average wind speed to account for severe gust events and turbulence effects. This amplification represents ultimate limit state (ULS) conditions and ensures a conservative estimation of the maximum thrust load acting on the rotor and tower. Although the aerodynamic pressure is distributed over the entire rotor disc, the resulting forces are transferred through the blades and hub and act as a resultant axial load on the main shaft. Therefore, the rotor swept area is appropriately used in the calculation of the shaft thrust force, as it represents the effective flow area interacting with the wind.

$$F_{x-shaft} = C_T \frac{1}{2} \rho (2.5 V_{ave})^2 A \qquad \text{Eq. 2.1}$$

Where C_T is the thrust coefficient, which is equal to 0.5, and ρ is the density of air, which is considered to be 1.225 kg/m^3. V_{ave} is the average wind speed and (A) is the rotor swept area.

For load case H, the horizontal drag force ($F_{x-shaft}$), with the consideration of survival wind and no fault is applied, can be calculated using Eq. 2.2. Following IEC 61400-1 and 61400-3, a drag-based formulation with the 50-year extreme wind speed and projected area of exposed components provides a conservative estimate of the load.

$$F_{x-shaft} = C_d \frac{1}{2} \rho V_{e50}^2 (A_{proj,B} B) \qquad \text{Eq. 2.2}$$

Where C_d is the drag coefficient taken as 1.5, V_{e50} is the extreme wind speed with a 50-year recurrence time interval, $A_{proj,}$ is the projected area of the blade, and B is the number of blades.

Furthermore, the aerodynamic forces on the tower and nacelle are computed via Eq. 2.3 and Eq. 2.4.

$$F_{tower} = C_{f,tower}\frac{1}{2}\rho V_{e50}^2 A_{proj,tower} \quad \text{Eq. 2.3}$$

$$F_{nacelle} = C_{f,nacelle}\frac{1}{2}\rho V_{e50}^2 A_{proj,nacelle} \quad \text{Eq. 2.4}$$

Where, $C_{f,tower}$ is the force coefficient of the tower considered to be 1.3 and $C_{f,nacelle}$ is the force coefficient of nacelle assumed to be 1.5. $A_{proj,tower}$ and $A_{proj,nacelle}$ are the projected area of the tower and nacelle, respectively.

The ultimate flap bending moment, M_{yB}, is calculated according to the Eq. 2.5.

$$M_{yB} = (C_d\frac{1}{2}\rho V_{e50}^2 A_{proj,B})(\frac{1}{2}R) \quad \text{Eq. 2.5}$$

Where R is the radius of the wind turbine.

For spinning or furling turbines, $F_{x-shaft}$ and M_{yB} are modified as follows:

$$F_{x-shaft} = (0.34\lambda_{e50}^2)\frac{1}{2}\rho V_{e50}^2 (A_{proj,B}B) \quad \text{Eq. 2.6}$$

$$M_{yB} = [(C_{l,max}\frac{1}{2}\rho V_{e50}^2 (\frac{1}{2}A_{proj,B})](\frac{2}{3}R) \quad \text{Eq. 2.7}$$

Where λ_{e50} is the 50-year extreme tip steep ratio and $C_{l,}$ is the maximum lift coefficient at the tip that is considered to be 2.0.

2.2. Previous research on wind turbine towers

There are no previous studies on CFFT wind turbine towers. Polyzois et al. (2009) evaluated the structural performance of GFRP wind turbine towers, including static and dynamic behaviour, through experimental and numerical studies. Two jointed scaled 4.88 m towers were tested as cantilevers for the experimental investigation. The towers were comprised of multi-cell sections, each section made of eight filament wound cells connected with each other by resin applied over their surface. The test program was completed in four phases. Phase I had two single GFRP cells tested as cantilevers to find the ultimate strength and determine the mode of failure. Phase II consisted of one single GFRP cell with several lengths that were verified under compression. In Phase III, a static load was applied to two GFRP multi-cell towers. In Phase IV, a dynamic loading was applied to the two GFRP multi-cell towers.

The two single GFRP cells used for Phase I had an average length of 2.44 m. The GFRP fibre orientations for each cell were (-86, +86, 0, -86, and +86) with an average thickness of 4.5 mm. Figure 2.5 presents the dimensions of the cell sections. The samples were embedded evenly into a composite sleeve, which was connected to the test fixture as illustrated in Figure 2.6. The load was applied to the specimen through a cable connected about 78 mm from the tip.

For Phase II, a compression test was used to estimate the buckling performance of the single cells. Two samples with heights of 1280 mm and 1780 mm were tested. The same cross-sectional properties and lamina fiber orientation as in Phase I was used for these specimens.

In Phase III, two jointed GFRP towers were tested under static lateral load conditions. The motivation behind these tests was to evaluate the structural performance of the multi-cell towers and confirm the finite element model used to evaluate the final results. The sectional properties are shown in Figure 2.7 and the testing setup is illustrated in Figure 2.8.

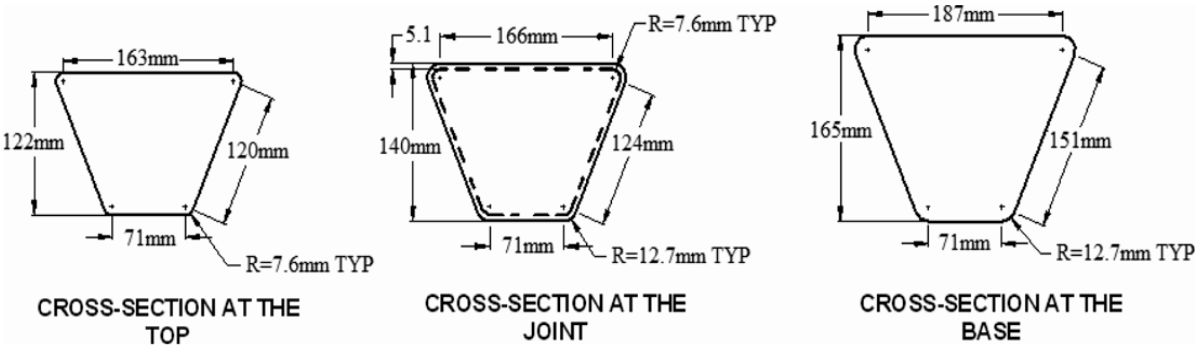

Figure 2.5. Single-cell cross-sectional details (Polyzois et al. 2009)

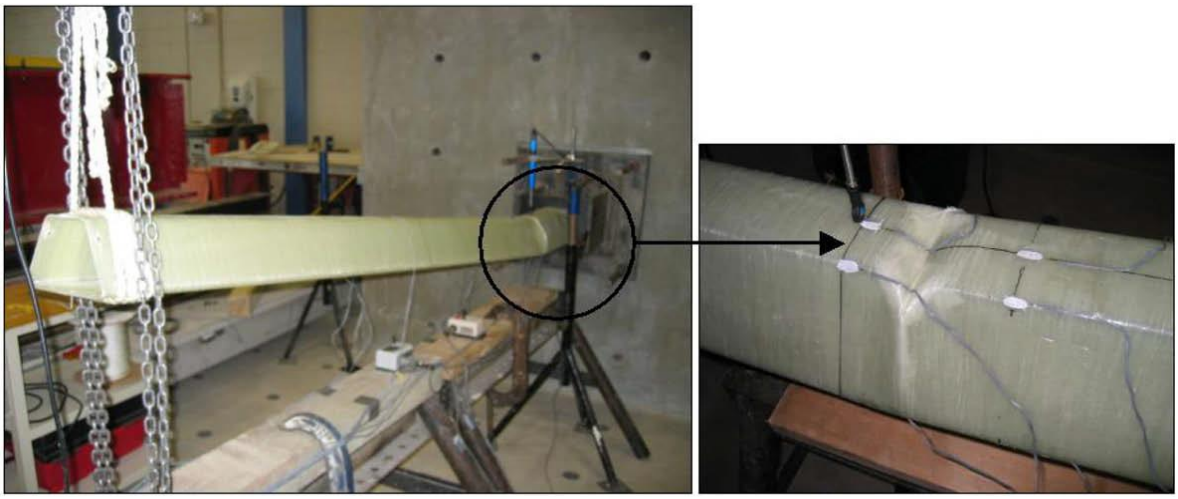

Figure 2.6. Phase I specimen after testing (Polyzois et al. 2009)

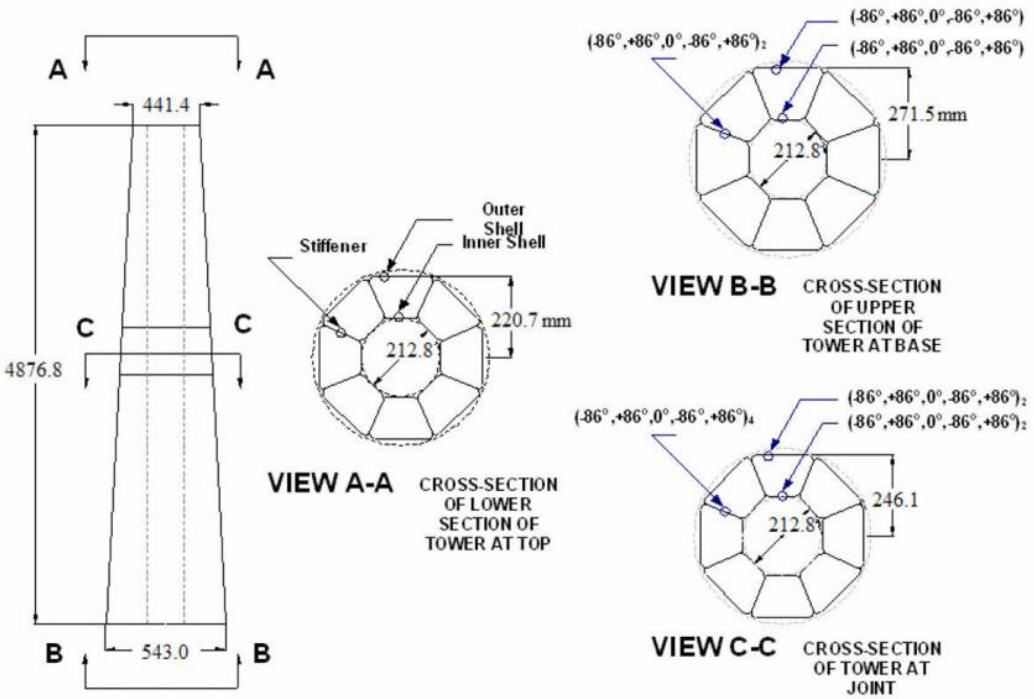

Figure 2.7. Sectional properties for the tested towers in Phase III (Polyzois et al. 2009)

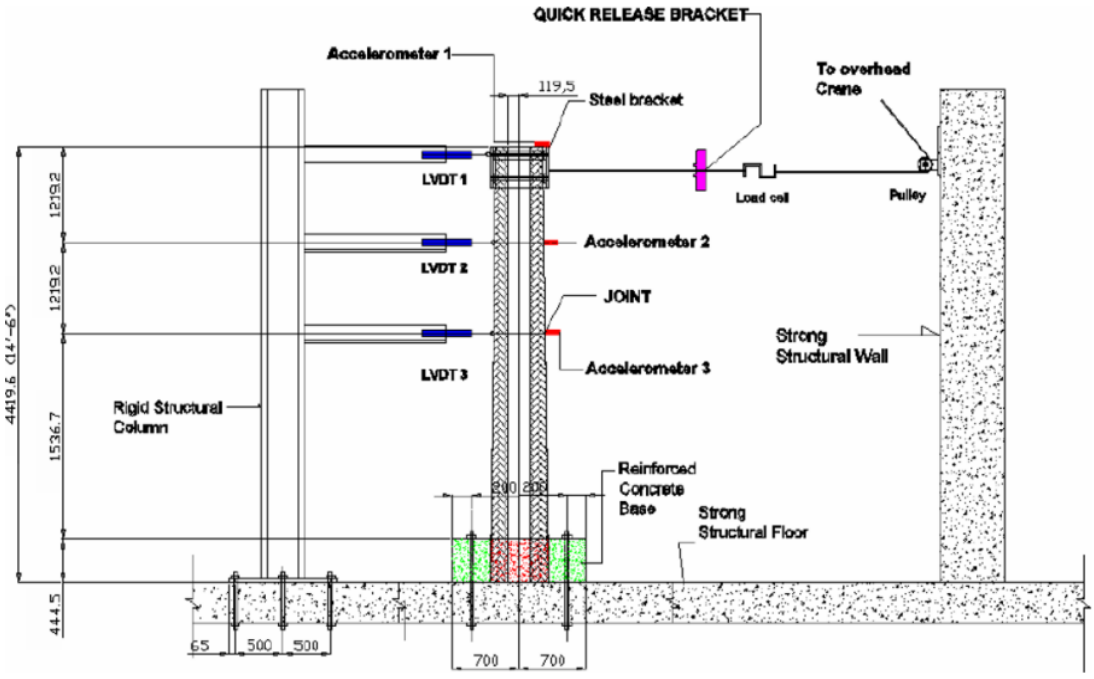

Figure 2.8. Dynamic testing setup for Phase IV (Polyzois et al. 2009)

The top and the mid-height lateral displacement for the specimens in Phase III is illustrated in Figure 2.9. The results showed that there was a slip between the tower and the solid base; therefore, an additional deflection was added to the towers' tip. The maximum flexural stiffnesses of the two towers were 293.41 kN/m and 283.22 kN/m, respectively.

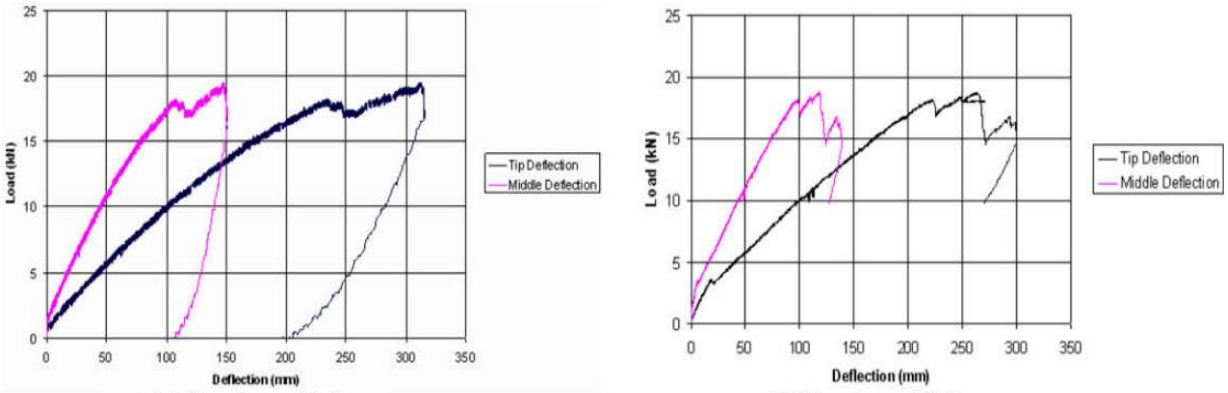

(a) Specimen P3-1 (b) Specimen P3-2

Figure 2.9. Top and mid height deflection for specimens in Phase III (Polyzois et al. 2009)

Table 2.2 shows the ultimate load and deflection for the two towers, which failed by shear rupture near the support (P3-1) and local buckling close to the support (P3-2). Figure 2.10 shows the damage within the bottom part of the specimens at the ultimate load.

For Phase IV, an overhead crane was used to apply the desired loads based on the pre-determined displacement of the tower. The load was released after reaching the desired displacement and the tower vibrated until the point that it arrived at a complete stop. The first test was conducted with a mass of 134.5 kg, same as the tower mass, added to the top of the tower and applying 28 mm lateral displacement. The second test was conducted without an additional mass. A single degree of freedom model was used to study the swaying of the towers. The dynamic properties for the towers are summarized in Table 2.3.

Comparisons of finite element models and experimental load-deflection curves are illustrated in Figure 2.11 for Phase I and Figure 2.12 for Phase III. The maximum load was determined using buckling analysis.

Table 2.2. Maximum load and deflection for Phase III (Polyzois et al.2009)

Specimen	Ultimate Load (kN)	Tip deflection at ultimate load (mm)	Stiffness (kN/m)
P3-1	19.48	78.21	293.41
P3-2	18.74	75.59	289.22
Average	19.11	76.9	291.32
C.O.V. (%)	2.74	2.41	1.02

Shear rupture of specimen P3-1

Local buckling failure specimen P3-2

Figure 2.10. Damage on specimens at maximum load (Polyzois et al. 2009)

Table 2.3 The dynamic properties for the towers in Phase IV (Polyzois et al. 2009)

Dynamic properties	Tower with a mass on top	Tower without a mass on top
Damped period T_d (s)	0.137	0.074
Damped natural frequency, f_d (Hz)	7.31	13.47
Damped circular frequency, ω_d (rad/s))	45.80	84.66
Logarithmic decrement, δ	0.050	0.10
Damping factor, C_c	0.011	0.016
Undamped circular frequency, ω_n (rad/s)	45.80	84.67
Damped natural frequency, f_n (Hz)	7.23	13.48
Bending stiffness (kN/m)	282.2	290.1

Where, f_d is the experimental natural frequency, and f_n is the finite element predicted natural frequency.

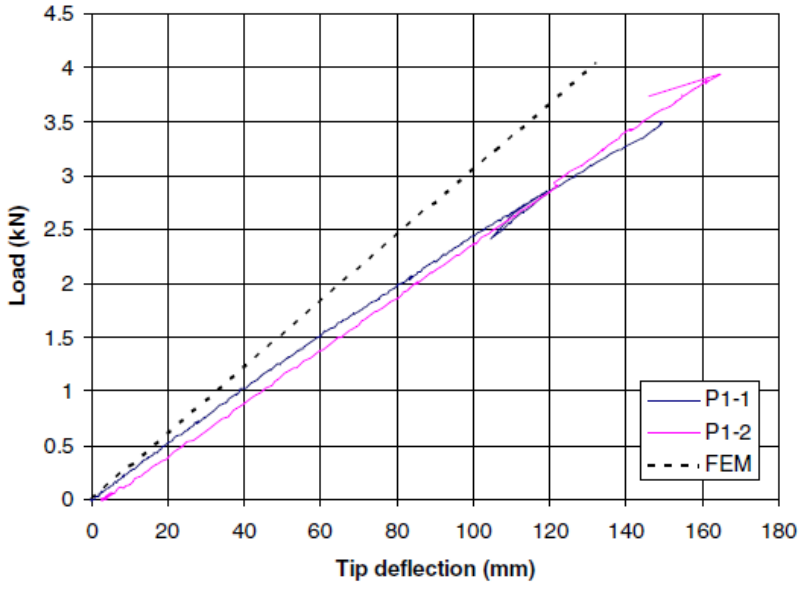

Figure 2.11. Comparison between load-tip deflection relationships computed using F.E.M with experimentally recorded results for Phase I (Polyzois et al. 2009)

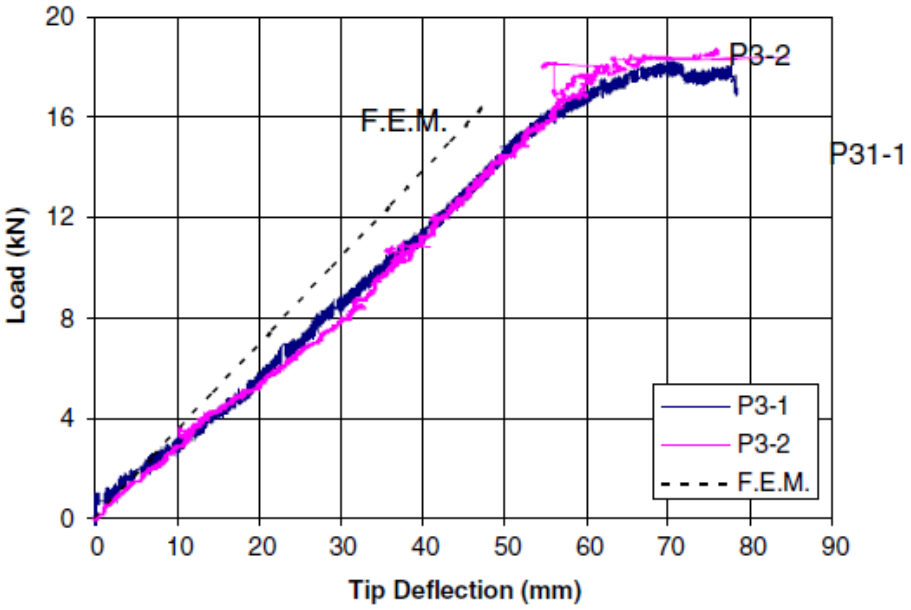

Figure 2.12. Phase III comparison between load-tip deflection relationships computed using F.E.M with experimentally recorded results (Polyzois et al. 2009)

Figure 2.12 shows that the finite element model gives a decent expectation of the FRP tower's performance in Phase III but shows a slightly stiffer response than the experimental results. Moreover, the finite element results indicate a linear relationship for the load-tip deflection while the towers' experimental results show a linear behaviour up to about 84% of the maximum load. After exceeding 84% of the applied load, the load behaviour changed to nonlinear. These consequences can be explained by the increasing degree of damage at the bottom and the progressive failure of the towers.

Phase IV was analyzed using the same finite element model, for free vibrations, frequencies, and corresponding periods. Errors of about 0.5% were seen between the tower's test results and FE outcomes. In addition, the average of the maximum load-carrying capacity and tip deflection of the two tested towers (P3-1 and P3-2) were 19.11 kN and 76.90 mm, respectively. The results indicated that the elastic jointed connection had no impact on the dynamic performance of the tower.

2.3. Concrete filled FRP tubes

2.3.1. Dynamic Behaviour of Concrete Filled FRP Tubes

Qasrawi et al. (2015) investigated the dynamic behaviour of concrete filled FRP tubes subjected to impact loading. The investigation's objective was to compare the dynamic response of CFFTs to traditional reinforced concrete (RC) specimens under controlled impact scenarios.

The experimental methodology involved subjecting six full-scale specimens—comprising both CFFTs and RC members—to monotonic and impact testing, with varying reinforcement ratios and kinetic energy inputs. The impact tests used a 561 kg hammer dropped from incrementally increasing heights to simulate real-world loading conditions, as illustrated in Figure 2.13 (a) and (b).

The comparative analysis showed that the GFRP tubes significantly enhanced the energy absorption and impact resistance of the concrete core. Specifically, CFFTs demonstrated a 487.5% increase in energy absorption during monotonic tests compared to RC members (Figure 2.4 (a) and (b)). Under impact conditions, the CFFTs exhibited improved energy absorption by up to 1223%, with the performance varying based on the reinforcement ratio.

Another critical finding was the superior ductility and failure resistance exhibited by CFFTs. The GFRP tubes confined the concrete, preventing common failure mechanisms such as spalling and crushing, which are typically observed in conventional RC members (Figure 2.14 (a) and (b)).

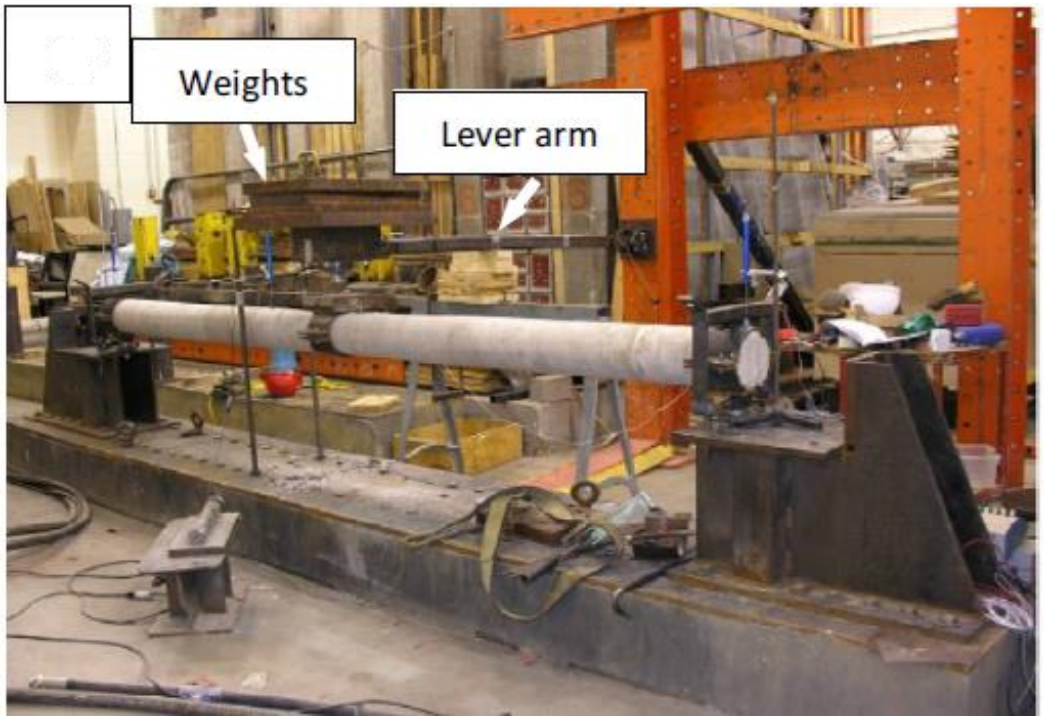

(a)

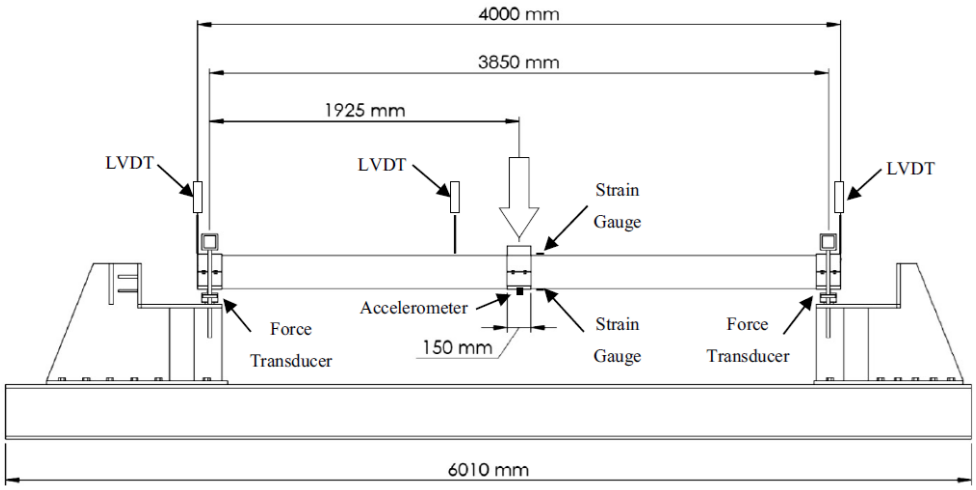

(b)

Figure 2.13. (a) photo of impact testing setup and (b) schematic of impact (Qasrawi et al. 2015)

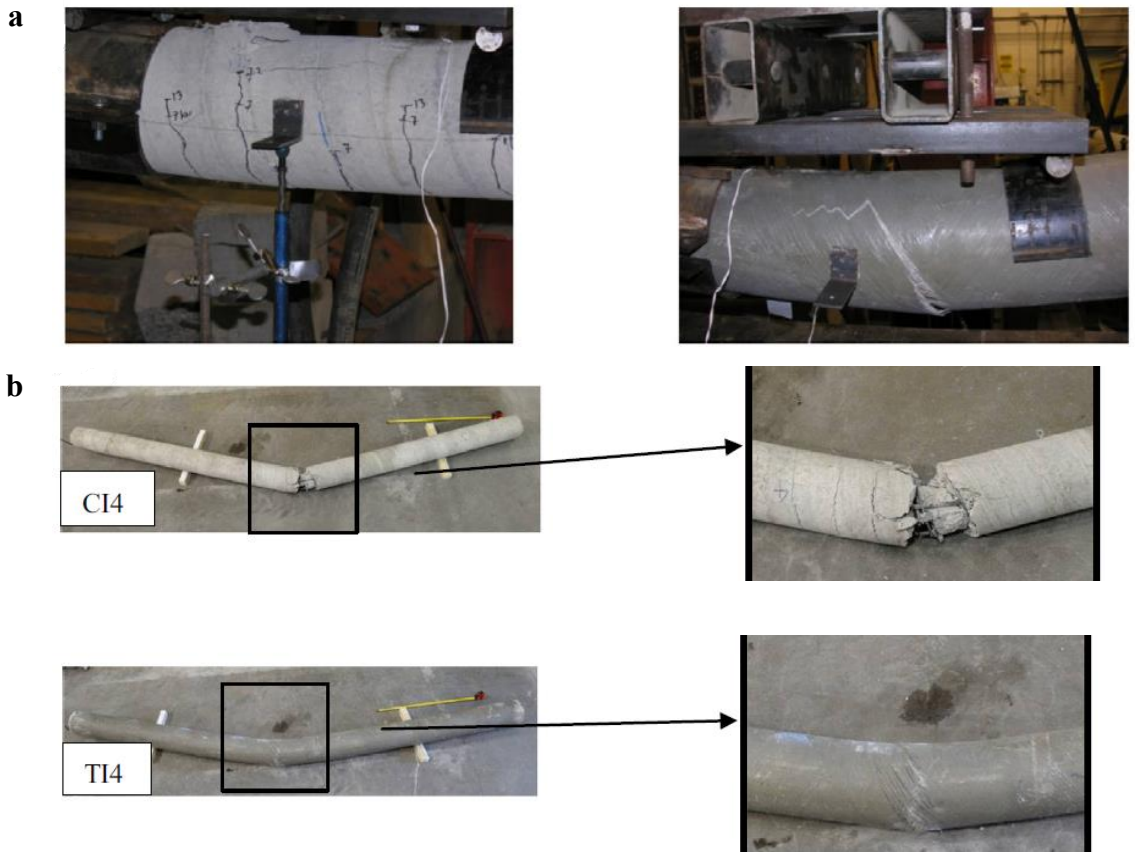

Figure 2.14. Failures mechanisms of (a) monotonic specimens and (b) impact specimens (Qasrawi et al. 2015)

This enhanced ductility and the ability of the GFRP tubes to delay concrete core failure suggest that CFFTs are highly suited for structural applications that require robust performance under dynamic loading, such as wind turbine towers in remote areas. Given that these towers must withstand extreme weather conditions, ice shedding, high winds, and potential risks posed by seismic forces, the resilience of CFFTs under high strain rates can help enhance durability and reduce maintenance needs.

A numerical single degree of freedom (SDOF) model was developed to simulate the dynamic response of CFFTs. The model incorporated parameters like damping and strain rate effects and was validated against the experimental displacement-time histories, demonstrating strong predictive accuracy as shown in Figure 2.15.

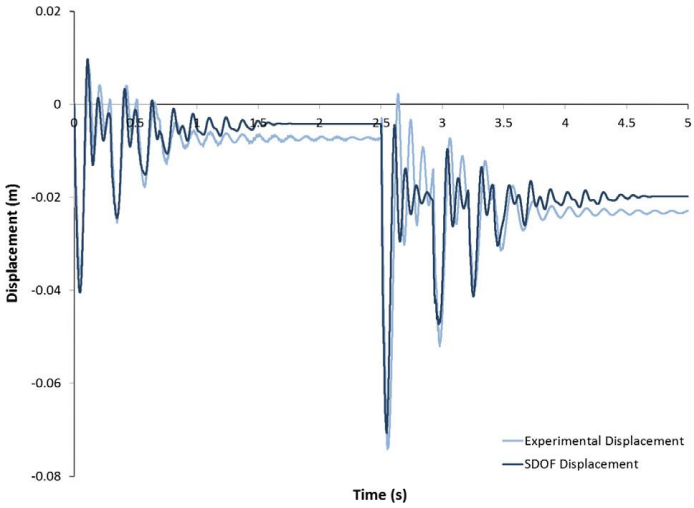

Figure 2.15. Measured and SDOF result displacements for specimens (Qasrawi et al. 2015).

The study also proposed a simplified energy-based design method for dynamically loaded structures, leveraging conservation of energy principles and the derived resistance functions to estimate maximum displacements and structural damage.

2.3. 2. Flexural behaviour

Fam et al. (2003) investigated the flexural behaviour of precast CFFT composite piles. Two full-scale composite piles were lab tested using a four-point bending setup while a full scale square precast composite concrete pile was tested in the field. The details for the square prestressed concrete piles and the GFRP tubes are shown in Figure 2.16 (a) and (b), respectively. The mechanical properties of the GFRP are provided in Table 2.4. The moment curvature response of the two identical composite piles is shown in Figure 2.17. The composite piles reached an average ultimate moment capacity of 502 kN.m, while the cracking moment was 126 kN.m. The figure shows vertical drops in the moment curve when cracks occurred since the piles were tested under displacement control. Furthermore, the behaviour of the composite piles after the first crack became almost linear. A slip between the concrete core and the FRP tube was noticed at each end of the specimen after testing. The laboratory test showed a flexural failure on the tension side, while the specimen remained in one piece and was able to hold the dead weight after failure. The rupture of fibers is illustrated in Figure 2.18(a). Figure 2.18(b) shows the compression zone of the concrete core at the failure location after testing.

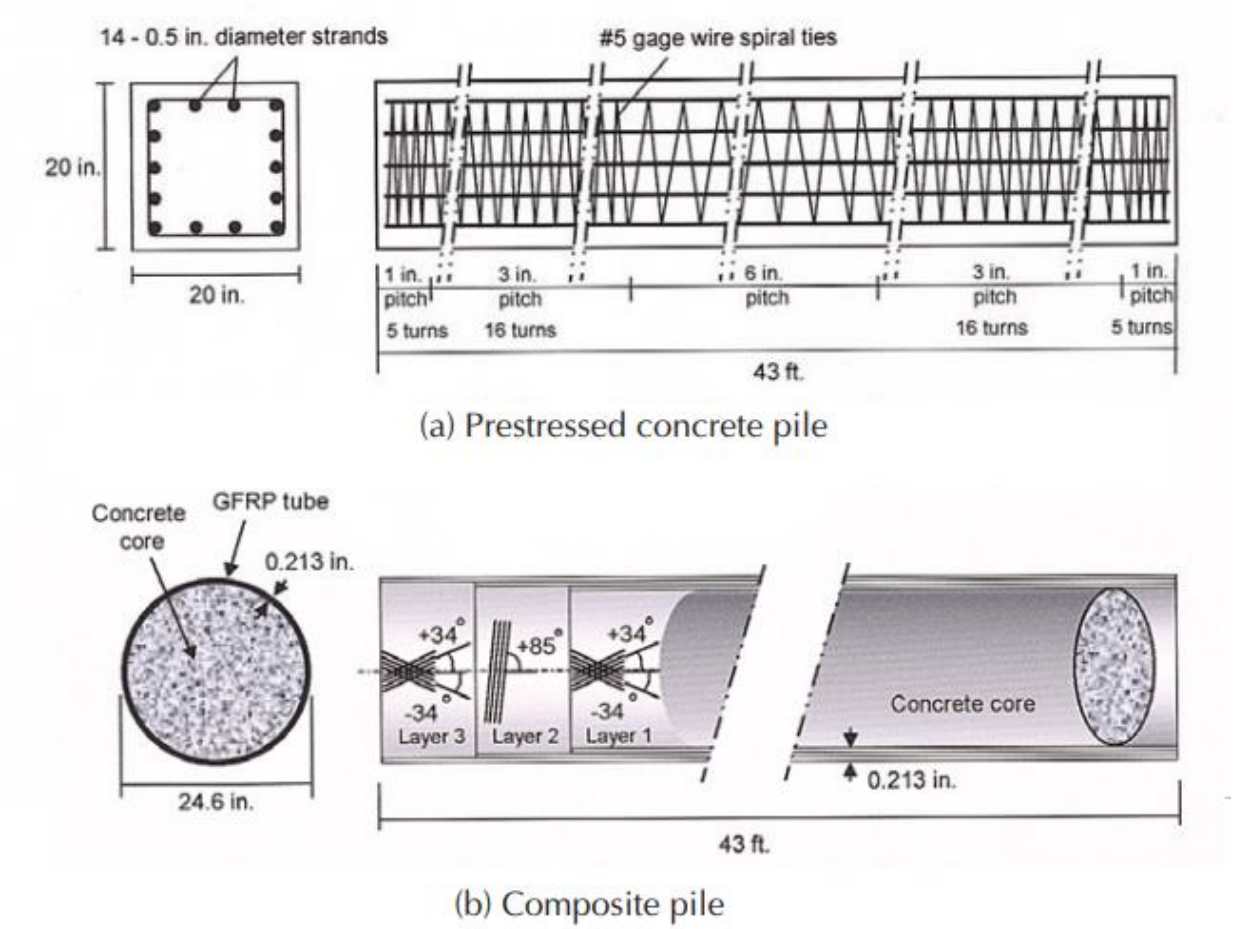

Figure 2.16. Details of (a) Prestressed concrete pile; (b) Composite pile (Fam et al. 2003).

Table 2.4. Mechanical properties of composite GFRP tube (Fam et al. 2003).

Mechanical property	Axial direction			Hoop direction
Tensile strength (MPa)	217.9*	206.6†	249.6‡	353.0‡
Compressive strength (MPa)	104.1‡			N/A
Elastic modulus (MPa)	15142.9*	15161.6†	16567.0‡	17698.9‡
Poisson's ratio	0.32‡			0.34‡

Where: * Coupon test, † Manufacturer, and ‡ Lamination theory.

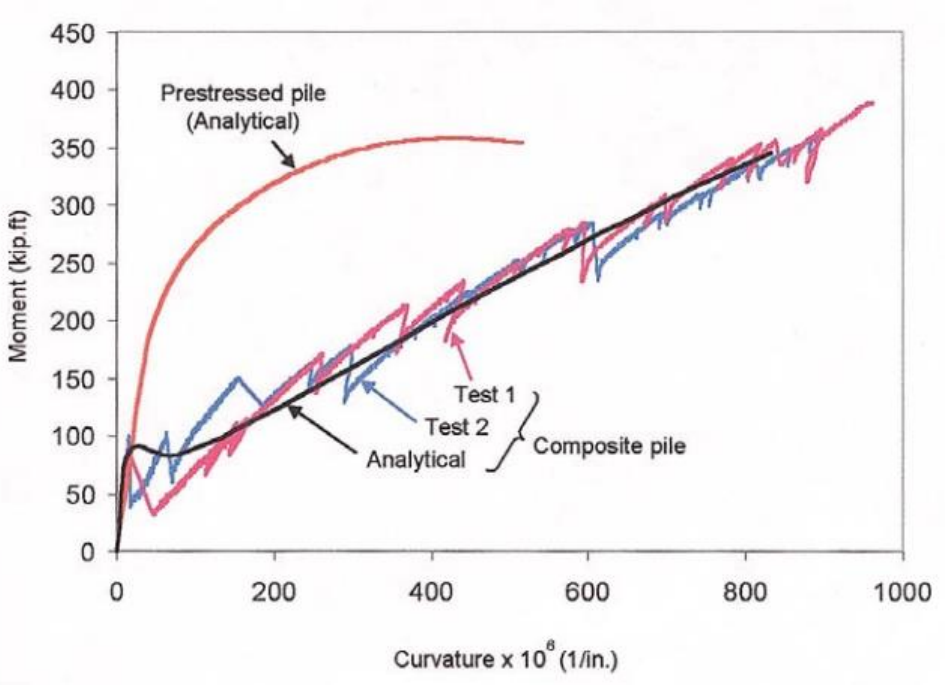

Figure 2.17. Moment- curvature responses of the composite and prestressed concrete piles (Fam et al. 2003).

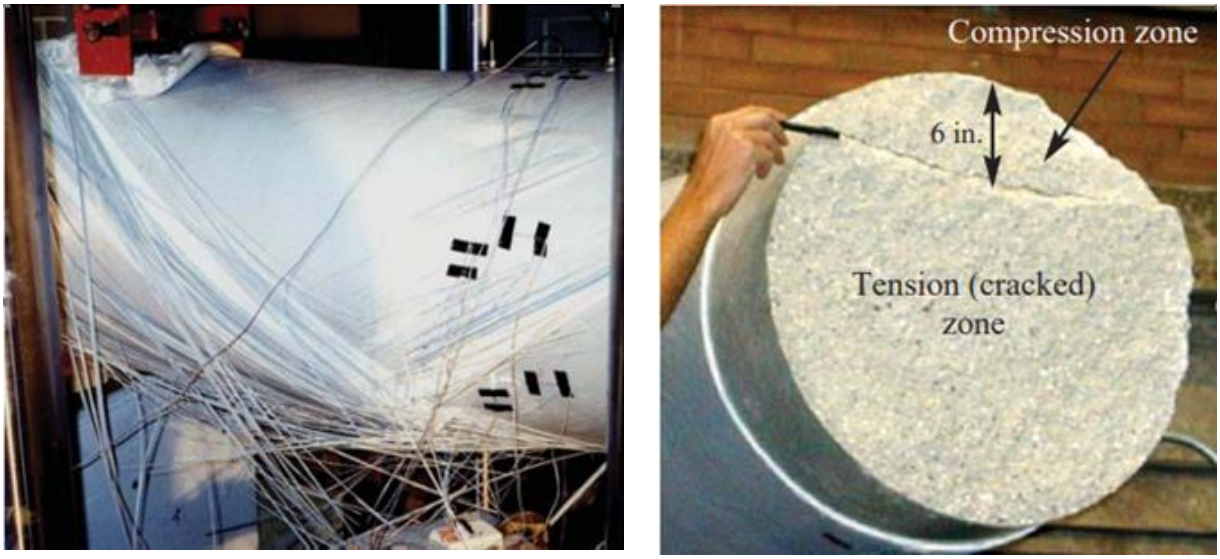

(a) Tension failure by rupture of FRP tube

(b) Cross section at failure location

Figure 2.18. Flexural tension failure of the composite pile (Fam et al. 2003).

For the modeling phase, a modified Ramberg- Osgood function was used to model the stress-strain relationship of the prestressing steel strands. The nonlinear stress-strain relationship of the concrete was modeled by using a generalized expression given by Popovics. The moment-curvature behaviour of the prestressed concrete pile with respect to maximum concrete compressive strain equal to 0.003 is illustrated in Figure 2.17. The moment-curvature response for the CFFT piles was also calculated according to an equilibrium and strain compatibility method. The section was divided into horizontal layers and a linear stress-strain relationship for the GFRP tube was considered. The force for the concrete and the FRP tube were calculated according to numerical integration. Then, the internal moment was determined based on the calculated forces at different strain levels. Figure 2.17 shows that the stiffness of the composite pile is considerably decreased, because of the lower elastic modulus of GFRP in compression to that of steel strands and the presence of a prestressing system.

A lateral test also was conducted on the composite and prestressed piles. The applied load and lateral displacement of the pile at different heights was conducted. Each pile was exposed to four loading cycles with increasing magnitude of the load. The lateral load versus lateral deflection response is illustrated in Figure 2.19.

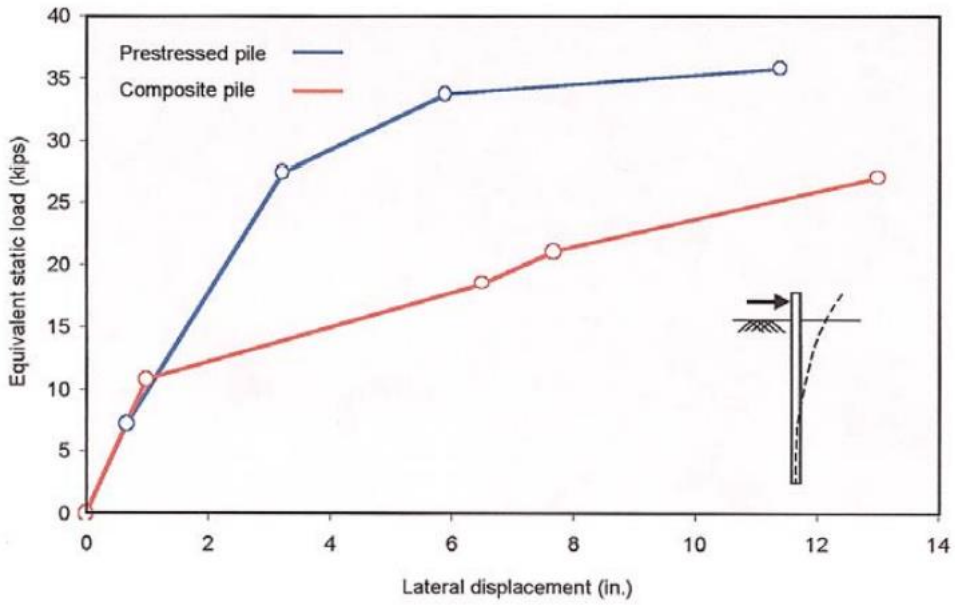

Figure 2.19. Lateral load versus deflection response of piles (Fam et al. 2003).

A similar moment capacity was observed for the prestressed concrete and the composite piles as illustrated in Figure 2.17. A sudden change in stiffness of the composite pile can be observed after cracking. The stiffness of the prestressed pile was improved due to the prestressing effect and the higher elastic modulus of steel. The results indicate that prestressing can enhance the stiffness of the specimens and improve their serviceability. Likewise, including the prestressing can add redundancy to the system.

Fam and Rizkalla (2001) investigated the behaviour of concrete-filled hollow GFRP tubes for axial and axial-flexural loading. The authors evaluated the effect of a hollow core on the confinement effectiveness of the exterior shell. The study showed that using GFRP tubes improves concrete confinement. This in turn results in further improvement of concrete compressive behaviour with increased strength and ductility. The highest confinement level was reached for entirely filled tubes. The central hole inside the tube reduced the confinement influence. However, adding an inner tube for these type of members can improve the confinement effects.

Helmi et al. (2006) investigated the effects of driving forces and bending fatigue on the structural performance of CFFTs. The study shows that driving forces had a minor effect, about a 5% reduction, on the flexural strength of CFFT piles. Besides, in comparison to a conventional square prestressed concrete pile of similar moment capacities, it was observed that the CFFT piles had a greater deflection than the prestressed piles. Furthermore, a reversed high-cycle bending test was performed on a full-scale CFFT pile. The support system was designed to take into account the push-pull loading and possible horizontal movement along with the pile height. According to the results obtained from the tests, the authors recommended using a service moment of 20%–30% of the ultimate moment to reach at least 1 million cycles.

Another study also indicates that adding a prestressing system to CFFTs subjected to bending improves the serviceability and activates the confinement mechanism of the concrete core restrained by the tube (Fam and Mandal, 2006). The research shows that this confinement should be considered in the design and ignoring this fact would greatly underestimate the flexural strength. However, the tube's thickness and laminate orientation have a greater effect on flexural strength in comparison to the number of prestressing strands (Mandal and Fam, 2006).

Mohamed & Masmoudi (2010) investigated the behaviour of reinforced CFFT beams. The research was conducted based on an experimental and theoretical study. The experiment phase consisted of ten beams tested under four-point bending load. Six beams were reinforced with GFRP bars while the other four were reinforced with traditional steel bars. Filament wound GFRP tubes were used as stay-in-place formwork. Two concrete mixes with compressive strengths of 30 and 45 MPa were used for the beams, mild steel bars with 3.4 (mm) diameter as spiral reinforcement for the control specimens, and deformed 15M steel bars for CFFT beams were used. In addition, sand-coated glass FRP bars were used as longitudinal reinforcement for some CFFT specimens. Furthermore, two types of FRP tubes (A and B) with different thicknesses and having the same internal diameter were targeted for this research.

Table 2.5 and Table 2.6 present the dimensions and details of specimens in each group, respectively. The detailed description of the test setup is illustrated in Figure 2.20.

Table 2.5 Dimension and mechanical properties of FRP tubes (Mohamed & Masmoudi, 2010).

Tube Type	D (mm)	t_{frp} (mm)	No. of Layers	Stacking Sequence	E_{ty} (MPa)	F_{ty} (MPa)	E_{ex} (MPa)	F_{tx} (MPa)	Fc (MPa)
A	213	2.9	6	$[60, 90_4, 60]$	32260 [a]	537 [a]	8865 [b]	55.16 [b]	135 [b]
B	213	6.4	12	$[\pm60, 90_2, \pm60, 90_6]$	30200 [a]	498 [a]	7897 [b]	59.24 [b]	138 [b]

E_{tx} and E_{ty} are, respectively, the Young Modulus in the longitudinal and hoop directions; F_{tx} and F_{ty} are, respectively, the ultimate tensile strength in the longitudinal and hoop directions.

[a] Calculated using lamination theory

[b] Based on coupon test.

Table 2.6. Details of specimens and summary of test results (Mohamed & Masmoudi, 2010).

Group No.	ID	Diameter (D = mm)	Shear reinforcement	Flexural reinforcement (ratio)	Concrete strength (MPa)	Moment (kN m)			Deflection [a] (mm)	Comp strain [b] (με)	Failure mode	Ductility (kN m)
						Crack	Yield	Ultimate				
	C305	203	–	6 No. 15M Steel bars (3.65)		3.84	24.86	32.85	11.99	2633	DT	0.78
	C3305	203	Steel spiral	6 No. 15M Steel bars (3.65)		4.88	26.4	48.95	136.25	3959	SC	17.75
Group No. 1	A305	213	Tube A	6 No. 15M Steel bars (3.65)	30	6.36	37.21	75.75	124.91	15160	FL	32.4
	A306	213	Tube A	6 No. 5 GRP bars (3.65)		5.09	—	46.33	43.13	6017	FL	5.78
	B306	213	Tube B	6 No. 5 GRP bars (3.65)		5.55	—	56.68	38.68	6479	FL	8.77
	C45G	203	–	6 No. 5 GRP bars (3.65)		4.24	—	24.67	24.33	2628	DT	1.09
	C545G	203	Steel spiral	6 No. 5 GRP bars (3.65)		4.40	—	44.55	57.47	3124	SC	5.53
Group No. 2	A45G	213	Tube A	6 No. 5 GRP bars (3.65)	45	5.09	—	48.53	45.14	5415	FL	5.92
	B45G	213	Tube B	6 No. 5 GRP bars (3.65)		6.24	—	64.78	43.75	7009	FL	9.76
	A455	213	Tube A	6 No. 15M Steel bars (3.65)		7.16	40	75.84	126.69	10629	FL	34

[a] The experimental results at the ultimate load; DT= diagonal tension failure; SC= shear compression failure; FL= flexural failure.

[b] At the top side of the tube.

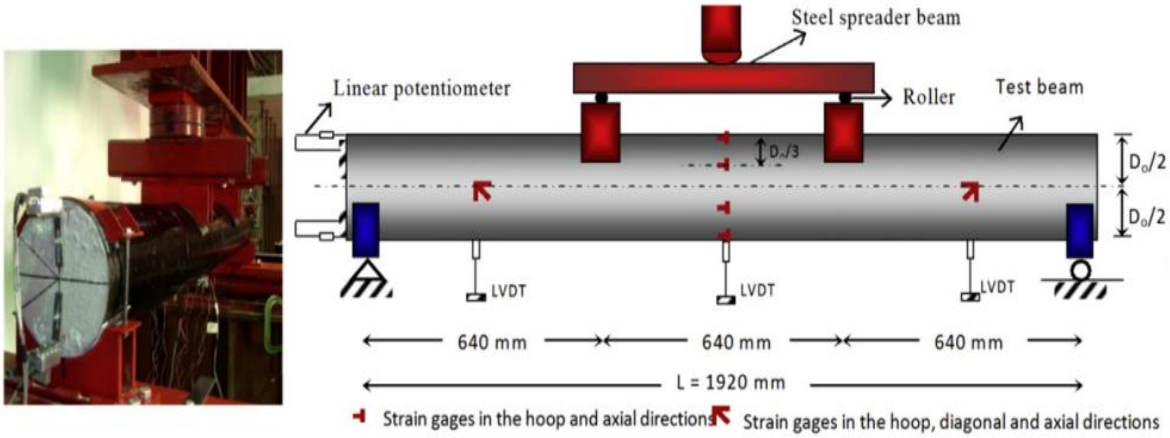

Figure 2.20. (a) Side view (b) Schematic of test setup (Mohamed & Masmoudi, 2010).

The results indicated that beams with GFRP tubes had a higher flexural strength by up to 113% compared to beams with steel spiral reinforcement. Figure 2.21 illustrates the results for CFFT specimen A30S, which exhibited a higher stiffness than CS30S specimens with steel spiral reinforcement. Likewise, the ductility of CFFTs was found to be higher as shown in Figure 2.22. The notable increase in performance of CFFTs is due to the larger confinement area that covers the entire concrete core. The GFRP tubes simultaneously offer reinforcement in the longitudinal direction and continuously confine the concrete core, while the steel spiral reinforcement can be influenced by spalling and crushing.

In addition to the improvement in ductility, the enhancement in the flexural strength for A30S (steel reinforcement) compared to A30G (GFRP reinforcing bars) is shown in Figure 2.22. The steel-reinforced beam also had a higher stiffness before and after yielding by about 61% and 49%, respectively.

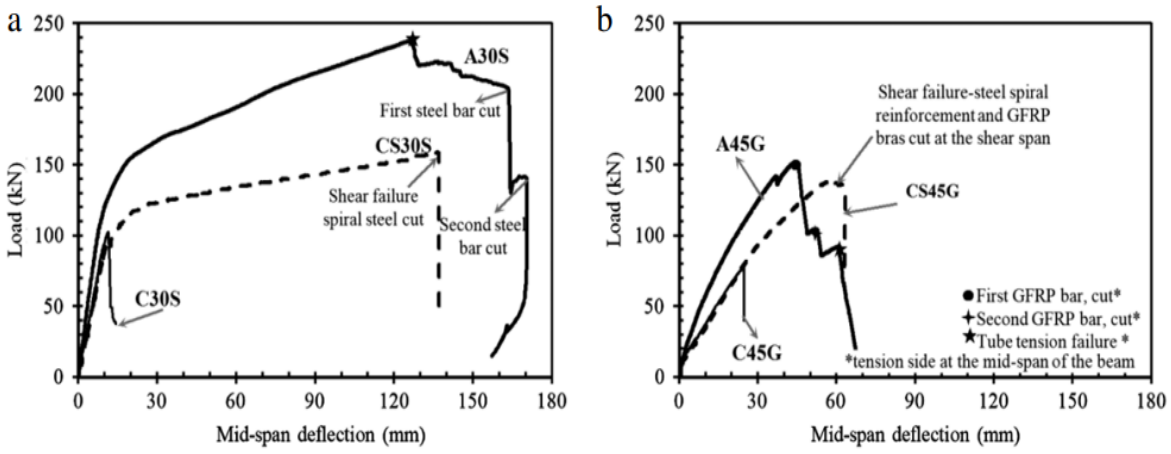

Figure 2.21. Effect of the type of transverse reinforcement on load–deflection curves (Mohamed & Masmoudi, 2010).

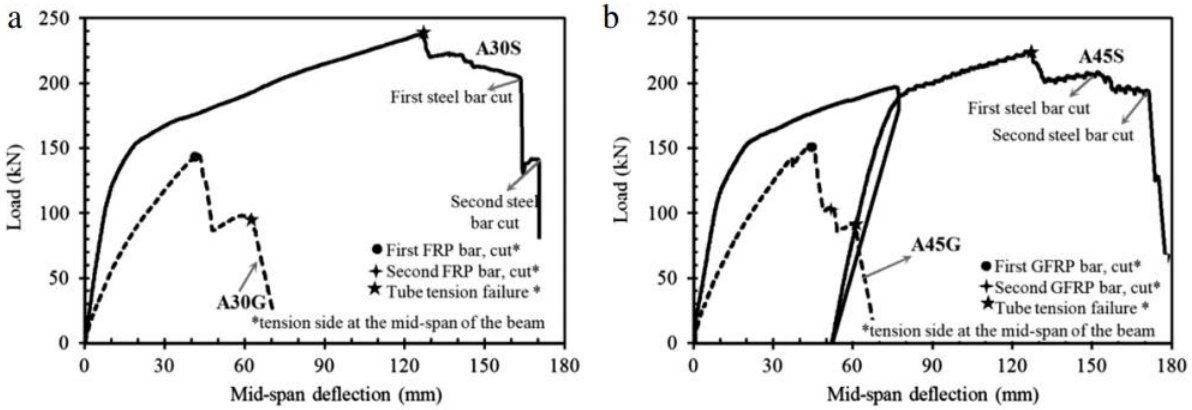

Figure 2.22. Effect of the type of flexural reinforcement on load–deflection curves (Mohamed & Masmoudi, 2010).

In another study, prestressed CFFT members were found to have higher strength, ductility, and energy absorption capacity compared to non-prestressed specimens (Vincent & Ozbakkaloglu, 2015). Moreover, the ultimate compressive strength increases, while the ultimate axial strain can be increased if the prestressed CFFT is properly confined. Furthermore, when high-strength concrete is used for the prestressed CFFT, the system can reduce the risk of having strength loss and brittle failure (Vincent & Ozbakkaloglu, 2015). Another study showed that circular tubes have better performance than rectangular tubes, but in some cases, rectangular tubes are preferable. The lateral pressure in the case of rectangular tubes is not constant around the section, and the concrete between the corners is not confined nearly as much as the corner regions where the lateral constraining forces provide much higher lateral pressures. Therefore, confinement effectiveness increases as the corner radius increases (Ozbakkaloglu, 2013a).

2.3. 3. Torsional Behaviour

St. Onge and Fam (2021) investigated the torsional behaviour of circular CFFTs to evaluate the effect of concrete infill on their performance under pure torsion. The experimental program involved testing six specimens, each with a diameter of 168 mm. The samples consisted of two hollow FRP tubes and four CFFTs with different concrete filling configurations and 1,800 mm in length, including two 400-mm square end blocks (Figure 2.23). The six tubes were divided into

two types based on their laminate structures. The geometric details of the FRP tubes and the mechanical properties of the FRP tubes are provided in Table 2.7 and Table 2.8, respectively.

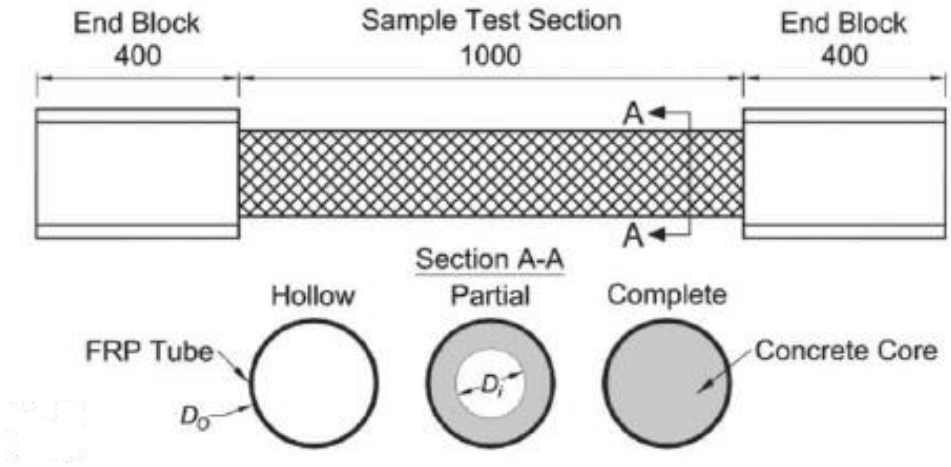

Figure 2.23. Sample geometric of CFFT (dim. in mm) (St. Onge and Fam, 2021).

Table 2.7. FRP tube structure (St. Onge and Fam, 2021).

Tube	Wall thickness (mm)			V_f (%)[a]	Laminate designation	θ_L or t_L[b]	Structural layer lamina						
	External coating	Structural layer (t_S)	Inner liner				1[c]	2	3	4	5	6	7
Type I	0.22	2.35	0.65	55	Cross-ply	θ_L	+86	−10	+86	−10	+86	−10	+86
						t_L	0.261	0.333	0.273	0.266	0.253	0.239	0.720
Type II	0.28	3.36	0.72	55	Angle-ply	θ_L	+55	−55	+55	−55	—	—	—
						t_L	0.841	0.884	0.807	0.829	—	—	—

Table 2.8. FRP tube properties (St. Onge and Fam, 2021).

Tube	Longitudinal tensile						Hoop tensile			In-plane shear
	Manufacturer			Coupon test			Manufacturer			Torsion test
	f_{xt} (MPa)	E_x (GPa)	ν_{xy}	f_{xt} (MPa)	E_x (GPa)	ν_{xy}	f_{yt} (MPa)	E_y (GPa)	ν_{yx}	G_{xy} (GPa)
Type I[a]	241	20.7	0.16	226.7	23.2	0.14	483	29.0	0.26	5.2
Type II[b]	58.6	11.0	0.37	73.3	11.8	0.44	165[c]	25.2	0.56	13.8

Concrete filling had a noticeable effect on enhancing the torsional strength and rigidity of the tubes. Concrete-filled specimens demonstrated a 250% increase in ultimate torque over the hollow

tubes, owing to the ability of the concrete core to prevent buckling and to reinforce the structural integrity of the FRP tube as shown in Figure 2.24.

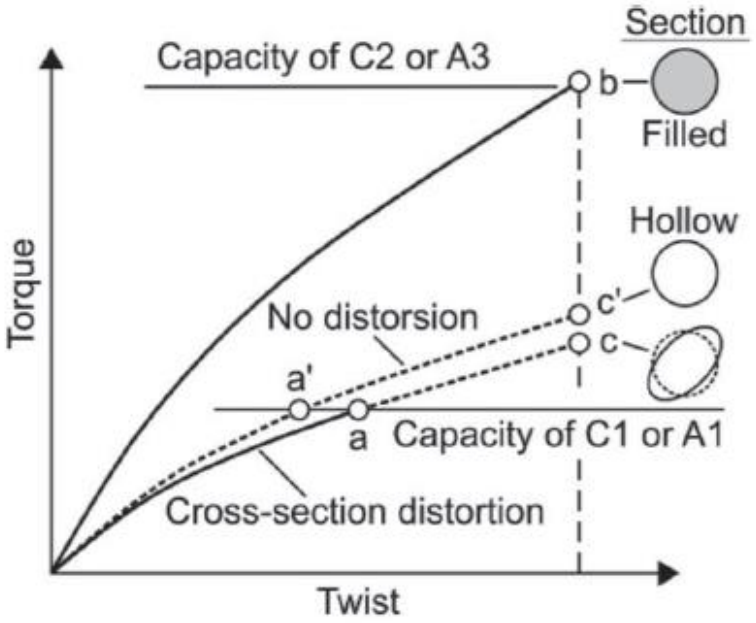

Figure 2.24. Conceptual illustration of the effect of concrete filling on the hollow tube (St. Onge and Fam, 2021).

Similarly, the twist angles of the CFFTs were improved by 14% and 45% for near-cross-ply and angle-ply tubes, respectively. The torque–twist behaviour of the hollow FRP tubes and CFFTs is illustrated in Figure 2.25 and Figure 2.26, respectively.

The main difference between Type I and Type II tubes comes down to how their fibers are arranged. Type I tubes used a near-cross-ply arrangement, with most fibers running along the hoop and length of the tube at $[+86°/-10°/+86°/-10°]_s$. This setup made them unbalanced and more dependent on the matrix to carry loads, which led to a more nonlinear response and lower torsional strength overall. In contrast, Type II tubes had a more balanced angle-ply design, with fibers oriented at $[\pm 55°]_2$. This orientation lined up better with the directions of stress that develop during twisting, making Type II tubes noticeably stiffer, stronger, and better able to resist torsion through efficient shear action across the tube wall.

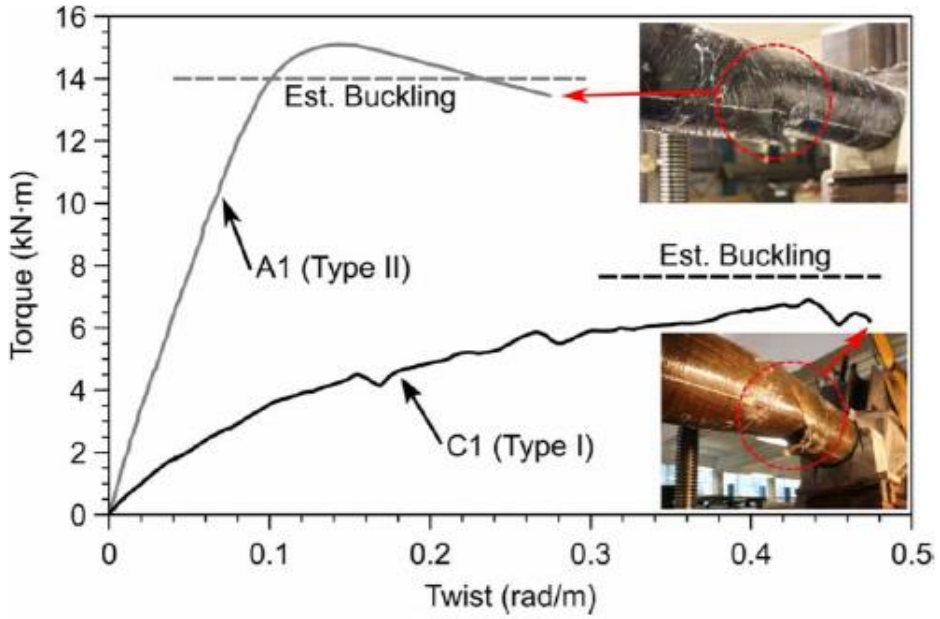

Figure 2.25. Torque–twist response of hollow FRP tubes (St. Onge and Fam, 2021).

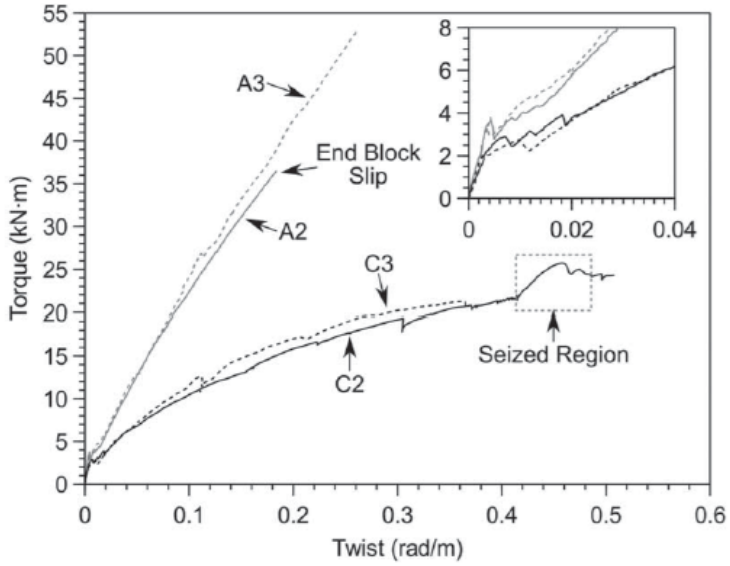

Figure 2.26. Torque–twist response of CFFTs (St. Onge and Fam, 2021).

The influence of the laminate structure on performance was a key finding. Angle-ply Type II tubes benefited from enhanced in-plane shear strength and efficient membrane action, wherein the FRP tube acts as a continuous membrane to support shear loads as illustrated in Figure 2.27b. In

contrast, Type I tubes primarily relied on truss action, involving diagonal compression struts in the concrete core, for additional strength.

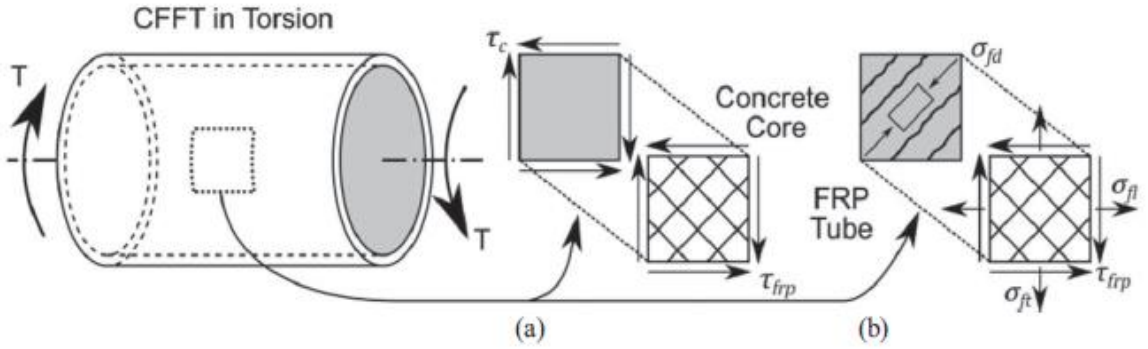

Figure 2.27. Simplified CFFT torque mechanism: (a) pre-cracking; and (b) post- cracking (St. Onge and Fam, 2021).

The study concluded that the different behaviour for tube A1 and C1, as observed in Figure 2.25, was due to the fibre orientation in the laminates relative to the direction of principal stresses. Besides, the failure was brittle and started by the rupture of the FRP tube due to the combination of shear stresses and transverse tension followed by local crushing of the concrete core. The authors also noticed little effect from the internal concrete hole on the torque–twist response of the CFFT and enhancement of the strength-to-weight ratio by 21%. However, the maximum torque and the twist had dropped to 12% and 20%, respectively, because of the concrete crushing from the lack of internal restraint.

2.3.4. Foundation design

Sadeghian and Fam (2010) developed a robust analytical model for a connection between circular CFFT members and reinforced concrete footings. The model predicts the critical embedded length (X_{cr}) of the CFFT part, which is the base length needed to accomplish material failure of the CFFT outside the foundation, and bond failure between the CFFT member and the foundation, simultaneously. The model was proposed based on the CFFT members being subjected to a general

state of axial load, bending moment, and shear force. Figure 2.28 illustrates the geometry of the problem that was considered for the model.

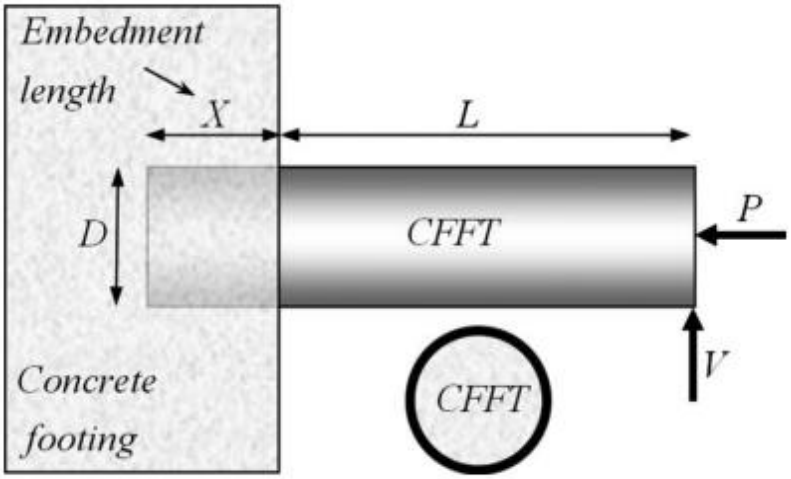

Figure 2.28. Geometric configuration used for the model (Sadeghian and Fam, 2010)

The CFFT is subjected to a lateral and axial loading at the free end. The general embedded length of the tube is X, L is the length of CFFT outside of the footing, and the outer diameter of the tube is D. It is assumed that if the embedment length is smaller than the critical value (i.e., $X < X_{cr}$), an early bond failure of the CFFT will ensue within the RC footing, before the CFFT reaches its maximum strength at a section outside the footing. However, if $X > X_{cr}$, even though bond failure is discarded, there might be a superfluously unnecessary installation length.

The model was developed based on imposed static equilibrium equations and compatibility relationships for the free body diagram of the construction section. Figure 2.29 shows the free-body diagram of the embedded CFFT segment.

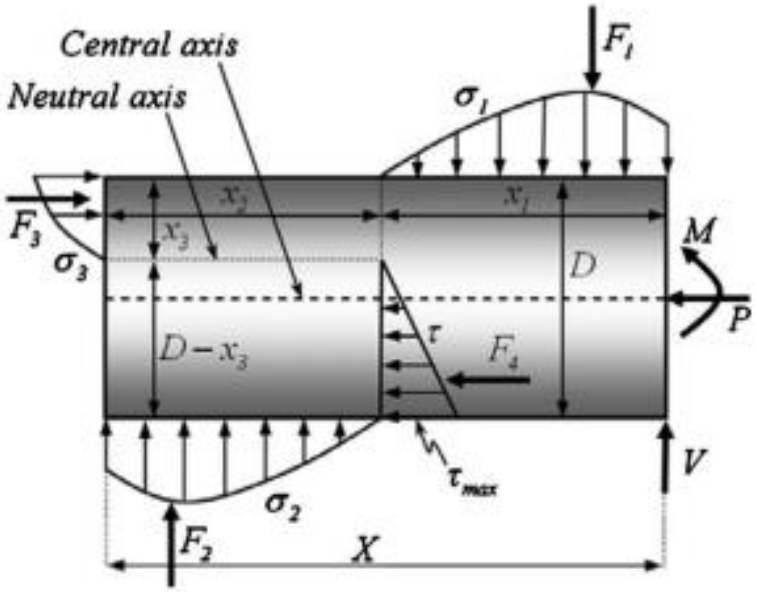

Figure 2.29. Free body of the general model within the embedment length of the tube (Sadeghian and Fam, 2010)

The considered external loads which have an effect on the CFFT are condensed to a moment M, a shear force V, and an axial load P, acting at the face of the RC footing. The moment and shear are considered as coupled through the moment arm L (M= V x L).

For the case where only lateral loading is applied, a simplified model is used to determine X_{cr} for CFFTs using Eq. 2.8:

$$\frac{x}{D} = \sqrt{\frac{3\pi M}{D^3 f'_c}} \qquad \text{Eq. 2.8}$$

Where M is the moment resistance of the tower, D is the tower diameter, and X is the critical embedment length of the tower.

2.3.5. Analytical and Numerical Modelling

Mander, Priestley and Park (1988)

Mander et al. (1988) developed a theoretical stress-strain model for confined concrete members with either circular or rectangular sections. The model can be used for sections under static or dynamic axial loading. The concrete section may enclose any kind of confining steel such as circular hoops, spirals, or rectangular hoops with or without cross ties. The impact of different types of confinement is taken into consideration by defining an effective lateral confining pressure as suggested by Sheikh and Unimen (1982), which is dependent on the effective confined concrete core's region.

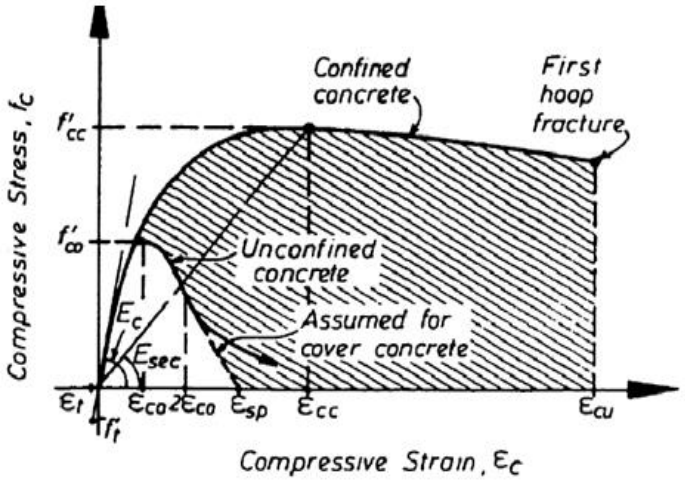

Figure 2.30. Stress-Strain Model Proposed for Confined and Unconfined Concrete (Mandar et al. 1988)

Figure 2.30 presents the suggested stress-strain relationships for monotonic loading of confined and unconfined concrete. It is described in terms of important parameters: the confined concrete compressive strength, f'_{cc}; the strain at confined compressive strength, ε_{cc}; the modulus of elasticity of concrete, E_c; and the ultimate compressive concrete strain corresponding to the first hoop fracture, ε_{cu}. At this point, the section is considered to have reached its ultimate deformation. For dynamic loading, these control parameters are modified by dynamic magnification factors. Stress-

strain relationships for cyclic unloading and reloading curves at slow strain rates are also developed for cyclic loading response.

The research showed that the strength and longitudinal strain of concrete confined by an active pressure can be presented by Eq. 2.9 and Eq. 2.10, respectively:

$$f'_{CC} = f'_{C0} + k_1 f_l \quad \text{Eq. 2.9}$$

$$\varepsilon_{Cu} = \varepsilon_{C0}\left(1 + k_2 \frac{f_l}{f'_{c0}}\right) \quad \text{Eq. 2.10}$$

Where f'_{cc} is the maximum concrete stress, f'_{co} is the unconfined concrete strength, $k_1 = 4.1$ and $k_2 = 5\ k_1$ are coefficients that are functions of the concrete mix and the lateral pressure, and f_l is the lateral pressure.

The tangent modulus of elasticity of the concrete can be calculated using Eq. 2.11.

$$E_C = 5000\sqrt{f'_{C0}} \quad \text{Eq. 2.11}$$

The test results for confined concrete reported by Mander et al. (1984) shows that the suggested analytical model gives excellent prediction of the improved strength and common shape of the stress-strain curves for confined concrete.

Lam & Teng (2003)

Lam and Teng (2003) developed a stress-strain model for FRP-confined concrete. The model was developed for new designs using FRP jackets in which the reinforcing fibres are only or mostly oriented in the hoop direction. Therefore, the ultimate condition of FRP-confined concrete can be reached when the hoop tensile stresses cause the FRP to rupture. The concrete expands laterally when it is subjected to axial compression. However, this expansion will be restricted by the FRP jacket in the hoop direction.

Using the FRP jacket as confinement will increase with the lateral strain of concrete because FRP does not yield, which differs from the use of steel where the lateral pressure is constant after yielding. Figure 2.31 illustrates the confining action in FRP-confined concrete, where the stresses are in their positive direction.

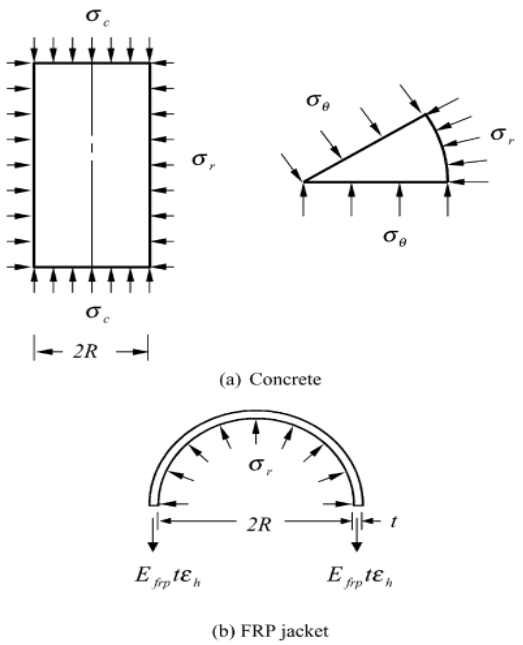

Figure 2.31. Confining action of (b) FRP jacket to (a) Concrete (Lam and Teng, 2003)

The lateral confining pressure on the concrete core can be calculated according to Eq. 2.12.

$$\sigma_r = \frac{\sigma_h t}{R} = \frac{2\sigma_h t}{d} \qquad \text{Eq. 2.12}$$

where σ_r= tensile stress in the FRP jacket in the hoop direction, t= thickness of the FRP layer, and R and d = radius and diameter of the confined concrete core, respectively.

The hoop stress in the FRP jacket will be proportional to the hoop strain due to the FRP linearity, as given by Eq. 2.13.

$$\sigma_h = E_{frp}\varepsilon_h \qquad \text{Eq. 2.13}$$

Where E_{frp} is the elastic modulus of FRP.

The maximum nominal confining pressure f_l can be calculate using Eq. 2.14.

$$f_l = \frac{2f_{FRP}t}{d} \qquad \text{Eq. 2.14}$$

where f_{frp} is the tensile strength of FRP in the hoop direction.

The authors concluded that the best methodology for characterizing the stress-strain curve of FRP-confined concrete is to consider a modified parabola for the first section and a straight line for the second part, with the different parameters being reliant upon the FRP properties. The adjusted parabola should have the option to reflect the gradual progress of confinement as the axial stress escalates. In summary, the stress-strain model for the FRP-confined concrete is developed based on; (i) the stress-strain curve consisting of a modified parabola for the first section and a straight line for the portion as illustrated in Figure 2.32; (ii) the slope of the parabola at $\varepsilon c = 0$ (initial slope) is considered the same as the elastic modulus of unconfined concrete E; (iii) the first part of the non-linear curve is impacted somewhat by the presence of an FRP wrapping; (iv) the first part of the parabola meets the linear second part without a change in slope between the two portions; (v) the curve ends at a point where the ultimate axial strain and the compressive strength of the confined concrete are reached.

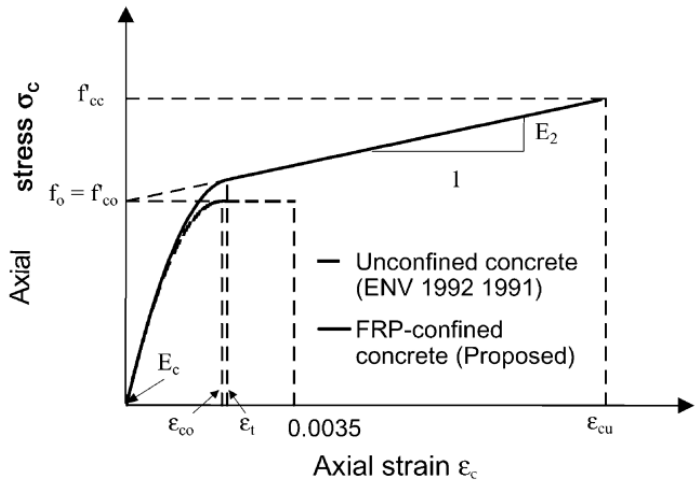

Figure 2.32. Developed stress–strain model for FRP-confined concrete (Lam and Teng, 2003)

Based on the assumptions mentioned previously, the stress-strain relationship is calculated according to Equations Eq. 2.15 and Eq. 2.16.

$$\sigma_C = E_C\varepsilon_C - \frac{(E_C - E_2)^2}{4f'_{C0}}\varepsilon_C^2 \text{ for } 0 \le \varepsilon_C \le \varepsilon_t \quad \text{Eq. 2.15}$$

$$\sigma_C = f'_{C0} + E_2\varepsilon_C \text{ for } \varepsilon_t \le \varepsilon_C \le \varepsilon_{Cu} \quad \text{Eq. 2.16}$$

The strain at which the parabola meets the linear second part is given by Equation Eq. 2.17.

$$\varepsilon_t = \frac{2f_0}{E_C - E_2} \quad \text{Eq. 2.17}$$

Where f_0 is the intercept of the stress axis by the linear second part.

The second slope of the confined model is calculated according to Equation Eq. 2.18.

$$E_2 = \frac{f'_{CC} - f_0}{\varepsilon_{Cu}} \quad \text{Eq. 2.18}$$

Where f'_{CC} = compressive strength of confined concrete.

The proposed model is appropriate for concrete confined by different types of FRP.

Gong (2021)

Gong (2021) conducted a parametric study to investigate the effect of FRP laminate structure, concrete filling ratio, steel reinforcement ratio, prestressing ratio, and taper ratio for small-scale CFFT wind towers using a finite element model (Figure 2.33). The performance of CFFT wind turbine towers subjected to a concentrated lateral load at the top of the tower was compared to the performance of steel tubular wind turbine towers and concrete wind turbine towers. Different materials were considered for the model such as FRP, steel bars, concrete, and tendons. Nineteen CFFT wind turbine tower models were created to investigate the impact of different parameters.

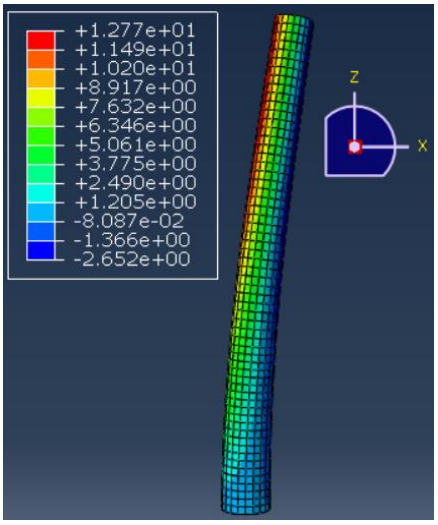

Figure 2.33. Finite element model of CFFT tower (Gong, 2021).

The effect of adding steel reinforcing bars on CFFT tower behaviour was studied, as well as the use of prestressed tendons (Figure 2.34). Generally, Figure 2.35 shows that the load-deflection for the CFFT tower models without inner reinforcement have a bilinear response, while increasing the steel reinforcement ratio and prestressing ratio shows more non-linear behaviour. In addition, Figure 2.35 shows that increasing the diameter of the CFFT tower, FRP tube wall thickness, steel reinforcement ratio, and prestressing ratio improved the performance of the CFFT wind turbine tower models. Changing the taper ratio did not affect the load capacity but slightly influenced the deflection of the CFFT wind turbine towers. Furthermore, a concrete filling ratio of at least 50% showed a similar load-deflection response to that of a completely filled section. The presence of small axial loads representing the mass of the turbine had a negligible effect on tower performance.

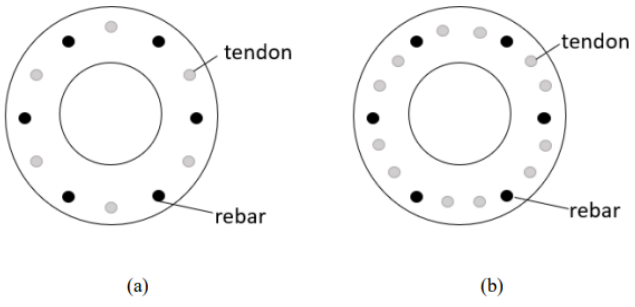

Figure 2.34. Cross-section of the two steel-prestressed CFFT models (Gong, 2021).

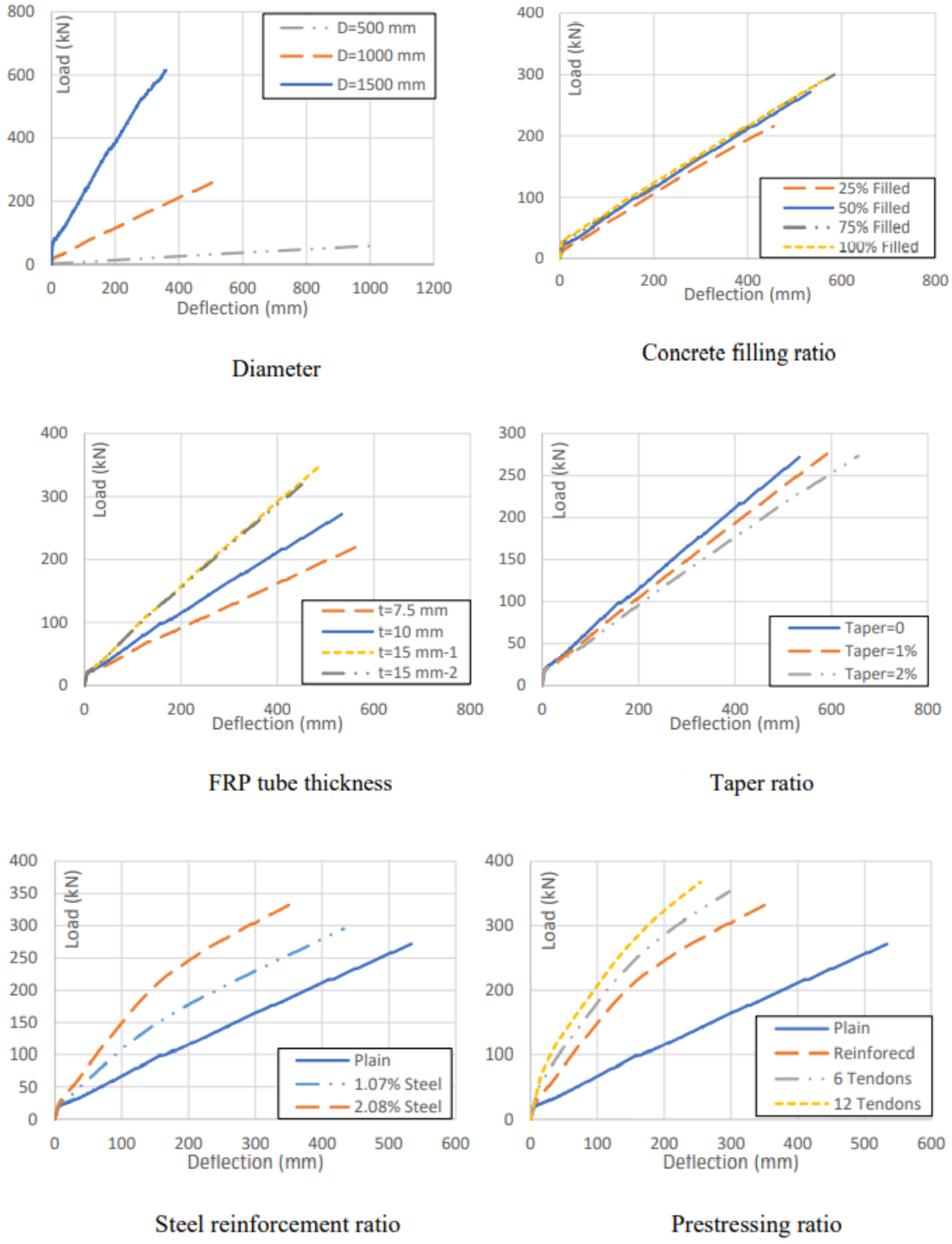

Figure 2.35. Load-deflection relationship of models with different diameter, concrete filling ratio, FRP tube thickness, taper ratio, steel reinforcement ratio, and prestressing ratio (Gong, 2021).

2.4. Summary and Research Gaps

2.4.1. Summary

The literature review provided an extensive investigation of wind turbine tower designs, highlighting the benefits and limitations of conventional steel and concrete towers. While steel tubular towers offer high strength and ductility, their vulnerability to corrosion and high maintenance costs make them less suitable for long-term applications in remote areas. Concrete towers, on the other hand, provide better durability but are significantly heavier, leading to increased transportation and installation challenges. Concrete-filled FRP tubes (CFFTs) have emerged as a promising alternative for wind turbine towers, mainly in remote regions. The advantages of CFFTs include high corrosion resistance, lightweight construction, and greater structural performance. Several experimental and numerical studies have explored the flexural, torsional, and dynamic behaviours of CFFTs in different structural applications. However, the application of large scale CFFTs in wind turbine towers remains a developing area of research.

2.4. 2. Research gaps

Despite the progress in understanding CFFTs, several knowledge gaps exist in the current body of research. This is the first ever study to test large scale CFFT cantilevers under loading conditions that are representative of wind turbine towers. The use of hollow CFFTs with a tapered geometry and post-tensioning system designed for segmental construction is a highly novel concept that has never been investigated in previous research studies. While this study aims to fill this important general knowledge gap to enable the use of CFFTs for a particular new structural application (i.e., wind turbine towers), several other contributions are also targeted that are relevant to all CFFT applications and advance knowledge in this field:

- **Limited studies on dynamic behaviour and combined loading**

While CFFTs have demonstrated promising static performance, there is a lack of comprehensive studies on their dynamic behaviour under wind-induced loading conditions. Moreover, while most previous research has focused on either flexural and torsional responses separately, the

performance of prestressed CFFTs under the combined effects of bending and torsion loads remains underexplored.

- **Effect of post-tensioning in CFFTs**

Existing research has not sufficiently investigated the influence of post-tensioned reinforcement within CFFTs, especially in large-scale specimens. The integration of post-tensioned systems could improve stiffness, reduce deflections, and enhance fatigue resistance, but further experimental validation is needed.

- **Numerical modeling limitations**

Although finite element models have been developed to simulate the performance of CFFTs, there is a need for more advanced modeling techniques to simulate the influence of key parameters on the performance of the GFRP tube, concrete core, and post-tensioning system under different load distribution and eccentricity.

This research aims to address these gaps by conducting large-scale experimental testing to evaluate the static and dynamic response of post-tensioned CFFTs. The study will evaluate their dynamic properties, flexural performance, and structural optimization for wind energy applications in remote regions. The findings will provide valuable insights for engineers looking to adopt post-tensioned CFFTs for sustainable energy infrastructure in challenging environments.

Chapter 3 - Experimental Program

3.1. Introduction

To the author's knowledge, there are no reported experiments of large CFFT cantilever towers subjected to lateral loads. As part of this PhD research, an experimental program was developed that involves tests of large-scale post-tensioned tapered CFFTs with different diameters intended for small scale wind turbine towers. Three full-scale towers were designed, built, instrumented, and tested in the structures laboratory of the University of Ottawa. This chapter presents the detailed information of the experimental program. It consists of: (i) materials' description; (ii) reinforcement and instrumentation; (iii) specimen preparation, including concrete casting and curing; and (iv) test set-up and test procedures.

The GFRP tubes used for this research are commercially available telecommunication poles with a tapered profile that enables them to be joined together in the field using an overlap connection as shown in Figure 3.1. Two nominal tube sizes are used in this study as summarized in Table 3.1: (i) one tower of size M5, with a base diameter of 532.5 mm; (ii) two towers of size M4, with a base diameter of approximately 465 mm.

Table 3.1. Tower specimen details

Tower	Group #	Bottom diameter (mm)	Top diameter (mm)	Length (mm)	Concrete thickness (mm)
1	M5	533	417	5800	125
2	M4	461	347	5800	100
3	M4	465	349	5800	100

(a)

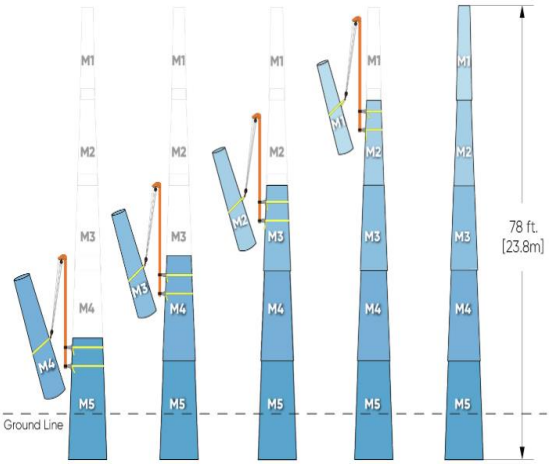

(b)

(c)

(d)

Figure 3.1. Tapered profile tubes ((a) FRP utility tower, (b) Size variations of FRP tube modules, (c) splice connection, (d) ease of transportation (R. S. Poles. (n.d.))

3.2. Material Properties

3.2.1. Glass Fibre Reinforced polymer (GFRP)

The GFRP tubes have a ply configuration of [±40, ±30] and a thickness ranging from 10 to 12 mm. Since the manufacturer did not provide specific properties for the GFRP materials, a total of 5 to 7 coupon tests were conducted for each tensile and compressive loading condition as part of the analysis. Longitudinal tension tests were carried out in accordance with ASTM D3039 using

specimens measuring 25 × 250 mm, as illustrated in Figure 3.2 (a). To prevent grip failure, four tabs (25 × 50 mm) were bonded to both ends of each specimen. For longitudinal compression testing, ASTM D3410 standards were followed, utilizing specimens with dimensions of 25 × 150 mm, reinforced with four tabs (25 × 60 mm) at both ends, as shown in Figure 3.2 (b). Additionally, tensile tests in the hoop direction were conducted on specimens with widths of either 50 mm or 100 mm, and diameters ranging from 325 mm to 375 mm, as shown in Figure 3.3.

For the M4 specimens, the mechanical properties were evaluated through both tensile and compressive tests in the longitudinal direction, as well as tensile tests in the hoop direction. Five samples were used for each of the longitudinal tests, with strain measured using axial strain gauges. Stress was calculated by dividing the maximum load by the average cross-sectional area, determined from manual width and thickness measurements taken before testing. For hoop tension, three M4 specimens were tested following ASTM D2290 (Procedure A). Strain gauges were placed on both the inside and outside surfaces of the tube, and the average of these readings was used to calculate the modulus from the linear portion of the stress–strain response. The hoop tensile strength was determined using Eq. 3.1. A summary of the measured GFRP tube properties for M4 is provided in Table 3.2.

(a) Tension (b) Compression

Figure 3.2. Test setup of GFRP coupon (courtesy of Watfa, 2025)

$$\sigma = \frac{P_b}{2A_m} \quad \text{Eq. 3.1}$$

where P_b is the maximum load at failure and A_m is the cross-sectional area.

Figure 3.3. Test setup of tension in hoop direction (courtesy of Watfa, 2025)

Table 3.2. GFRP properties

Test Type	Average Strength (MPa)	Average Ultimate Strain	Average Initial Modulus (GPa)
Tension (Longitudinal)	366.8	0.016	27.0
Compression (Longitudinal)	389.4	0.015	26.3
Tension (Hoop)	92	*	6.2

*The ultimate tensile strain for the tension (hoop) test is not recorded because the strain gauges failed prior to reaching the ultimate load.

3.2.2. Concrete

The concrete used for the towers and foundation blocks was ordered from a local ready-mix company. The specifications given were for a self consolidating concrete with a target compressive strength of 50 MPa (towers) and 70 MPa (foundation blocks) and a 14 mm nominal coarse aggregate size. The slump flow of the self-consolidating concrete measured before casting was 580 mm for the towers and 590 mm for the foundation, respectively, as shown in Figures 3.2 a, b.

Both mixes had adequate workability and self consolidated well during the pouring of the specimens; no segregation was observed. The foundation was kept under wet burlap and plastic sheets for the first 3 days, after which the formwork was removed, and the foundation was cured under wet burlap covered by plastic sheets for an additional four weeks.

a. Slump flow for towers

b. Slump flow for foundation

Figure 3.4. Slump flow test for self-consolidating concrete

The compressive strength of each concrete batch was obtained by compressive tests of cylindrical concrete specimens following ASTM standard C39. Nine concrete cylinder samples (100 mm x 200 mm) were taken from each mix and tested at 7, 14, and 28 days after casting.

Table 3.3 provides the compressive strength of the tested cylinders. The average 28 days compressive strengths for the towers and foundation were 61.6 MPa and 78.4 MPa, respectively.

Table 3.3. Compressive strength of the tested cylinders

Age of Cylinder (Days)	Average f'c for towers (MPa)	Average f'c for foundation (MPa)
7	46.0	58.0
14	54.5	72.3
28	61.6	78.4

3.3. Construction of towers

3.3.1. Reinforcing cages

The towers were reinforced longitudinally with four 15M (16 mm) steel bars and laterally with 10M (11.3 mm) closed steel ties as shown in Figure 3.5. These reinforcement sizes were selected following ACI 318 guidelines for reinforced concrete design, considering the axial and bending demands of tall, slender tubular structures. After the concrete had cured, the towers were prestressed with four longitudinal 12.7 mm 7-wire strands (steel tendons).

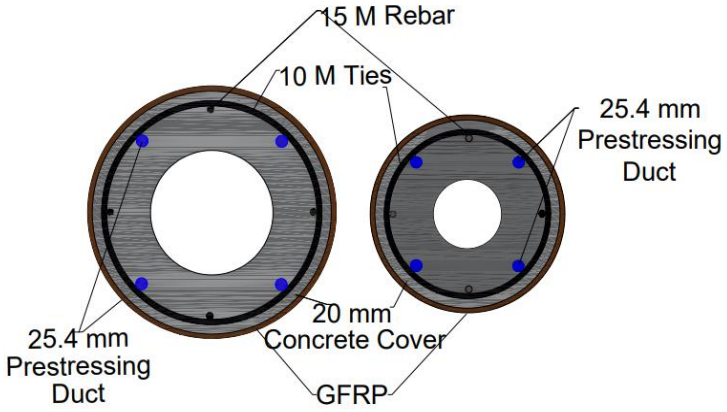

Figure 3.5. Steel bar and strand layout

The ties used for all towers were ordered from a local steel supplier. The size of each tie was adjusted to the required diameter depending on the location of the tie within the tower using the template shown in Figure 3.6. The ties were placed on the marked locations on the longitudinal

steel bars and tied together using rebar ties, then the post-tensioning ducts were attached to the ties and secured in the designated locations as illustrated in Figure 3.7. Starting at a height of 120 mm from the base of the tower, nine ties were placed at spacing of 120 mm. The remaining ties were distributed at 350 mm spacing as illustrated in Figure 3.8. Circular 19 mm-thick steel plates were connected to the reinforcing cages at the top and bottom of each specimen. The steel plates had openings with four holes for the longitudinal reinforcing bars and four for steel tendons as illustrated in Figure 3.9. The steel plates were intended to distribute the prestressing load on the concrete section and improve its axial bearing capacity.

Plastic spacers were mounted along the four longitudinal reinforcement bars to maintain a uniform concrete cover of 25.4 mm (1 inch). Six to eight spacers were clipped at 50-100 cm spacing and diagonally opposite to each other on the longitudinal bars as illustrated in Figure 3.10. Figure 3.11 shows a 3 mm galvanized wire that was wrapped around both ends of each conduit to resist spalling stresses at the anchorage zone.

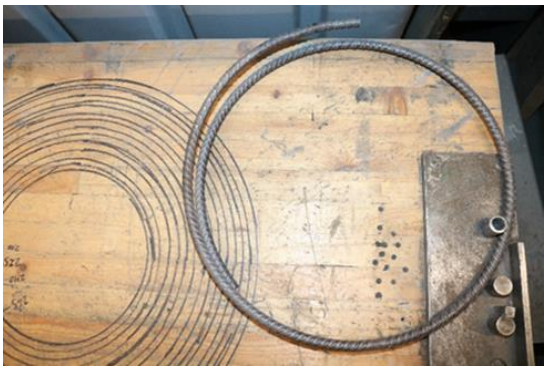

Tie bending jig and a completed tie

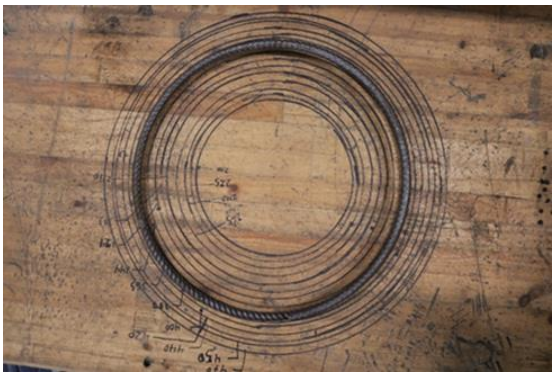

Size template for ties

Figure 3.6. Tie bending jig and size template

Steel bars secured to ties at marked locations

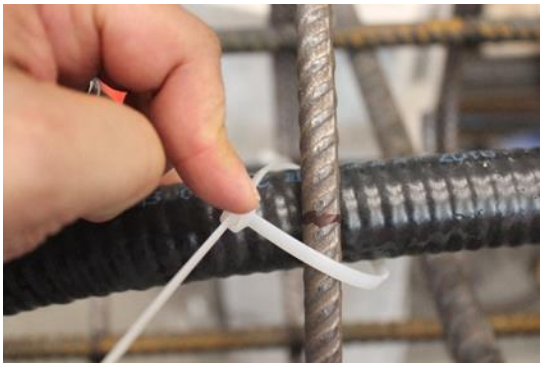

Prestressing duct secured to ties at marked locations

Figure 3.7. Longitudinal steel bars and prestressing duct attached to ties and secured in the designated locations

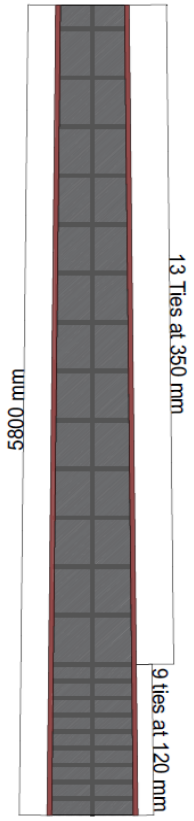

Figure 3.8. Ties location for the tower specimens

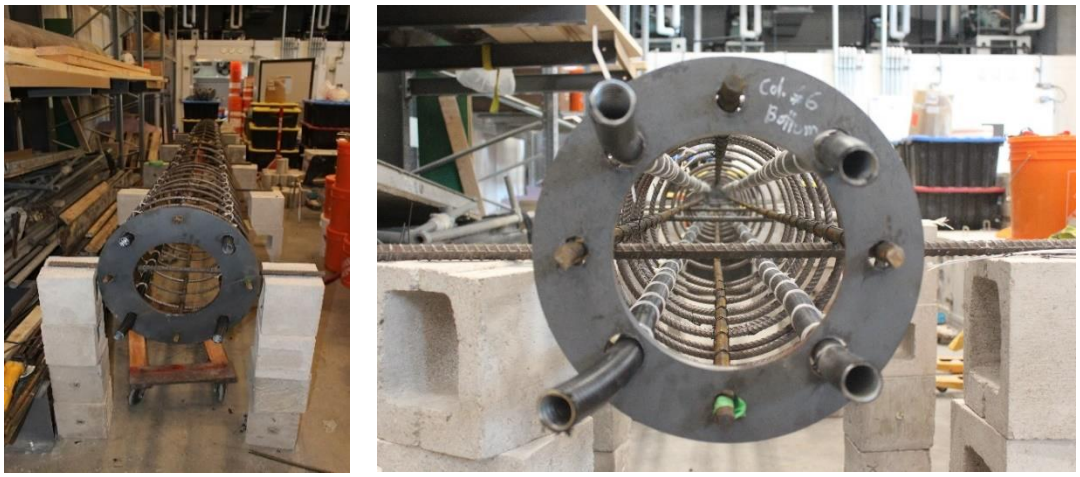

Figure 3.9. Steel plates on top and bottom of the towers

Figure 3.10. Plastic spacers mounted along the longitudinal reinforcement bars

Figure 3.11. Galvanized wire wrapped around the end of the conduit

3.3.2. Strain gauges

Each 5.8 m tower was instrumented with a total of 30 strain gauges, installed along the four longitudinal reinforcing bars as illustrated in Figure 3.12. Ten strain gauges were installed on both the tension bar and the compression bar (labelled A and B respectively), totaling 20 strain gauges. The remaining ten strain gauges were installed in an alternating pattern between the two neutral axis bars (labelled C and D), resulting in 5 strain gauges for each neutral axis bar. For the 5.8 m towers strain gauges were positioned as follows for longitudinal bars A and B; starting at a height of 200 mm from the base of the tower, six strain gauges were installed at a spacing of 250 mm. Then the remaining strain gauges were distributed at a 1000 mm spacing. For bars C and D (neutral axis), the same spacing convention was held, however strain gauges were only installed in alternating positions between the two neutral axis bars. All the strain gauges used were 6.35 mm long. The strain gauges were checked individually before and after the cage assembly, using a voltmeter to ensure all strain gauges were working properly. Once all strain gauges passed the performance check and connected to the extension wires in the sonotube (cardboard tubes), the instrumented reinforcement cages were set in the GFRP tubes for concrete casting.

3.3.3. Sonotube

The three towers contained tapered sonotubes to create the hollow core. The sonotubes were originally manufactured with a constant diameter ranging from 6 to 12 inches (152-305 mm). To create the required tapered shape, each sonotube was cut from top to bottom longitudinally and re-rolled to ensure a constant taper slope of approximately 1.3% along the length as illustrated in Figure 3.13.

During the rolling of the sonotubes, the diameters were measured at 350 mm increments along the height to ensure the proper constant taper shape was being achieved. After the sonotube was rolled into the proper tapered shape, it was fastened with plastic ties at 350 mm increments and nails were screwed along the length of the tube to rigidly attach the overlapped layers. Finally, the excess overlap was trimmed at an angle matching that of the tapered shape to ensure a constant overlap of 100 mm along the sonotube. The concrete wall thickness achieved in this manner for each tower is summarized in Table 3.1.

A two conductor extension cable was attached to the sonotube close to the installed strain gauge locations and extended through the inside of the sonotube towards the top of the tower. Then, the strain gauge wires were inserted into a plastic tube and connected to the extension wires as illustrated in Figure 3.14. The plastic tube was used to protect the strain gauge wires from damage while the concrete was being poured and cured. The extension cable passed through the plastic tube into the central sonotube and then extended to the top of the tower to be connected to the data acquisition system.

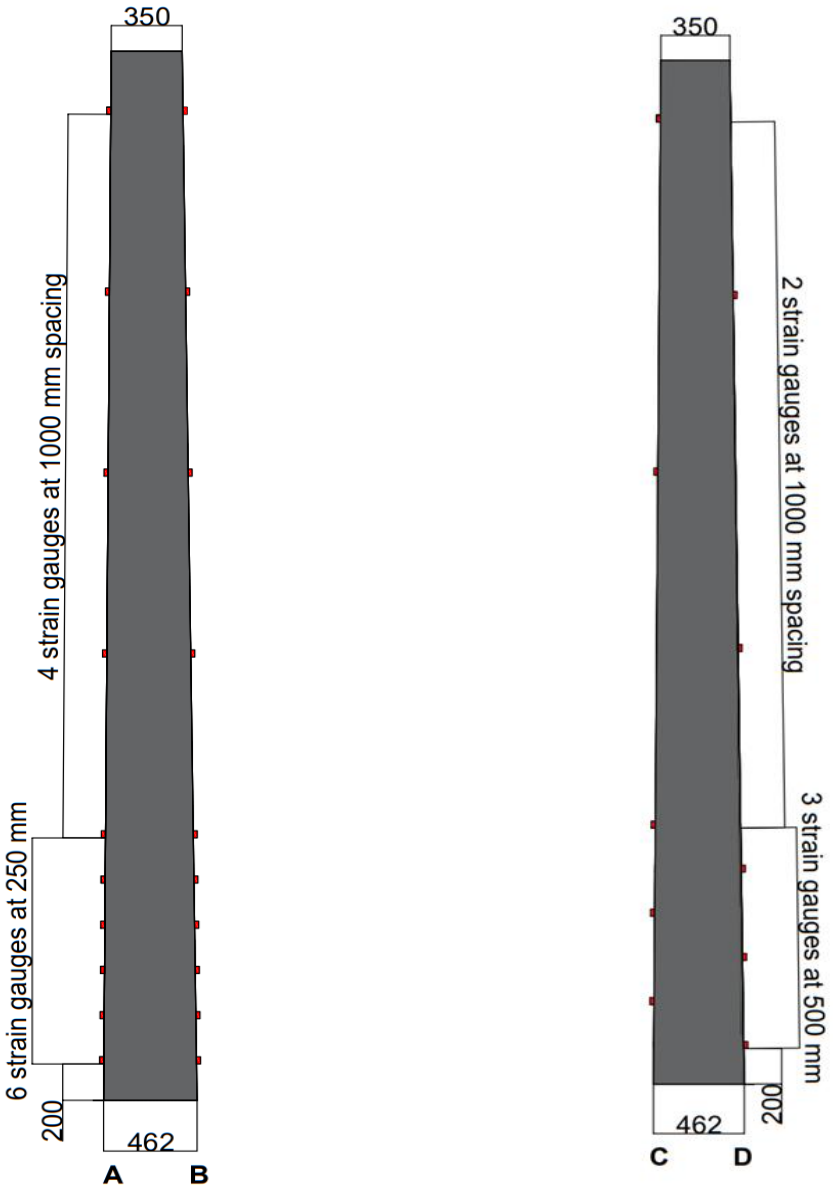

Figure 3.12. Strain gauges' location on steel bars

Stage 1. Cutting Sonotubes to the required diameters

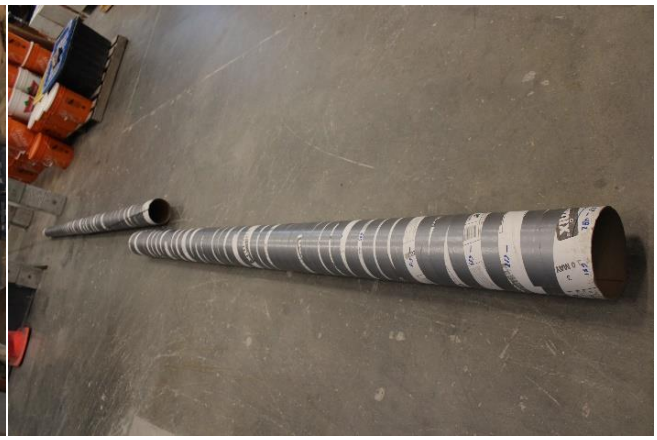

Stage 2. Rolling Sonotubes to the proper tapered shape

Stage 3. Connecting Sonotubes segments together

Stage 4. Wrapping sonotubes with duct tape

Figure 3.13. Preparation stages for Sonotubes

Extension wires attached to the sonotube

Extension wires inside the sonotube

Strain gauges passing through the plastic tube and connected to the extension wires

Extension wires passing through sonotube to top of the tower

Figure 3.14. Extension wires attachment to the sonotube and passing through the hollow core to the top of the tower

3.3.4. Concrete

Each tower specimen was cast vertically using the GFRP tube as a stay-in-place form as illustrated in Figure 3.15. The steel cages were positioned vertically and the GFRP tubes were subsequently placed over the steel cages using the overhead crane. One inch (25.4 mm) Styrofoam sheets were

placed underneath the base of the towers to reduce concrete leaking and increase the stability of the specimens. Lumber was used to secure the top and bottom of the specimens in place for fabrication. Next, the sonotubes were filled with fine sand from the top to prevent collapsing due to concrete pressure during pouring.

The concrete was transported from the truck mixer in the delivery area to the location of towers using a concrete pouring bucket lifted by an overhead crane. The ready-mix concrete was poured through the openings at the top of each tower as shown in the Figure 3.16, using the gutter from the pouring bucket. Finally, the 19 mm circular steel plate was placed on top of the tower before the setting of the concrete.

After the concrete was cured and achieved the desired strength, a post tensioning system was introduced to the column specimens. Each of the four tendons was stressed to a target value of 1000 MPa ($0.54f_{pu}$) then locked with prestressing wedge anchors. Two diagonally opposite tendons were stressed at a time to achieve a uniform stress distribution in the concrete. Next, a high strength grout was mixed with W/C ratio of 0.4 and injected from an inlet hose to the conduit ducts to provide a bond transfer mechanism between the prestressing strands and the concrete.

Steel cages before placing the GFRP tubes on them

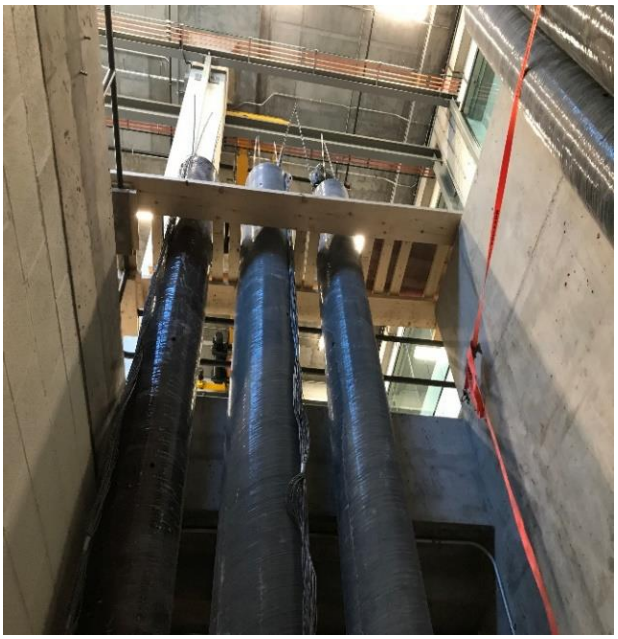

GFRP tubes placed on steel cages and secured at the top with lumber

Styrofoam sheets underneath the towers' base

Lumber to secure the bottom of the specimens

Figure 3.15. Preparing tower specimens before casting

(a) Using a concrete pouring bucket to pour the concrete into the towers

(b) 19 mm circular steel plate placed on top of the tower

Figure 3.16. Tower specimens during casting

(a) Octagon plate

(b) Octagon plate with steel tendons installed

Figure 3.17. Octagon steel plates

3.3.5. Foundation units

A heavily reinforced reusable concrete foundation was constructed to fix the towers to the laboratory strong floor during testing. The foundation unit consisted of two parts with a hexagonal hole in the middle as illustrated in Figure 3.22. Each part has dimensions of 870 mm long and 1740 mm wide. The depth of the foundation units was 790 mm as determined in the analysis section. The dimensions of the foundation units were selected based on the size and capacity of the largest tower as well as the spacing of the openings in the strong floor of the structural laboratory at STEM building. The foundation depth was increased by 90 mm from the design value (700 mm) to account for the prestressing anchors extending from the base of the tower as shown in Figure 3.19. The two foundation units were anchored to the strong floor at four points using 64 mm diameter high-strength bolts and also clamped together horizontally at four points using 50.8 mm diameter high-strength bolts. The reinforcement used in the foundation consisted of two layers of 30M and 25M Grade 400 MPa bars in the longitudinal and transverse directions, respectively. Figure 3.18 provides details of the foundation reinforcement. Hooks made from bent 25M bars were installed near the bolt openings and the hexagonal opening to increase the shear capacity and decrease vertical deformation of the foundation during testing.

First, the steel cages were placed in the formwork as illustrated in Figure 3.20. Then, the concrete was transported from the truck mixer in the delivery area to the formwork using a concrete pouring bucket via the crane in STEM laboratory. The ready-mix concrete was poured in the formwork from a low height and it was guided using the gutter from the pouring bucket as shown in Figure 3.21. Finally, after the concrete was placed in the formwork and leveled, a trowel was used to smooth the surface of the concrete.

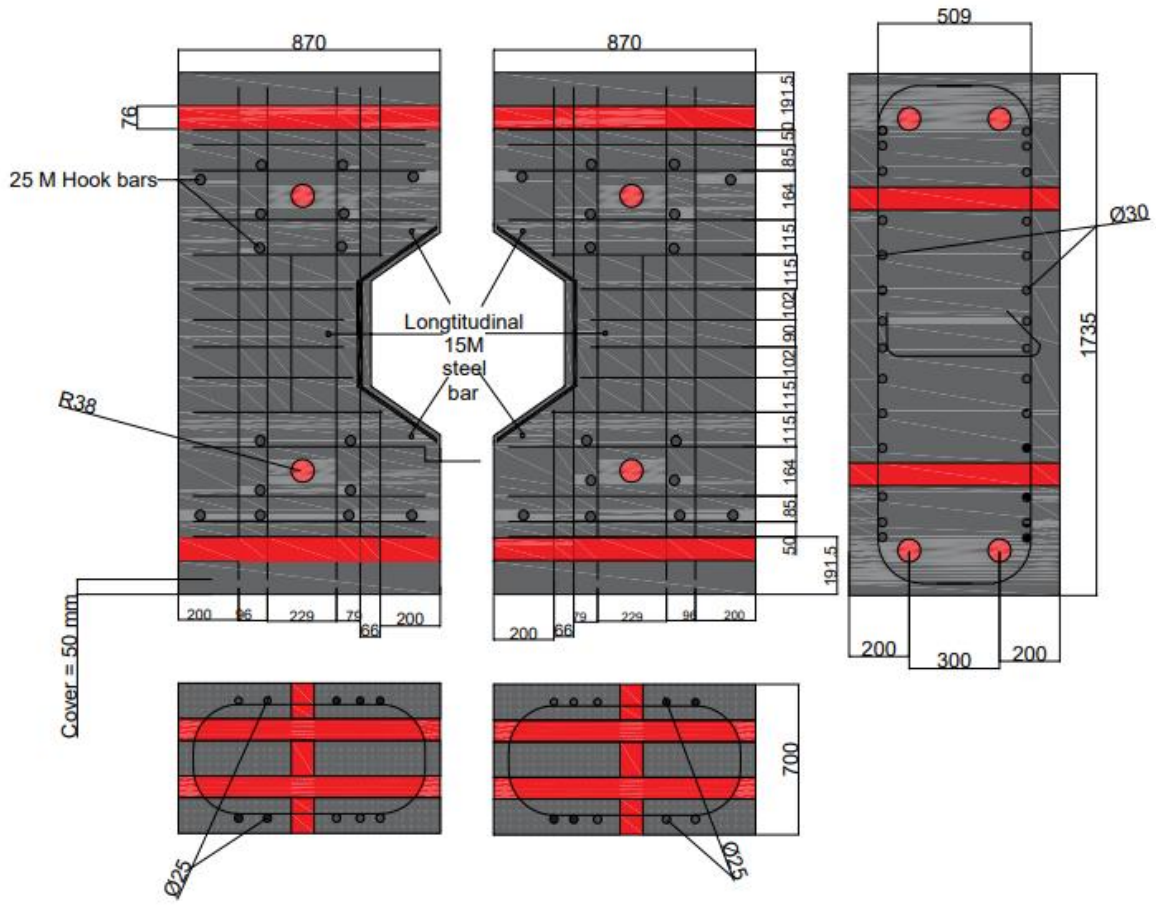

Figure 3.18 - Foundation Design Details

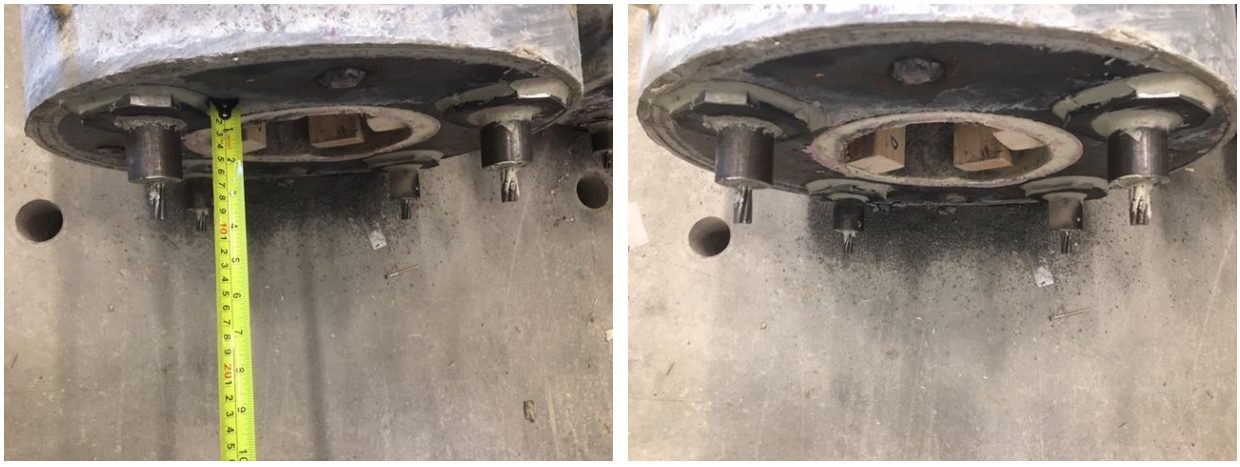

Figure 3.19. Prestressing tendons extension

Figure 3.20. Steel cage in the formwork

Figure 3.21. Pouring the concrete in the formwork

Figure 3.22. Foundation with a hexagonal hole in the middle

3.4. Tower Testing

3.4.1. Test procedures

The setup for the test procedure, as illustrated in Figure 3.24, can be summarized as follows: Initially, the two foundation units were anchored to the strong floor at four points using 64 mm diameter high-strength bolts. The four bolts were used to restrict the foundation from vertical and horizontal movements during the tests. Then, the tower specimen was transported from the storage area to the foundation zone using the overhead crane in the STEM laboratory. The tower was placed vertically inside the hexagonal opening of the foundation via the overhead crane. Once the tower was placed inside the foundation opening and securely positioned using lumber, four plumbs were employed at the top of the tower in four cross locations, as illustrated in Figure 3.23, to ensure its precise vertical alignment. These plumbs were crucial for controlling and maintaining the tower's verticality throughout the construction phase of the test setup process.

(a)

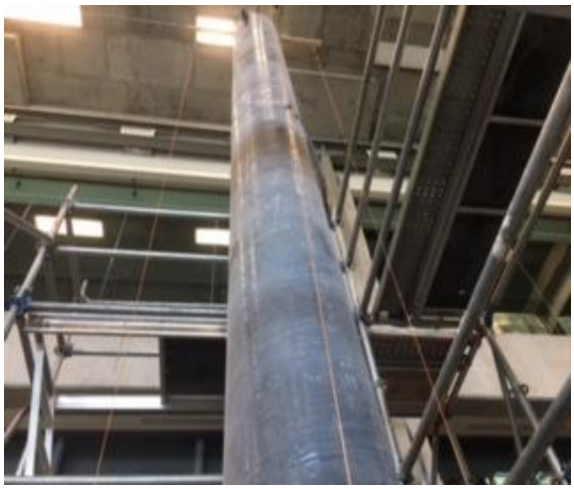

(b)

Figure 3.23 (a) Lumber to secure the tower (b) Using plumbs in four cross positions to control verticality of the tower

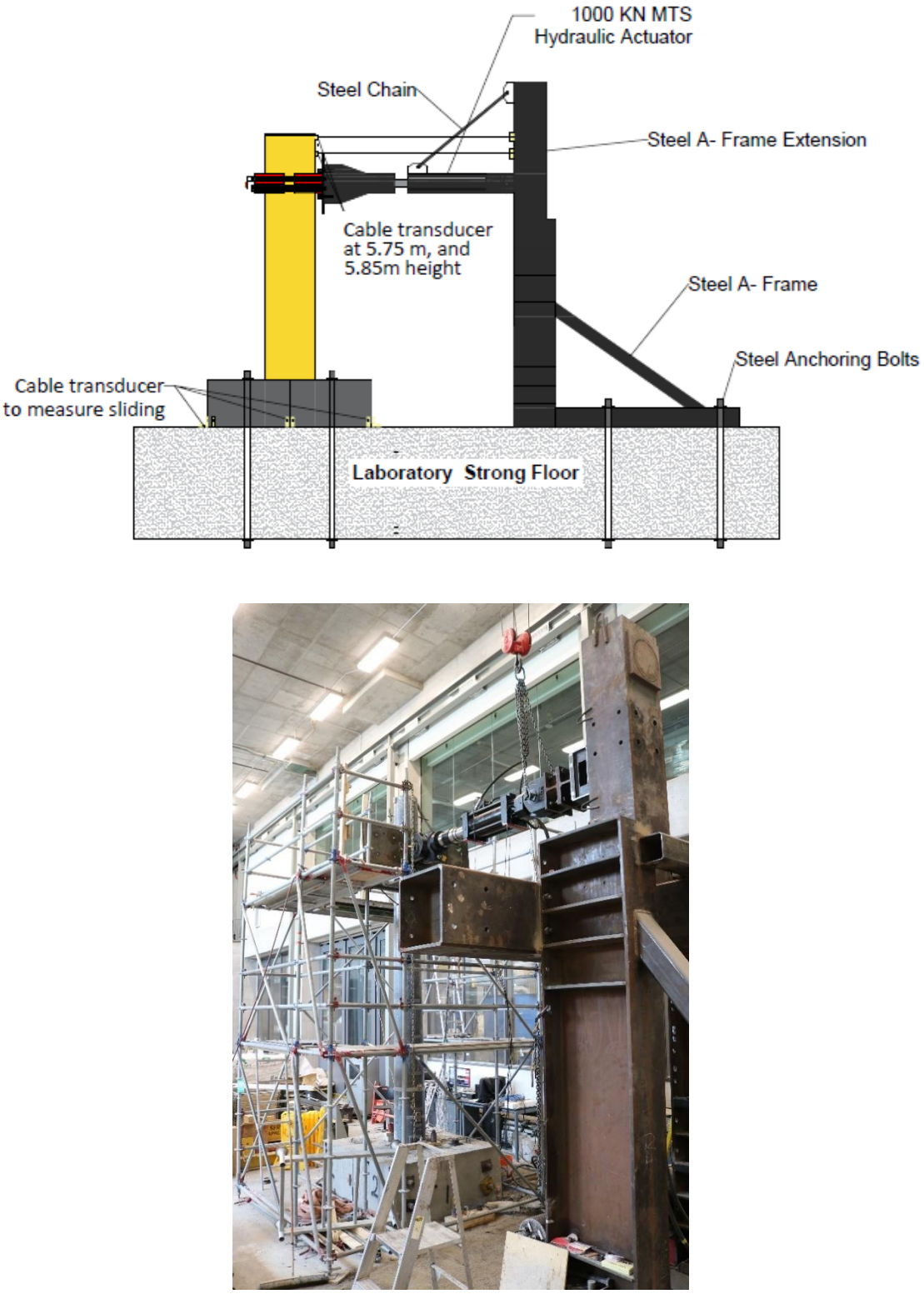

Figure 3.24. Test setup and A-frame attached to the laboratory strong floor

The loading setup consisted of an MTS hydraulic actuator of 1000 KN capacity and 500 mm stroke attached to a rigid steel A-frame, as illustrated in Figure 3.24. A 4.5 m braced scaffolding was used to prepare the test setup. The scaffolding was installed by a local full-service scaffolding company and mounted in a C-shape around the tower.

A clamping system was added to the test setup at the top of the tower as illustrated in Figure 3.25. The external UV-protective coating layer of the tower was grinded at the clamping area and covered with epoxy to increase the friction between the tower and the clamps to prevent slipping while eccentric load was applied. Two boxes welded to the actuator plate were connected to the tower's top at 5 meter height using the scaffolding and connected to the opposite two welded boxes through 1.5 inch (38.1 mm) diameter anchor bolts.

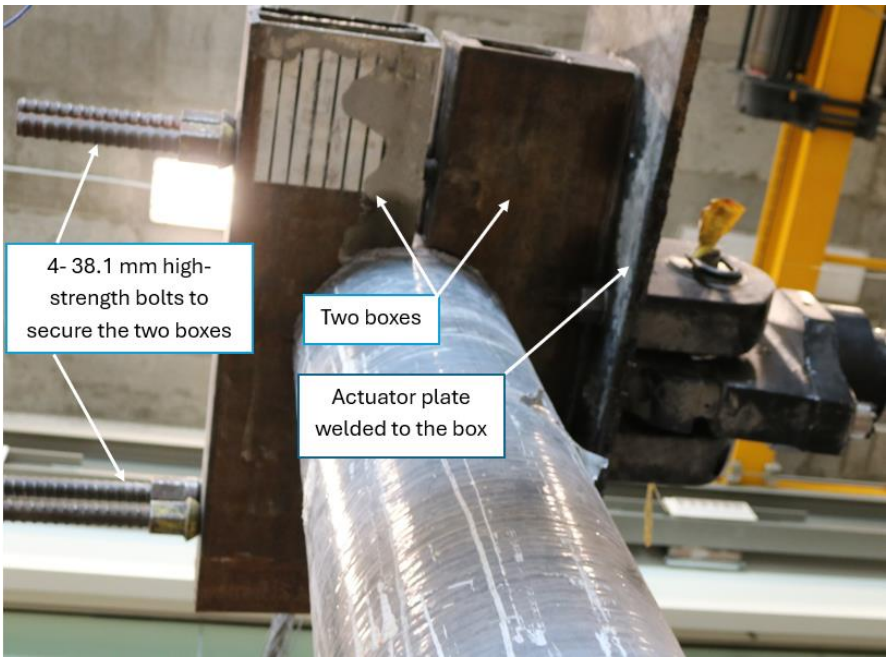

Figure 3.25. Clamping system installed at the top of the column

A steel chain with high safe workload capacity, as shown in Figure 3.26, was used to support the actuator from the end and connected to the top of the A-frame steel extension, while the actuator was not connected to the tower. The actuator was set close to the height of the top clamping system and fixed at one end to the steel A-Frame and to the top clamp at the other end. The top clamping

system included an actuator steel plate that provided five possible positions for the actuator to be attached in order to provide the required eccentric loading as illustrated in Figure 3.27.

The tower to be tested was installed at the front of the actuator. The load was applied at a distance of approximately 900 mm from the tip of the tower. While the actuator was connected to the top clamping system, high strength grout of 82 MPa was used to fill the empty space between the circular tower and the hexagonal opening as well as the 90 mm height/gap at the base of the tower created by the extension of the prestressing wedges plates and barrels. A plastic sheet was placed between the foundation and the grout to facilitate the easy removal of the grout after the test, preparing the setup for the next tower test. The grout was used to stabilize the tower within the foundation and increase the friction between the column and the foundation. The extension of the prestressing barrels and the grout underneath the tower created a strong footing to ensure the torsional moment at the base of the column could be resisted while eccentric loading was applied. When the grout was cured properly, the two foundation units were anchored to each other horizontally at four points using 50.8 mm diameter high-strength bolts. The tower segment prior to testing is shown in Figure 3.28.

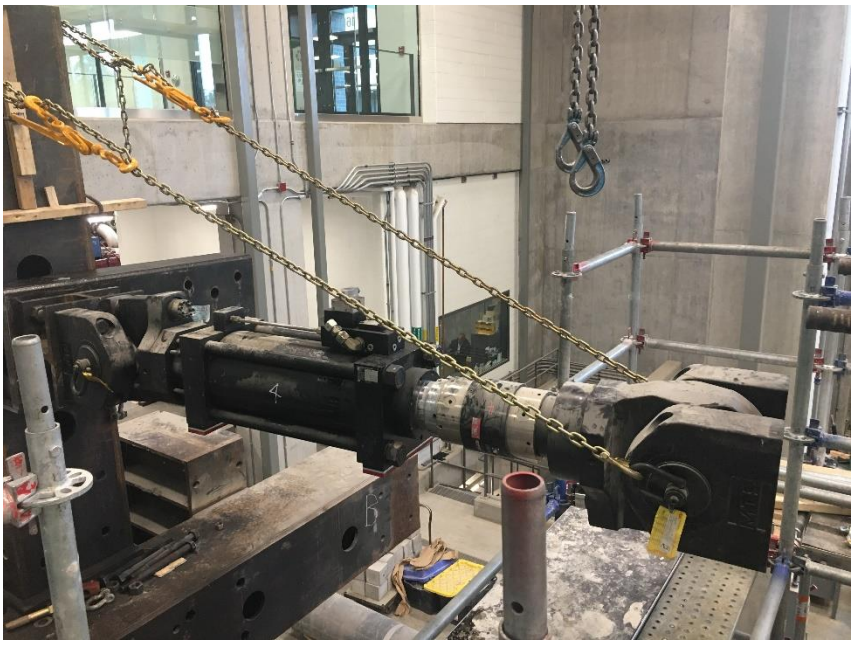

Figure 3.26. Steel chain with high safe workload capacity to support the actuator

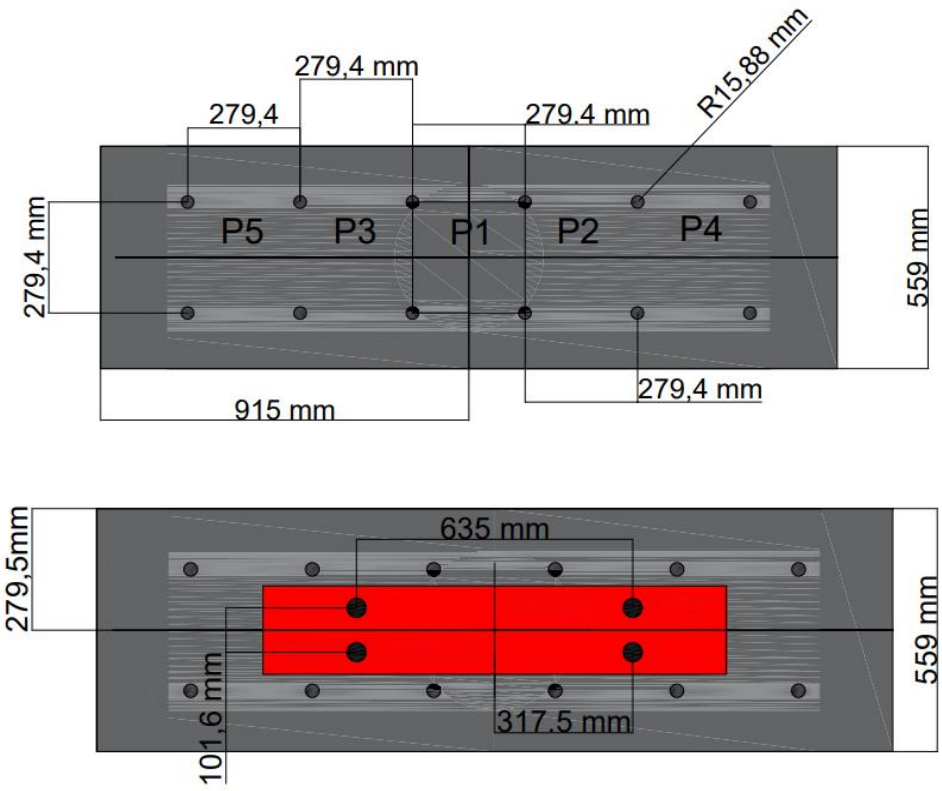

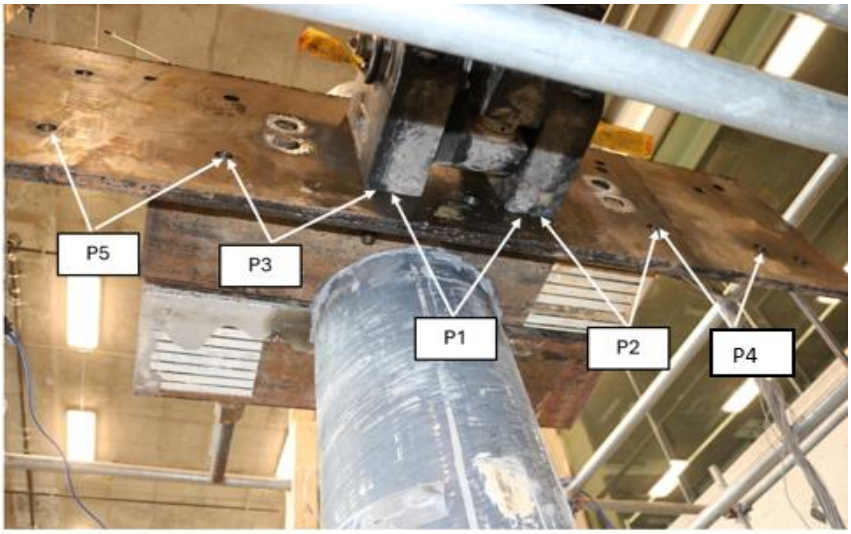

Figure 3.27. The actuator steel plate with actuator positions

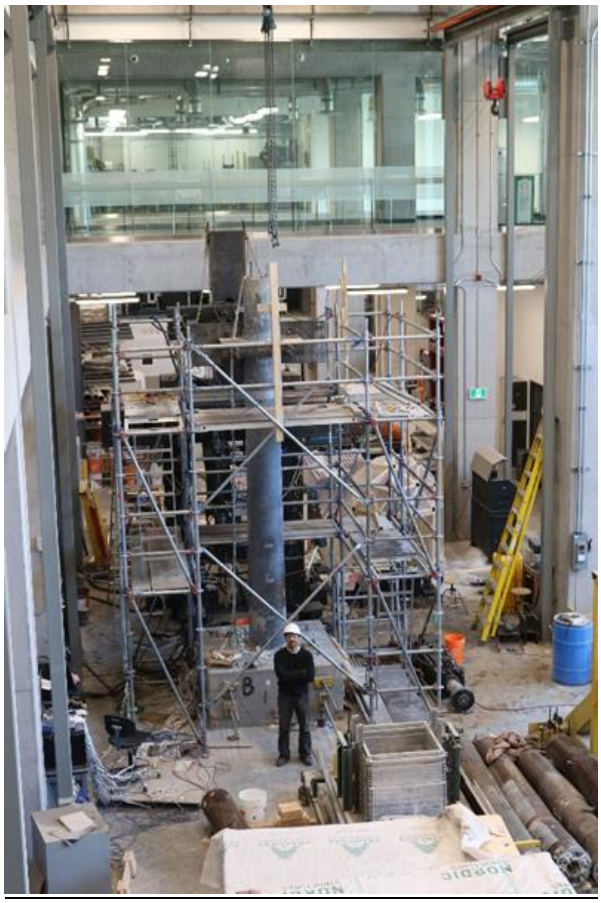

Figure 3.28. CFFT tower segment prior to testing

Test Procedure I: Free vibration test: All three towers were subjected to vibration testing. A high strength cable connected to a winch was used to exert a pulling force on the top free end of the tower. To facilitate controlled testing, a notched rectangular steel plate, as illustrated in Figure 3. 29, was designed as a "fuse" with one side of the plate linked to the winch through a screw pin shackle and the other side connected to the top free end of the tower. The steel plate was specifically engineered to rupture when subjected to a force equivalent to 15% of the maximum expected load. This intentional rupture allowed the tower to experience free flexural vibrations under the applied force upon release.

The connected cable transducers at the top of the tower were able to detect the dynamic reaction and through the data acquisition system the damped motions of the regenerating force versus time were recorded.

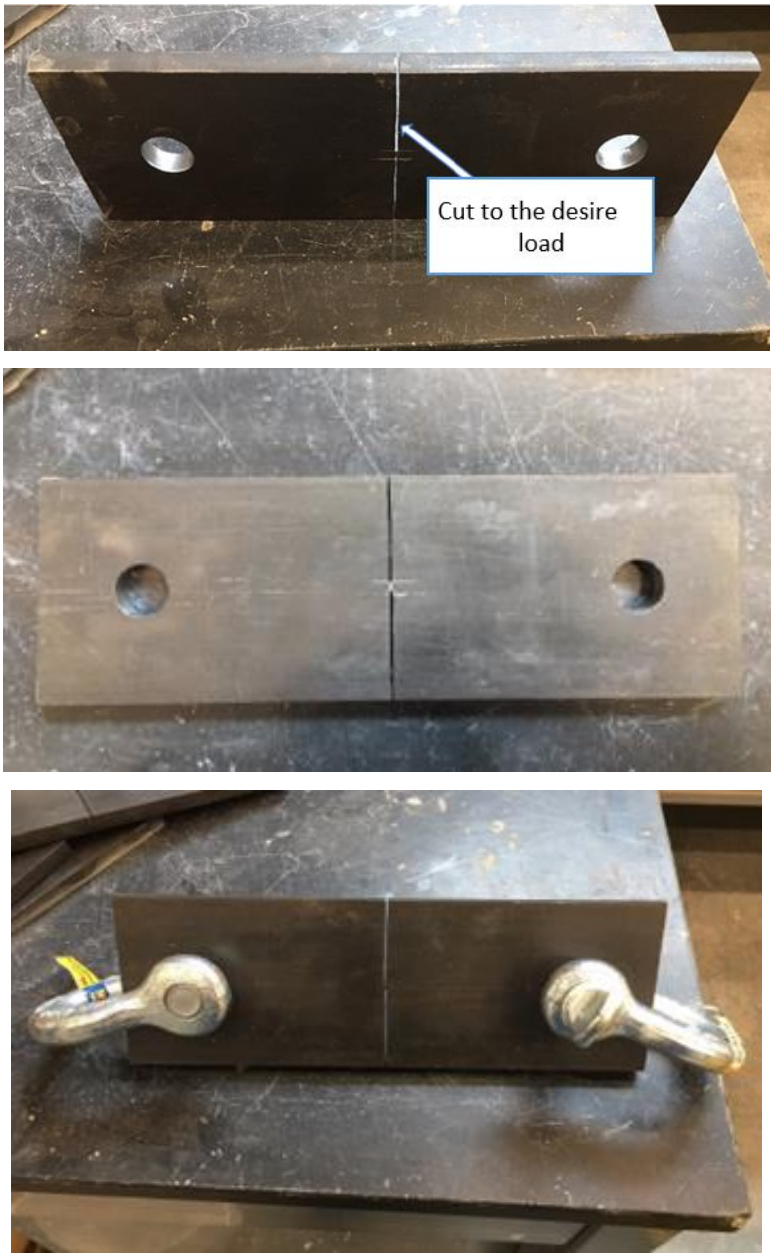

Figure 3. 29. Notched rectangular steel plate

Test Procedure II: Cyclic flexural testing under concentric loading: The three towers were subjected to a series of gradually increasing reversed loading cycles (push and pull) corresponding to approximately 10%, 15%, 20%, 25%, and 40% of the theoretical failure load. Each load increment was repeated for three cycles.

The actuator was connected in the center of the actuator plate (P1) as shown in Figure 3.27. The loading was applied in displacement control to capture the initial flexural stiffness of the tower.

Test Procedure III: Cyclic flexural-torsional testing under eccentric loading: Wind turbines are typically designed to swivel on the top of their towers to capture wind energy from different directions. As a result of friction, this can induce torsional moments in the tower structure. The three towers were subjected to a service load test with eccentric loading. The actuator was relocated to different positions on the actuator plate as follows: A) Position P2, corresponding to a small eccentricity (approximately one-half of the tower diameter, D/2) on the right side of the tower; B) Position P4, corresponding to a large eccentricity (D) on the right side of the tower; C) Position P3, corresponding to a small eccentricity (D/2) on the left side of the tower; and D) Position P5, corresponding to a large eccentricity (D) on the left side of the tower. In each case, loading was applied in displacement control up to 40% of the theoretical failure load.

Test Procedure IV: Originally, the plan included subjecting two towers to eccentric loading up to failure. The actuator would be connected to different positions on the actuator plate as follows: A) Position P2, corresponding to a small eccentricity (D/2); B) Position P4, corresponding to a large eccentricity (D). The goal was to apply loading until the towers reached their ultimate flexural capacity and obtain in- and out-of-plane displacement. However, the loading with large eccentricity could not be completed as the actuator reached its maximum stroke, and there was no practical solution to proceed with this type of test. Consequently, the plan was revised to proceed with centric loading until failure.

Test Procedure V: The three towers were loaded to failure with the load applied at the center. The actuator was connected to the center of the actuator plate (P1) as shown in Figure 3.27. Loading was applied up to final failure to capture the ultimate flexural capacity and displacement of the tower.

3.4.2. Instrumentation

At critical locations with the purpose of receiving the necessary test data, cable transducers were connected to the foundation units, while strain gauges were positioned on the tension,

compression, and the two sides of the towers' surface (Figure 3.30 and Figure 3.31). In addition, strain gauges were mounted at critical locations on the longitudinal reinforcing bars to determine and record the strain behaviour during the test. All the installed strain gauges are positioned vertically, except for those on the C and D faces of the GPRP surface, which are oriented horizontally. These horizontally oriented gauges are specifically placed to measure hoop expansion. The recorded data includes the applied load, lateral deflection, sliding and uplifting of foundation, and reinforcing steel strains.

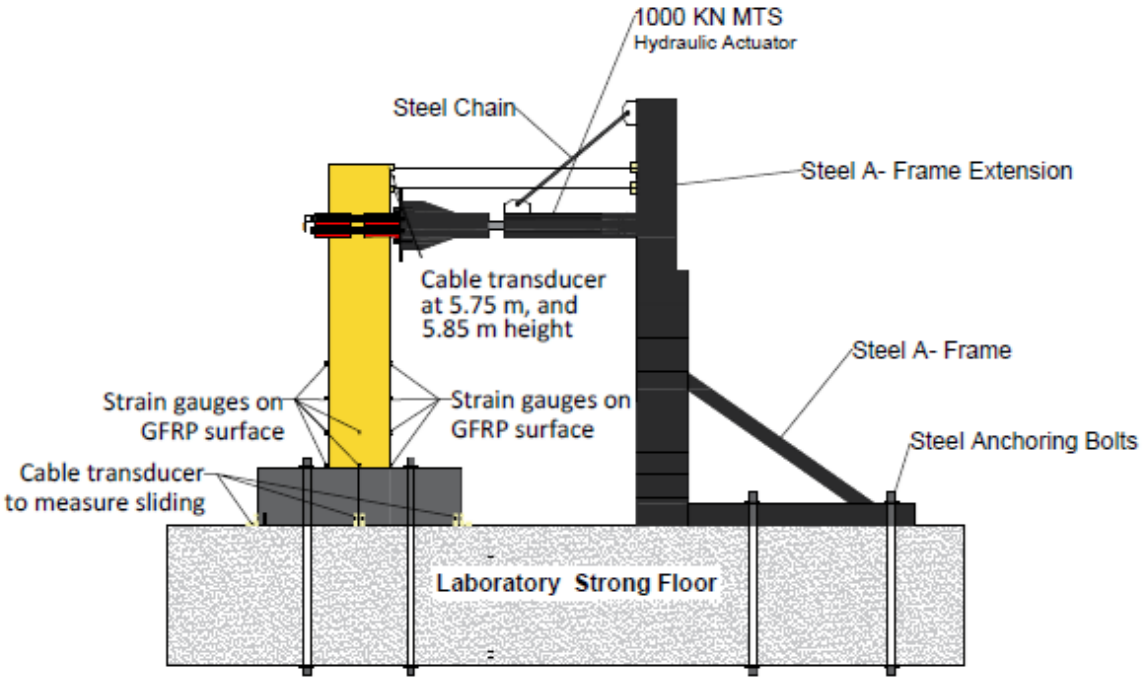

Figure 3.30. Cable transducer and strain gauge's locations

(a) Tension side of the towers' surface (b) Sides of the towers' surface

Figure 3.31. Strain gauges Locations on the GFRP surface

According to the review of instrumentation strategies used in previous experimental programs which are presented in the literature review, the following information were collected during tests:

- Lateral load: the applied lateral load was measured via a built-in load cell in the MTS hydraulic actuator. Moreover, the digitized data from the test was connected to the data acquisition system and stored in the computer.
- Lateral displacement: the lateral displacement was recorded at two different locations using cable transducers installed at 5.75 m and 5.85 m height (50 mm above the tower, utilizing the extended steel rebar at the top).

- Sliding and uplift of foundation: cable transducers were installed along the length and the end of the foundation units to measure its uplift and sliding during tests, respectively. In addition, the same transducers were used to measure any potential slip at the base of the tower relative to the foundation.

- Natural frequencies of the cantilever towers: Cable transducers were connected at the top free end of the towers to record the distributed natural frequencies of each tower.
- General observations: the towers' general behaviour including damage, failure mode, and rupture of GFRP layers were monitored during tests.

Chapter 4- Analysis and Modeling

4.1. Introduction

This chapter presents a comprehensive analytical and numerical modelling study to complement the experimental program described previously. The investigation consists of two primary components: detailed analytical calculations and the development of a finite element (FE) model. First, a series of analytical calculations are presented to determine key structural properties of the post-tensioned hollow tapered CFFT towers. These calculations include determining the moment resistance along the tower height using a layered sectional analysis, evaluating the shear resistance based on design codes, and predicting deflection profiles through curvature integration. These calculations provide a theoretical baseline and insight into the structural behaviour of the system.

Building on this, a finite element (FE) model was developed using the commercial software ABAQUS to simulate the flexural behaviour of post-tensioned hollow tapered CFFTs with different diameters in cantilever tower configurations subjected to lateral loading. This model was validated using the experimental results of this research and used to develop a better understanding of the effects of key design parameters on tower performance. The simulations were conducted to replicate both the static and dynamic responses recorded during the experimental testing phase.

The aim of this chapter is to present both the analytical calculations and the development and calibration of this FE model, and to use these approaches to conduct a parametric study to further investigate the influence of critical design parameters on the tower behaviour of the system.

4.2. Analytical Work

4.2.1. Natural frequency and damping ratio ζ

The experimental natural frequency and damping ratio ζ were determined using the Logarithmic Decrement Method (Yokoyama et al., 2023). The vibration test results, including amplitudes, time at which each amplitude is measured, and the time difference between two consecutive amplitudes (T_d), are analyzed. First, two successive peak amplitudes, $X(t_n)$ and $X(t_{n+1})$, were identified from

the free decay response, where 'n' is the number of oscillation cycles between the selected peaks. The logarithmic decrement (δ) was then calculated for each interval using Eq. 4.1. Subsequently, the damping ratio (ζ) was computed using Eq. 4.2. The natural frequency was determined by taking the reciprocal of the oscillation period (T_d), which is the time it takes for one complete cycle of vibration using Eq. 4.3

$$\delta = \ln\left(\frac{x(t_n)}{x(t_{n+1})}\right) \quad \text{Eq. 4.1}$$

$$\zeta = \frac{\delta}{2\pi} \quad \text{Eq. 4.2}$$

$$f_d = \frac{1}{T_d} \quad \text{Eq. 4.3}$$

4.2.2. Moment resistance

The moment resistance at various points along the tower height was estimated using a layered sectional analysis. The tower base cross-section was divided into approximately 100 thin layers, considering the hollow section when calculating the area of each layer. The Modified Hognestad stress-strain curve (Hognestad, 1951) was used for concrete. Assuming a linear strain distribution, stress for each material was determined using appropriate stress-strain relationships. Internal forces in each layer were obtained by multiplying the stress in each material by the corresponding layer area. To ensure equilibrium, the total compressive force was balanced against the tensile force, requiring iterative adjustments to the neutral axis position. Finally, the bending moment capacity was calculated by summing the force contributions across all layers multiplied by their respective lever arms. Since the degree of concrete confinement in the partially filled tubes is uncertain, the analysis was conducted twice for each tower size, assuming either fully confined or fully unconfined conditions. A summary of the geometric and mechanical properties for tower M5 are presented in Table 4.1 through Table 4.6.

Table 4.1. Concrete properties

Unconfined concrete strength, f'_{c0} (MPa)	61.6
Unconfined concrete strain at peak stress, ε_0	0.02
Unconfined concrete ultimate strain, ε_{cu}	0.0035
Unconfined concrete modulus of elasticity, E_c (MPa)	37124

Note: The unconfined concrete properties are based on the Hognestad constitutive model. The detailed steps are shown in Appendix A. Concrete strength in tension was neglected.

Table 4.2 shows the sizes and material properties of steel bars used in this analysis. Figure 4.1 shows the experimental stress–strain curves for the 10M and 15M reinforcing bars. As expected, both bars demonstrate typical steel behaviour, starting with a linear-elastic response, followed by yielding and strain hardening. The 15M bar (in red) reached a higher peak stress and maintained its strength over a longer strain range, suggesting greater ductility. On the other hand, the 10M bar (in blue) showed an earlier strength drop after peak stress due to fracture. These results were used to define the material properties in the analytical model. Table 4.3 shows the nominal material properties for the prestressing strands. Table 4. 4 illustrate the prestress level and average microstrain (με) in towers, and Table 4.5 shows the GFRP properties.

Table 4.2. Steel rebar sizes and material properties

Steel ID	Nominal diameter	Cross-sectional area	Yield		Ultimate	
size	(mm)	(mm^2)	ε_y	f_y (MPa)	ε_u	f_u (MPa)
10M	11.3	100	0.0175	444	0.077	575
15M	16	200	0.0149	411	0.153	607

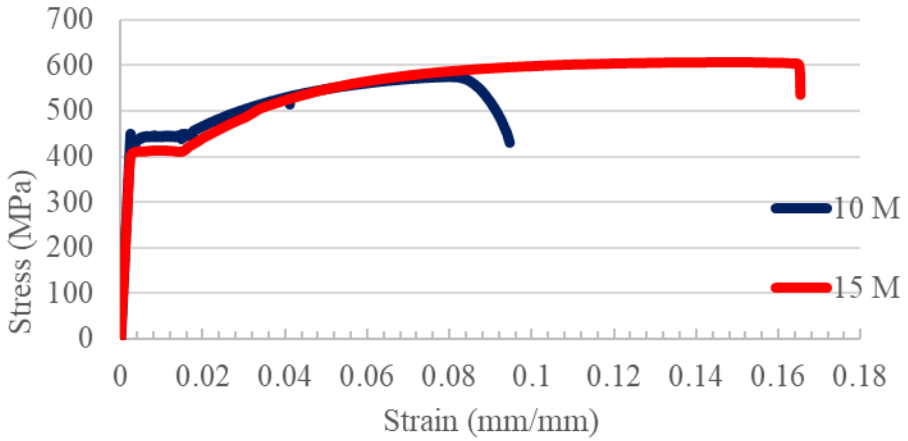

Figure 4.1. Steel stress-strain relationship

Table 4.3. Prestressing strand properties

Ultimate tensile strength, f_{pu} (MPa)	1860
Modulus of elasticity, $E_{s.pre}$ (MPa)	190000
Yield strain of the strands, ε_{sy}	0.013
Ultimate strain of the strands, ε_{su}	0.07
Number of steel strands	4
Area of single steel strand, A_P (mm^2)	99
Yield stress, $f_{py}=0.9*f_{pu}$ (MPa)	1674
Stress at transfer, f_{pe} (MPa)	1000

Table 4. 4. Prestress level and average microstrain (με) in towers

Tower	Average stress at transfer (MPa)	Micro Strain (Average of Calibration Tests) με
M5	793	3936
M4-1	1020	5101
M4-2	1031	5207

Table 4.5. GFRP properties

	Coupons Test	Manufacturer
Ultimate longitudinal tensile strength, $f_{ut,GFRP}$ (MPa)	366.8	205
Ultimate longitudinal tensile strain, $\varepsilon_{ut,GFRP}$ (mm/mm)	0.016	0.01
Longitudinal tensile elastic modulus, E_{GFRP} (MPa)	27000	28060

Confined concrete properties were calculated according to Lam and Teng's model. Table 4.6 presents a summary of the results. The detailed steps are shown in Appendix B.

Table 4.6. Summary of confined concrete properties

Hoop tensile strength, $f_{J,GFRP}$ (MPa)	92
Confining pressure, f_l (MPa)	3.57
Ultimate confined concrete strain, ε_{ccu}	0.0102
Ultimate confined concrete strength, f'_{cc} (MPa)	69
Slope of linear second portion, E2 (MPa)	1181
Transition strain, ε_t	0.0034

A strain compatibility analysis was used to estimate the moment resistance of the CFFT towers at different points along the height having different diameters. A flow chart of this procedure is presented in Figure 4.2.

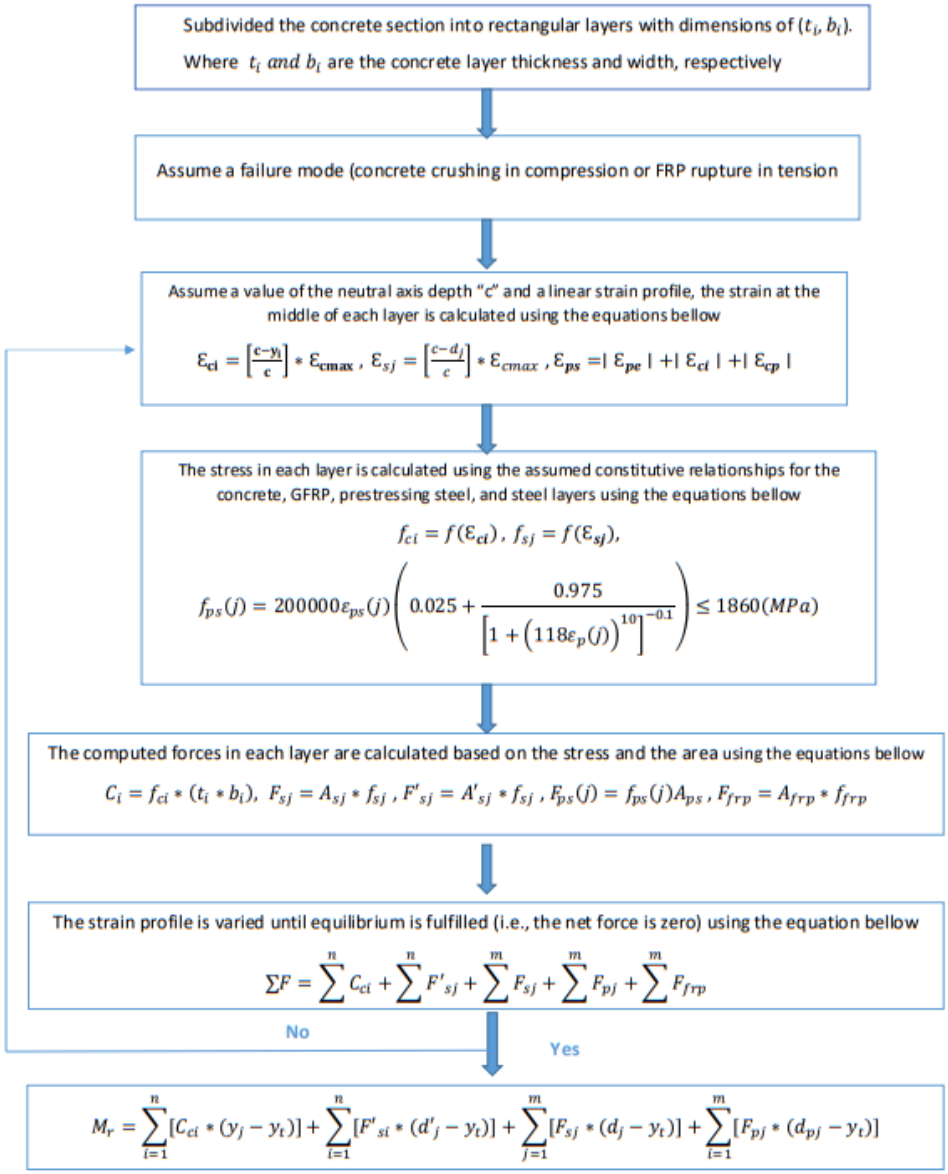

Figure 4.2. Flow chart of the layer by layer sectional analysis

Table 4.7 presents the total calculated moment resistance at the base of each tower using confined and unconfined concrete.

Table 4.7. Maximum moment resistance (M_r) for each tower

Towers' Group	Mr (kN.m), unconfined concrete	Mr (kN.m), confined concrete
M5	594	754
M4	449	651

Figure 4.3 shows the moment resistance of the two tower sizes along their height using the confined concrete model. The base of the towers for these tests is located 790 mm from the bottom of the tube to account for the embedment in the foundation block.

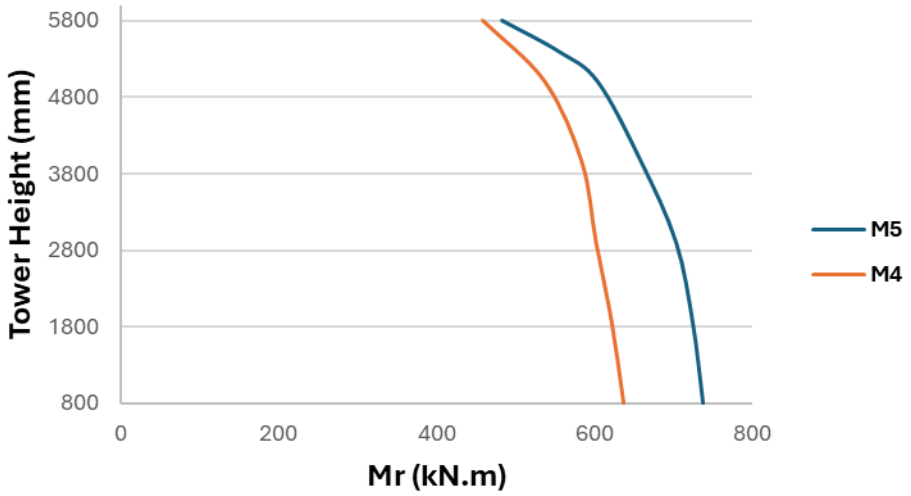

Figure 4.3. Moment resistance of towers along the height for confined concrete model

4.2.3. Shear resistance

The shear resistance of each tower was also analyzed. The contributions from GFRP, concrete, prestressing, and steel were calculated using the CSA A23.3-14 code. Table 4.8 presents a summary of the results for Tower M5. It was determined that the total shear resistance of the tower significantly exceeds the maximum applied shear for both M4 and M5 towers. Consequently, the structure is adequately designed to prevent shear failure. The detailed steps are shown in Appendix C.

Table 4.8. Summary of shear resistance calculation

Shear Resistance Component	Result (kN)
GFRP Contribution (V_{GFRP})	512
Concrete Contribution (V_C)	72
Steel Contribution (V_s)	215
Prestressing Contribution (V_p)	0
Total Shear Resistance (V_r)	799

4.2.4. Deflections

The theoretical deflection of the tower can be estimated using the same sectional model developed for moment resistance, by integrating the curvature along the height of towers (Figure 4.2). Once the neutral axis depth (c) and the concrete compression strain corresponding to the calculated moment were determined, these values were then used to calculate the curvature (Φ). From the curvature diagram, the deflection (Δ) was obtained using the moment–area method, where Δ equals the area under the curvature curve multiplied by the distance from its centroid to the point of zero moment. Figure 4.5 compares the predicted deflection profiles of the M4 and M5 towers along their height to the measured top displacement at failure. The experimental profiles were obtained at the maximum applied loads, which were 132 kN for the M4 tower and 182 kN for the M5 tower. It is worth noting that Tower M4-1 has a concrete core thickness of 100 mm, while Tower M5 has a thicker concrete core of 125 mm. Using the analytical model with these different concrete thicknesses showed that the increased thickness in Tower M5, along with its larger diameter, contributed to its higher stiffness and load capacity. Figure 4.6 shows the experimental load–deflection results with the corresponding theoretical calculations. The difference between the theoretical and experimental deflections is partially attributed to the difference between the assumed and actual prestressing forces. Each of the three towers was reinforced with four prestress tendons. The prestress levels in these tendons varied between 700 and 1450 MPa, with the average values summarized in Table 4. 4. For the theoretical model, prestresses of 750 MPa for M5 and 800 MPa for M4 were assumed, representing ideal conditions with no losses. In practice, however, the actual prestress applied during testing may have been lower. Despite this variation, these values

were used in the model to represent average prestress levels. Consequently, the graph shows very good agreement between the theoretical predictions and the experimental results, although the small differences observed in the M5 response are likely due to the concrete core not being compressed to the extent predicted by the model. This reduced the overall stiffness of the tower and led to slightly larger lateral deflections. Additional factors, such as early concrete cracking, minor bond slip between materials, or construction inconsistencies, may have further contributed to these deviations. The influence of prestressing on the load–deflection response is discussed in greater detail in Chapter 8, and the full calculation procedure is provided in Appendix D.

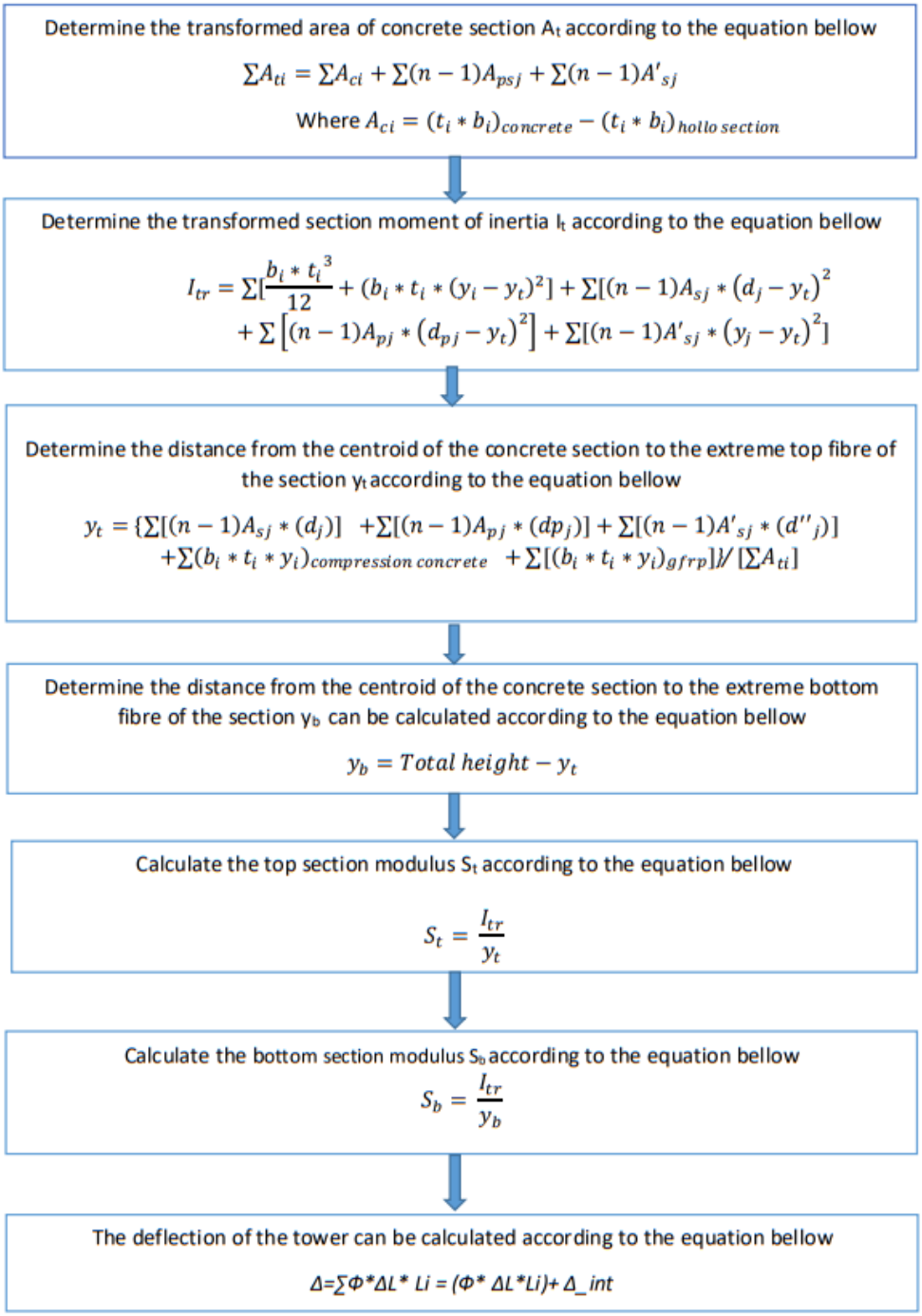

Figure 4.4. Flow chart of tower's deflection calculation

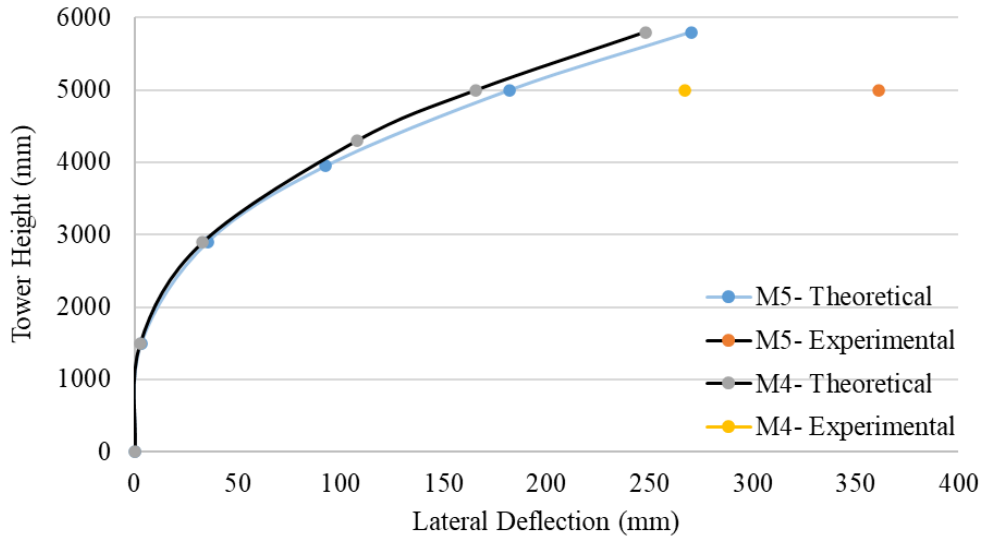

Figure 4.5. Predicted deflection profiles of the M4 and M5 towers along their height at their respective peak loads, 132 kN and 182 kN, respectively

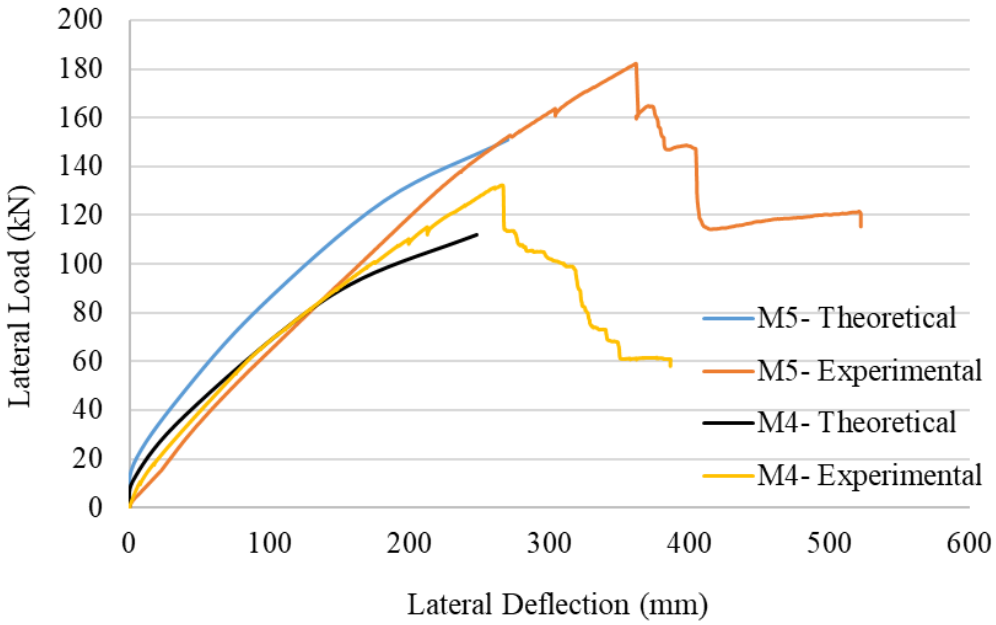

Figure 4.6. Comparison of experimental and theoretical load–deflection profiles at a height of 5 m for the M4 and M5 towers

4.2.5. Foundation

In order to predict the critical embedment length (X_{cr}) of the towers into the foundation and achieve the material failure of the CFFT outside the footing, the robust analytical model was used to calculate X_{cr} (Sadeghian and Fam, 2010). The critical embedded length of the tower into the foundation was found to be 413 mm. A conservative height of 700 mm was used for the foundation to avoid material failure of the CFFTs inside the foundation. The calculations are detailed in Appendix E.

4.3. Finite Element Modeling

4.3. 1. Element Types and Material Models

This section covers the material models for concrete, GFRP, steel reinforcement, steel tendons, end steel plates of tendon, and the associated failure criteria. These fundamental parts are illustrated in Figure 4.7.

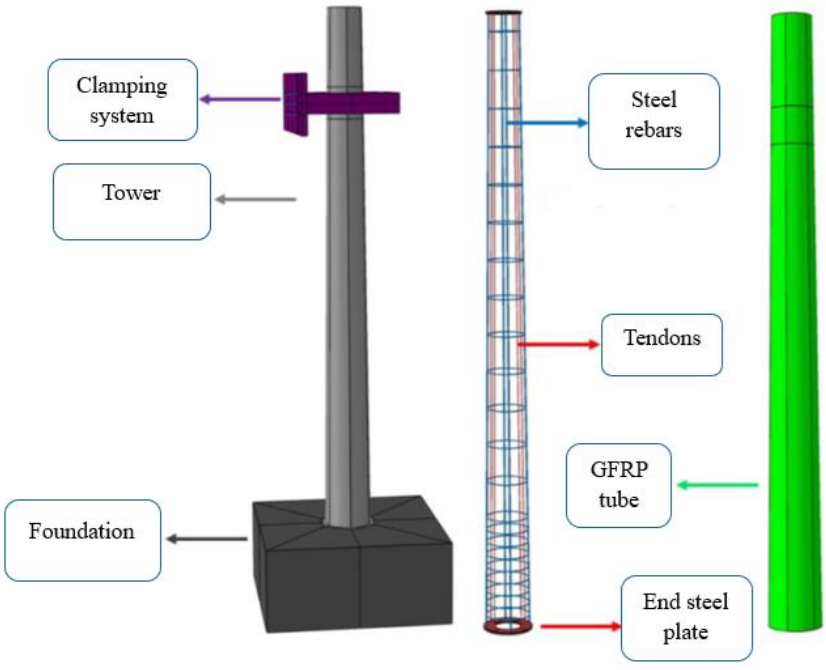

Figure 4.7. Schematic of the numerical model showing fundamental parts

The modeling effort focused on two towers (M4 and M5), which were modeled as follows:

4.3. 2. Concrete

The concrete tower and foundation were meshed using 8-node solid elements with reduced integration and hourglass control (C3D8R), which are effective for capturing nonlinear behaviour of concrete while minimizing shear locking. The use of reduced integration also helps in reducing computational time without significantly compromising accuracy. The overall mesh configuration, including the tower and foundation, is illustrated in Figure 4.8. The nonlinear material behaviour of the concrete was modeled using the Concrete Damaged Plasticity (CDP) model in ABAQUS, which captures both tensile cracking and compressive crushing under lateral loading. The elastic properties of the concrete are summarized in Table 4. 9. The CDP parameters used in this study are provided in Table 4. 10. Within the CDP framework, the compressive stress–strain relationship for unconfined concrete was defined using the Hognestad model, allowing for a realistic simulation of the nonlinear response up to the peak strength and through the post-peak softening region. The compressive behaviour and damage parameters are listed in Table 4. 11, while the tensile behaviour and damage parameters are given in Table 4. 12.

For the confined regions, the stress–strain behaviour of FRP-confined concrete was characterized using the Lam and Teng (2003) model, as presented in Section 2.3.5.2 of the Literature Review. This model was specifically developed for FRP jackets with fibres oriented mainly in the hoop direction. Under axial compression, the concrete core undergoes lateral expansion, which is restrained by the surrounding GFRP tube, generating confining pressure. The ultimate confined strength is reached when the hoop tensile stress in the GFRP exceeds its tensile capacity, leading to rupture. Furthermore, due to the relatively high rigidity of the foundation compared to the tower, it was modeled as rigid and merged directly with the tower in this model. By doing so, the model avoids the need for defining additional contact or interaction properties in ABAQUS, which would otherwise increase computational complexity without significantly affecting the accuracy of the results.

Table 4. 9. Elastic properties of concrete

Parameter	Value
Elastic modulus, E (MPa)	30297
Poisson's ratio, ν	0.25

Table 4. 10. CDP parameters

Dilation Angle	Eccentricity	σ_{b0}/σ_{c0}	K	Viscosity Parameter
30	0.1	1.16	0.6667	0.001

Table 4. 11. Compressive behaviour and damage

Yield Stress (MPa)	Inelastic Strain	Damage Parameter	Inelastic Strain
30.800000	0.000000	0.000000	0.000000
36.909844	0.000032	0.011038	0.000032
43.375379	0.000068	0.020042	0.000068
49.108853	0.000129	0.033002	0.000129
53.904866	0.000221	0.050495	0.000221
60.093970	0.000516	0.100394	0.000516
61.531205	0.000969	0.169774	0.000969
59.034710	0.001551	0.254419	0.001551
54.084873	0.002215	0.347141	0.002215
42.037134	0.003612	0.527371	0.003612
31.500273	0.004960	0.671552	0.004960
23.666763	0.006219	0.773338	0.006219
18.080767	0.007403	0.841684	0.007403

Table 4. 12. Tensile behaviour and damage

Yield Stress (MPa)	Cracking Strain	Damage Parameter	Cracking Strain
4.842350	0.000000	0.000000	0.000000
0.242100	0.001598	0.950000	0.001598

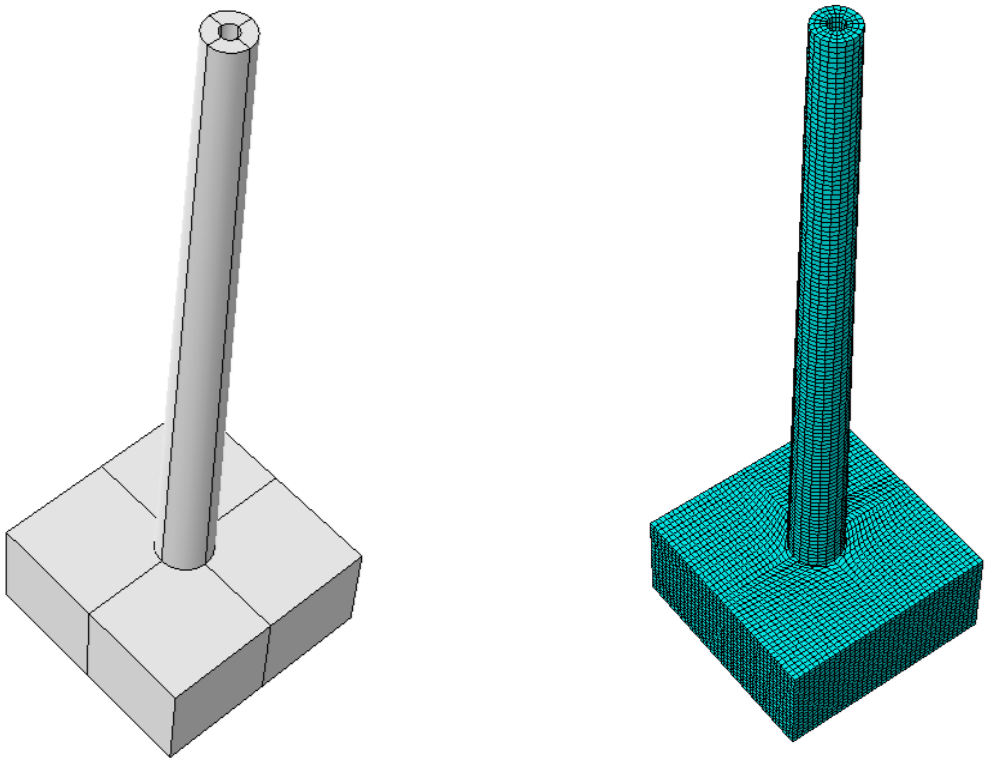

Figure 4.8.3D model and FE mesh of the M4 tower including foundation

4.3. 3. GFRP

The outer GFRP tube was treated as an orthotropic material modeled using 4-node shell elements (S4R), implemented through the Skin tool in Abaqus. The engineering constants for the GFRP material used in this study are summarized in Table 4.13. The Skin tool provides an efficient method for applying a thin reinforcement layer, such as a GFRP shell, to the surface of an existing part without the need to model it as a separate part. Therefore, this skin is modeled as a shell or membrane element that is bonded to the exterior of the host part and assigned with independent material and section properties. When the model is meshed, the skin automatically generates shell elements on the selected faces of the host part. These elements share the same nodes as the underlying solid mesh, allowing for complete compatibility in deformation and stress transfer

between the skin and the substrate. As a result, the composite action between the reinforcement and the base structure is fully preserved.

Table 4.13. Material Parameters of GFRP

$E_1(MPa)$	$E_2(MPa)$	ϑ_{12}	$G_{12}(MPa)$	$G_{13}(MPa)$	$G_{23}(MPa)$
32000	7440	0.38	3500	3500	3500

An important advantage of the skin modeling approach is the reduction in the total number of degrees of freedom. By avoiding the duplication of interface nodes and eliminating the overhead associated with constraint equations, the model becomes simpler and faster to solve. The skin elements effectively overlay the host mesh, providing additional stiffness or strength while accurately preserving composite action since both layers respond together at every node. This modeling approach ensures full connection at the nodal level, allowing continuous deformation and stress transfer between the skin and the core as if they act as a single composite unit. The reduced integration of S4R elements helps prevent artificial stiffening and improves computational efficiency. By employing these element types and integration techniques, the model achieves a balance between accuracy and numerical performance, providing a realistic representation of the structural behaviour of concrete-filled GFRP tubes (see Figure 4.9).

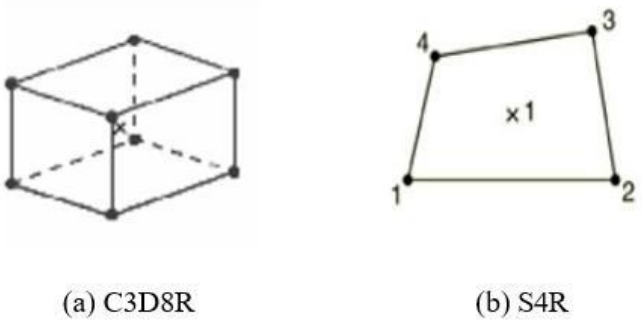

(a) C3D8R (b) S4R

Figure 4.9 Element types used for concrete and GFRP (Abaqus, 2014)

Similarly, the GFRP tube's behaviour was governed by Hashin's damage initiation criteria, which accounts for both fibre and matrix failure modes in tension and compression. This criterion is

widely used for simulation damage in fibre-reinforced composites due to its ability to capture the different failure mechanisms accurately (Boules, 2022). Hashin's damage initiation occurs when any of the following conditions are met:

(a) Fibre Tension Failure ($\sigma_{11} \geq 0$) using Eq. 4.4:

$$F_f^T = \left(\frac{\sigma_{11}}{X_T}\right)^2 + \left(\frac{\tau_{12}}{S}\right)^2 \geq 1 \quad \text{Eq. 4.4}$$

Where;

- σ_{11}: Longitudinal normal stress in the fiber direction
- X_T: Fiber tensile strength
- τ_{12}: In-plane shear stress, and
- S: Longitudinal shear strength

- Occurs when the axial tensile stress (σ_{11}) exceeds the tensile strength of the fibre (X_T).
- Shear effects are also considered in the model (τ_{12})

(b) Fibre Compression Failure ($\sigma_{11} < 0$) using Eq. 4.5:

$$F_f^C = \left(\frac{\sigma_{11}}{X_C}\right)^2 \geq 1 \quad \text{Eq. 4.5}$$

Where:

- X_C: Fiber compressive strength

Failure in the fiber direction under compression occurs when the axial compressive stress (σ_{11}) exceeds the fiber's compressive strength (X_c).

(c) Matrix Tension Failure ($\sigma_{22} \geq 0$) using Eq. 4.6

$$F_m^T = \left(\frac{\sigma_{22}}{Y_T}\right)^2 + \left(\frac{\tau_{12}}{S}\right)^2 \geq 1 \quad \text{Eq. 4.6}$$

Where;

σ_{22} : Transverse normal stresses perpendicular to fibers

Y_T: Matrix tensile strength

Matrix cracking occurs when transverse stress (σ_{22}) exceeds matrix tensile strength Y_T.

(d) Matrix Compression Failure ($\sigma_{22}<0$) using Eq. 4.7 :

$$F_m^c = \frac{\sigma_{22}^2}{Y_C^2} + \frac{\sigma_{22}\sigma_{33}}{Y_C^2} + \frac{\tau_{12}^2}{S^2} \geq 1 \qquad \text{Eq. 4.7}$$

Where:

- σ_{33}: Transverse normal stresses perpendicular to fibers
- Y_C: Matrix compressive strength

Matrix crushing or delamination occurs under excessive compressive stress (σ_{22}).

4.3. 4. Damage Evolution

Once failure is initiated, the material response follows a progressive damage evolution mechanism. Abaqus models this behaviour by gradually degrading the material stiffness according to the fracture energy (G_f) parameter, ensuring a smooth and stable failure progression. The level of degradation is measured by the damage variable d, as defined in Eq. 4.8.

$$d = 1 - \frac{G_c}{G_f} \qquad \text{Eq. 4.8}$$

where:

- d is the damage variable (0 for undamaged, 1 for fully damaged).
- G_c is the energy dissipated until failure.
- G_f is the total fractured energy.

4.3. 5. Steel Reinforcement and Tendons

The transverse steel reinforcement (ties) was modeled using wire elements (truss) to capture their axial stiffness contribution, while longitudinal reinforcement was simulated with truss elements (T3D2) as shown in Figure 4.10. Truss elements were specifically selected for their ability to efficiently simulate axial force transfer without resisting bending effects, providing both computationally efficient and accurate simulation of reinforcement behaviour. To ensure a perfect bond between the reinforcement and the surrounding concrete, the longitudinal reinforcement bars, post-tensioning tendons, end steel plates, and ties were embedded within the concrete using an embedded region constraint. Internal steel reinforcement and post-tensioning tendons were modeled using an elastic–plastic material model with isotropic hardening, calibrated according to the actual yield strength and modulus of the steel. The material parameters for the steel reinforcement are summarized in Table 4.14.

This approach efficiently captures the behaviour of the reinforcement while ensuring proper load transfer between the reinforcing bars and the concrete matrix.

Table 4.14. Material parameters for steel reinforcement.

Property	Value
Elastic Modulus, E (GPa)	200
Poisson's Ratio, ϑ	0.3
Yield Stress, σ_{γ} (MPa)	411.84
Ultimate Stress, σ_{u} (MPa)	699.871
Ultimate Strain, ε_{u}	0.1459

For post-tensioning simulation, predefined stress fields were applied to the tendons, enabling them to carry initial tensile forces prior to the application of external loads. This method effectively replicates the mechanical behaviour of prestressed concrete, resulting in improved structural stiffness and reduced deformation. The complete modeling approach successfully captures the composite interaction between all components, providing both computational efficiency and accurate prediction of the tower behaviour and local stress distributions under various load cases.

The combination of accurate reinforcement modeling and post-tensioning simulation was critical to achieving realistic load transfer, stress development, and reliable prediction of structural performance.

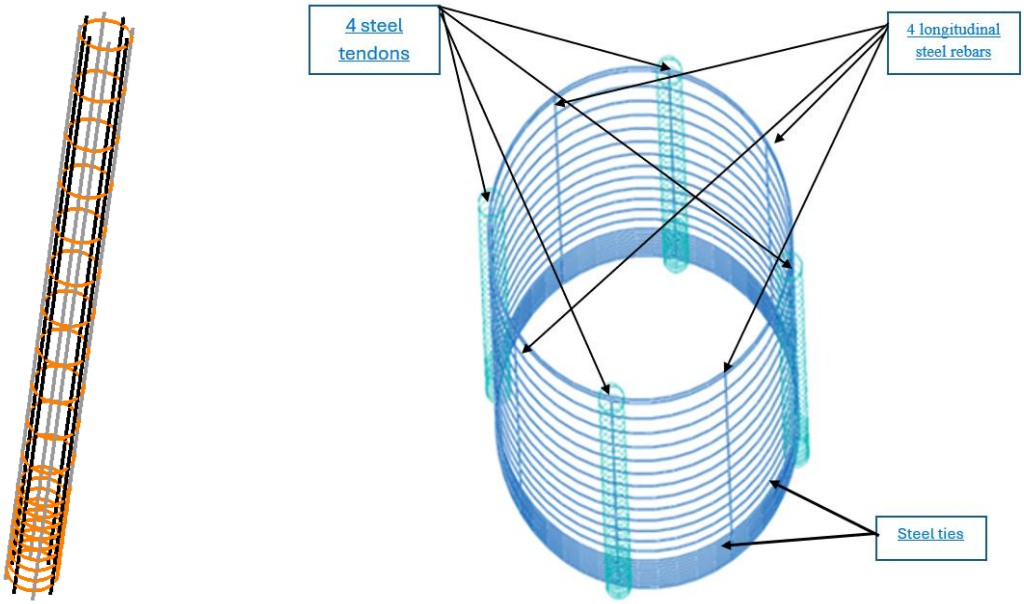

Figure 4.10. FE model of the reinforcement grid and post-tensioning tendons.

4.4. Mesh Sensitivity Analysis

Several models with different mesh sizes varying from 35 mm to 60 mm were developed to study the mesh sensitivity of the wind tower simulation. Figure 4.11 illustrates the effect of mesh refinement on the lateral load–deflection response of the M4 tower. Models with 35 mm and 40 mm mesh sizes demonstrated strong agreement, particularly within the initial linear elastic range and near the peak load capacity. In contrast, coarser 50 mm meshes tended to overestimate the peak load and displayed a more gradual softening response, suggesting a delayed or smeared failure mechanism resulting from insufficient element refinement.

The post-peak response further highlighted the drawbacks of coarse meshes, with a mesh size of 50 mm showing irregular degradation of load-carrying capacity, attributed to numerical instabilities and artificial stiffness. After comparison, a mesh size of 35 mm was selected for

subsequent analyses as it achieved convergence with acceptable computational effort. Further mesh refinement was considered unnecessary, as it would significantly increase simulation time without offering additional accuracy.

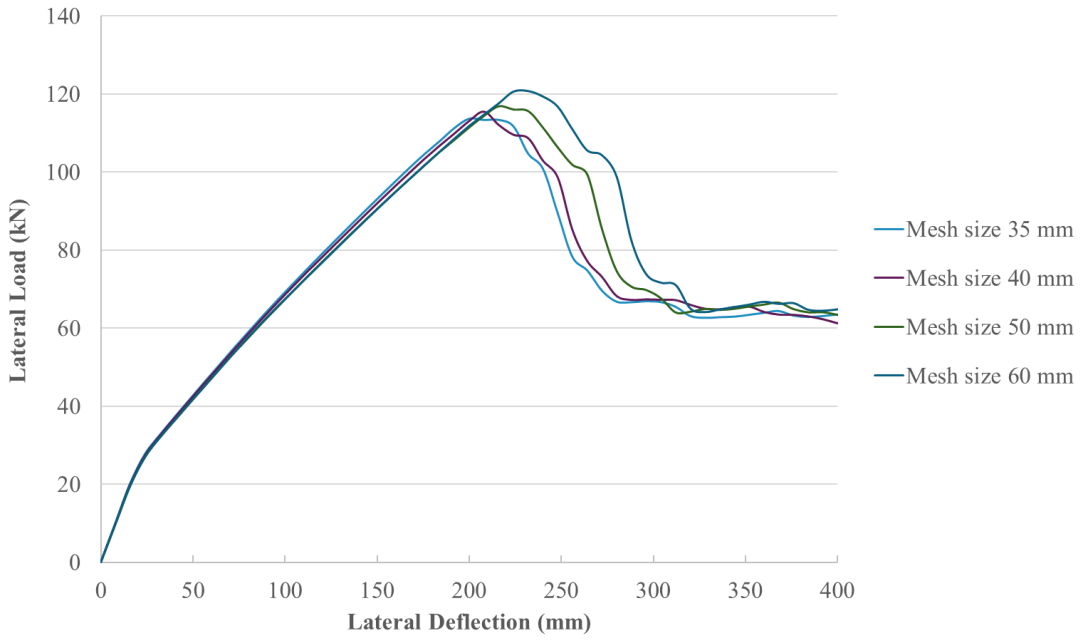

Figure 4.11. Lateral load–lateral deflection response from the mesh sensitivity analysis for different mesh sizes

4.5. Interaction

In addition to the embedded parts mentioned in Section 4.2.4, a contact type interaction was defined between the tower and the clamping system to realistically simulate their interface behaviour (Figure 4.12). In the normal direction (perpendicular to the surface), hard contact was used to prevent penetration between the surfaces, while no tensile stresses were transmitted across the interface. In the tangential direction (along the surface), a friction coefficient of 0.6 was applied, allowing shear stresses to develop and resist sliding. This approach captures the realistic mechanical response at the interface, ensuring that the parts interact as they would physically under loading.

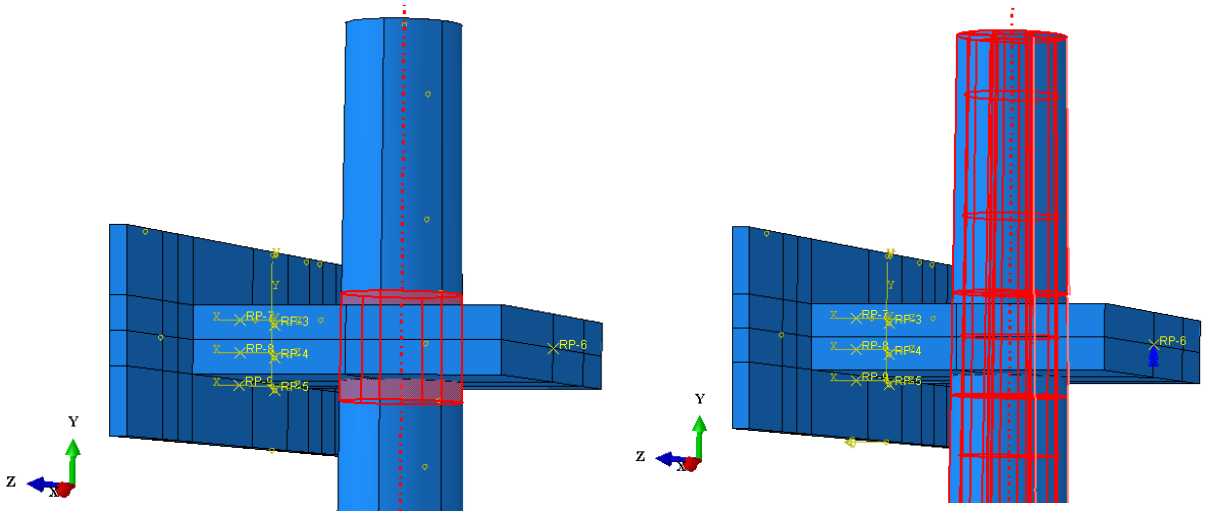

Figure 4.12. Illustration of the finite element model showing the locations of embedded constraints and applied contact interactions.

4.6. Boundary Conditions and Loading

A mesh size of 75 mm was used for the foundation, 30 mm for the clamping system, and 35 mm for the tower and grout, ensuring stable results and realistic hysteresis behaviour under cyclic loading. The clamping system was also meshed using the same method with 8-node solid elements. For solid elements, three mesh layers were assigned through the thickness, which helped reduce hourglass effects and better represent the strain distribution across the section depth (Dassault Systèmes, 2006). Table 4.15 summarizes the element types and mesh configuration used in the model, while

Figure 4.13 and Figure 4.14 illustrate the overall mesh, including the tower, clamping system, and foundation.

Table 4.15. Element Classification and Applications in the FE Model

Element Type	ABAQUS Element	Description	Application in Model
Solid Element	C3D8R	8-node linear brick, reduced integration, hourglass control. High accuracy, high computational demand	Tower, foundation, clamping system
Shell Element	S4R	4-node doubly curved thin or thick shell, reduced integration, hourglass control, finite membrane strains. Good accuracy, normal computational demand	GFRP tube, end steel plates of tendon
Wire Element (Truss)	T3D2	2-node linear 3-D truss. Good accuracy, computationally efficient	Reinforcement, tendon
Link Element	–	Spring and friction link	Boundary conditions

For the boundary conditions in the FE model, several constraints were applied to ensure numerical stability. The first boundary condition was applied at reference point RP6 (Figure 4.15a) to prevent the clamping system from rotating about the y-axis. The second set of constraints was applied at the ends of the connector links attached to the clamping plate (indicated by arrows) with respect to reference points RP7–RP10 (CF loading case). This second boundary condition was adjusted according to the type of loading, reflecting the different experimental setups. Finally, RP1 (Figure 4.15b) was constrained to prevent rigid-body motion and provide overall model stability. These boundary conditions together allowed the FE model to accurately capture the tower's cyclic response.

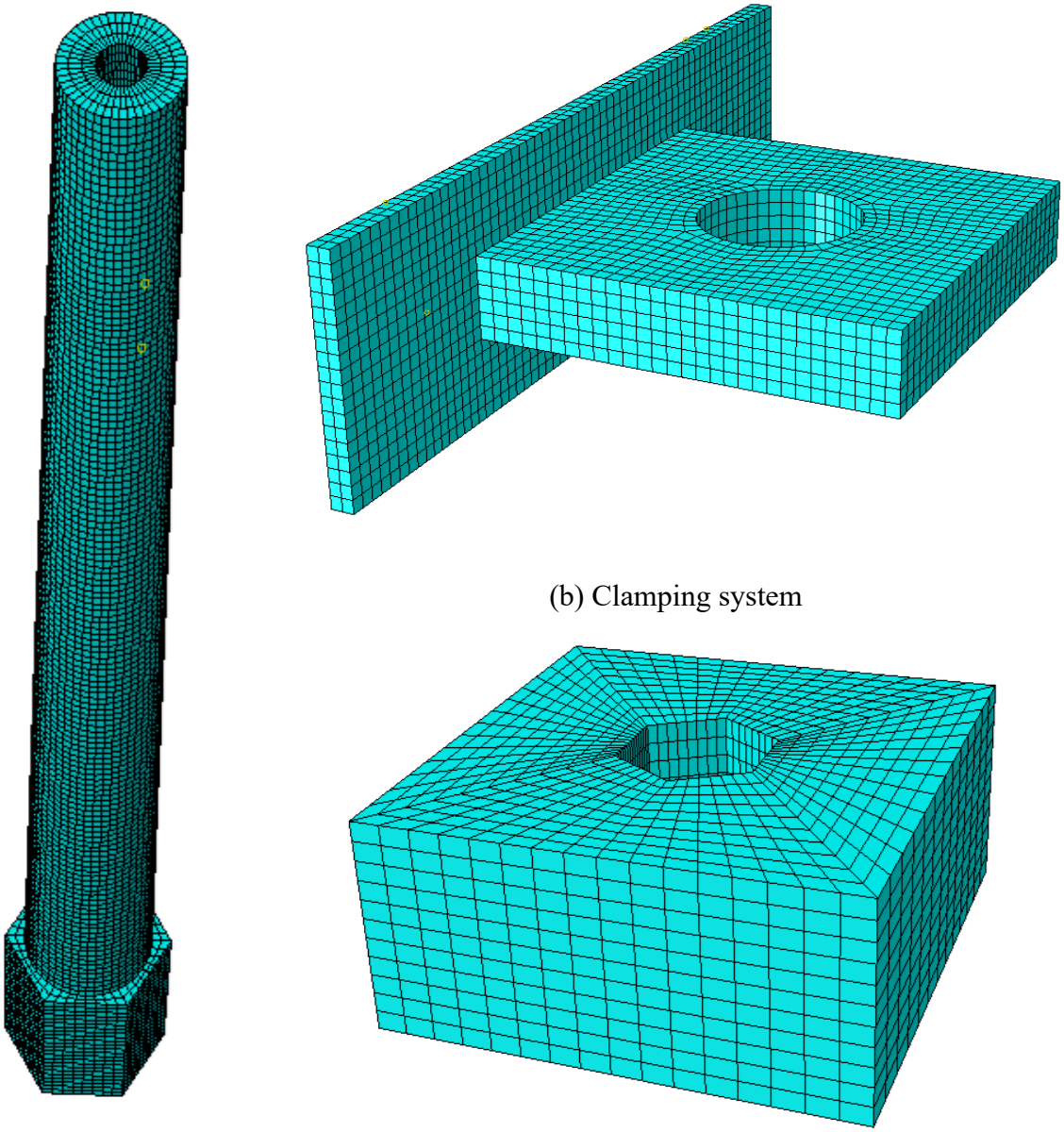

(a) Tower with grout

(b) Clamping system

(c) Foundation

Figure 4.13. FE mesh of the M4 tower

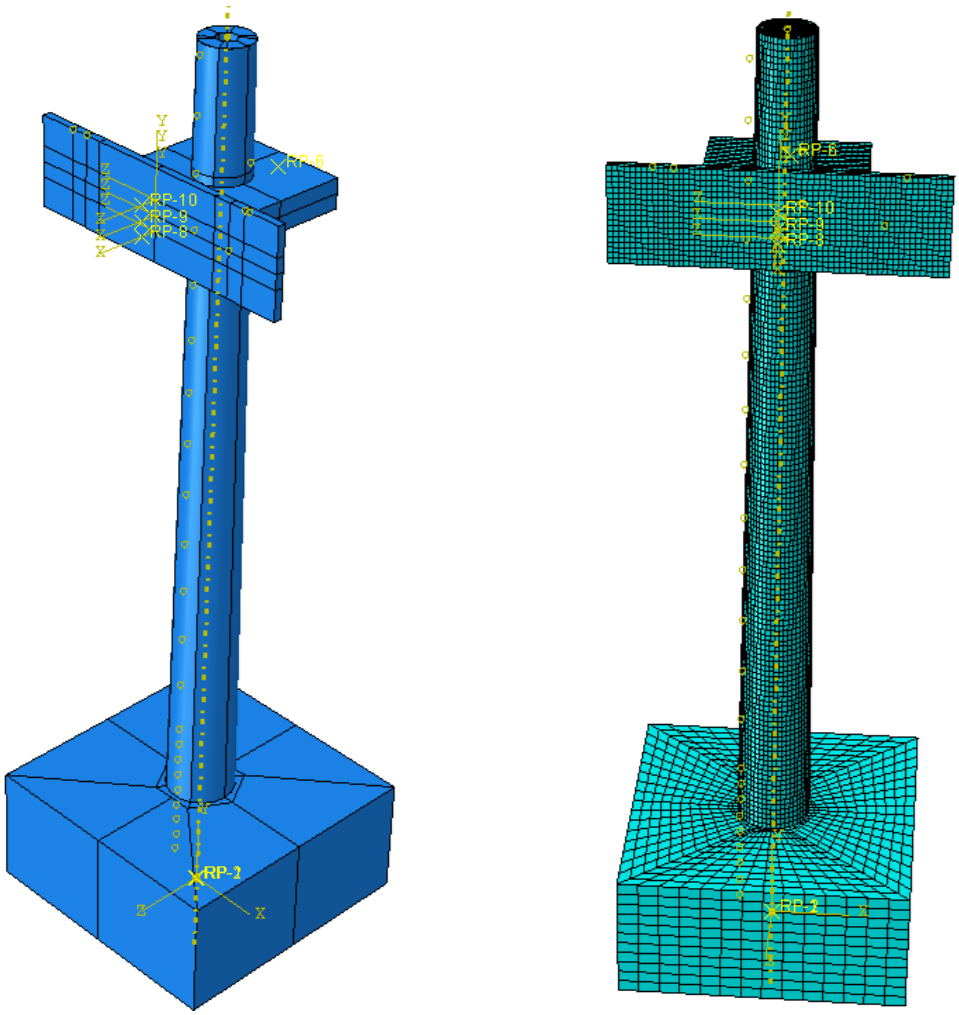

Figure 4.14.3D model and FE mesh of the M4 tower, including the clamping system and foundation

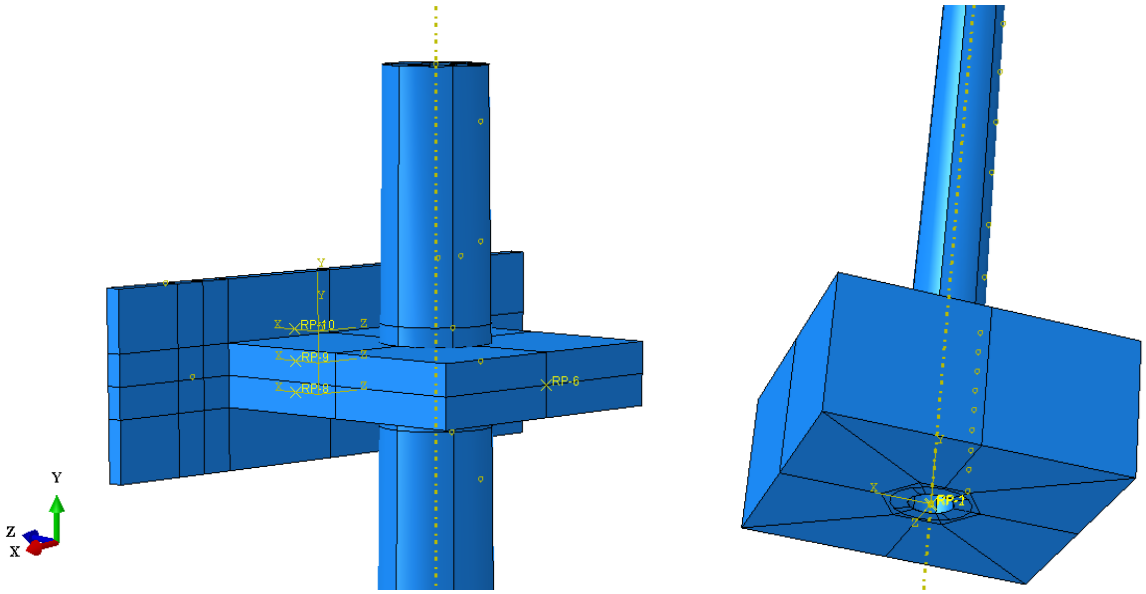

(a) Reference point 6 (RP6)

(b) Reference point 1 (RP1)

Figure 4.15. Reference points RP1 and RP6 on the tower model used for boundary conditions

4.7. Solver

Since the experimental loading during the cyclic and monotonic stages was applied slowly, a quasi-static solver was used in the numerical model. This approach neglects acceleration and velocity effects, allowing the analysis to focus on the material and structural response under gradually increasing loads consistent with the recommendations in the Abaqus Analysis User's Guide (Dassault Systèmes, 2024). The solver setup followed a clear sequence. After defining the material and section properties, a quasi-static step was introduced with a defined time duration to capture the model response.

Increment controls were specified to balance accuracy and efficiency, with limits set for initial, minimum, and maximum step sizes as well as the total number of increments. Once these parameters were in place, the applied loads and boundary conditions were introduced, and the model was meshed. The main stages of this process are shown in Figure 4.16.

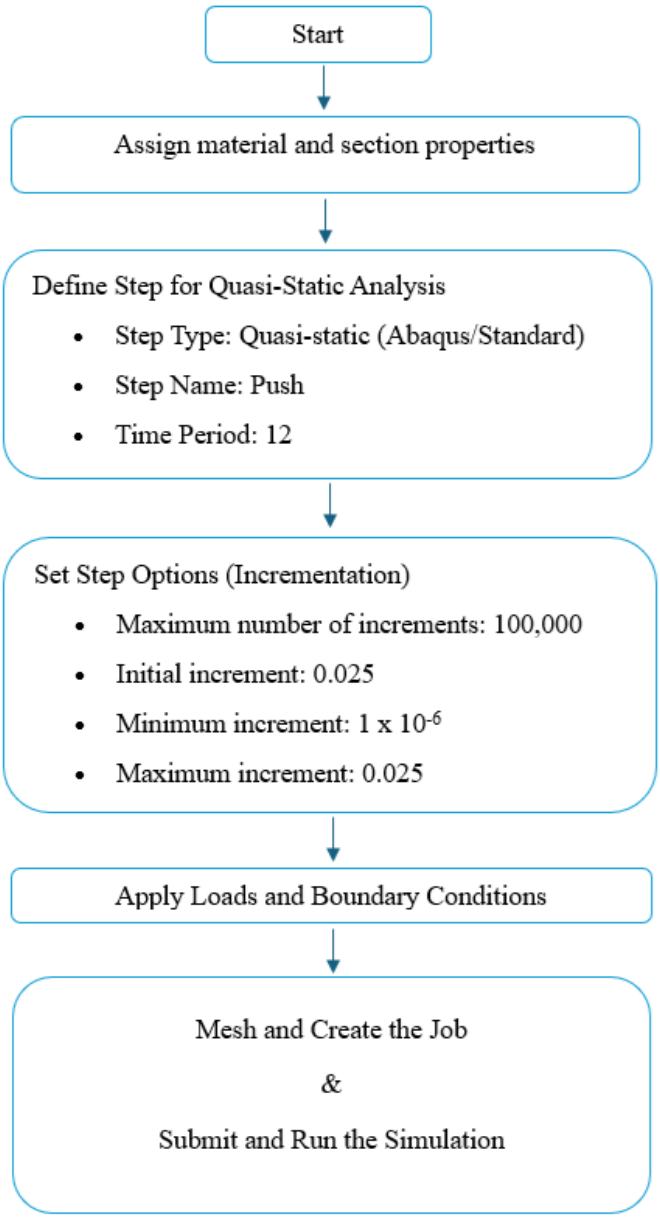

Figure 4.16. Flowchart of quasi-static analysis procedure in Abaqus

4.8. Load

In the initial model used for the failure analysis of the CFFT towers, displacement-controlled loading was employed to simulate the structural response of the CFFT towers. For the cyclic analysis, however, load control was applied instead of displacement control due to the presence of constraints on the tower, such as the prevention of rotation about the x-axis. In contrast, in the initial failure analysis model, displacement-controlled loading was used to simulate the structural response of the CFFT towers. Using displacement control in the cyclic analysis of such a constrained system might force unrealistic deformation paths or lead to convergence issues. This happens because displacement control forces the structure to follow a specified movement, even when the constraints, like restrictions on rotation, make such movement difficult or unnatural. The solver then has to redistribute stresses in ways that may not match the actual behaviour of the tower, which can cause the analysis to struggle or fail to converge. Load control allows the solver to determine displacements naturally in response to the applied forces while respecting the boundary conditions. To accurately reproduce the experimental behaviour under cyclic loading, a modified tabular amplitude was defined based on the measured load history. This amplitude captures the positive and negative load reversals observed in the tests and was assigned to the applied load at the tower's clamping pate. Using this approach, the model was able to reproduce the tower's force -displacement behaviour, including sharp load drops and energy dissipation resulting from minor slippage at the clamping interface, while keeping numerical stability.

Chapter 5 - Tower M4-1: Experimental results and analysis

5.1. Overview

This chapter presents the detailed experimental results obtained from testing the M4-1 tower specimen with corresponding analysis and modelling. The research explores vibration performance, centric and eccentric lateral load-deflection characteristics, and structural failure mechanisms. The results from the cyclic flexural testing under concentric loading (CF), as well as the cyclic flexural-torsional tests conducted with small left eccentricity (SLE) at 279.4 mm, big left eccentricity (BLE) at 559 mm, and big right eccentricity (BRE) at 559 mm from the centroidal axis of the tower, are presented in an integrated format to enable direct comparison among the four loading conditions. The load–deflection behaviour, GFRP surface strain, and internal reinforcement bar strain are discussed by grouping the data according to measurement height or location. This structured presentation improves clarity and offers a comprehensive understanding of how varying eccentricities influence the structural response. Furthermore, the chapter includes a summary subsection that compares CF, SLE, BLE, and BRE loading scenarios for displacement behaviour, peak load capacity, steel and GFRP strain responses, and overall tower's stability.

5.2. Stage 1: Free vibration test

The displacement versus time plot from the free vibration test is illustrated in Figure 5.1. The average fundamental period of vibration (T_d), over the first six cycles, was about 0.152 seconds corresponding to a damped natural frequency of vibration of about 6.6 Hz for the free-standing tower (as seen in Table 5.1). Moreover, the average damping ratio ζ, determined by Eq. 5.1 and Eq. 5.2, was found to be around 4%. This damping value likely results from the interaction between the various components of the concrete-filled GFRP tube and between the tower and foundation. Damping is crucial for structures subjected to dynamic loads as it influences their ability to absorb and dissipate energy during vibrations. In wind turbine towers, damping helps to reduce fatigue damage and ensure safety. The tower's vibration test results reveal a moderate damping ratio for this specimen comparable to a previous study (5%) on FRP towers conducted by Polyzois et al. (2009). For wind turbine design, it is important that the tower's fundamental natural frequency is higher than the rotor rotational frequency but lower than three times the blade passing frequency,

in accordance with IEC 61400-1 for soft-stiff towers. This range ensures that the tower avoids resonance with both rotor rotation and blade-induced loads while maintaining sufficient flexibility to reduce dynamic amplification. The measured natural frequency of 6.6 Hz is typically above the fundamental frequency range (0.3 to 2.5 Hz) of most small to medium wind turbines, indicating reduced risk of resonance (Lian et al., 2022). It is worth mentioning that this behaviour reflects the natural damping response of the tower during testing without any specific effort to control vibrations through external dampers or other means. Moreover, this behaviour reflects the vibration characteristics of a single tower segment and not of a taller segmental tower assembly and turbine. Nevertheless, this value indicates that the tower segment has a reasonable ability to dissipate energy during vibrations, minimizing its risk of experiencing severe deflection and vibrations under dynamic loading. The use of a concrete-filled GFRP tube enhances both stiffness and energy dissipation under dynamic and cyclic loading conditions, while the addition of the prestressed system increases its rigidity and reduces deformation under dynamic loads (Fam and Rizkalla, 2001; Mohamed & Masmoudi, 2010).

A relatively high damping ratio is a favourable characteristic for wind turbine towers, as it helps reduce fatigue damage and ensures structural safety under wind-induced vibrations. The results of the vibration tests demonstrate that prestressed CFFT towers have satisfactory dynamic characteristics for wind turbine tower applications in remote areas. However, further research is needed to optimize the design of these towers and their dynamic characteristics to reduce the impact of wind-induced vibrations on both the turbine and tower. The test was conducted at a scanning rate of 22 reading points per second, ensuring high-resolution data collection for analyzing the tower's vibrational response with precision.

$$\delta = \ln \frac{x(t_{n0})}{x(t_{n1})} \qquad \text{Eq. 5.1}$$

$$\zeta = \frac{\delta}{2\pi} \qquad \text{Eq. 5.2}$$

Where δ is the logarithmic decrement, $x(t_{n0})$ is the peak amplitude at the beginning of measurement, $x(t_{n1})$ is peak amplitude after n cycles, t_n is the time at which the amplitude is measured, and T_d is the time difference between two consecutive peaks.

Table 5.1. Damping values and frequency results of the tested tower

t_n #	Amplitudes x(t_n) (mm)	t_n (s)	T_d (s)	Frequency (Hz)	$\zeta = (\delta/2\pi)$
0	42.393	8.1429			
1	34.257	8.2878	0.1450	6.8970	0.0339
2	28.446	8.4345	0.1467	6.8173	0.0296
3	22.702	8.5846	0.1500	6.6653	0.0359
4	17.701	8.7392	0.1547	6.4653	0.0396
5	12.746	8.9014	0.1622	6.1667	0.0523

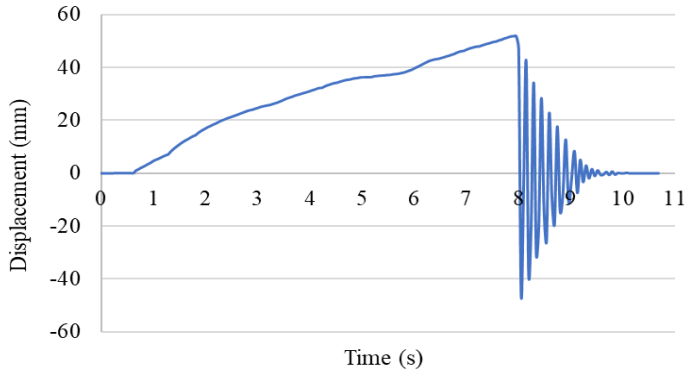

(a) Full test duration

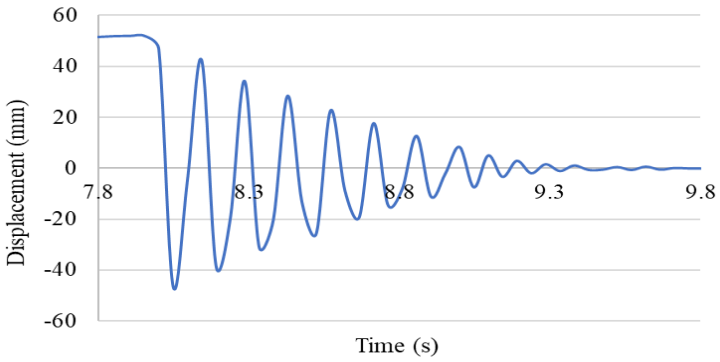

(b) Time segment from 7.8s to 9.8s

Figure 5.1. Tower M4-1 free vibration response

5.3. Combined load–deflection results

The load–deflection responses of the tower under all four cyclic loading configurations (CF, SLE, BLE, and BRE) are shown in Figure 5.2. The response for the CF loading (stage 2) was almost symmetrical under push (positive force) and pull (negative force) loading, primarily displaying linear elastic behaviour with limited hysteresis at service load levels. The tower reached a maximum lateral load of +53 kN at a drift of 73 mm (approximately 1.3% of its height), and -50 kN at -72 mm in the reverse direction. The negative drift (pulling) indicated a reversal of loading conditions which provided insight into the tower's balanced deformation, stiffness characteristics, and overall response to cyclic flexural forces. Throughout the test, both rebars experienced tensile strains that exceeded the yield threshold at some points under the maximum applied loads, indicating the development of inelastic behaviour. The hysteresis loop formed by plotting lateral load versus lateral drift is essential for evaluating energy dissipation, stiffness degradation, and possible structural damage over multiple loading cycles. Although no visible damage was observed during testing, tensile strains in the reinforcement exceeded the yield threshold under peak loading, indicating some degree of degradation under cyclic loading.

Under SLE (stage 3A) loading (279.4 mm left side of the tower) the tower's behaviour remained nearly symmetrical and comparable to the CF loading case. The peak loads recorded were +44 kN at 54 mm and -42 kN at -54 mm, equivalent to a lateral drift of roughly 1% of the tower height. Compared to CF loading, displacements under similar force levels were slightly reduced (54 mm vs.57 mm and -54 mm vs -55 mm), likely due to minor torsional effects induced by eccentricity (i.e., out-of-plane displacement component that was not captured by the main cable transducers). During testing, a slight twist in the loading clamp was observed, possibly contributing to this behaviour. Despite these minor differences, the tower again responded mainly within the linear-elastic range, with no evidence of cracking, residual deformation, or stiffness degradation over the cycles.

For BLE loading (stage 3B), with a 559 mm left-side eccentricity, the tower response became slightly asymmetrical. The tower reached an ultimate lateral cyclic load of +41 kN at a displacement of 44 mm, corresponding to approximately 1% of its height. In contrast, a lateral

load of -38 kN was monitored at a displacement of -47 mm. Compared to CF loading, the tower showed reduced displacement capacity for equivalent force levels (e.g., 44 mm vs.52 mm under +41 kN, and -47 mm vs. -51 mm under -38 kN), indicating a moderate influence of torsional effects at higher eccentricity. When comparing the BLE to the SLE under similar applied lateral loads (41 kN and -38 kN), the resulting displacements remained comparable (e.g., 44 mm vs.48 mm and -47 mm vs. -47 mm). This suggests that the slight increase in eccentricity had a small effect on the overall displacement magnitude and did not significantly change the general tower response.

For the BRE loading (stage 3C), with a 559 mm right-side eccentricity, the tower response was fairly symmetrical under push (positive force) and pull (negative force) loading, displaying mainly linear elastic behaviour with limited hysteresis. The tower reached a peak lateral cyclic load of +47 kN at a lateral displacement of 55 mm, equivalent to approximately 1% of its height. In comparison, a lateral load of -43 kN was recorded at a lateral displacement of -57 mm, reflecting the tower's response to loading in the opposite direction.

Generally, the response was similar to that observed under the concentric loading scenario. However, for similar applied lateral loads (47.0 kN and -43.0 kN), the average resulting displacements were slightly lower (55 mm vs 62 mm, and -57 mm vs -61 mm). This reduction in lateral drift is likely due to minor torsional effects induced by the eccentric loading, consistent with observations from the SLE and BLE tests. The behaviour remained mainly elastic in both directions.

The lateral load vs time response under cyclic loading conditions for all four tests is presented in Figure 5.3. Overall, the findings confirm that the tower shows reliable performance under all cyclic loading test scenarios. While eccentricity introduced minor variations in displacement and load capacity, especially in the BLE loading under the pushing (positive) load, the tower consistently maintained stability with no visible damage. These results provide strong evidence of the tower’s resilience under cyclic flexural and flexural-torsional loads within the expected service range.

During cyclic testing, a noticeable load drop appeared at the points where the loading direction reversed, especially in the CF, SLE, and BLE tests. This drop shows up as a sharp, almost vertical line in the load-deflection curve. It is important to note that this effect is not due to material damage

but rather to how the test setup behaved during reversal. In SLE and BLE, the eccentric load induced torsion that slightly opened one side of the clamping system, possibly an indication that the bolts securing the two clamping boxes were not fully tightened. This slight unseating of the clamping plates requires re-engagement when the actuator changes direction, producing a noticeable vertical drop in the load deflection loop. Additionally, if the foundation was not completely secured to the strong floor, the tower base may have had slight rotational freedom, causing the tower to shift and re-seat with the foundation each time the load reversed. This is consistent with observations in some tests where one of the bolts connecting the foundation to the strong floor was found to be loose. It should be noted that the bolts used to secure the foundation and the clamping system against movements were tightened by hand using a large wrench; for future testing, a power tool with high torque capacity is recommended. Although this load drop is mainly a result of the test setup, the sharp vertical segment in the hysteresis loop represents energy dissipation. This will be investigated and discussed further using the FE model to identify the main source of this energy loss and understand its effect on the overall response. In contrast, under BRE loading, the torsion acted in the opposite direction and the base behaved in a more rigid manner, keeping both the clamp and tower fully engaged throughout the reversal. This confirms that the load drop is mostly a mechanical response of the testing system rather than an indication of material failure.

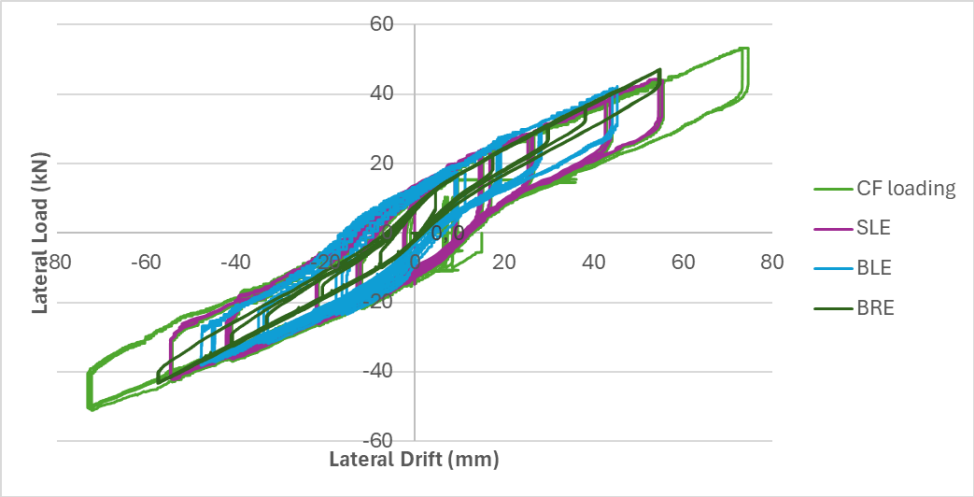

Figure 5.2. Lateral load–lateral drift response under concentric, small left eccentric (279 mm), and big right and left eccentric (± 559 mm) cyclic loading conditions

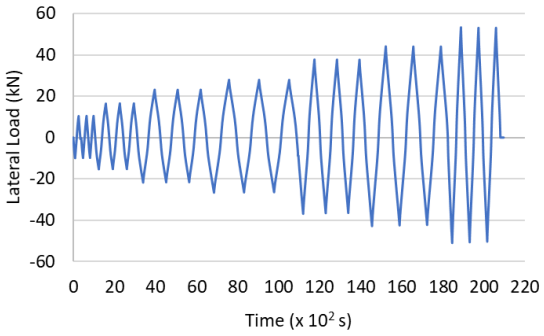

(a) CF loading

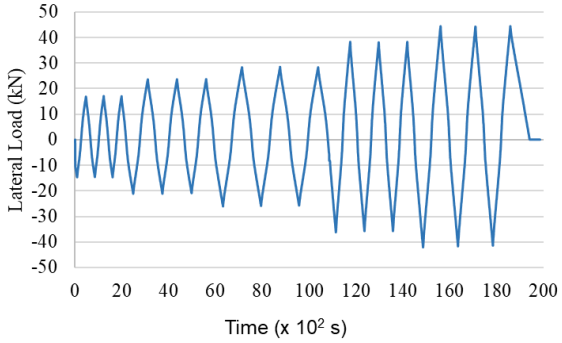

(b) SLE

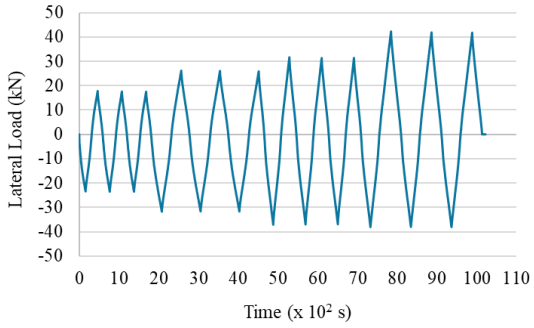

(c) BLE

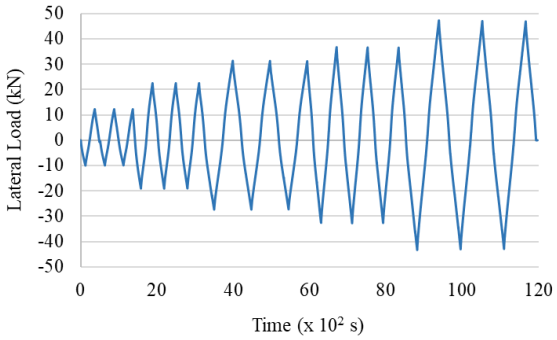

(d) BRE

Figure 5.3. Lateral load vs time response under (a) concentric, (b) small left eccentric (279 mm), (c) big left eccentric (559 mm), and (d) big right eccentric (559 mm) cyclic loading conditions

5.4. Strain in internal longitudinal steel reinforcement bars

The strain behaviour of internal steel reinforcement bars during the final loading cycles of the tower under the four tested cyclic loading configurations: CF, SLE, BLE, and BRE are shown in Figure 5.4. The strains results presented in this section correspond to the maximum load reached during each test, which was approximately (+53 kN, -50 kN) for CF loading, (+44 kN, -42 kN) for SLE, (+41 kN, -38 kN) for BLE, and (+47 kN, -43kN) for BRE. The results highlight the alternating tensile and compressive strain patterns observed in reinforcing bars ‘A’ and ‘B’ under reversed loading directions. Specifically, reinforcing bar ‘A’ experienced tensile strain during

pushing (positive) loads and compressive strain during pulling (negative) loads, while reinforcing 'B' displayed the opposite behaviour. Importantly, both reinforcing bars reached yield strain at some elevations, indicating the development of inelastic behaviour throughout most tests.

5.4.1. Strain response in rebars 'A' and 'B' under concentric flexural (CF) loading

Under CF loading, the maximum tensile strains occurred at 950 mm and 1200 mm above the tower base (160 and 410 mm above the top of the foundation, respectively), with reinforcing bar 'A' reaching 3710 με and reinforcing bar 'B' reaching 2705 με, respectively. The maximum compressive strains were -820 με for reinforcing bar 'A' and -933 με for reinforcing bar 'B', both at 950 mm. These findings suggest that the region between 950 mm (near the top of the foundation block) and 1200 mm experienced the highest stress concentration. Notably, no strain was recorded at 1450 mm for either rebar, possibly due to sensor failure or detachment. Although the absence of strain data at 1450 mm height introduces a minor element of uncertainty, the consistency and reliability of the remaining sensor readings suggest that the remainder of the tower remained elastic.

5.4.2. Strain response in rebars 'A' and 'B' under small left eccentric (SLE) loading

The strain behaviour of the reinforcing bars under SLE loading showed a response pattern largely consistent with that observed under CF loading. As illustrated in Figure 5.4, reinforcing bar 'A' experienced tensile strain under pushing (positive) loads and compressive strain under pulling (negative) loads, while reinforcing bar 'B' displayed the inverse response—developing tensile strains under pulling and compressive strains under pushing. At the maximum SLE load, reinforcing bar 'A' exceeded its yield strain, but reinforcing bar 'B' stayed within the elastic range, indicating that inelastic behaviour was localized to reinforcing bar A. Strain magnitudes were consistently greater in tension than in compression for both bars likely due to cracking in the surrounding concrete, which reduces the effective stiffness of the section and transfers tensile stresses to the reinforcement. The peak tensile strains were recorded at a height of 950 mm near the upper interface of the foundation block, with reinforcing bar 'A' reaching 2958 με and reinforcing bar 'B' reaching 1548 με. The maximum compressive strains were -717 με for reinforcing bar 'A' at 950 mm and -1130 με for reinforcing bar 'B' at 1200 mm. These findings

suggest that the critical strain zone under SLE loading was concentrated between 950 mm and 1200 mm above the tower base.

When compared to CF loading under equivalent peak loads (44 kN pushing and -42 kN pulling), both induced comparable tensile strains in reinforcing bar ‘A’ at the height of 950 mm and 1200 mm, as illustrated in Figure 5.5. However, the strain at 700 mm was slightly lower than the CF loading condition. In contrast, reinforcing bar ‘B’ recorded increased compressive strains under pulling during SLE, by approximately 24% at 700 mm to 40% at 950 mm, and up to 82% at 1200 mm. These differences indicate the effect of slight load eccentricity on the strain distribution within the reinforcement. Overall, the observed shifts in strain magnitude under SLE loading confirm that small eccentricities can cause changes in the flexural-torsional response of the tower.

5.4.3. Strain response in rebars ‘A’ and ‘B’ under big left eccentric (BLE) loading

In line with the patterns identified under CF and SLE loading, the strain response of the reinforcement during BLE loading maintained similar behaviour, with no evidence of yielding in either bar throughout the test. As illustrated in Figure 5.4, both reinforcing bars ‘A’ and ‘B’ once again showed greater strain magnitudes in tension than in compression. Under BLE loading, the maximum tensile strain was recorded at 1200 mm above the tower base, where reinforcing bar ‘A’ reached 1585 με and reinforcing bar ‘B’ reached 1351 με. The maximum compressive strains were measured at -845 με for reinforcing bar ‘A’ at 950 mm and -943 με for reinforcing bar ‘B’ at 1200 mm. These results further confirm that the zone between 700 mm and 1200 mm consistently experiences the highest stress concentration, in line with findings from both the CF and SLE loading scenarios.

When BLE results are compared with CF loading under equivalent peak loads (42 kN pushing and -38 kN pulling), a noticeable increase in strain was seen in reinforcing bar ‘A’ at 700 mm, as presented in Figure 5.5. At this height, the tensile strain increased by about 10% compared to CF. However, at the 950 mm and 1200 mm heights, tensile strains were reduced by roughly 25% to 45%. On the compression side, BLE loading produced higher compressive strains than CF by approximately 25% at 950 mm and 35% at 1200 mm. This may be an indication of a redistribution of cracks under the eccentric loading.

For reinforcing bar ‘B’ under compressive (pushing) loads, strains between the 700 mm and 1200 mm heights increased by approximately 10% to 50% compared to CF loading, while slightly decreasing at 1450 mm by 3%. Under tensile (pulling) loads, reinforcing bar ‘B’ experienced increased strains across all elevations of approximately 10% to 50%. This variation suggests that local stress redistribution under eccentric loading can affect the strain profile asymmetrically, particularly when combined with torsional effects. Overall, the results confirm the importance of the 700–1200 mm height region (directly above the foundation block) as a critical stress zone and show that even small eccentricities can change neutral axis location, cracking profiles, and intensify flexural-torsional interaction.

5.4.4. Strain response in rebars ‘A’ and ‘B’ under big right eccentric (BRE) loading

Under BRE loading configuration, both reinforcing bars ‘A’ and ‘B’ exceeded their yield strain, indicating that inelastic behaviour developed throughout the test. As shown in Figure 5.4, both bars ‘A’ and ‘B’ once again demonstrated higher strain magnitudes in tension than in compression. Under BRE loading, the peak tensile strains were recorded at 950 mm above the tower base, reaching 2777 με in reinforcing bar ‘A’, and 2388 με at 1200 mm in reinforcing bar ‘B’. The highest compressive strains were -652 με for bar ‘A’ at 950 mm and -749 με for bar ‘B’ at 1200 mm. These findings further confirm the earlier finding that the segment between 700 mm and 1200 mm consistently represents a critical stress zone across all loading scenarios. Furthermore, a direct comparison between BRE and BLE loading at the same peak load level highlights key differences in strain response. In reinforcing bar ‘A’, tensile strain at 700 mm was approximately 65% lower under BRE, while it was higher by 34% at 950 mm and 25% at 1200 mm, as shown in Figure 5.5. Compressive strains were lower at all elevations under BRE by about 40% to 55% between 950 mm and 1200 mm. Reinforcing bar ‘B’ showed a similar trend. Compressive strains under BRE were generally lower across all measured heights, with decreases ranging from approximately 10% to 65%. However, under tensile loading, reinforcing bar ‘B’ showed a clear increase in strain under BRE loading by approximately 8% to 50% between 700 mm and 1450 mm. Overall, the BRE loading case induced a clear strain profile considered by elevated tensile strains in both reinforcing bars, especially bar ‘B’, and a consistent decrease in compressive strains throughout the height of the tower.

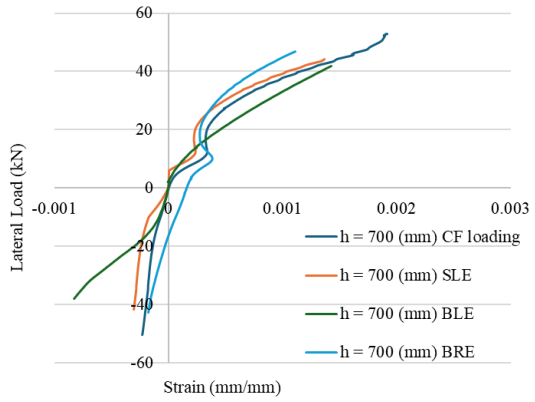

(a) Strain reading on rebar 'A' at 700 (mm)

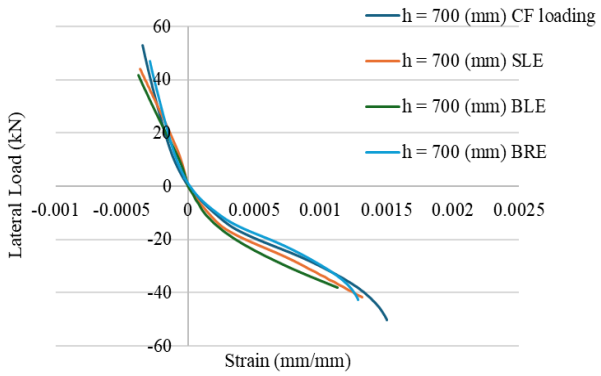

(d) Strain reading on rebar 'B' at 700 (mm)

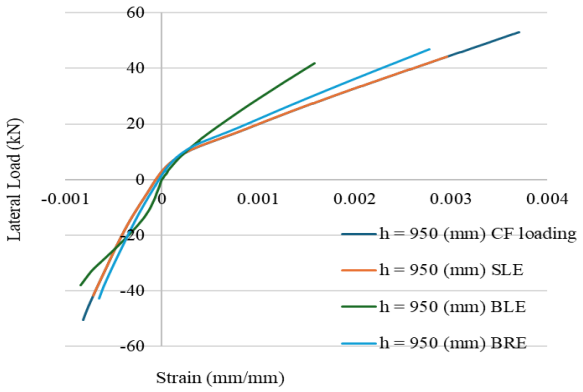

(b) Strain reading on rebar 'A' at 950 (mm)

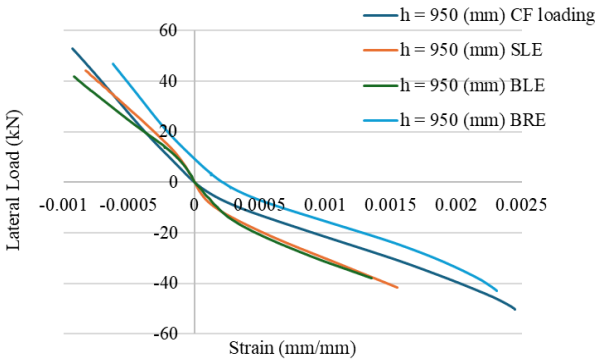

(e) Strain reading on rebar 'B' at 950 (mm)

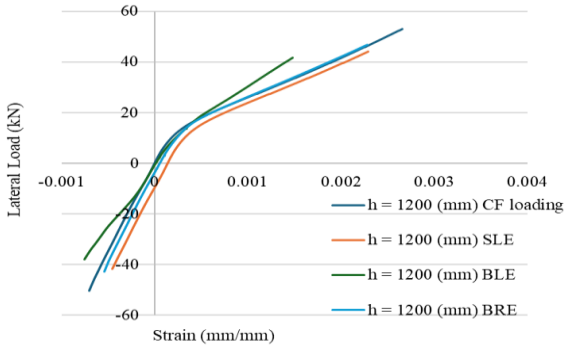

(c) Strain reading on rebar 'A' at 1200 (mm)

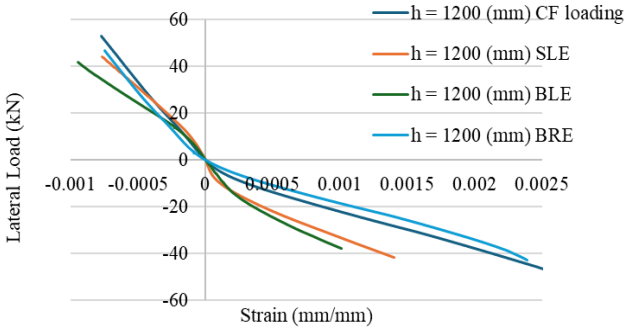

(f) Strain reading on rebar 'B' at 1200 (mm)

Figure 5.4. Strain readings recorded on rebars 'A' and 'B' under both push and pull loading phases for concentric, small left eccentricity (279 mm), big left and right eccentricity (559 mm) cyclic loading conditions.

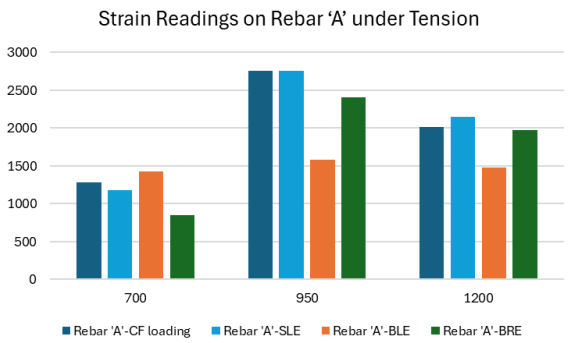

(a) Under pushing loading

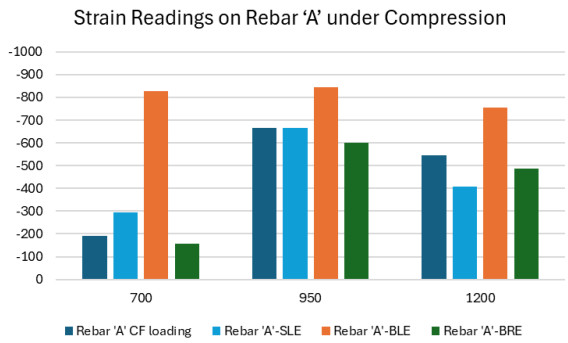

(c) Under pulling loading

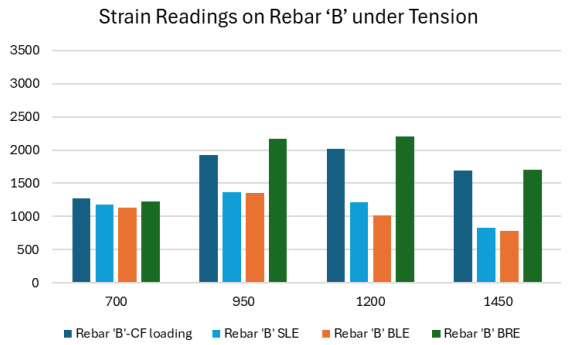

(b) Under pulling loading

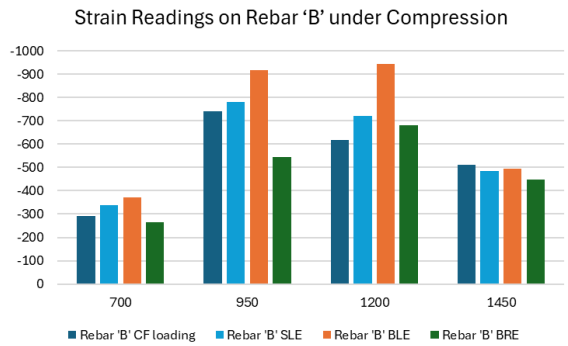

(d) Under pushing loading

Figure 5.5. Comparison of strain values on rebars 'A' and 'B' under CF loading, SLE, BLE, and BRE cyclic loading conditions (+42 kN and -38 kN applied loads)

5.4.5. Strain response in rebars 'C' and 'D' under concentric flexural (CF) loading

Figure 5.6 presents the strain responses of steel reinforcing bars 'C' and 'D', where strain gauges were installed in an alternating pattern between the two central bars, reinforcing bar 'C' on the left side and reinforcing bar 'D' on the right side of the tower. These responses were recorded under both pushing (positive) and pulling (negative) loading conditions. Under CF loading, during the pushing phase, reinforcing bar 'C' recorded a maximum strain value of 737 με at 700 mm, while reinforcing bar 'D' showed notably higher strain of 1863 με at 950 mm and 1491 με at 1450 mm. During pulling loading, reinforcing bar 'C' showed strain values of 1591 με at 700 mm, with

reinforcing bar ‘D’ recording lower strain values of 358 με at 950 mm and 414 με at 1450 mm. Despite variations between loading directions, both bars ‘C’ and ‘D’ maintained positive strain values throughout, aligning with analytical predictions that the neutral axis shifts above the section's midpoint after concrete cracking. The observed difference between bars ‘C’ and ‘D’ is likely attributed to the initial stress state of the individual tendons which varied due to difficulty in controlling the prestressing losses.

Variations in prestress losses among individual tendons could result in an additional axial load eccentricity and slight rotation of the neutral axis. At a height of 700 mm rebar ‘C’ initially shifted from tension to compression as the applied load increased beyond -5 kN. However, with further loading, it transitioned back into tension at approximately 17.8 kN. In contrast, rebar ‘D’ at a height of 950 mm, shifted from tension to compression as the applied load increased beyond -7 kN and returned to tensile strain at approximately 2 kN, while at 1450 mm, rebar ‘D’ shifted from tension to compression at -17 kN and returned to tensile strain at approximately 12 kN. This behaviour indicates a localized redistribution of stresses along the height of the tower.

5.4.6. Strain response in rebars ‘C’ and ‘D’ under small left eccentric (SLE) loading

Under SLE loading, as illustrated in Figure 5.6, the strain responses of steel reinforcing bars ‘C’ and ‘D’ highlighted the impact of flexural-torsional interaction introduced by eccentric loading. Peak strain values under pushing loads for reinforcing bar ‘C’, which is on the same side as the SLE loading, were recorded as 437 με at 700 mm, while reinforcing bar ‘D’ showed 1501 με at 950 mm, and 1209 με at 1450 mm, with no available data at 1200 mm. Under pulling loads, reinforcing bar ‘C’ exposed higher strain magnitudes of 1030 με at 700 mm, while reinforcing bar ‘D’ reached a lower value of 320 at 950 mm, and 328 at 1450 mm, again with limited data at other heights. Reinforcing bar ‘C’ showed a progressive change in strain behaviour under pushing loads, transitioning from initial tension into compression beyond -3 kN, before returning to tension as the load increased at approximately 11 kN at 700 mm. During pulling loading, reinforcing bar ‘D’ showed a similar transitional pattern, initially in tension before shifting to compression at -7 kN, then returning to tension at approximately 2 kN at 950 mm and from -17 kN to 13 kN at 1450 mm.

These transitional behaviours underscore a localized redistribution of stress along the tower's height under eccentric cyclic loading.

A comparison with CF loading at an applied load of 44 kN and -42 kN, which matches the peak loads applied in the SLE test, shows that SLE loading induced slightly lower strain magnitudes in the critical zone (700 mm to 1450 mm). For reinforcing bar 'C' under pushing loading, the SLE test recorded a strain of 437 με at 700 mm (vs.527 με in CF). Under pulling loading, reinforcing bar 'C' also showed an increased strain of 1030 με at 700 mm (vs.1388 με in CF). Reinforcing bar 'D', on the other hand, exhibited higher strains under pushing at 950 mm (1501 με vs.1464 με in CF) and 1450 mm (1209 με vs.1162 με). Under pulling loading, reinforcing bar 'D' also showed a slightly higher strain at 950 mm (320 με vs.312 με in CF), and at 1450 mm (328 με vs.315 με). Despite localized variations, both reinforcing bars consistently recorded positive (tensile) strain at the peak applied load levels in both loading directions.

5.4.7. Strain response in rebars 'C' and 'D' under big left eccentric (BLE) loading

Under BLE loading, peak strain values under pushing loads for reinforcing bar 'C' were recorded as 376 με at 700 mm, while reinforcing bar 'D' showed 982 με at 950 mm, and 920 με at 1450 mm, with no strain data available for reinforcing bar 'C' at 1200 mm in this test. Under pulling loads, reinforcing bar 'C' exposed higher strain magnitudes of 1117 με at 700 mm, while reinforcing bar 'D' recorded a lower value of 435 at 950 mm, and 395 at 1450 mm, again with limited data at other heights. Reinforcing bar 'C' showed a progressive change in strain behaviour under pushing loads, transitioning from initial tension into compression beyond 0 kN, before returning to tension as the load increased at approximately 8 kN at 700 mm. During pushing loading, reinforcing bar 'D' showed a similar transitional pattern, initially in tension before shifting to compression at 4 kN, then returning to tension at approximately 13 kN at both 950 mm and 1450 mm. These transitional behaviours underscore a localized redistribution of stress along the tower's height under eccentric cyclic loading.

A comparison with CF loading at an applied load of 42 kN and -38 kN, which is the same load level applied in the BLE test, shows that BLE loading induced slightly lower strain in the critical zone (700 mm to 1450 mm). For reinforcing bar 'C' under pushing loading, the BLE test recorded

a strain of 376 με at 700 mm (vs.473 με in CF). Under pulling loading, reinforcing bar ‘C’ also showed a strain of 1116 με at 700 mm (vs.1279 με in CF). Reinforcing bar ‘D’, on the other hand, showed lower strains under pushing at 950 mm (982 με vs.1360 με) and 1450 mm (920 με vs.1076 με in CF). In pulling loading, however, reinforcing bar ‘D’ showed a slightly higher strain at 950 mm (435 με vs.289 με in CF), and at 1450 mm (395 με vs.269 με). Despite localized variations, both reinforcing bars consistently recorded positive (tensile) strain at the peak applied load levels in both loading directions.

5.4.8. Strain response in rebars ‘C’ and ‘D’ under big right eccentric (BRE) loading

Under BRE loading, the strain responses of steel reinforcing bars ‘C’ and ‘D’ under both pushing and pulling loading are illustrated in Figure 5.6. During pushing loads, reinforcing bar ‘C’ showed a lower peak strain of 604 με at 700 mm, while reinforcing bar ‘D’ developed a higher strains of 1715 με at 950 mm and 1021 με at 1450 mm. In contrast, under pulling loads, reinforcing bar ‘C’ showed an increased strain response, reaching 1405 με at 700 mm, higher than its corresponding value in pushing loading. Reinforcing bar ‘D’ showed lower strain magnitudes under pulling, measuring 324 με at 950 mm and 361 με at 1450 mm.

In addition, within the height between 700 mm and 1450 mm, both reinforcing bars ‘C’ and ‘D’ exhibited a shift from tension to compression during the loading process. Reinforcing bar ‘C’ initially shifted from tension to compression as the applied pulling load increased beyond 5 kN. However, with further loading, this trend reversed again, and the reinforcing bar transitioned back into tension at approximately 13 kN at 700 mm positions. During pulling loading, reinforcing bar ‘D’ showed a similar transitional pattern, initially in tension before shifting to compression at -3 kN, then returning to tension at approximately 4 kN at 1450 mm. No noticeable transition was monitored at 1450 mm. These transitional behaviours highlight a localized redistribution of stress along the tower’s height under eccentric cyclic loading. Despite these transitions, both reinforcing bars ‘C’ and ‘D’ maintained positive strain values throughout, aligning with analytical predictions that the neutral axis shifts above the section midpoint after cracking occurs in the concrete.

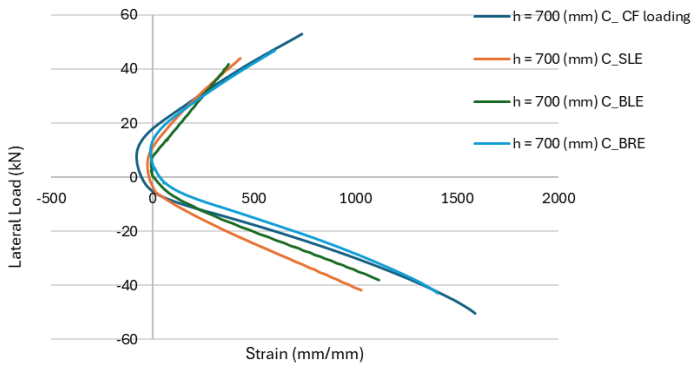

(a) Strain readings recorded on reinforcing bars 'C' and ‘D’ at 700 (mm)

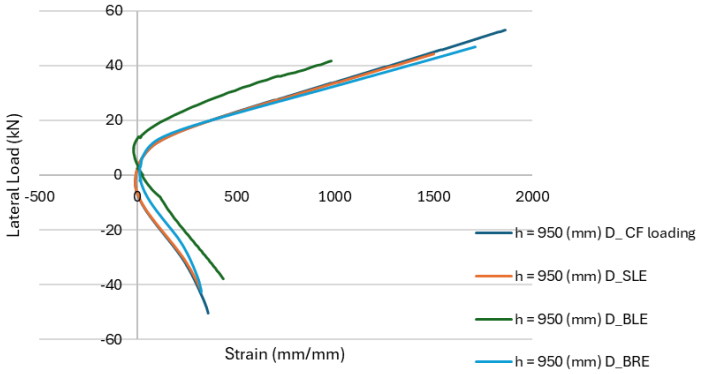

(b) Strain readings recorded on reinforcing bars 'C' and ‘D’ at 950 (mm)

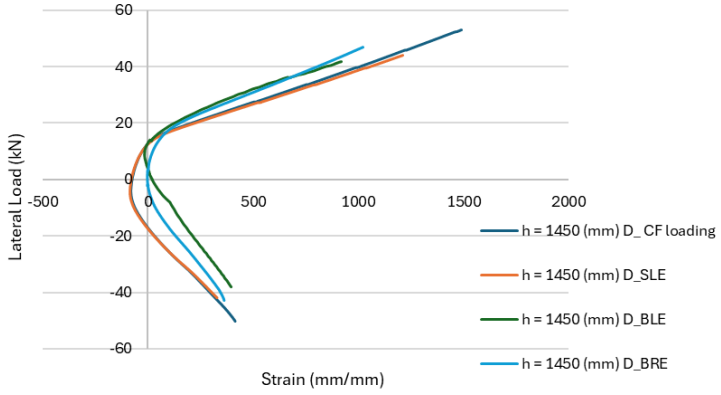

(c) Strain readings recorded on reinforcing bars 'C' and ‘D’ at 1450 (mm)

Figure 5.6. Strain readings recorded on rebars 'C' and ‘D’ under both push and pull loading phases for concentric, small left eccentricity (279 mm), big left and right eccentricity (559 mm) cyclic loading conditions

5.5. GFRP surface strain response under cyclic loading

This section presents the measured surface strain responses of the GFRP during the final load cycles of all four cyclic loading configurations: CF, SLE, BLE, and BRE. Figure 5.7 and Figure 5.8 display the strain data for sides 'A' and 'B', respectively, which experienced tension and compression depending on the direction of the applied load. For clarity, Figure 5.9, provides the detailed strain values at different heights, offering a direct comparison of the GFRP response under each loading condition.

5.5.1. Strain response in sides ‘A’ and ‘B’ under concentric flexural (CF) loading

Under CF loading, the strain profiles indicate nearly symmetrical cyclic behaviour, consistent with the recorded load vs. top deflection response. Peak tensile strains were observed on both sides 'A' and 'B' at a height of 1340 mm, measuring 2264 με and 2285 με, respectively. In contrast, maximum compressive strains were -1439 με on side 'A' at a height of 1340 mm and -1629 με on side 'B' at 840 mm. This behaviour confirms that the tensile strains exceeded the compressive ones, likely due to the development of cracks in the concrete core, which shifted the neutral axis.

A critical concentration of strain was consistently observed between 840 mm and 1340 mm, identifying this zone as a critical stress region in the tower. Notably, this zone aligns with the peak strain zones identified in steel reinforcement strain data for reinforcing bars 'A' and 'B', even though the exact strain gauge positions differed slightly. The convergence of both GFRP and steel strain readings in this region strongly confirms the identification of this zone as the critical region for stress development during cyclic loading.

Furthermore, the strain readings in the hoop direction, measured on the GFRP surface along sides C (left side of the tower) and D (right side), remained close to zero throughout the test.

5.5.2. Strains response in sides ‘A’ and ‘B’ under small left eccentric (SLE) loading

The strain behaviour under SLE loading followed a similar trend to CF, but with minor notable differences. As illustrated in Figure 5.7 and Figure 5.8, under pushing (positive) loading, side 'A'

experienced tensile strains while side 'B' was in compression. Conversely, under pulling (negative) loading, side 'A' experienced compression and side 'B' experienced tension. Strain magnitudes were higher in tension than in compression, with no gauge indicating strain levels approaching the failure strain observed in coupon tests (0.016). This absence of high strain magnitudes and the lack of visible surface damage confirm the integrity of the GFRP tube under the maximum SLE loading.

As shown in Figure 5.9, peak tensile strains under SLE were recorded at 1340 mm, with 1852 με on side 'A' and 1811 με on side 'B'. Compressive strains reached -1216 με on side 'A' and -1422 με on side 'B', also within the critical vertical region. When compared to CF loading at similar peak forces (44 kN and -42 kN), SLE loading produced slightly higher tensile strains along side 'A' from 700 mm to 1450 mm, while compressive strains on the same side were slightly reduced.

For side 'A' under pushing (tensile) loads, strain values under SLE were as follows: 1562 με at 840 mm (vs.1488 με in CF), 1852 με at 1340 mm (vs.1764 με), 1381 με at 1840 mm (vs.1315 με), and 1190 με at 2340 mm (vs.1134 με). Under pulling (compressive) loading, the SLE test recorded -1182 με at 840 mm (vs. -1244 με in CF), -1216 με at 1340 mm (vs. -1281 με), -900 με at 1840 mm (vs. -996 με), and -743 με at 2340 mm (vs. -786 με), as illustrated in Figure 5.7.

For side “B,” the pattern changed slightly. Under pushing (compressive) loads, the SLE test consistently produced higher compressive strains than CF, with values such as –1422 με at 840 mm (compared to –1354 με in CF), –1318 με at 1340 mm (vs. –1256 με), –920 ε at 1840 mm (vs. –906 με), and –707 με at 2340 mm (compared to –674 με). However, under pulling (tensile) conditions, side “B” showed some reduction in strain: 1717 με at 840 mm (vs.1808 με in CF), 1811 με at 1340 mm (vs.1907 με), 1510 με at 1840 mm (vs.1590 με), and 1179 με at 2340 mm (compared to 1241 με), as presented in Figure 5.8.

5.5.3. Strain response in sides ‘A’ and ‘B’ under big left eccentric (BLE) loading

The BLE loading case followed the same cyclic strain trend observed in CF and SLE tests but showed more differences in strain magnitudes. As in previous tests, side 'A' was in tension and side 'B' in compression during pushing, and the roles reversed under pulling. Tensile strains consistently exceeded compressive strains, with all measured values remaining well below the

failure strain threshold indicating that the GFRP tube maintained its structural integrity. At the critical height of 1340 mm, the peak tensile strains reached 1878 με on side 'A' and 1443 με on side 'B', while compressive strains were -1048 με and -1314 με, respectively, also within the critical vertical region.

When compared to CF loading at similar peak forces (42 kN and -38 kN), BLE loading produced higher tensile strains along side 'A' from 700 mm to 1450 mm, while compressive strains on the same side were slightly reduced (Figure 5.9). For side 'A' under pushing (tensile) loads, strain values under BLE were as follows: 1586 με at 840 mm (vs.1386 με in CF), 1878 με at 1340 mm (vs.1634 με), 1562 με at 1840 mm (vs.1224 με), and 1227 με at 2340 mm (vs.1052 με). Under pulling (compressive) loading, the BLE test recorded -1014 με at 840 mm (vs. -1159 με in CF), -1048 με at 1340 mm (vs. -1198 με), -795 με at 1840 mm (vs. -931 με), and -675 με at 2340 mm (vs. -722 με). Side 'B' showed a consistent pattern with previous observations. Under pushing (compressive) loads, BLE produced slightly higher compressive strains, such as -1314 με at 840 mm compared to -1279 με in CF, while under pulling (tensile) conditions, the strain reduced to 1443 με at 1340 mm vs.1714 με in CF. These shifts in strain magnitudes clearly confirm the increasing effect of larger eccentricities on flexural-torsional strain behaviour, while confirming the GFRP tube's role in maintaining integrity despite elevated localized stresses.

5.5.4. Strain response in sides 'A' and 'B' under big right eccentric (BRE) loading

The BRE loading configuration showed a strain response trend consistent with previous eccentric cases (SLE and BLE). Under pushing (positive) loading, side 'A' experienced tensile strain while side 'B' was in compression. At 1340 mm, peak tensile strains were measured as 1907 με on side 'A' and 1990 με on side 'B', while compressive strains reached -1208 με on side 'A' at a height of 1340 mm and -1384 με on side 'B' at 840 mm. As in earlier tests, tensile strains were consistently higher than compressive strains, and all values remained below the GFRP failure threshold of 0.016. Notably, the tensile strain in side 'B' was slightly higher than side 'A', which is consistent with previous observations.

When compared to CF loading at similar peak forces (42 kN and -38 kN), BRE loading produced very similar tensile and compressive strains along side 'A' from 700 mm to 1450 mm. For instance

on side 'A' under pushing (tensile) loads, BRE strain readings were 1368 με at 840 mm compared to 1386 με in CF. The remaining strain measurements also closely matched those recorded during CF loading, indicating overall comparable behaviour.

In contrast, side 'B' showed a different pattern than was found in previous observations. Under pushing (compressive) loads, BRE produced slightly lower compressive strains, such as -1219 με at 840 mm compared to -1279 με in CF, while under pulling (tensile) conditions, the strain increased to 1726 με at 840 mm vs.1613 με in CF, 1807 με at 1340 mm (vs.1714 με), 1538 με at 1840 mm (vs.1418 με), and 1215 με at 2340 mm (vs.1116 με). These observations highlight the directional dependency of strain responses and show that increasing rightward eccentricity results in strain redistribution that shifts tensile demand toward side 'B'. Despite this redistribution, no failure or surface damage was observed.

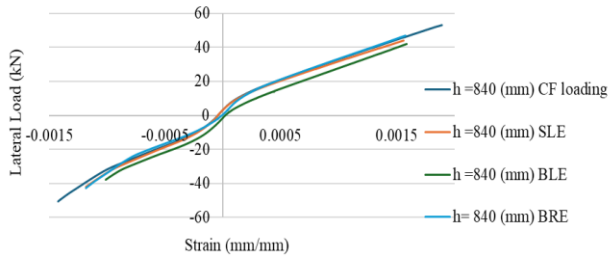

(a) Strain reading at a height of 840 (mm)

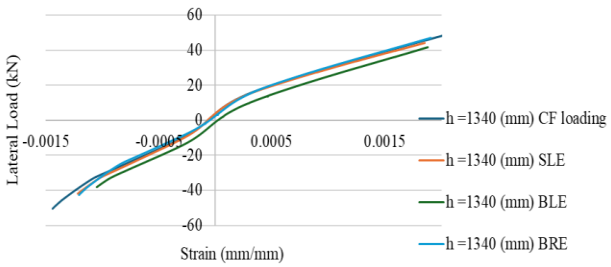

(b) Strain reading at a height of 1340 (mm)

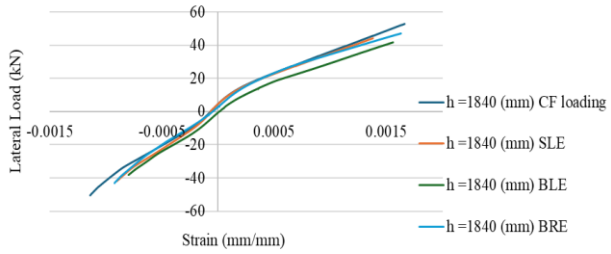

(c) Strain reading at a height of 1840 (mm)

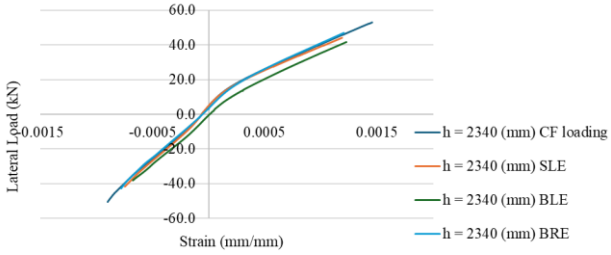

(d) Strain reading at a height of 2340 (mm)

Figure 5.7. Strain readings recorded on Side 'A' under both push and pull loading phases for concentric, small left eccentricity (279 mm), big left and right eccentricity (559 mm) cyclic loading conditions.

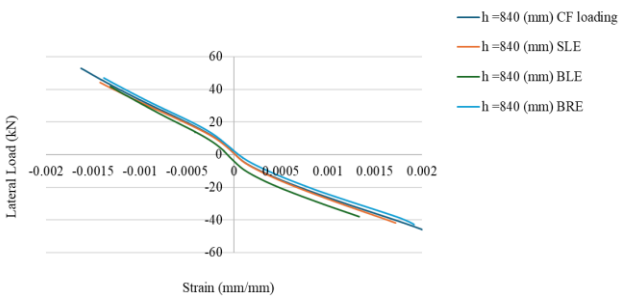

(a) Strain reading at a height of 840 (mm)

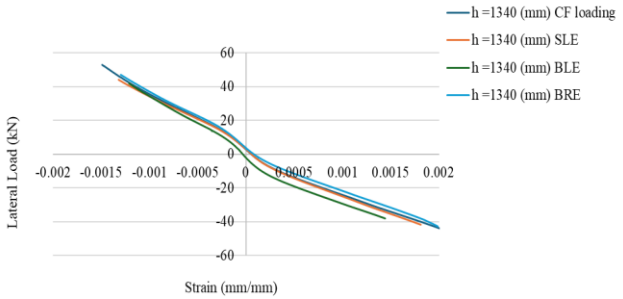

(b) Strain reading at a height of 1340 (mm)

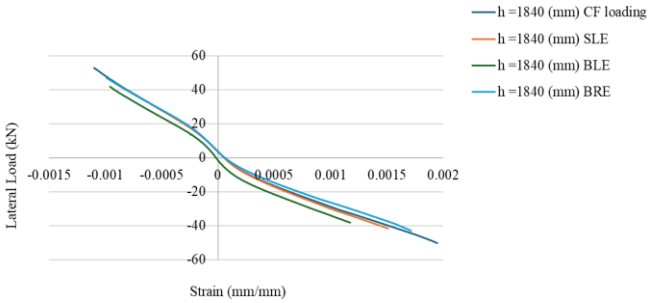

(c) Strain reading at a height of 1840 (mm)

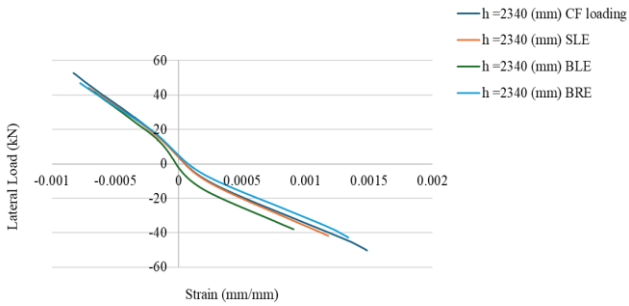

(d) Strain reading at a height of 2340 (mm)

Figure 5.8. Strain readings recorded on Side 'B' under both push and pull loading phases for concentric, small left eccentricity (279 mm), big left and right eccentricity (559 mm) cyclic loading conditions.

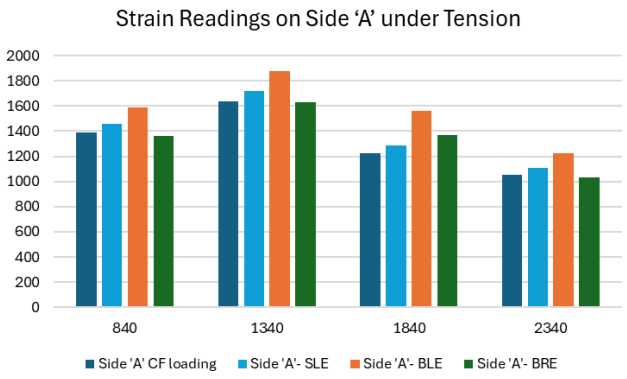

(a) Under pushing loading

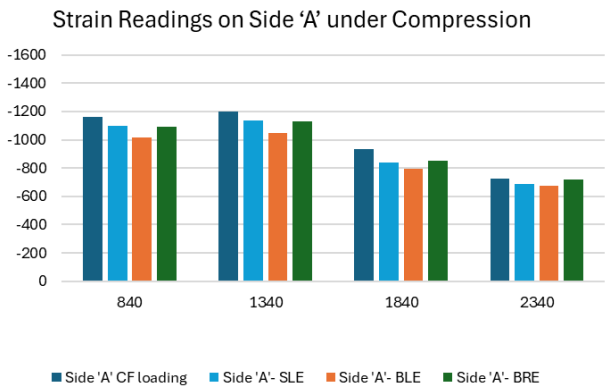

(b) Under pulling loading

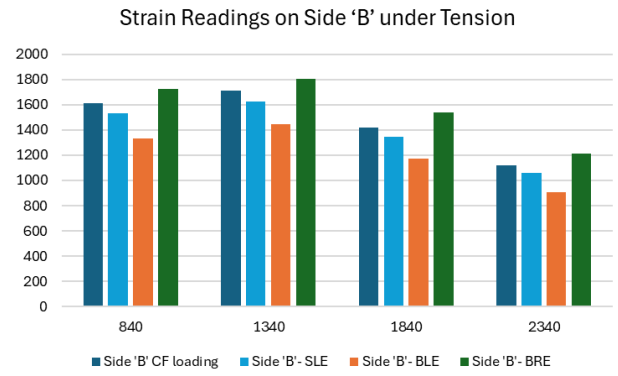

(c) Under pulling loading

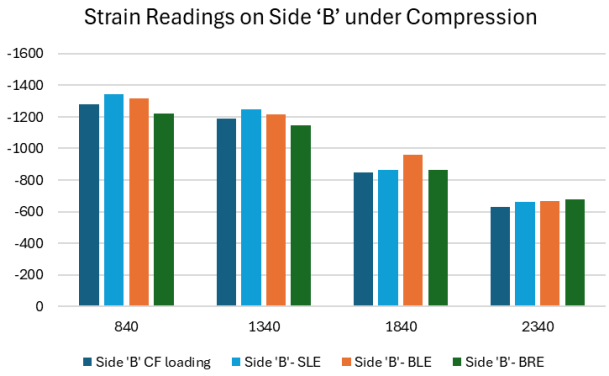

(d) Under pushing loading

Figure 5.9. Comparison of strain values on sides 'A' and 'B' under CF, SLE, BLE, and BRE cyclic loading conditions (+42 kN and -38 kN applied loads)

5.6. Test to failure

Stage 4 focused on the monotonic loading to failure. The load-deflection response of the tower is characterized by significant linearity up to the point of initial failure (Figure 5.10). Failure was initiated by GFRP rupture on the tension side of the tower near the top of the foundation block at an applied load of 132 kN and a displacement of 267 mm. This initial failure marked a critical point in the structural response, leading to a noticeable change in behaviour. At a height of 950

mm, the yield strain in steel in the compression zone was exceeded at around 93 kN, which accounts for approximately 70% of the failure load. In comparison, the yield strain in the tension zone at the same height was measured at around 58 kN, representing approximately 44% of the failure load, as illustrated in Figure 5.11.

The maximum strains recorded in the FRP tube were -5307 με in compression at 50 mm above the foundation, and 8537 με in tension at 550 mm above the foundation, as illustrated in Figure 5.12. While the maximum recorded strain (8537 με) was below the coupon test failure strain (0.016), the actual failure strain was likely higher but not captured by the gauge due to the location of the strain gauges, as the GFRP failure occurred between them. After a significant drop in load readings was observed, the test was stopped for safety reasons. The ultimate displacement reached during the test was 389 mm, corresponding to a reduced load of 59 kN, indicating a 55% drop from the peak load. These results underscore the tower's considerable ability to absorb energy and deform before ultimate failure. The lateral displacement of the tower was recorded at a height of 5.75 m. The lateral deflection measurements were critical for understanding the structural response under loading. The data indicated that the tower exhibited a consistent load–deflection response up to the onset of initial failure.

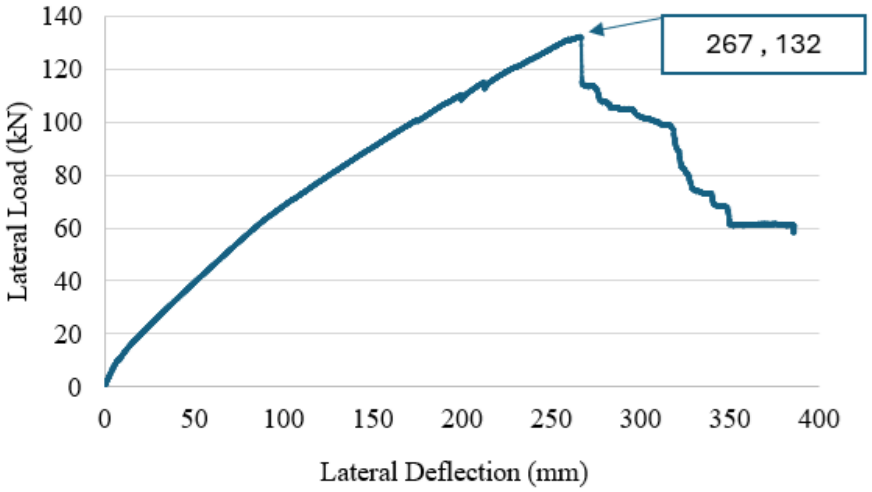

Figure 5.10. Lateral load vs lateral deflection response of tower M4-1

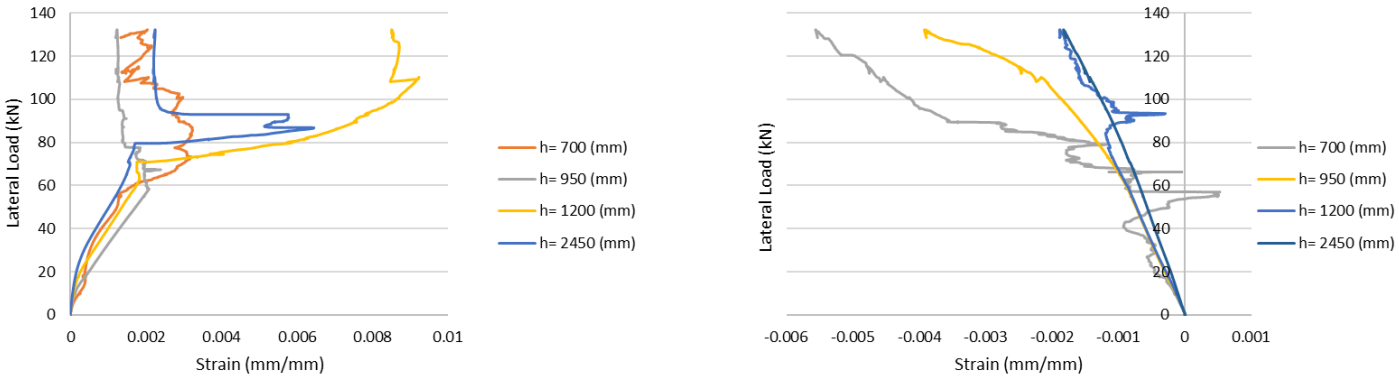

(a) Strain reading on rebar 'A' Strain reading on rebar 'B'

Figure 5.11. Lateral load vs longitudinal strain curves for tower M4-1

The relationship between load and deflection remained fairly linear up to failure at 132 kN and displacement of 267 mm. Beyond this point, the load capacity dropped significantly and displacement continued to increase until complete failure occurred. The longitudinal tension and compression strains, measured using gauges on the GFRP surface, were recorded along the height of the tower. The corresponding strain curves are presented in Figure 5.13. These curves highlight the difference between tensile and compressive strain behaviours, showing areas (840 mm- 1340 mm) where stress concentrations were particularly evident.

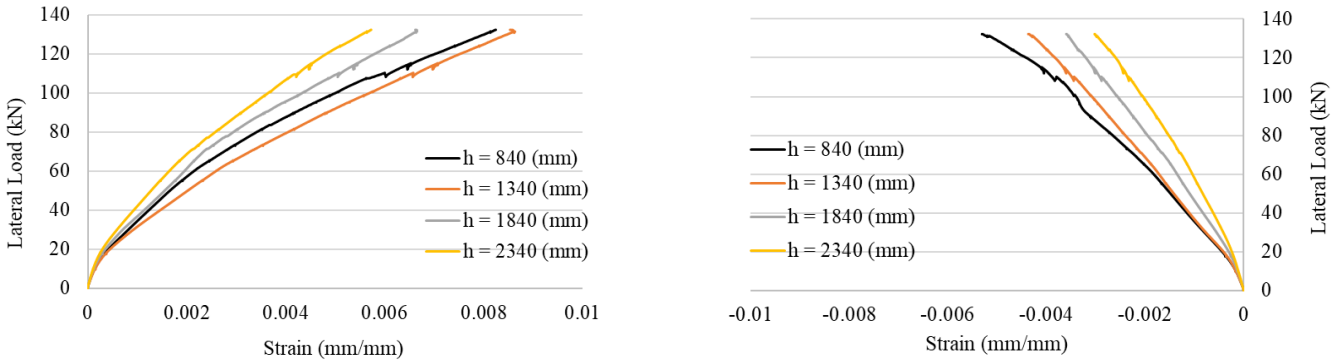

(a) Side A (b) Side B

Figure 5.12. Strain readings recorded on the GFRP surface

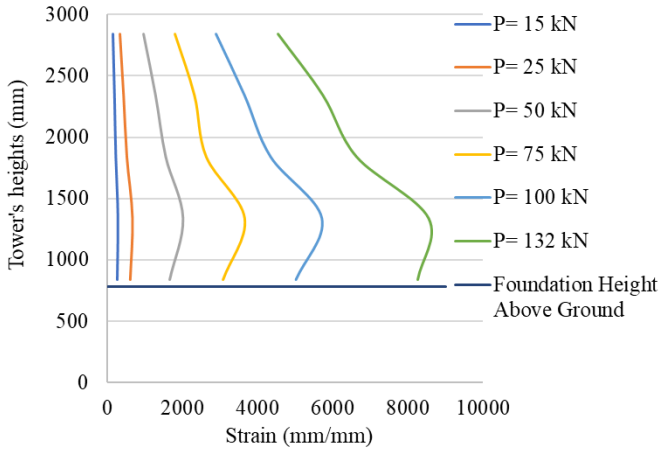

(a) GFRP tension strain reading

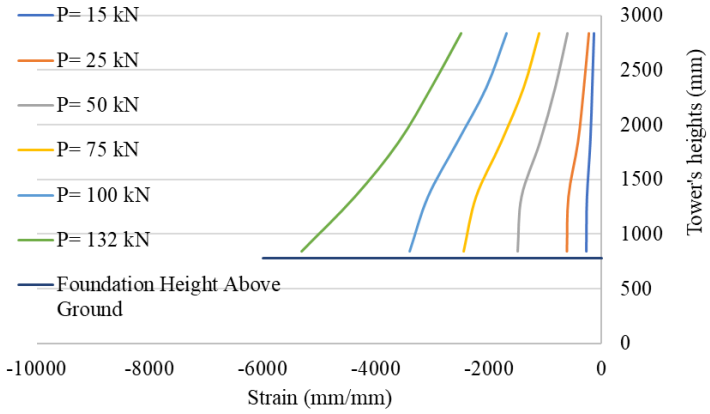

(b) GFRP compression strain reading

Figure 5.13. Tower height vs GFRP strain reading

The stiffness of the M4-1 specimen was analyzed to evaluate its structural deformation characteristics. Calculations show that the flexural rigidity of the tower was approximately 18.2 N·m². The flexural rigidity of the tower was determined using the moment–curvature relationship. Specifically, it was calculated as the ratio of the bending moment to the corresponding curvature at a reference section (in this case, 840 mm from the bottom of the tower, slightly above the top of the foundation block, where the GFRP strain gauges were located), reflecting the tower's resistance to bending under the applied load. Detailed calculations are shown in Appendix F. (Note that the

flexural rigidity was calculated using strain values measured on the GFRP tube; the curvature obtained from steel bar strains was slightly lower.)

The curvature vs tower height at the maximum applied load (132 kN) is illustrated in Figure 5.14. Notably, the GFRP tube shows higher curvature than the steel reinforcing bars which is likely an indication of imperfect bonding. A critical zone, which extends from the foundation's base to approximately 1350 mm, represents the transition from elastic to inelastic behaviour (i.e., plastic hinging). In this region, the structure experiences significant stress and deformation. Understanding the behaviour within this zone allows for more accurate predictions of the structure's response to loads and helps to identify potential failure mechanisms.

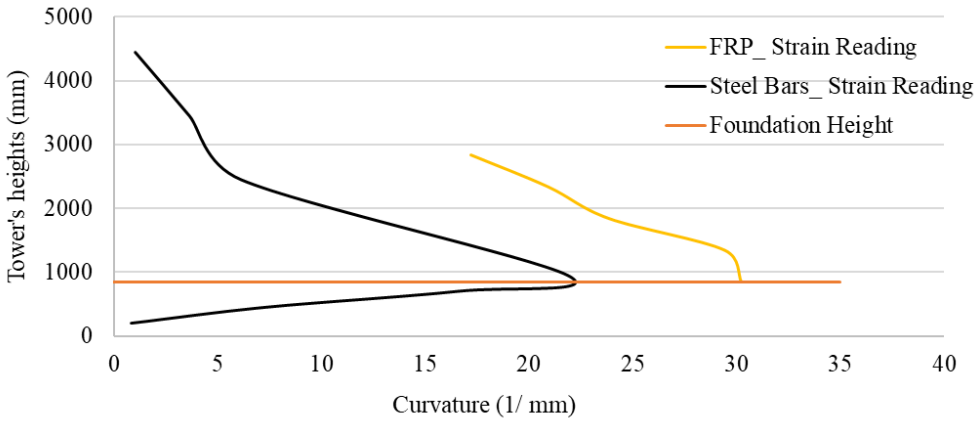

Figure 5.14. Tower’s curvature vs tower's height at maximum failure load of 132 kN

The observed failure mode for the tower involved GFRP tensile rupture at a height of approximately 1050 mm from the foundation. This corresponds to the zone where the highest levels of stress were identified, as illustrated in Figure 5.15.

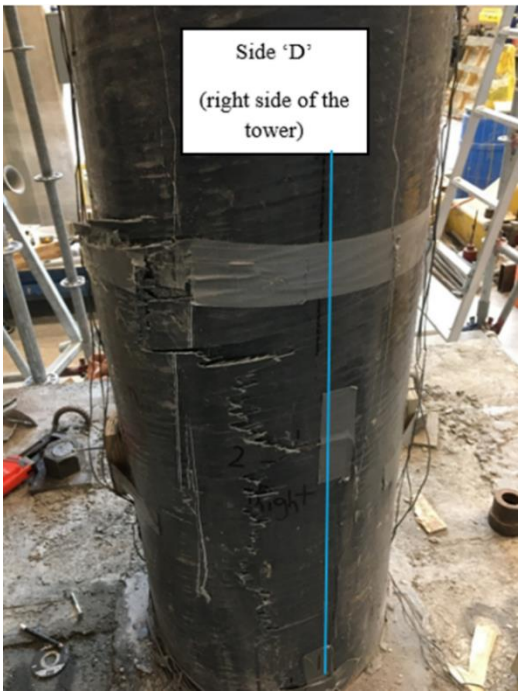

Figure 5.15. Failure mode of tower specimen M4-1

5.7. Numerical Model Verification

5.7.1. Stage 1. Free Vibration Test

The dynamic performance of the M4 tower was evaluated through a free vibration test. The free-vibration test of all towers was performed by laterally pulling and releasing the top of the tower using a notched steel plate, which induced oscillation. The displacement-time history of M4-1 revealed a fundamental vibration period of 0.152 seconds (about 6.6 Hz) and a damping ratio of 4%. The FE simulation replicated the experimental procedure by applying an initial displacement at the tower top (via boundary condition BC-2, as illustrated in Figure 5.16) and releasing it at the start of the dynamic analysis step 3, allowing the tower to vibrate freely. The numerical results showed excellent agreement with the experimental data, accurately predicting the first-mode frequency and capturing the amplitude decay corresponding to the measured damping level, as illustrated in Figure 5.17. The oscillation frequency in the simulation closely matched the test data with both frequencies approximately 6.6 Hz, ensuring that the timing of the peaks and zero-crossings corresponded accurately. The displacement time-history curves from both the simulation and experiment showed close alignment, with consistent decay rates, confirming that the model accurately captured the dynamic response of the M4 tower. The amplitude decay in the model reflected a damping level equivalent to the measured ~4% critical damping, indicating that the vibrations diminished at a rate consistent with the experimental observations. Overall, the FE model effectively represented the tower's free vibration as a decaying sinusoidal motion. The successful replication of both static and dynamic behaviours provides strong validation for the developed FE model, reinforcing its reliability for subsequent parametric studies and predictive analyses.

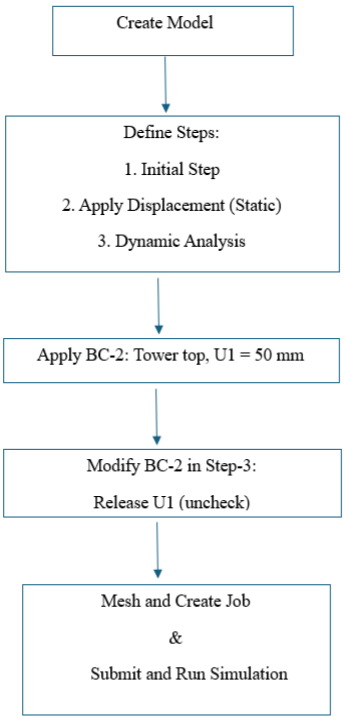

Figure 5.16. Flowchart structure for free vibration analysis

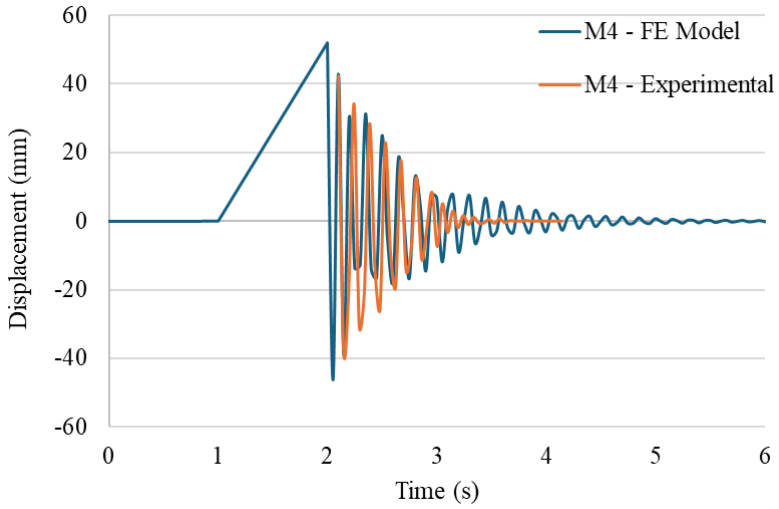

Figure 5.17. Comparison of displacement-time history for free vibration response of M4-1 – experimental and modeling results

5.7.2. Stage 2: Cyclic flexural testing under concentric loading

When the initial FE model was first used to simulate the CF loading, the results did not align well with the experimental response (Figure 5.18). In particular, the simulation predicted a stiffer response compared to the tests, since the experimental curves showed noticeable energy dissipation that the original model could not capture. The experimental peak load under CF loading was about 53 kN, whereas the FE model predicted 77 kN (31% higher). In the reverse cycle, the peak was -50 kN experimentally compared with -76 kN numerically (34% higher). This inconsistency highlighted the need for improvement. Therefore, the model was modified and calibrated to better reflect the tower's behaviour under the different loading protocols.

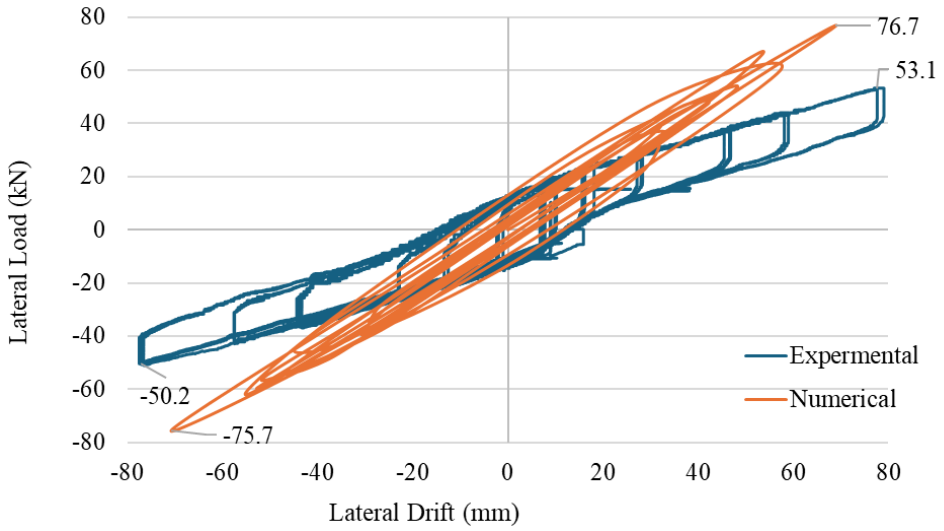

Figure 5.18. Load–Displacement Response of M4-1 under Concentric Cyclic Flexural Loading: Experimental vs. Initial Model Result

Since the cyclic loading protocol involved cases with eccentricity, the clamping system was added to the initial FE model to better replicate the real experimental setup. This addition allowed the model to reflect not only the tower's structural response but also the influence of boundary and support conditions during testing.

For verification, the modified FE model was compared against experimental results from cyclic flexural testing under concentric loading (CF). In the simulation, displacement-controlled loading

was applied at the center of the actuator steel plate (Figure 5.19), consistent with the experimental setup. The displacement response was recorded at the top of the tower, enabling a direct comparison with the measured load–displacement behaviour.

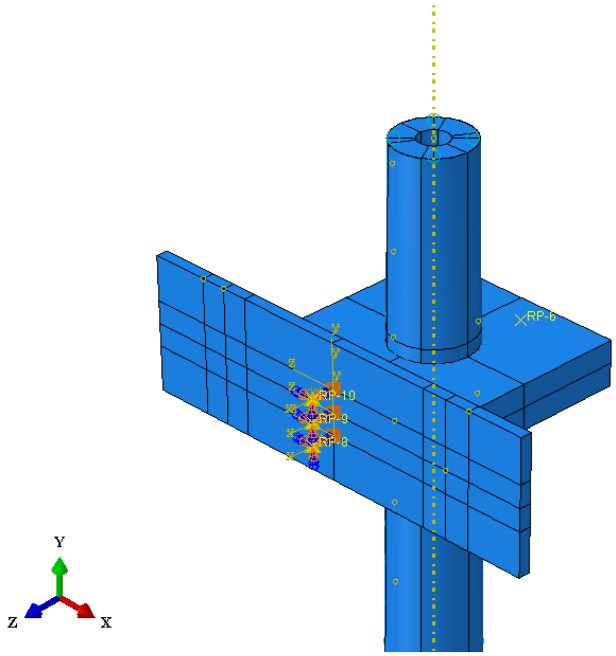

Figure 5.19. Loading position for CF testing at the clamping system center.

Experimentally, the tower showed no visible signs of cracking, yielding, or GFRP rupture under CF loading at the early cycles. However, the cyclic curves displayed clear energy dissipation beginning from the very first cycle, even at relatively small displacement amplitudes of 10 mm, as illustrated in Figure 5.20. This suggested that the source of dissipation was external to the tower itself, most likely related to the test setup. In addition, a sharp load drop appeared each time the loading direction reversed, most noticeably in the CF, SLE, and BLE tests (as discussed in Section 5.3). This effect was not caused by material damage but by how the setup behaved during reversal. The most likely contributors were components containing bolted connections, particularly the clamping system and foundation. Observations from some tests in which bolts securing the foundation to the strong floor were found to be loose further supported this interpretation. These issues were therefore investigated in the FE model to identify the source of energy loss and its impact on the overall cyclic response.

To simulate this behaviour in the FE model under cyclic loading, two additional modeling components were incorporated into the FE model. A frictional link was introduced in parallel connection at the clamping steel plate interface. This link was defined by two parameters; the friction coefficient and the internal contact force, both of which were calibrated for each cyclic test to reflect the variations observed in the experimental results. For the CF loading case, the friction coefficient for the tangential behaviour was set to 0.6 and the internal contact force to 4500 N. This mechanism allows the model to release energy whenever the loading direction reverses, thus reproducing the sharp load drops and additional energy dissipation recorded in the experiments (Dassault Systèmes, 2009).

In addition, the flexibility of the tower foundation was modeled using a rotational spring about the x-axis, which was assigned a stiffness value of D44 = 5.0 x 10^{10}. This spring stiffness was calibrated to reproduce the reduced rotational stiffness observed in the experiments, which was attributed to a combination of foundation flexibility and slippage within the clamping system. The calibration was carried out by first estimating the rotational stiffness from the linear portion of the experimental base moment–rotation response using ($K_0 = M_x / \Theta_x$), a commonly adopted approach for representing foundation compliance in numerical models ((Dassault Systèmes, 2009). The spring stiffness was then adjusted in the FE model until the simulated base rotations closely matched the experimental measurements. This procedure ensured that the numerical model realistically captured the combined effects of foundation compliance and clamping behavior under cyclic loading.

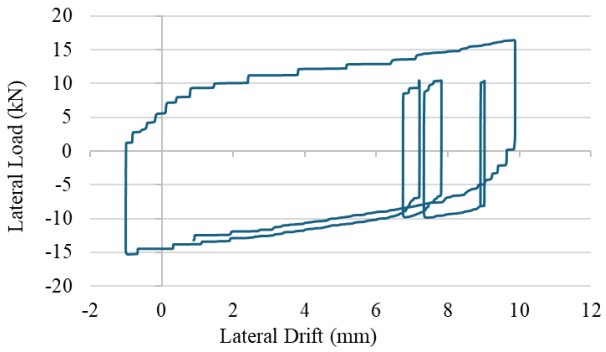

Figure 5.20. Experimental early-stage load–displacement response of the tower during cyclic flexural testing under concentric loading

The use of parallel connection type for these links provided a load–displacement response that closely matched the experimental cyclic curves. This modification successfully captured the nearly vertical slopes, and the load deflection behaviour up to 43 kN and -35 kN (Figure 5.21).

The modified FE model exhibited strong agreement with the experimental response in the elastic range, with both curves closely aligned up to approximately 58 mm and -45 mm of lateral deflection (Figure 5.21). At 58 mm, the peak experimental lateral load reached +43 kN, while the simulation predicted +45 kN, about 4.4% higher than the test result. Similarly, at -45 mm the experimental peak load was -35 kN, compared with -38 kN in the simulation, which is 7.9% higher. This agreement validates the accuracy of the material definitions, boundary conditions, and applied loading protocols. Likewise, the model appropriately captured the initial stiffness and load deflection response of the tower up to approximately +43 kN and -35 kN. Beyond this range, the simulation predicted a higher post-peak response, slightly overestimating the maximum load, whereas the experimental test showed a sudden vertical load drop, characteristic of energy dissipation. These differences are likely due to limitations in the Concrete Damaged Plasticity (CDP) model in reproducing localized cracking and energy dissipation mechanisms, as well as variability in GFRP manufacturing. The model also assumed perfect bond between all components and did not capture potential slip between GFRP tube and concrete.

As shown in Figure 5.22(a), the first signs of tensile damage (red zone) developed near the base of the tower near the foundation, where bending moments and tensile forces are most pronounced. The concrete showed an average damage of about 58.4%, based on the elements/nodes in the bottom part of the tower. This observation aligns with the highest strain values recorded in both the GFRP tube and steel reinforcement, confirming these areas as the critical stress zones under CF cyclic loading.

The von Mises stress distribution in Figure 5.22(b) provides further insight, showing that while tendon stresses on the tension side were higher, tendons on the compression side also sustain significant stress, balancing the bending forces and contributing to structural stability. The reinforcing bars showed lower stresses at the base where they were embedded within the foundation, and were highest just above the foundation block as expected and observed

experimentally. Stress levels gradually decrease with height as bending effects diminish. Figure 5.22(c) shows the stress contours in the concrete core. The damage in the concrete is relatively small and localized, appearing mainly near the anchorage zone at the top of the tower where the prestressing tendons are anchored. This concentration occurs because the prestressing force is transferred into the surrounding concrete at these points, creating local stress concentrations, while the rest of the concrete core remains largely in compression and therefore protected from significant damage.

The strain contours (LE11) in Figure 5.22(d) highlight greater bending near the base, consistent with curvature measured by strain gauges on the longitudinal steel bars (Figure 5.14). Together, these findings confirm that the FE model captures the tower's flexural behaviour with high accuracy.

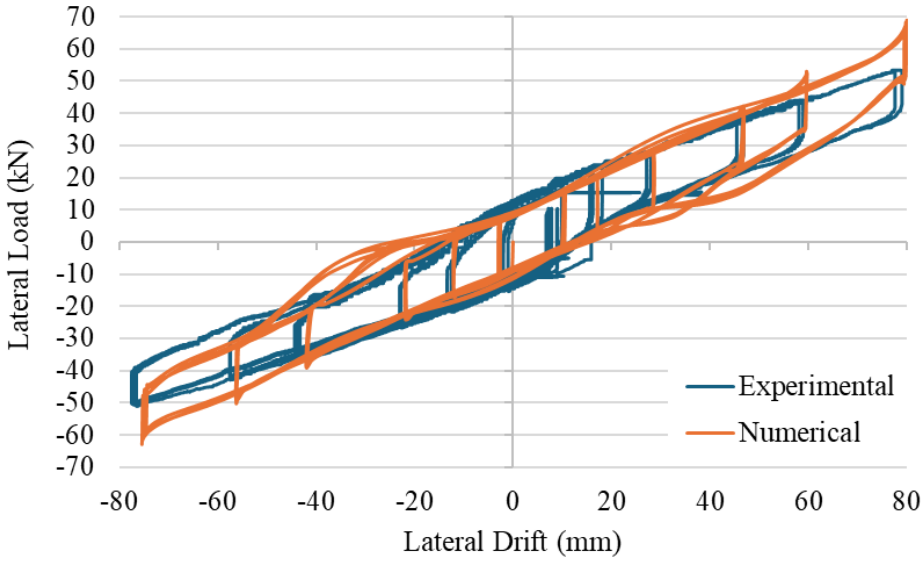

Figure 5.21. Load–displacement response of M4-1 under CF loading: Experimental vs. Model

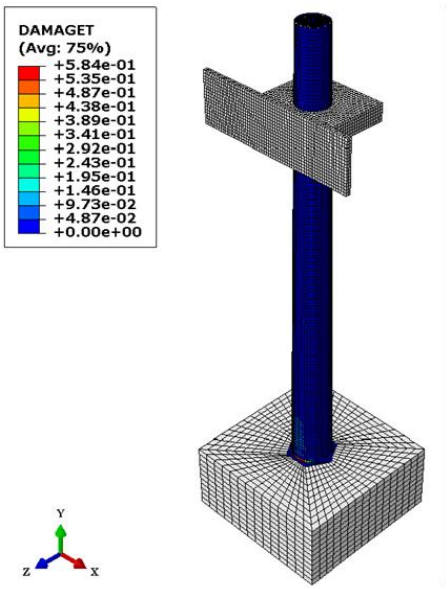

(a) Tensile damage distribution

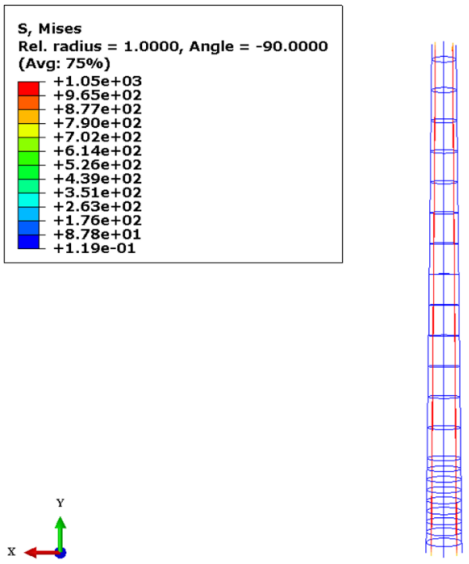

(b) Stress contours in rebars (blue) and tendons (red)

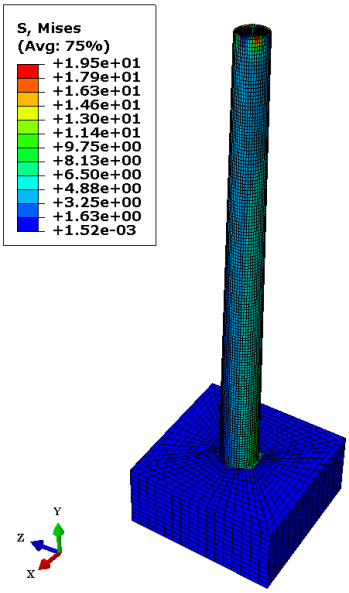

(c) Stress contours in concrete core

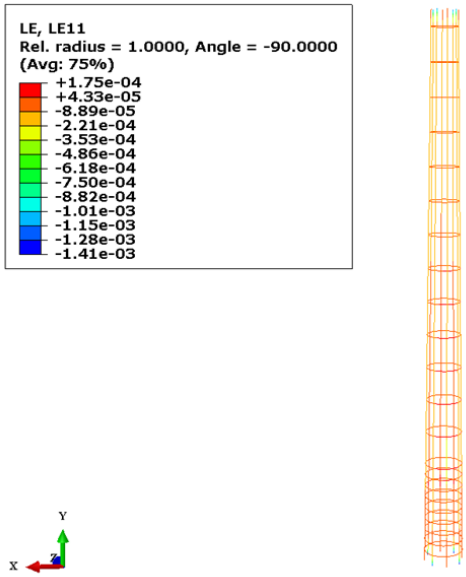

(d) logarithmic strain contours in rebars and tendons

Figure 5.22. FE simulation of the M4 tower under CF loading illustrating stress contours and damage distribution

5.7.3. Stage 3A: Small left eccentric loading at 279.4 (mm)

The FE model for the SLE loading case was modified from the BLE loading configuration. The modification involved repositioning the applied load to an eccentricity of 279.4 mm. To apply this offset, the boundary conditions were modified so that the control points were assigned at RP7–9 (279 mm) instead of RP3–5 (559 mm), as illustrated in Figure 5.23. The load was then applied through the same quasi-static procedure, with tower-top displacement monitored as before, while base shear was obtained from RP2 (tower base) and RP7–9. Once the load was defined, the model parts were remeshed to ensure numerical accuracy, while keeping the mesh size (30 mm) identical to that used in the BLE simulation for consistency.

The comparison between the experimental and numerical load–displacement curves under SLE loading is shown in Figure 5.24. Overall, the FE model reproduced the key features of the experimental response, including the initial stiffness, and the characteristic sharp load drops that occurred at displacement reversals. As mentioned in Section 5.7.2, these load drops and the reduced stiffness are captured in the FE model using a frictional link at the clamping system plate and a rotational spring at the foundation base. For the SLE loading case, the friction coefficient was 0.6, the internal contact force was 4500 kN, and the stiffness of the rotational spring (D44) was 5.0×10^{10}.

Quantitatively, the FE model provided a close match with the experimental results. As shown in Figure 5.24, the experimental and numerical SLE load–deflection curves match well up to approximately 46 mm and -35 mm. At 46 mm, the experiment reached a peak load of +40 kN, while the model predicted +44 kN, about 9.1% higher. At -35 mm, the experimental peak was -31 kN, compared with -33 kN from the model (6.1% higher). Up to these points, the agreement was strong, confirming that the chosen material properties, boundary conditions, and loading setup were appropriate. The initial stiffness and overall response up to the peak values (40 kN, -31 kN) were also well reproduced. However, in the peak region (+ 42 mm, and – 42 mm), the model slightly over-predicted load and energy dissipation, whereas the experiment showed a sudden drop in vertical load. As previously discussed in Section 5.7.2, these differences are likely linked to

CDP model limitations in simulating localized cracking and energy dissipation, combined with variability in the GFRP behaviour.

Figure 5.25 (a) illustrates that the initial development of tensile damage (red zone) appeared at the lower portion of the tower. This location corresponds to the region of maximum bending and tensile demand, which also corresponds with the peak strain values recorded in the GFRP tube and reinforcing steel. The eccentric base region is therefore identified as the most critical under SLE cyclic loading, consistent with the damage localization observed under CF loading.

The von Mises stress contours in Figure 5.25 (b) indicate that the tendons on the tension side of the attract most of the applied stresses, much like in the CF loading case. Tendons on the opposite side also remain active, resisting torsional rotation and helping the tower remain stable. The reinforcing bars experience relatively low stresses near the base because they are embedded within the foundation, and above this point their role remains secondary, since the tendons continue to carry the bulk of the load, consistent with the CF response. Stress magnitudes gradually reduce with height as the combined effects of bending and torsion decrease, similar to the CF loading case. The stress contours in Figure 5.25 (c) indicate that the concrete core experiences relatively small, localized damage restricted to the upper anchorage region where prestressing tendons are located. This behaviour is consistent with the damage patterns seen in both CF and BLE loading cases, where stress transfer is concentrated near the anchorage zone. The longitudinal strain contours (LE11) shown in Figure 5.25 (d) confirms higher bending near the base, in line with the patterns identified under CF loading. Overall, these findings confirm that the finite element model reliably captures the flexural–torsional behaviour of the tower under SLE cyclic loading, reinforcing confidence in its use for further parametric studies.

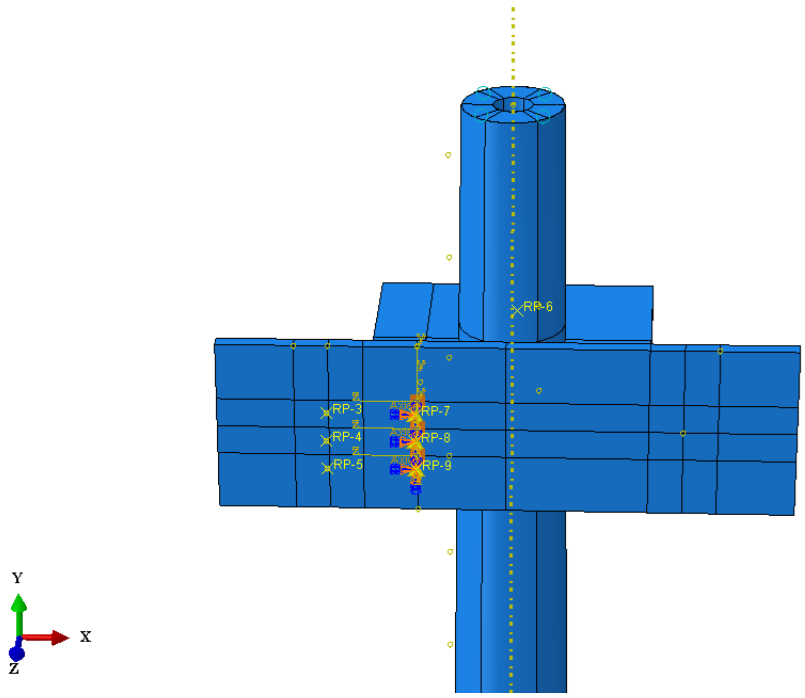

Figure 5.23. Adjustment of boundary conditions and loading position for SLE loading at 279.4 mm eccentricity.

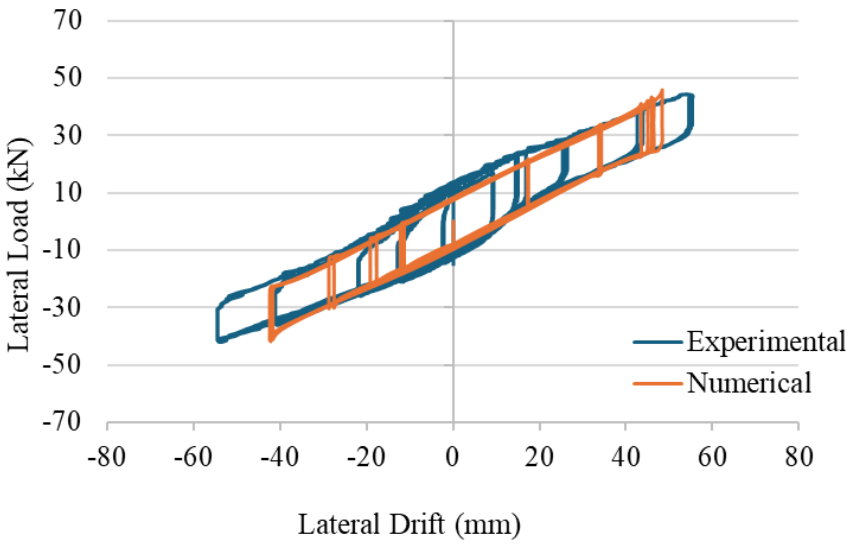

Figure 5.24. Load–Displacement Response of M4-1 under SLE Loading: Experimental vs. Model

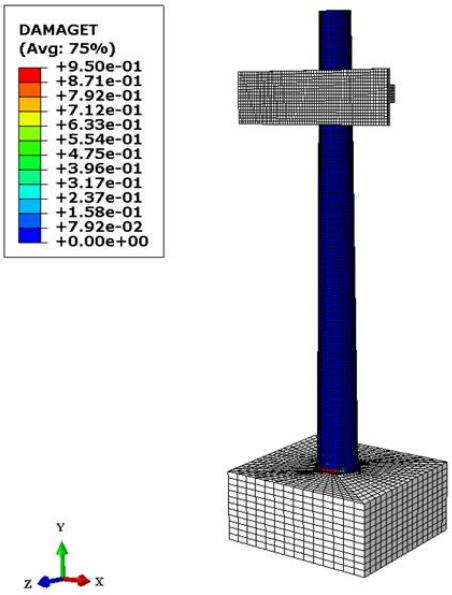

(a) Tensile damage distribution

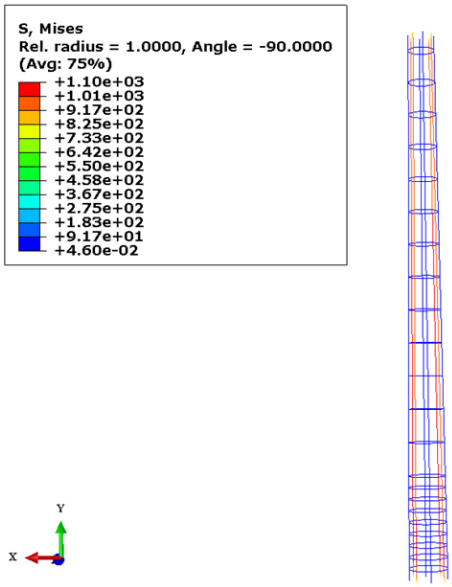

(b) Stress Contours in rebars (blue) and tendons (red)

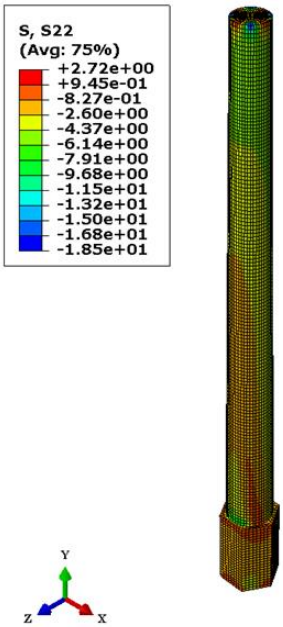

(c) Stress contours in concrete core

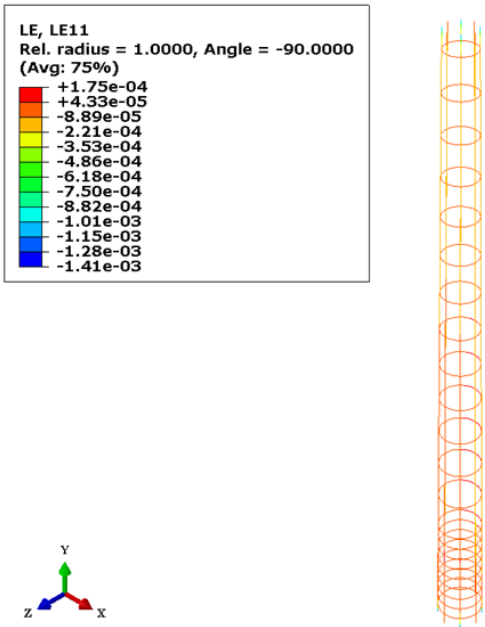

(d) logarithmic strain contours in rebars and tendons

Figure 5.25. FE simulation of the M4 tower under SLE loading illustrating stress contours and damage distribution

5.7.4. Stage 3B: Big left eccentric loading at 559 (mm)

The FE model for the BLE loading scenario was adapted from the CF loading configuration. In this case, the control points were reassigned to RP3–5, corresponding to an eccentricity of 559 mm, instead of the concentric position at RP8–10 (0 mm), as illustrated in Figure 5.26. The applied load followed the same quasi-static procedure as in the previous cases, with tower-top displacement used for response monitoring and base shear recorded from RP2 and RP3–5. Once the load was defined, the model was remeshed to maintain numerical accuracy, while the element size was kept consistent with the SLE and CF models. The numerical results under BLE loading, shown in Figure 5.27, captured the main experimental trends, including initial stiffness and the sharp load drops observed during displacement reversals. Similar to the CF and SLE cases, these drops are linked to small amounts of slip at the clamping system and foundation rotation, represented in the FE model through a frictional link at the clamp and a rotational spring at the base. For the BLE loading case, the friction coefficient was 0.5, the internal contact force was 4500 kN, and the stiffness of the rotational spring (D44) was 5.0×10^{10}.

The experimental and numerical results matched closely up to approximately +43 mm and -30 mm of displacement. At +43 mm, the experiment reached a peak of +40 kN, while the model predicted +41 kN, just 2.4% higher. At -30 mm displacement, the experimental peak was -27 kN compared to -30 kN predicted by the model (10% higher). At larger negative displacements, however, the model slightly over-predicted load and energy absorption (17.8% at -47 mm), while the experiment showed a sharper drop. As noted earlier in Section 5.7.2, this difference is likely due to limitations of the CDP approach in capturing localized cracking and energy dissipation, along with the variability in GFRP performance.

Damage patterns were consistent with expectations. Figure 5.28(a) shows tensile damage initiating near the tower base, coinciding with the maximum bending and tensile demand and the peak measured strains in both GFRP and steel reinforcement. Stress contours in Figure 5.28(b) indicates that tendons on the tension side carried most of the applied stress, while those on the opposite side provided stability. Reinforcement stresses remained relatively low near the base due to foundation embedment, with their role secondary above this region. The concrete core (Figure 5.28c)

experienced only localized damage around the upper anchorage zone, consistent with CF and SLE observations. Longitudinal strain contours (LE11) in Figure 5.28(d) confirmed the dominance of bending at the tower base. These findings highlight the ability of the FE model to accurately simulate flexural–torsional behaviour under BLE loading, validating its ability to simulate large eccentric load cases and reinforcing confidence in its application for extended parametric studies.

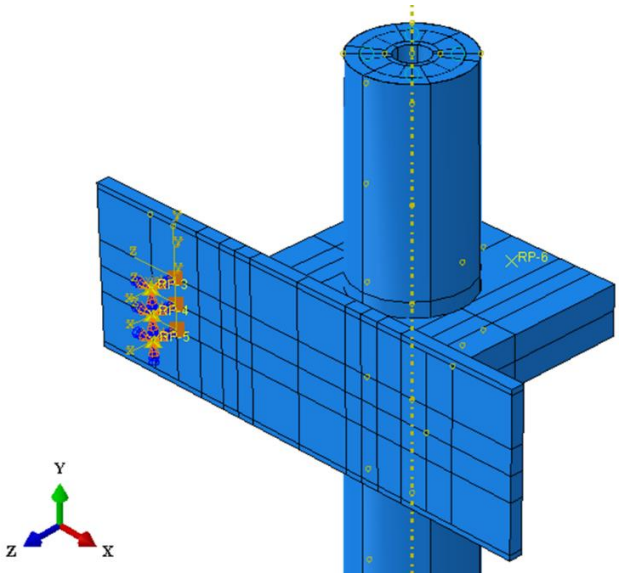

Figure 5.26. Adjustment of boundary conditions and loading position for BLE loading at 559 mm eccentricity.

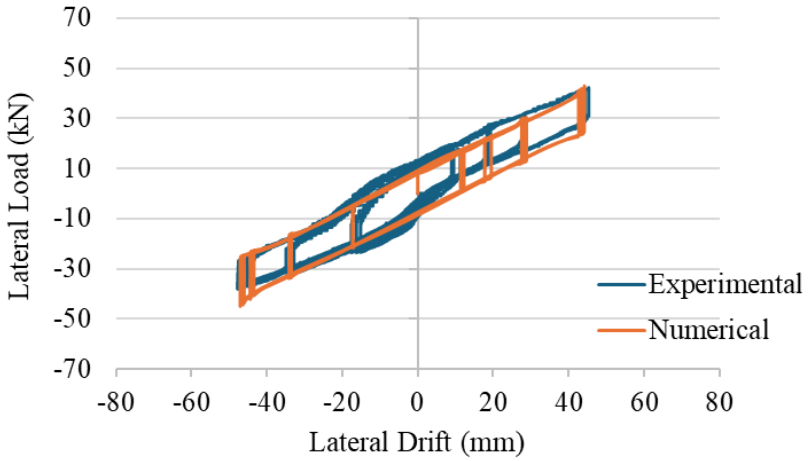

Figure 5.27. Load–Displacement Response of M4-1 under BLE Loading: Experimental vs. Model

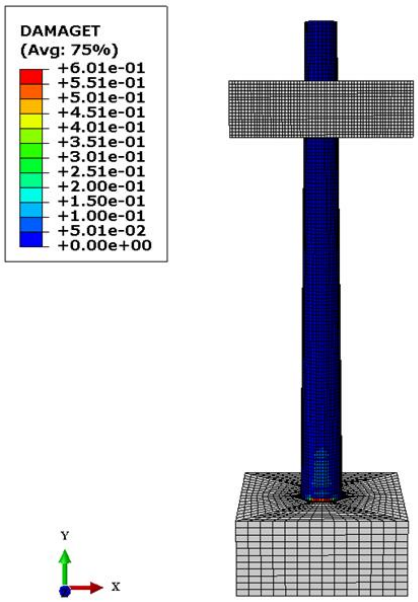

(a) Tensile damage distribution

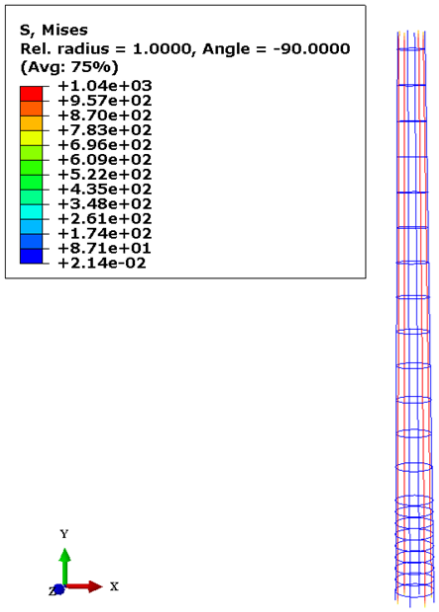

(b) Stress contours in rebars (blue) and tendons (red)

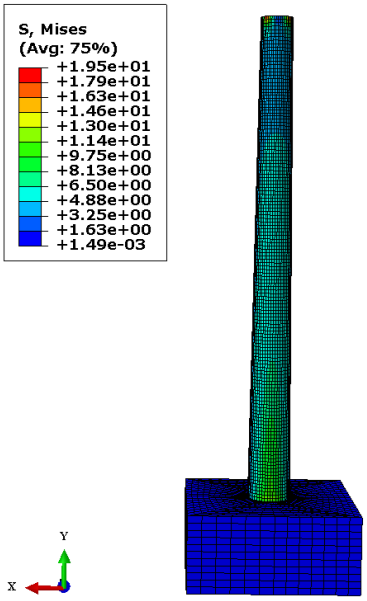

(c) Stress contours in concrete core

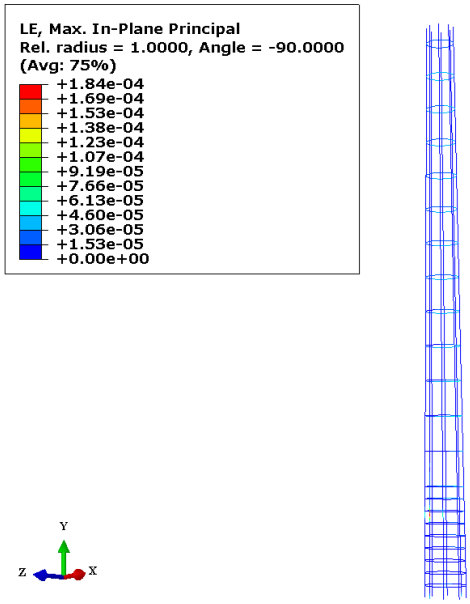

(d) logarithmic strain contours in rebars and tendons

Figure 5.28. FE simulation of the M4 tower under BLE loading illustrating stress contours and damage distribution

5.7.5. Stage 4: Test to failure

The final stage of model verification focused on evaluating the FE model's performance under monotonic lateral loading to failure, replicating the experimental test conducted on the M4-1 tower. This phase is essential in assessing the numerical model's ability to capture strength capacity, material yielding, and failure progression under extreme flexural condition. The FE model exhibited strong agreement with the experimental response in the elastic range, with both curves closely aligned up to approximately 250 mm of lateral deflection (Figure 5.29). This agreement validates the accuracy of the material definitions, boundary conditions, and applied loading protocols. Likewise, the model appropriately captured the initial stiffness and yield point of the tower. Beyond this range, the simulation predicted a smoother post-peak softening response, slightly underestimating the maximum load, whereas the experimental test showed a sudden load drop followed by oscillations, characteristic of brittle fracture and progressive failure of the GFRP surface. These differences, consistent with what was noted in Section 5.7.2, are likely due to limitations in the Concrete Damaged Plasticity (CDP) model in reproducing localized cracking and energy dissipation mechanisms, as well as variability in GFRP manufacturing. Damage and stress distributions within the FE model provided further insight into the experimental failure mechanism. As illustrated in Figure 5.30 (a), regions of high tensile damage (red zones) in the GFRP developed near the bottom of the tower, aligning with zones of maximum moment regions during bending of the experiment results. However, the FE model indicates that stress levels gradually decrease with increasing height, reflecting the reduction in bending demand and corresponding reinforcement stress. This observation aligns well with the tensile strain measurements recorded during the experimental testing. Similarly, the Von Mises stress contours, as shown in Figure 5.30 (b) confirmed that the tension-side of tendons and reinforcing bars experienced the highest stresses, in line with the expected flexural behaviour of a post-tensioned system. Moreover, Figure 5.30 (c) presents the stress distribution within the concrete, with noticeable stress concentrations observed near the base of the tower. Additionally, the deformation pattern was also confirmed by the strain contour E11 (Figure 5.30 d), which showed significant flexural curvature at the tower base near the top of the foundation block. This matched the strain gauge data recorded from embedded reinforcement and the GFRP surface during testing. The

numerically predicted strain values confirmed the onset of steel bar yielding prior to GFRP rupture, as observed in the experimental data (Figure 5.14).

The failure mode predicted by the model was evaluated using Hashin's composite damage criteria, which identified fibre tensile rupture (HSNFTCRT) as the dominant failure mode, with matrix tensile cracking (HSNMTCRT) acting as a secondary contributor (see Figure 5.31). While the location of predicted failure initiation was slightly lower than observed experimentally, the damage pattern overall closely matched the test results. This deviation is likely due to simplifications in the fibre architecture, assumptions in the GFRP layup, or variations in bond quality.

In summary, despite minor deviations in post-peak response and damage location, the model successfully captured the essential structural behaviour of the M4 tower under monotonic loading up to failure. These results underscore the model's reliability for further parametric investigation and performance-based assessment of GFRP-confined, post-tensioned concrete towers under lateral loading.

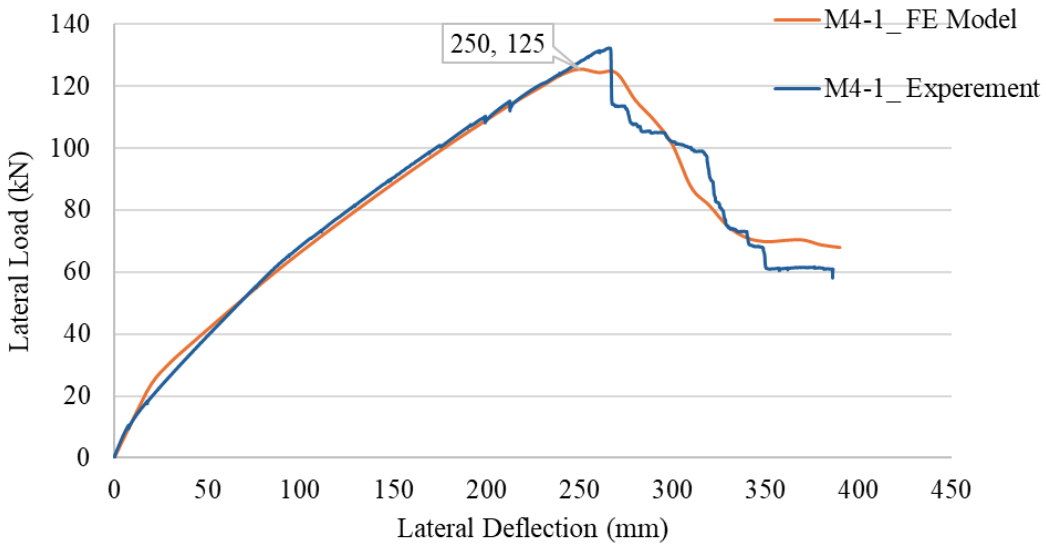

Figure 5.29. Comparison of load- displacement response of M4-1 – experimental and modeling results

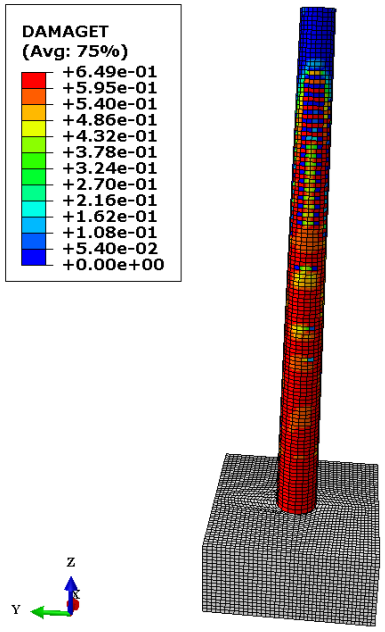

(a) Tensile Damage Distribution

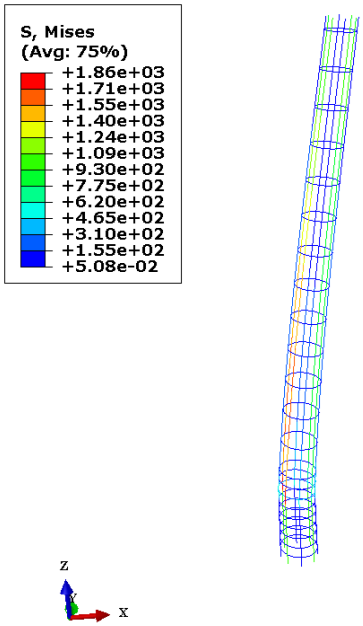

(b) Stress Contours in rebars and tendons

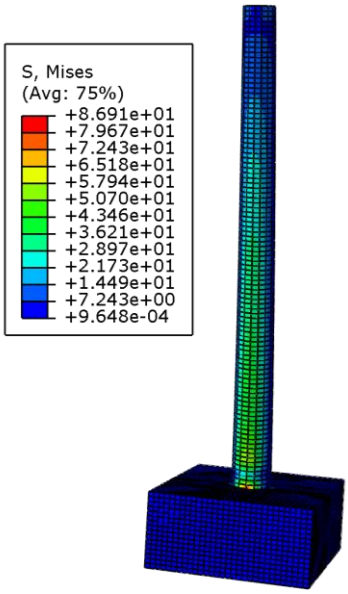

(c) Stress Contours in concrete core

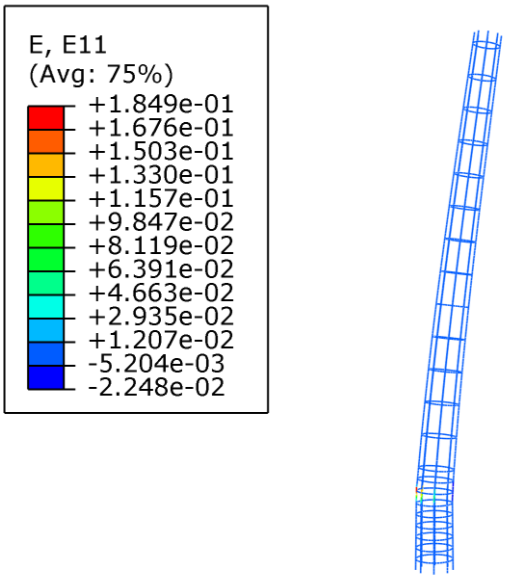

(d) logarithmic strain contours in rebars and tendons

Figure 5.30. FE simulation of the M4 tower illustrating stress contours and damage distribution

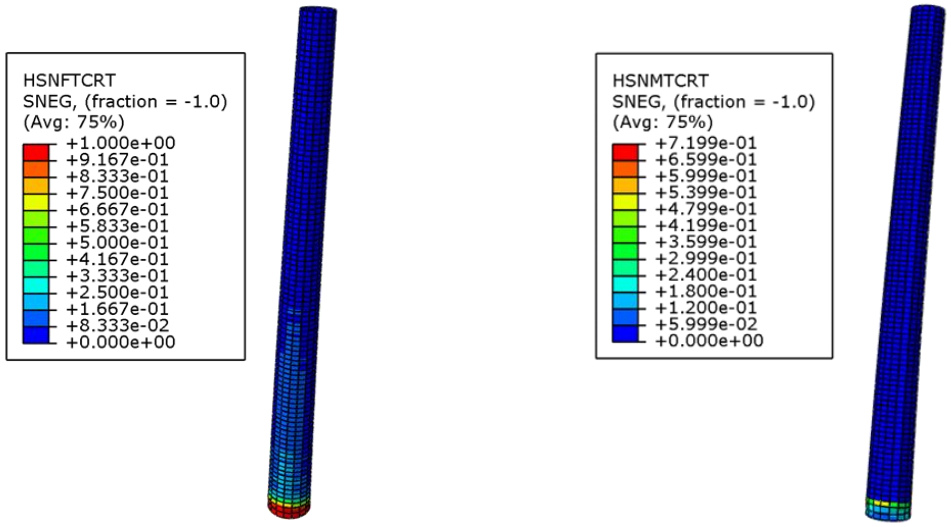

Figure 5.31. Numerical simulation of the M4-1 tower showing fiber tensile damage (HSNFTCRT) and matrix tensile failure (HSNMTCRT) based on Hashin's damage criteria.

Chapter 6 - Tower M4-2: Experimental results and analysis

6.1. Overview

This chapter presents the detailed experimental results obtained from testing the M4-2 tower specimen, integrating both static and dynamic analyses. The research explores vibration performance, centric and eccentric lateral load-deflection characteristics, and structural failure mechanisms. The results from the cyclic flexural testing under concentric loading (CL), as well as the cyclic flexural-torsional tests conducted with big right eccentricity (BRE) at 559 mm, and big left eccentricity (BLE) at 559 mm from the centroidal axis of the tower, are presented in an integrated format to enable direct comparison among the three loading conditions. The load–deflection behaviour, GFRP surface strain, and internal reinforcement bar strain are discussed by grouping the data according to measurement height or location, like the M4-1 tower. Along with the insights observed from tower M4-1, this structured presentation of tower M4-2 helps clarify how different eccentricities affect the tower's structural behaviour.

Since the detailed analysis and modelling of the towers were presented in Chapter 5, this chapter focuses on the experimental results of the tower M4-2, avoiding repetition of any analysis or modelling content.

6.2. Free vibration test

The displacement vs time plot from the free vibration test is illustrated in Figure 6.1. The average fundamental period of vibration (T_d), over the first six cycles, was about 0.152 seconds (the same as M4-1) corresponding to a damped natural frequency of vibration of about 6.598 Hz (compared to 6.602 Hz for M4-1) for the free-standing tower (Table 6.1). Moreover, the average damping ratio ζ, determined by Eq.5.1 and Eq.5.2, was found to be around 4.4% (compared to 4.0% in M4-1). This damping value likely results from the interaction between the concrete-filled GFRP tube, the foundation, and the prestressing system, all of which contribute to energy dissipation. Damping is crucial for structures subjected to dynamic loads as it influences their ability to absorb and dissipate energy during vibrations. In wind turbine towers, high damping helps to reduce fatigue damage and ensure safety. The tower's vibration test results reveal a moderate damping ratio for

this specimen comparable to a previous study on prestressed CFFT towers (Polyzois et al., 2009; Fam and Rizkalla, 2001; Mohamed & Masmoudi, 2010).

As discussed in Chapter 5, the natural frequency of this tower is above the typical fundamental frequency range of most small to medium wind turbines, indicating a low risk of resonance. The following results therefore focus on the experimental vibration response without repeating detailed analysis or modelling.

The test results confirm that the M4-2 tower maintains the same favourable dynamic characteristics observed for M4-1, including sufficient stiffness and damping to reduce vibration effects (see Chapter 5). The test was conducted at a scanning rate of 22 reading points per second, ensuring high-resolution data collection for precise evaluation of the vibrational response.

Table 6.1. Damping values and frequency results of the tested tower

tn #	**Amplitudes x(tn) (mm)**	**tn (s)**	**Td**	**Frequency (Hz)**	**$\zeta = (\delta/2\pi)$**
0	43.391	7.5714			
1	36.255	7.7168	0.1454	6.8776	0.0286
2	27.444	7.8641	0.1473	6.7883	0.0443
3	21.700	8.0149	0.1508	6.6320	0.0374
4	15.699	8.1698	0.1549	6.4549	0.0515
5	10.744	8.3301	0.1603	6.2396	0.0604

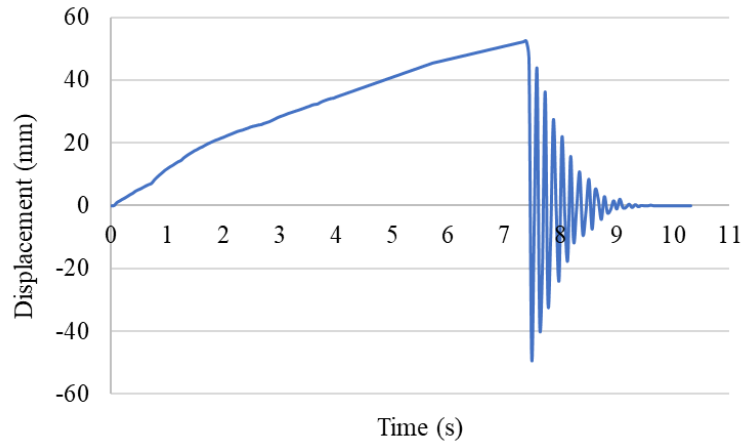

(a) Full test duration

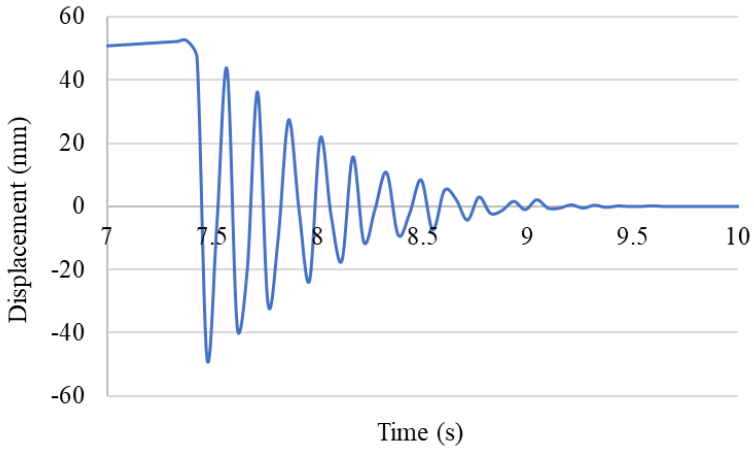

(b) Time segment from 7 s to 10 s

Figure 6.1. Tower M4-2 free vibration response

6. 3. Combined Load–Deflection Results

The load–deflection responses of the tower under all three cyclic loading configurations; CF, BLE, and BRE are shown in Figure 6.2. The tower response for the CF loading was fairly symmetrical under push (positive force) and pull (negative force) loading.

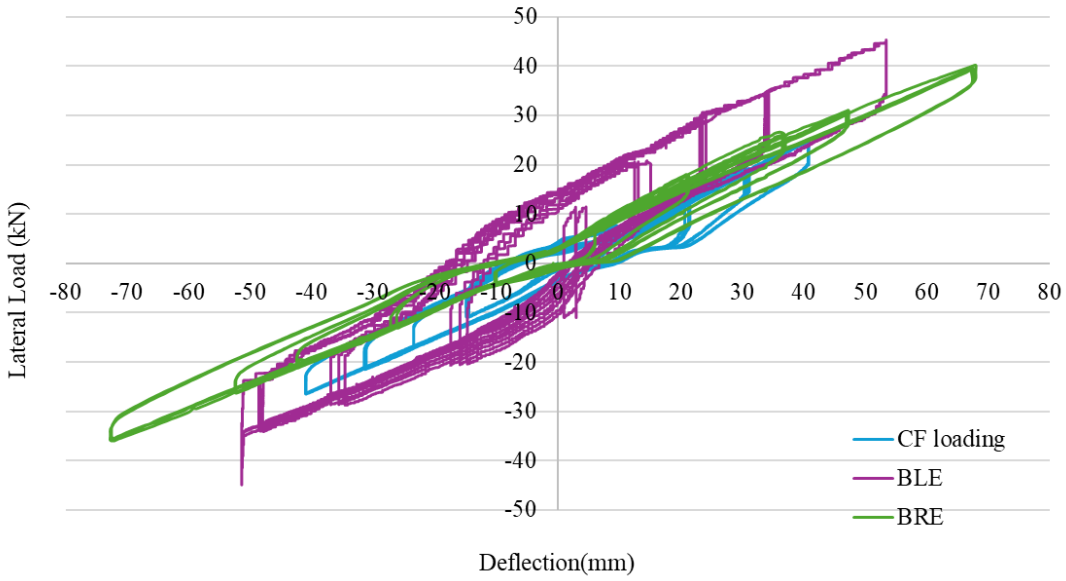

Figure 6.2. Lateral load–lateral drift response under concentric, and big right and left eccentric (± 559 mm) cyclic loading conditions

For the CF loading, the tower reached a lateral cyclic load of +25 kN at a displacement of 41 mm, corresponding to approximately 1% of its height. In contrast, a lateral load of -26 kN was monitored at a displacement of -41 mm. During testing, a shift was noticed at the top of the foundation, resulting from the loosening of a connection bolt between the foundation and the strong floor. This loose bolt, located in the front part of the foundation between the tower and the A-frame, was confirmed through visual inspection. As a result of this loose bolt, the foundation moved slightly, which caused the tower to shift at the top opening of the foundation. This movement was captured by cable transducers attached to the foundation, which recorded a displacement of approximately 0.77 mm at a height of 175 mm from the base (Figure 6.3).

The shift resulted in an increase in the tip deflection of the tested specimens, as confirmed through a comparison with the cyclic flexural testing of M4-1 under concentric loading. At an applied load of 25 kN, the displacement was approximately 26 mm for M4-1. The test was displacement-controlled, and during the final cycle of the seventh displacement increment, the tip deflection reached 41 mm. This deflection accounted for both the bending deformation and the rigid body movement of the tower.

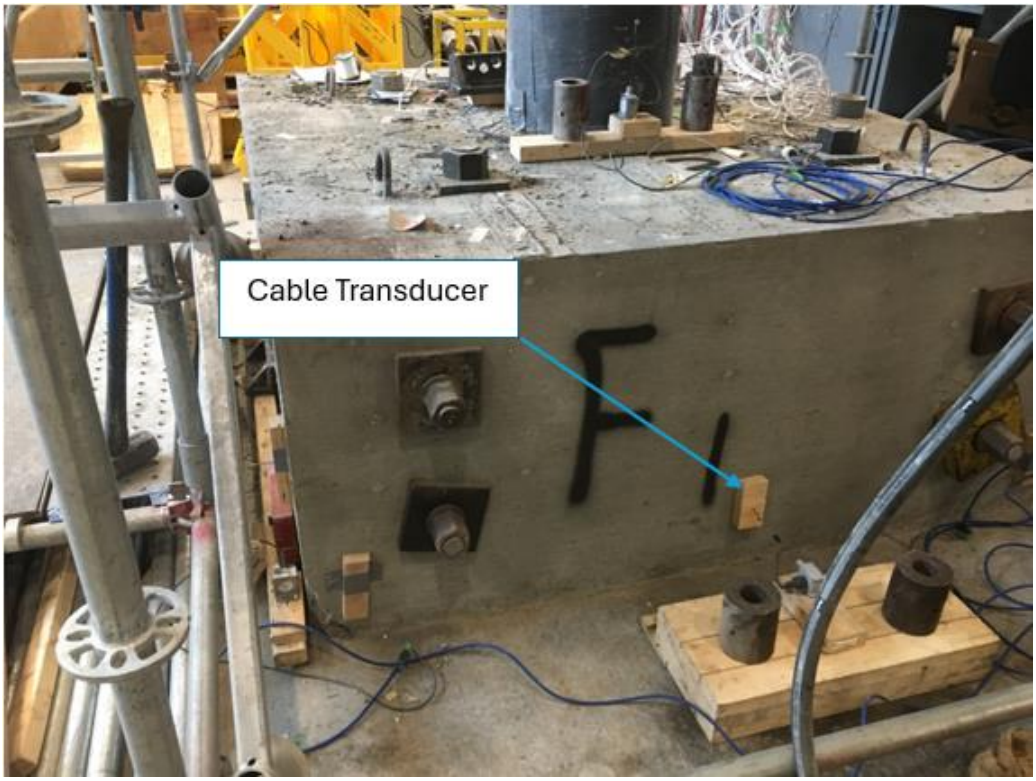

Figure 6.3. Cable transducer attached on the front side of the foundation

For the BRE loading, with a 559 mm right-side eccentricity, the tower response was slightly unsymmetric under pushing (positive) loading and pulling (negative) loading, displaying mainly linear elastic behaviour with limited hysteresis. The tower reached a peak lateral cyclic load of +39 kN at a lateral displacement of 67 mm, equivalent to approximately 1.2% of its height. In comparison, a lateral load of -36 kN was recorded at a lateral displacement of -72 mm, reflecting the tower's response to loading in the opposite direction.

Overall, the response was similar to that observed in M4-1 under BRE loading, except that the maximum force was slightly less (39 kN vs.45 kN, and -28 kN vs -43 kN). When comparing the BRE and CF results at equivalent lateral loads (+25 kN and –26 kN), the response in both directions for both cases remained essentially elastic (Figure 6.4 and Figure 6.5). The exception was reinforcing bar B at 700 mm height, where the strain values reached 2090 με in the CF loading and 2122 με in the BRE loading.

For BLE loading, with a 559 mm left-side eccentricity, the tower response was noticeably different. The tower reached an ultimate lateral cyclic load of +45 kN at a displacement of 53 mm, corresponding to approximately 1 % of its height. In contrast, at a lateral load of -44 kN, the tower reached a lateral displacement of -51 mm. However, the maximum displacement of -51 mm was already reached when the load was only -36 kN. This suggests that the cable transducer may have reached the limit of its measurement range and was not able to capture any further movement beyond that point.

When comparing the BLE and BRE cases under similar applied lateral loads (+39 kN and -36 kN), the BLE loading displays a stiffer response but with larger load drops after each cycle that are potentially indicative of one side of the clamp being loosened and/or one side of the foundation experiencing more movement than the other. The influence of the test setup is further investigated in Chapter 8.

6.4. Strain in internal longitudinal steel reinforcement bars

The strain behaviour of internal steel reinforcing bars during the final loading cycles of the tower under the three cyclic loading configurations: CF, BRE, and BLE, are shown in Figure 6.4. The results highlight the alternating tensile and compressive strain patterns observed in reinforcing bars ‘A’ and ‘B’ under reversed loading directions. Specifically, reinforcing bar ‘A’ experienced tensile strain during pushing (positive) loading and compressive strain during pulling (negative) loading, while reinforcing bar ‘B’ displayed the opposite behaviour. Importantly, reinforcing bar ‘A’ experienced tensile strains that exceeded the yield threshold across most cyclic service loading test scenarios (except for the CF cyclic loading which was at a lower load level), indicating the development of inelastic behaviour. Rebar ‘B’, however, only exceeded the yield strain in certain tests and at specific elevations, suggesting that yielding in reinforcing bar ‘B’ was more localized and dependent on the load orientation and position.

6.4.1. Strain response in rebars ‘A’ and ‘B’ under concentric flexural (CF) loading

Under CF loading, the peak tensile strains occurred at a height of 700 mm for both reinforcing bars ‘A’ and ‘B’ above the tower base, with reinforcing bar ‘A’ reaching 1475 με and bar ‘B’ reaching

2090 με during the final cycle. The maximum compressive strains were -550 με for reinforcing bar ‘A’ and -413 με for reinforcing bar ‘B’, both at 700 mm. These strain levels indicate that the region between 700 mm (top of foundation block) and 1200 mm experienced the most significant stress concentration, corresponding with the expected moment peak for cantilever behaviour.

Importantly, the tension strain magnitudes were consistently and significantly greater than those in compression for both ‘A’ and ‘B’ bars, except for reinforcing bar ‘B’ at the height of 950 mm which shows a slightly lower value. This difference is likely due to cracking in the surrounding concrete under tensile stress, which reduces the section’s ability to resist tension, thus transferring most of the load to the steel reinforcement. It is also noted that the tensile strain levels in reinforcing bar ‘B’ exceeded the typical yield strain for steel reinforcement, occurring at an applied load of 25 kN, confirming the onset of plastic behaviour under the applied cyclic loads.

6.4.2. Strain response in rebars ‘A’ and ‘B’ under big right eccentric (BRE) loading

The strain behaviour of the reinforcing bars under BRE loading shows a combination of flexural and torsional effects due to the imposed asymmetry. As illustrated in Figure 6.4, bar ‘A’ experienced tensile strain during pushing (positive) loads and compressive strain under pulling (negative) loads, while bar ‘B’ showed the inverse response, consistent with load reversal.

Throughout the test, both reinforcing bars experienced tensile strains that exceeded the yield threshold at some points under the maximum applied BRE loads, indicating the development of inelastic behaviour. The peak tensile strains for both reinforcing bars ‘A’ and ‘B’ were recorded at a height of 700 mm near the upper edge of the foundation block, with bar ‘A’ reaching 2409 με and bar ‘B’ reaching 2824 με. In contrast, the maximum compressive strains were -757 με for bar ‘A’ and -693 με for bar ‘B’ both at 1200 mm. These levels show slightly higher tension than those under CF loading, confirming the presence of inelastic deformation in both bars and demonstrating the interaction between flexural and torsional stress conditions. These findings suggest that the critical strain zone under BRE loading was concentrated between 700 mm and 1450 mm above the tower base, likely due to localized stress concentrations in this region.

When compared to CF loading under similar peak cyclic loading (25 kN pushing and -26 kN pulling), BRE loading induced slightly higher tensile strains in most cases, as illustrated in Figure 6.4 and Figure 6.5. Reinforcing bar 'A', for instance, showed higher strain at 950 mm and 1200 mm while the strain was slightly lower at 700 mm and 1450 mm. In contrast, reinforcing bar 'B' with the BRE loading recorded slightly higher tensile strain across most elevations under pulling loading, about 2% at 700 mm, 47% at 950 mm, and 4% at 1200. At 1450 mm, however, the tensile strain was slightly lower in BRE by 5%, suggesting localized moment redistribution caused by torsion effects. In terms of compressive strains, BRE loading produced more compression in lower sections of both bars. Reinforcing bar 'A' experienced higher compression of 9% at 700 mm, 11% at 950 mm, 3% at 1200 mm, and 15% at 1450 mm. Reinforcing bar 'B' followed a similar trend, with greater compression under BRE of about 6% at 700 mm, 12% at 950 mm, 11% at 1200 mm, and 4% at 1450 mm. The strain concentration under BRE loading was particularly concentrated between 950 mm and 1200 mm from the tower base.

6.4.3. Strain response in rebars 'A' and 'B' under big left eccentric (BLE) loading

In line with the patterns identified under BRE loading, the strain response of the reinforcement during BLE loading shows a combination of flexural and torsional effects due to the imposed asymmetry. As illustrated in Figure 6.4, reinforcing bar 'A' experienced tensile strain during pushing (positive) loading and compressive strain under pulling (negative) loading, while bar 'B' developed the inverse behaviour, consistent with load reversal. Throughout the test, both bars experienced tensile strains that exceeded the yield threshold at most points, revealing the development of inelastic behaviour.

The highest tensile strains were recorded at a height of 700 mm near the upper surface of the foundation block, with reinforcing bar 'A' reaching 3120 με and bar 'B' reaching 2529 με. In contrast, the maximum compressive strains were recorded as -676 με for bar 'A' at 1200 mm and -681 με for bar 'B' at 700 mm. These tensile values are slightly higher than those under CF loading, indicating the inelastic deformation in both rebars. These findings suggest that the critical strain zone under BLE loading was concentrated between 700 mm and 1200 mm above the tower base

(similar with what was observed in BRE loading), likely due to localized stress concentrations in that part of the tower.

Analytical comparison between CF and BLE under equivalent peak loads (25 kN pushing and -26 kN pulling) shows perceptive trends at some heights. Compared to CF, BLE loading induced slightly higher tensile strains in most cases for reinforcing bar ‘A’, as illustrated in Figure 6.4. However, at 700 mm, BLE produced a slightly lower strain, possibly due to geometric effects and localized stress redistribution. For bar ‘B’, BLE produced slightly lower tensile strains at 700 mm, 1200 mm, and 1450 mm, but higher at 700 mm suggesting a localized redistribution of internal forces.

When comparing BLE to BRE loading under the same cyclic amplitude, BLE induced variable tensile strains in most locations, as illustrated in Figure 6.4 and Figure 6.5. Reinforcing bar ‘A’ recorded a higher strain at 950 mm, and 1450 mm, while the strain was slightly lower at 700 mm and 1200 mm. Bar ‘B’ similarly showed reduced strain with BLE loading at 700 mm, 1200 mm, and 1450 mm. The only exception was observed at 950 mm, where BLE recorded a slightly higher strain compared to BRE (Figure 6.6).

The compressive strain patterns give more insight into this difference in behaviour. Under BLE loading, reinforcing bar ‘A’ generally showed slightly lower compressive strains across most heights compared to CF. At 700 mm, the strain was 36% lower in BLE loading, and 17% at 1200. For bar ‘B’, BLE loading induced lower compression at the lower levels by 12% at 700 mm,13% at 950 mm, 0.2% at 1200 mm, and 44% at 1450 mm.

When compared with BRE, BLE again showed slightly lower compressive strains. Reinforcing bar ‘A’ recorded a lower strain by 32% at 700 mm, and 23% at 950 mm. However, at 1200 mm, BLE loading produced a slightly higher compressive strain of 3%, and much higher was observed at 1450 mm (94%). Similarly, side ‘B’ produced slightly lower compressive strains under BLE loading, such as 15% at 700 mm, 21% at 950 mm, 10% at 1200 mm, and 33% at 1450 mm.

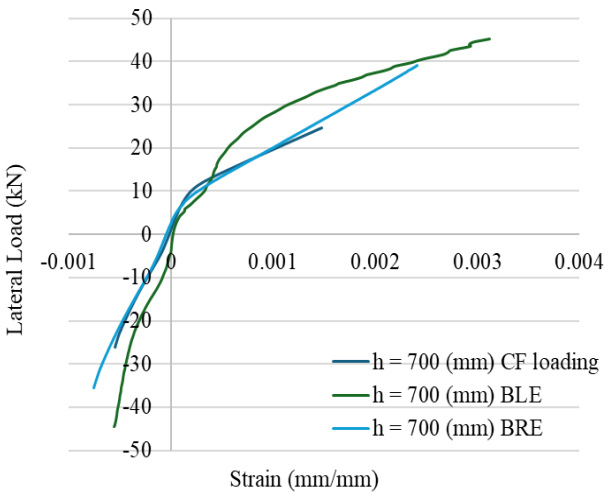

(a) Strain reading on rebar 'A' at 700 (mm)

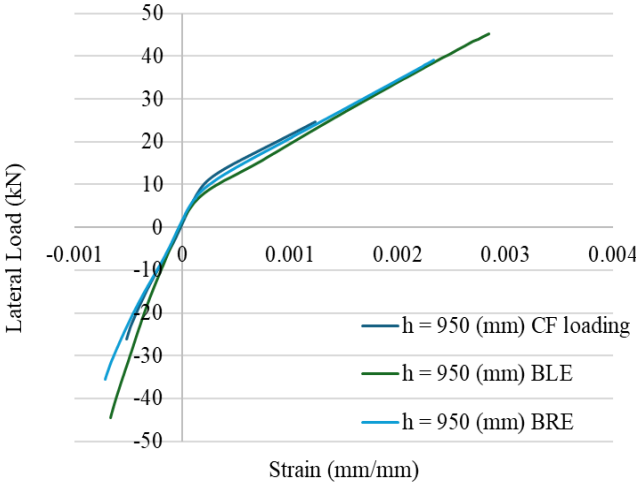

(b) Strain reading on rebar 'A' at 950 (mm)

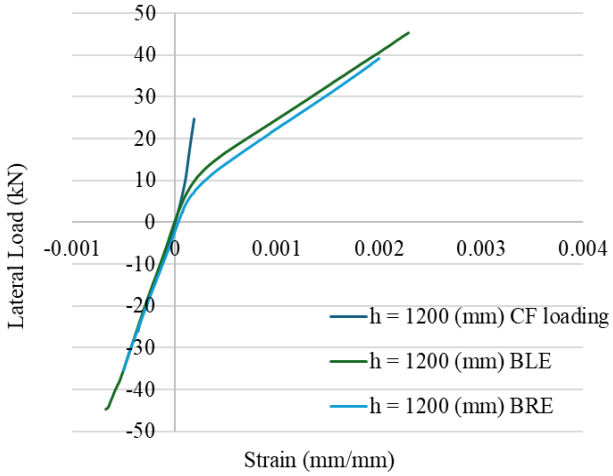

(c) Strain reading on rebar 'A' at 1200 (mm)

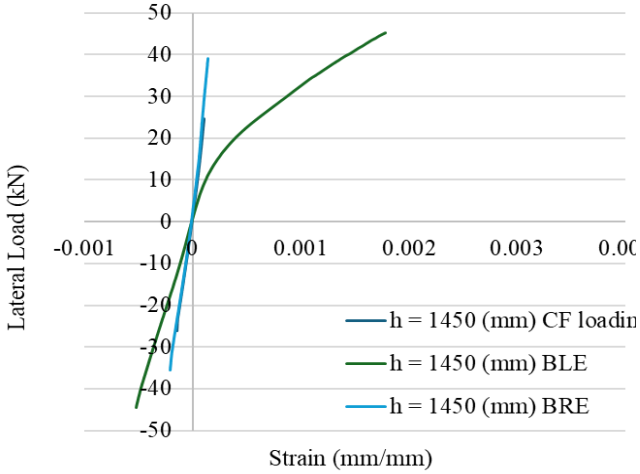

(d) Strain reading on rebar 'A' at 1450 (mm)

Figure 6.4. Strain readings recorded on rebars 'A' under both push and pull loading phases for concentric, and big left and right eccentricity (559 mm) cyclic loading conditions.

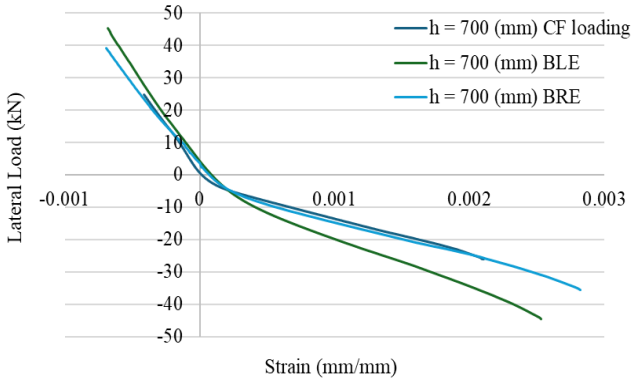

(a) Strain reading on rebar 'B' at 700 (mm)

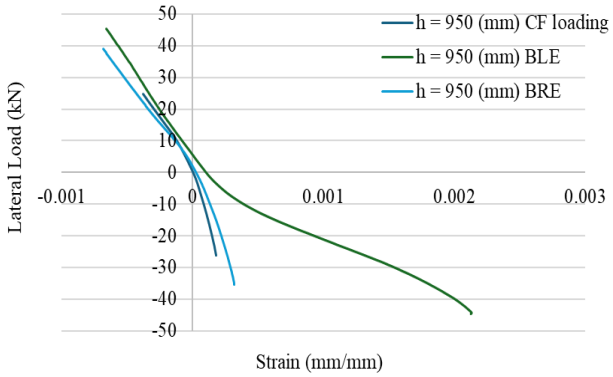

(b) Strain reading on rebar 'B' at 950 (mm)

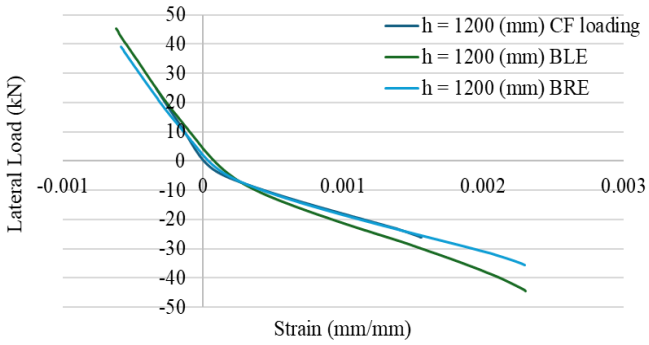

(c) Strain reading on rebar 'B' at 1200 (mm)

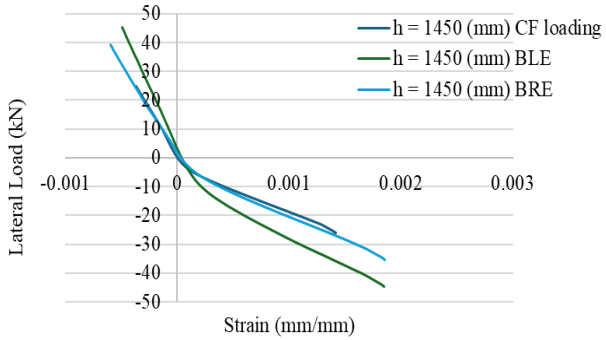

(d) Strain reading on rebar 'B' at 1450 (mm)

Figure 6.5. Strain readings recorded on rebar 'B' under both push and pull loading phases for concentric, and big left and right eccentricity (559 mm) cyclic loading conditions.

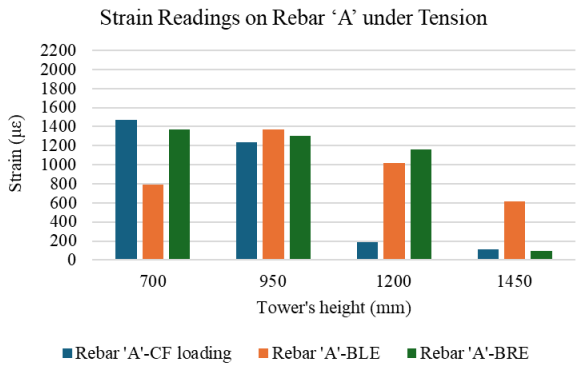

(a) Under pushing loading

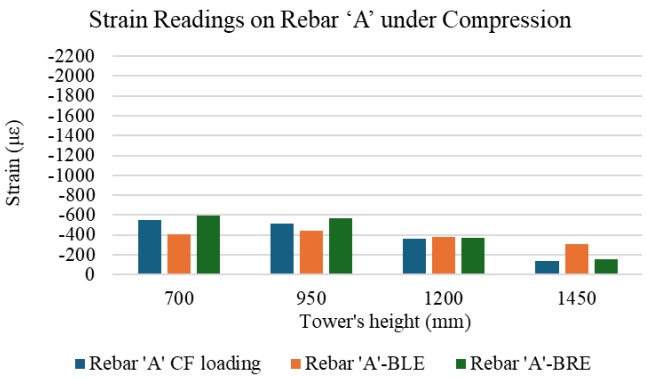

(c) Under pulling loading

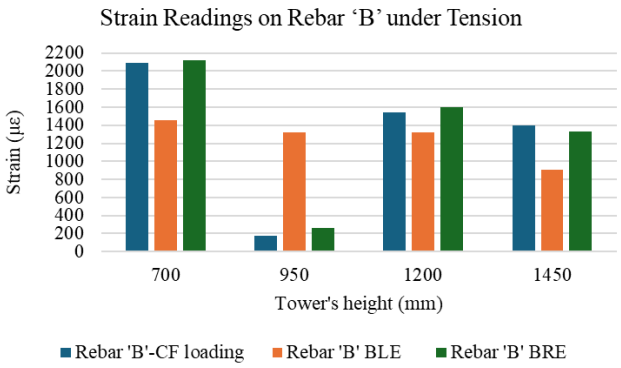

(b) Under pulling loading

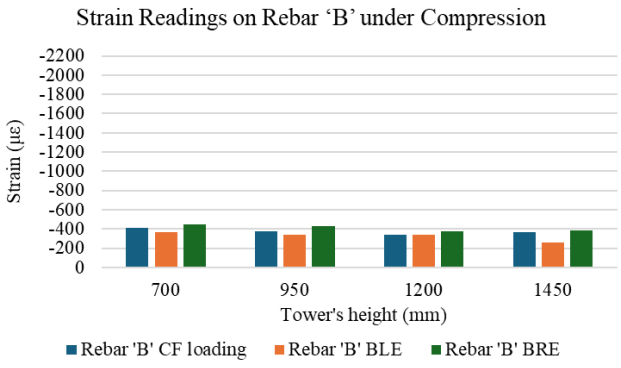

(d) Under pushing loading

Figure 6.6. Comparison of strain values on rebars 'A' and 'B' under CF loading, BLE, and BRE cyclic loading conditions (+25 kN and -26 kN)

6.4.4. Strain response in rebars 'C' and 'D' under concentric flexural (CF) loading

Figure 6.7 presents the strain responses of steel reinforcing bars 'C' and 'D', where strain gauges were installed in an alternating pattern between the two neutral axis bars, reinforcing bar 'C' on the left side and reinforcing bar 'D' on the right side of the tower. These responses were recorded under both pushing (positive) and pulling (negative) phases of CF cyclic loading. Under pushing loading, reinforcing bar 'C' recorded strain values of 565 με at 700 mm, while bar 'D' showed peak values of 148 με at 950 mm and 130 με at 1450 mm. During the pulling phase, bar 'C'

measured 640 με at 700 mm, while bar 'D' recorded 126 με at 950 mm and 312 με at 1450 mm. Notably, throughout both loading directions, all recorded strains remained tensile (positive), which aligns with analytical predictions indicating a shift of the neutral axis due to concrete cracking and progressive stiffness degradation.

Similar to what was seen in M4-1 tower, all recorded strains during the final full load cycle remained positive, indicating consistent tensile behaviour, which is expected for cracked concrete sections. This consistent tensile response can be attributed to the shift of the neutral axis caused by cracking on the tension side. There were also some slight differences in the strain readings between bars 'C' and 'D', which are likely a result of minor variations in the prestressing levels of the four tendons. Additionally, no data was available from the strain gauge at 1200 mm on bar 'C', possibly due to sensor failure or a connection issue during testing.

6.4.5. Strain response in rebars 'C' and 'D' under big right eccentric (BRE) loading

Under BRE loading, the strain responses in reinforcing bars 'C' and 'D' again showed directional asymmetry due to the applied eccentricity. As shown in Figure 6.7, reinforcing bar 'C' recorded peak strains of 1294 με at 700 mm during the pushing phase, while bar 'D' showed lower strain values under pushing loads: 713 με at 950 mm and 409 με at 1450 mm. In contrast, under the pulling phase, bar 'C' showed a reduced response, with 614 με at 700 mm, while bar 'D' showed strain values of 339 με at 950 mm and 600 με at 1200 mm.

A comparative analysis between BRE and CF loading under equivalent peak loads (25 kN pushing and -26 kN pulling) shows several important trends. Under pushing load, BRE generally induced slightly higher tensile strains in reinforcing bar 'C', particularly at the 700 mm elevation (626 με in BRE vs.565 με in CF). However, the strain values in bar 'C' are slightly lower during pulling at 700 mm (614 με in BRE vs.640 με in CF). This suggests a redistribution of stress, likely caused by torsional interaction. Reinforcing bar 'D' followed a similar but inverted trend. Under pushing loads, BRE recorded lower strains at 950 mm compared to CF (55 με vs.148 με), but slightly higher at 1450 mm (146 με in BRE vs.130 με in CF). During pulling load, BRE again showed slightly increased strains relative to CF at both 950 mm (242 με BRE vs.126 με) and 1450 mm (354 με BRE vs.312 με). These differences suggest that while BRE generated higher strain levels on the

side of the tower subjected to eccentric flexure (rebar ‘D’), the opposing side (rebar ‘C’) experienced reduced strain due to the different stress distribution. Similar to what was seen in M4-1 tower test, both rebars continued to experience tensile strain across all locations and phases, reinforcing the conclusion that the neutral axis stayed well above the mid-height of the section during the entire cyclic load.

6.4.6. Strain response in rebars ‘C’ and ‘D’ under big left eccentric (BLE) loading

Figure 6.7 illustrates the strain response of reinforcing bars ‘C’ and ‘D’ under BLE loading, where the applied torsion was in the opposite direction compared to BRE. During the pushing phase, bar ‘C’ showed peak strains of 1409 με at 700 mm, while bar ‘D’ reached 556 με at 950 mm and 377 με at 1450 mm. Under pulling loads, reinforcing bar ‘C’ again showed a reduction in strain levels (287 με at 700 mm), while reinforcing bar ‘D’ exhibited a significant increase, peaking at 1370 με at 950 mm and 840 με at 1450 mm.

When compared with CF loading under equivalent peak loads (25 kN pushing and -26 kN pulling), BLE induced slightly higher tensile strains for reinforcing bar ‘C’ during pushing load: 1409 με at 700 mm vs.565 με in CF. However, under pulling, the BLE value dropped below those noted in CF for bar ‘C’: 158 με vs.640 με at 700 mm. Reinforcing bar ‘D’ also displayed slightly higher strains in BLE compared to CF under pushing: 137 με vs.126 με at 950 mm, while lower strain at 1450 mm (4 με vs.312 με). Under pulling, reinforcing bar ‘D’ showed higher strains in BLE compared to CF: 842 με vs.126 με at 950 mm, and 380 με vs.312 με at 1450 mm.

A direct comparison between BLE and BRE under identical cyclic loading levels further highlights the effect of eccentricity direction. In pushing, reinforcing bar ‘C’ recorded higher strains in BRE. Reinforcing bar ‘C’ recorded 626 με in BRE at 700 mm vs.610 με in BLE. In contrast, bar ‘D’ showed a higher value of 174 με in BLE vs.54 με in BRE at 950 mm, and 4 με in BLE vs.146 με in BRE at 1450 mm. Under pulling, bar ‘C’ in BRE recorded slightly higher strain than in BLE (411 με vs.158 με), while bar ‘D’ showed a higher value of 842 με in BLE vs.242 με in BRE at 950 mm, and 380 με in BLE vs.354 με in BRE at 1450 mm.

Overall, the comparative analysis confirms that both BRE and BLE produce asymmetric strain patterns due to the interaction of torsion with flexure loading. While the strain magnitudes differ slightly depending on the direction of eccentricity, the overall response in both rebars remained tensile across all measurement points. This reinforces the conclusion that the neutral axis had shifted above mid-height due to tension cracking, and confirms that flexural behaviour remained the dominant response mode in the tower under cyclic eccentric loading.

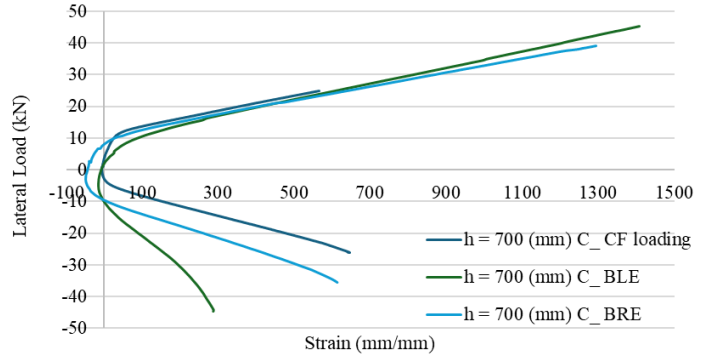

(a) Strain readings recorded on rebars 'C' at 700 (mm)

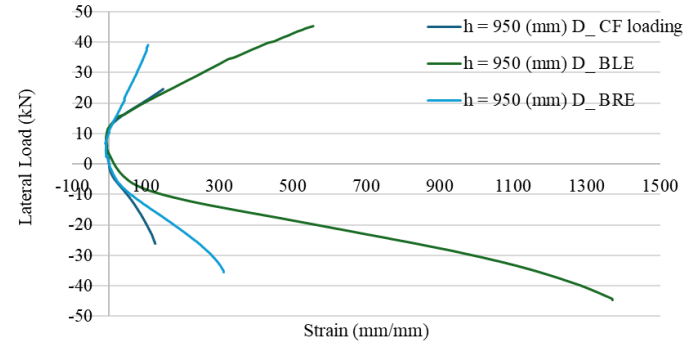

(b) Strain readings recorded on rebars ‘D’ at 950 (mm)

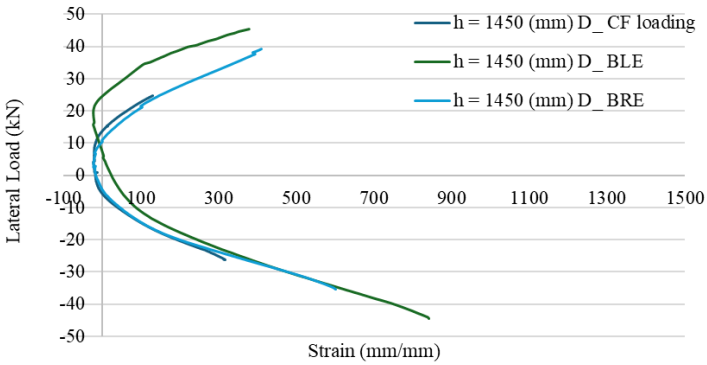

(c) Strain readings recorded on rebars ‘D’ at 1450 (mm)

Figure 6.7. Strain readings recorded on rebars 'C' and ‘D’ under both push and pull loading phases for concentric, big left and right eccentricity (559 mm) cyclic loading conditions

6.5. GFRP surface strain response under cyclic loading

This section presents the surface strain responses of the GFRP during the final load cycles of all three cyclic loading cases: CF, BRE, and BLE. Figure 6.8 displays the strain data for sides ‘A’ and ‘B’, respectively, which experienced tension and compression depending on the direction of the applied load.

6.5.1. Strain response in sides ‘A’ and ‘B’ under concentric flexural (CF) loading

Under CF loading, the strain profiles showed an uneven cyclic pattern, which fully align with the strain behaviour recorded in the internal longitudinal rebars.

Peak tensile strains were monitored at 840 mm on both sides, measuring 708 με on side ‘A’ and 878 με on side ‘B’. In contrast, the maximum compressive strains were -746 με on side ‘A’ and -554 με on side ‘B’ both at the same height of 840 mm. This behaviour confirms that the tensile strains exceeded the compressive ones, likely due to the development of cracks in the concrete core. A critical concentration of strain was consistently observed between 840 mm and 1340 mm, identifying this zone as a critical stress region in the tower which closely match the strain values obtained from the GFRP surface on sides ‘A’ and ‘B’ in tower M4-1.

Furthermore, the strain readings in the hoop direction, measured on the GFRP surface along sides C (left side of the tower) and D (right side), remained close to zero throughout the test.

6.5.2. Strain response in sides ‘A’ and ‘B’ under big right eccentric (BRE) loading

The BRE loading configuration showed a strain response trend consistent with previous CF loading cases, but with slight differences due to the torsional component directed toward the right side of the tower cross-section. Under pushing (positive) loading, side ‘A’ experienced tensile strain while side ‘B’ was in compression.

At 840 mm, the peak tensile strains were measured as 1477 με on side ‘A’ and 1189 με on side ‘B’, while compressive strains reached -1016 με on side ‘A’ and -941 με on side ‘B’ both at 840 mm. Just like in the CF loading test, tensile strains were consistently higher than compressive strains,

and all values remained below the GFRP failure threshold of 0.016, confirming the tower adequacy of the GFRP tube. Notably, the tensile strain in side ‘B’ was slightly higher than side ‘A’, showing a different pattern than what was previously observed in tower M4-1.

When compared to CF loading at similar peak forces (25 kN pushing and -26 kN pulling), BRE loading produced similar tensile and compressive strains along sides ‘A’ and ‘B’ from the height of 1340 mm to 2340 mm. For side ‘A’ under pushing (tensile) loads, BRE showed slightly higher tensile strains at all measured elevations, as shown in Figure 6.10, while compressive strains on the same side decreased slightly at 1340 mm, but were higher at 840 mm, 1840 mm, and 2340 mm. Similarly, side ‘B’ under BRE loading showed slightly higher compressive strains at all elevations (1340 mm, 1840 mm, and 2340 mm) under pushing (compressive) loads. However, under pulling (tensile) conditions, the strain on side ‘B’ decreased across the same heights. This consistent increase further highlights the torsional influence introduced by the eccentric load. It is important to note that no strain data was recorded at 840 mm on side ‘B’ due to a malfunctioning strain gauge at that location.

6.5.3. Strain response in sides ‘A’ and ‘B’ under big left eccentric (BLE) loading

The strain behaviour under BLE loading showed a similar trend to CF, but with minor notable differences occurring from the added torsional component. When the tower was subjected to pushing (positive) loading, side ‘A’ experienced tensile strains while side ‘B’ was in compression. Conversely, under pulling (negative) loading, side ‘A’ experienced compression and side ‘B’ experienced tension. Strain magnitudes were higher in tension than in compression, with no recording indicating strain levels approaching the failure strain observed in coupon tests (0.016). This absence of high strain magnitudes and any visible surface cracking confirm the integrity of the GFRP tube under the maximum BLE loading. Peak tensile strains were recorded with 1902 με on side ‘A’, and 1560 με on side ‘B’ both at 1340 mm. The maximum compressive strains reached -1147 με on side ‘A’ at 840 mm and -1054 με on side ‘B’ at 1340 mm.

When compared to CF loading at similar peak forces (25 kN pushing and -26 kN pulling), BLE loading produced slightly higher tensile strains along side ‘A’ at all elevations (840 mm to 2450 mm), while compressive strains on the same side were slightly reduced at the height of 840 mm

but increased at all other elevations (Figure 6.10). For side ‘B’ the pattern slightly changed. During pushing (compressive) loads, the BLE test produced higher compressive strains at 1340 mm, but lower strains at 1840 mm and at 2340 mm. However, under pulling (tensile) loading, side ‘B’ showed some reduction in strain recording at all elevations (1340 mm, 1840 mm, and 2340 mm).

In summary, all three loading scenarios confirmed that tensile strains on the GFRP surface consistently exceeded compressive strains. This trend is most likely due to the development of flexural cracks in the concrete and the resulting shift in stress distribution within the concrete core. A critical stress region was consistently identified between 840 mm and 2340 mm, corroborated by both GFRP and steel strain readings. Despite the presence of torsional moments in BRE and BLE loading, the tower mainly maintained a flexural response, with localized strain variations reflecting the influence of eccentricity. Importantly, all recorded strain levels stayed well below the failure threshold of the GFRP material, demonstrating that the GFRP tube maintained its structural integrity under all tested loading conditions. Furthermore, the strain readings in the hoop direction, measured on the GFRP surface along sides C and D remained close to zero throughout the test.

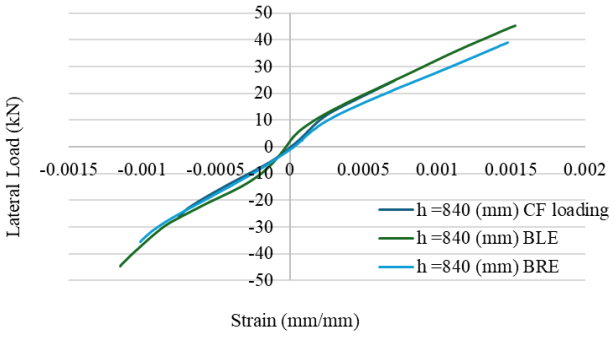

(a) Strain reading at a height of 840 (mm)

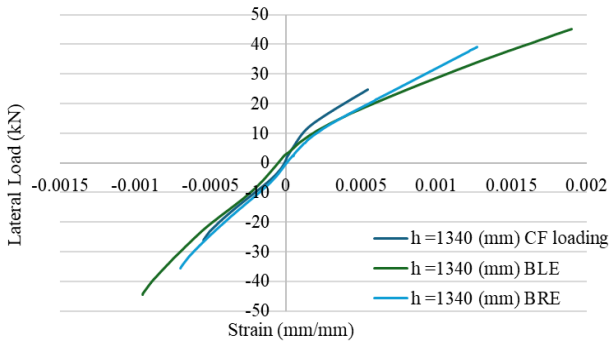

(b) Strain reading at a height of 1340 (mm)

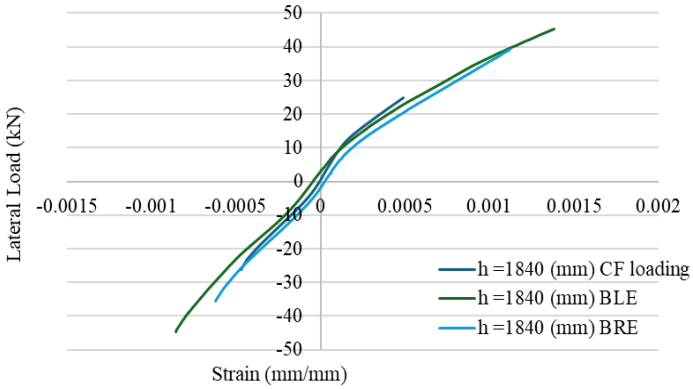

(c) Strain reading at a height of 1840 (mm)

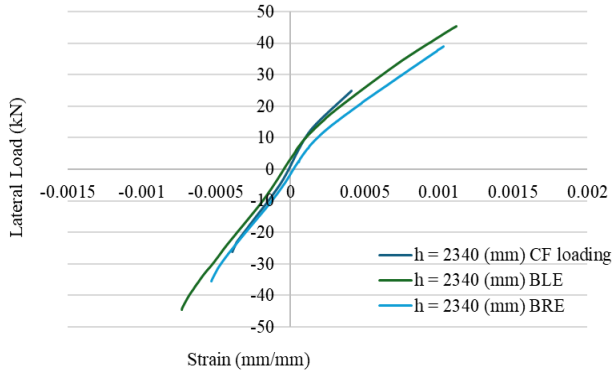

(d) Strain reading at a height of 2340 (mm)

Figure 6.8. Strain readings recorded on Side ‘A’ under both push and pull loading phases for concentric, big left and right eccentricity (559 mm) cyclic loading conditions.

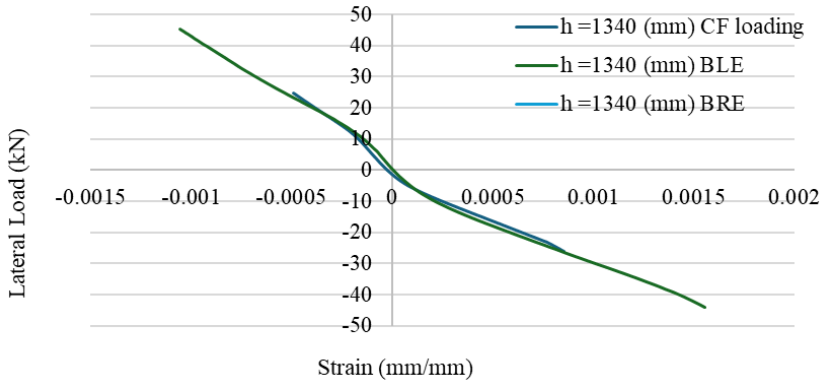

(a) Strain reading at a height of 1340 (mm)

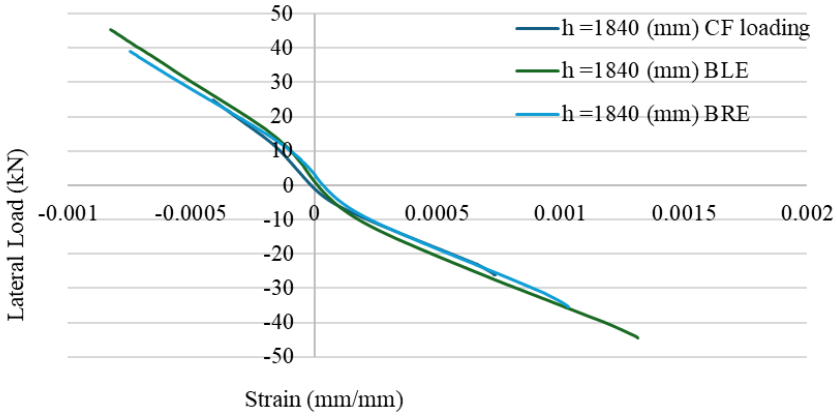

(b) Strain reading at a height of 1840 (mm)

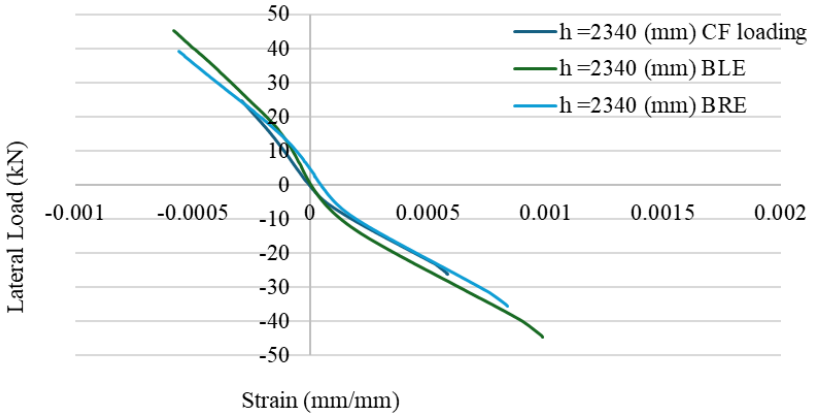

(c) Strain reading at a height of 2340 (mm)

Figure 6.9. Strain readings recorded on Side ‘B’ under both push and pull loading phases for concentric, small left eccentricity (279 mm), big left and right eccentricity (559 mm) cyclic loading conditions.

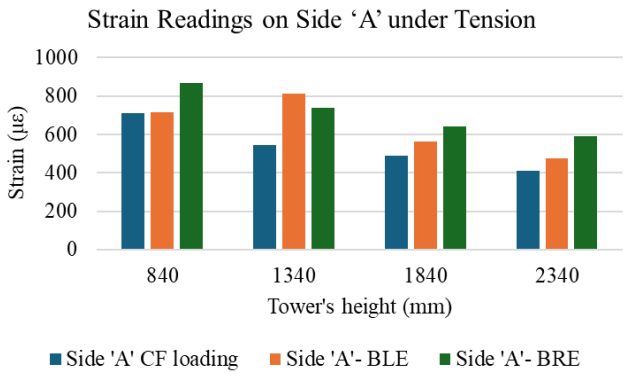

(e) Under pushing loading

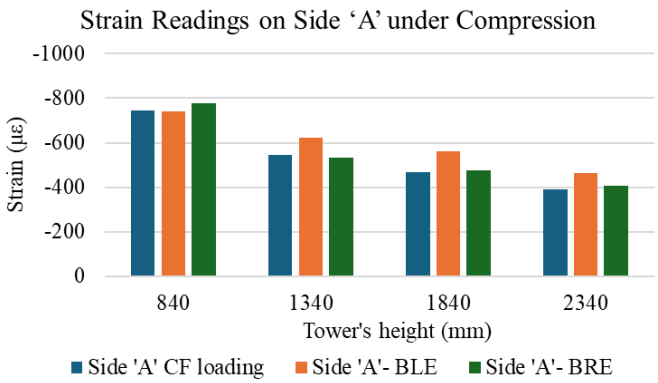

(f) Under pulling loading

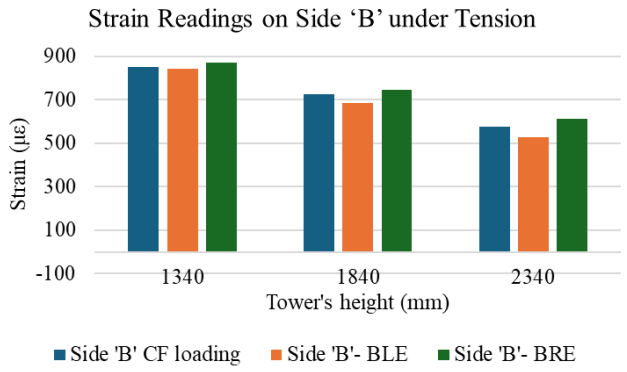

(g) Under pulling loading

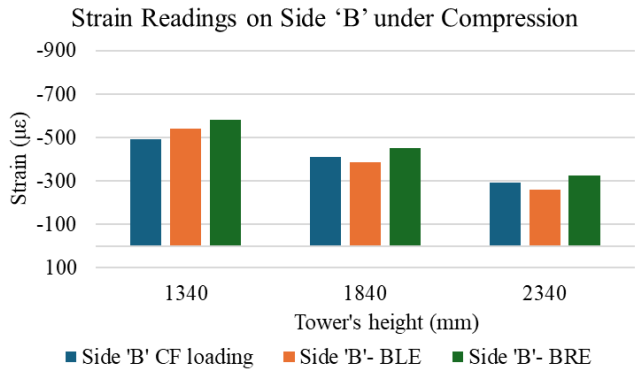

(h) Under pushing loading

Figure 6.10. Comparison of strain values on sides 'A' and 'B' under CF, BLE, and BRE cyclic loading conditions (+25 kN and -26 kN)

6.6. Test to failure: Combined Flexural-Torsional and Monotonic Loading Tests

The final monotonic testing of tower M4-2 was carried out in two phases: first under flexural-torsional eccentric loading, which did not induce failure within the stroke capacity of the hydraulic actuator, followed by reloading the tower under centric loading up to failure. Together, these tests provided a clear picture of how the tower performed under different critical loading conditions.

It was initially intended to apply BRE loading until the tower reached its ultimate flexural capacity and out-of-plane displacement. However, the tower did not show signs of failure even after the actuator reached its stroke limit when loaded at a large right eccentricity of 559 mm. Consequently,

the tower was unloaded after it reached a lateral load of approximately 143 kN with a displacement of 213 mm, as illustrated in Figure 6.11. Strain gauge data indicated that the steel reinforcing bars at the tension and compression sides near the top of the foundation block were yielded. The load corresponding to steel yielding was approximately 35 kN for rebar 'A' under tension and 88 kN for rebar 'B' under compression, both at a height of 700 mm, as illustrated in Figure 6.12. These values represent approximately 25% and 62% of the ultimate load, respectively. Peak strains were monitored on the GFRP surface at side 'A' (840 mm height) and side 'B' (1340 mm height), measuring 10562 με and -4626 με, respectively (Figure 6.13). Notably, all strain values remained below the GFRP failure threshold of 0.016, confirming the tower adequacy of the GFRP tube even under BRE loading to a peak of 143 kN. This behaviour confirms that the tensile strains exceeded the compressive ones due to the development of cracks in the concrete core, as expected. As the load approached its peak, cracking noises were heard, indicating localized bond failure between the concrete core and FRP tube and potential rupture of some fibres; however, there were no visible signs of rupture on the surface of the tube at this stage.

The second phase of testing involved reloading the tower monotonically until complete failure. The load–displacement curve was fairly linear up to approximately 40 kN (29 mm), followed by a slight decrease in stiffness up to the peak load (Figure 6.11). Failure was initiated by GFRP rupture on the tension side of the tower near the top of the foundation block at an applied load of 125 kN and a displacement of 231 mm. The recorded results align with those of the M4-1 tower, which reached a maximum load of 132 kN at a displacement of 267 mm. The initial failure of M4-2 marked a critical point in the structural response, leading to a noticeable change in behaviour.

Importantly, the sequence of testing played a significant role in shaping this response. Since the BRE loading was carried out first, the tower had already experienced reinforcement yielding, cracking of the concrete core, and debonding between the GFRP tube and concrete (as evidenced by rebar and GFRP strain readings), and likely damage to the FRP tube (although not visibly apparent). When the second monotonic test was conducted, the tower was no longer in its original condition but instead carried residual inelastic damage from the first phase. As a result, the monotonic curve reflects the residual capacity of a previously damaged specimen. This sequence

effect explains why the monotonic test reached a slightly lower peak load (125 kN) but achieved a similar deflection, along with a more noticeable reduction in stiffness.

Strain gauge data suggests that the steel reinforcing bars at the tension and compression sides near the top of the foundation block yielded prior to FRP rupture. After a significant drop in load readings was observed, the test was stopped for safety considerations. The ultimate displacement reached was 238 mm, corresponding to a reduced load of 80 kN, indicating a 36% drop from the peak load.

The strain behaviour of internal steel reinforcement bars are shown in Figure 6.14. The results highlight the tensile and compressive strain patterns observed in reinforcing bars ‘A’ and ‘B’. Notably, the strain response of reinforcing bar ‘A’ in this test differs from the behaviour observed in tower M4-1 as yielding initiated at a lower load, further supporting that the earlier BRE loading had already pushed the bars into inelastic ranges before the monotonic test began. In the previous test, both reinforcing bars ‘A’ and ‘B’ exceeded their yield thresholds at all measured heights, indicating the development of inelastic behaviour throughout the critical zone of the tower (700 mm to 2450 mm).

The strain patterns (Figure 6.14) highlighted differences in reinforcing bar response compared to tower M4-2 first phase, most likely because the earlier eccentric test had already pushed the reinforcing bars into inelastic behaviour within the critical zone between 700 mm and 2450 mm. Maximum FRP strains during monotonic loading were recorded at 1340 mm: -5946 με in compression and 9956 με in tension (Figure 6.15). The strain at failure was lower than the strain capacity measured during coupon tests, which may indicate that higher strains developed between the strain gauge locations. The longitudinal strain profiles along the GFRP surface (Figure 6.16) clearly showed differences between tension and compression zones, with stress concentrations developing around areas of concrete cracking.

Overall, the brittle failure of M4-2 was strongly influenced by the testing sequence; first being loaded eccentrically to near failure and then reloaded concentrically, as well as the accumulated inelastic damage in both steel and concrete. Despite this, the tower maintained a stable load–deflection response up to rupture. Its flexural rigidity at a height 840 mm was calculated at 16.9

N·m², which is very close to the 18.2 N·m² observed for M4-1. The critical zone extended from the base to approximately 1350 mm, marking the transition from elastic to inelastic behaviour and defining the key zone of structural response under both eccentric and monotonic loading.

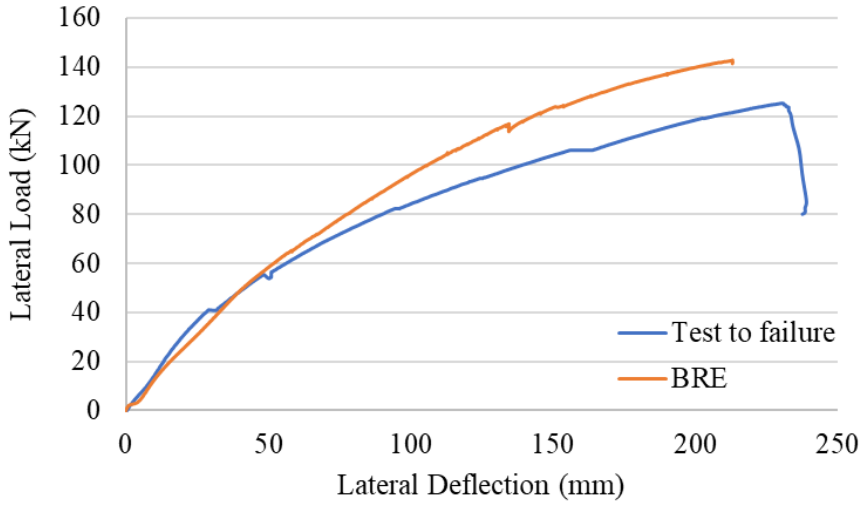

Figure 6.11. Lateral load verses lateral drift response of tower M4-2 under large eccentric loading and test to failure

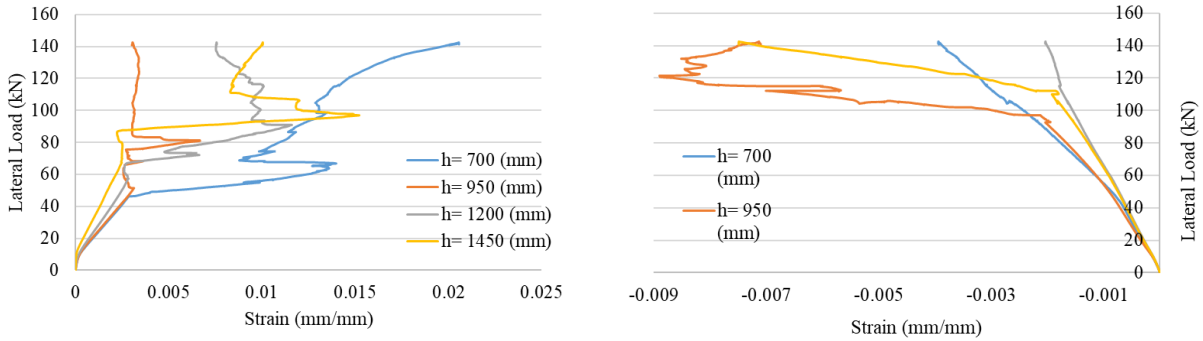

(a) Strain reading on rebar 'A'

(b) Strain reading on rebar 'B'

Figure 6.12. Lateral load vs longitudinal strain response of tower M4_2 under BRE loading, with the peak load reaching 143 kN.

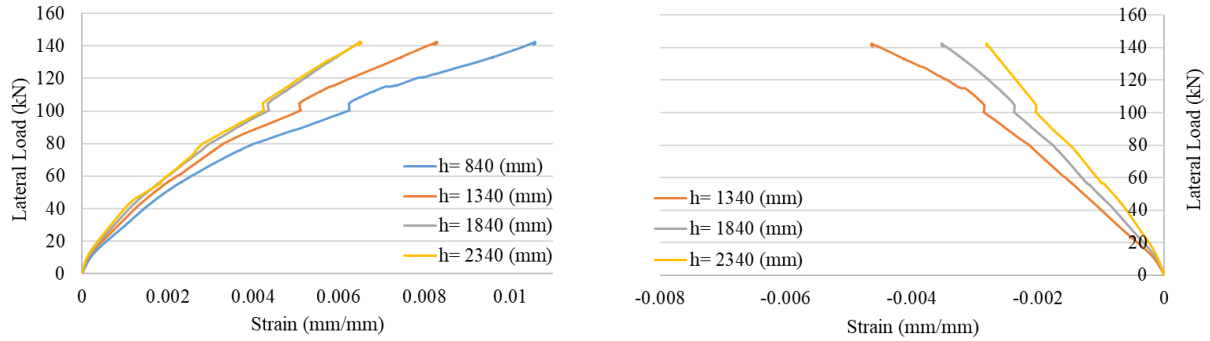

(a) Strain reading on side 'A' (b) Strain reading on side 'B'

Figure 6.13. Strain readings recorded on the GFRP surface under BRE loading, with the peak load reaching 143 kN.

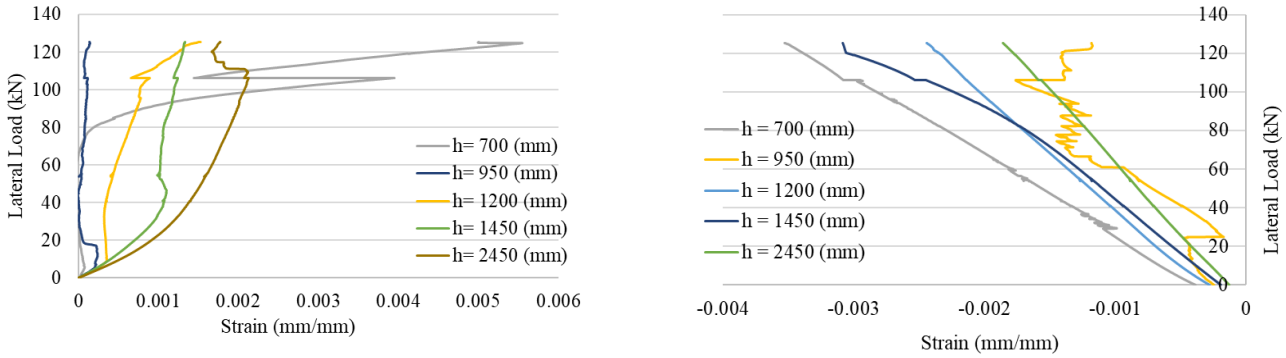

(a) Strain reading on rebar 'A' (b) Strain reading on rebar 'B'

Figure 6.14. Lateral load vs longitudinal strain curves under monotonic loading to failure

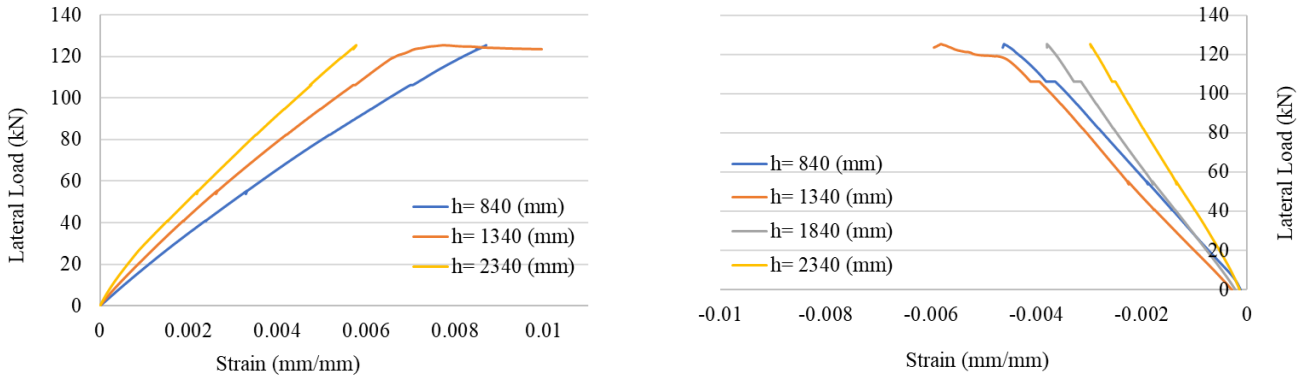

(a) Strain reading on side 'A' (b) Strain reading on side 'B'

Figure 6.15. Strain readings recorded on the GFRP surface under monotonic loading to failure

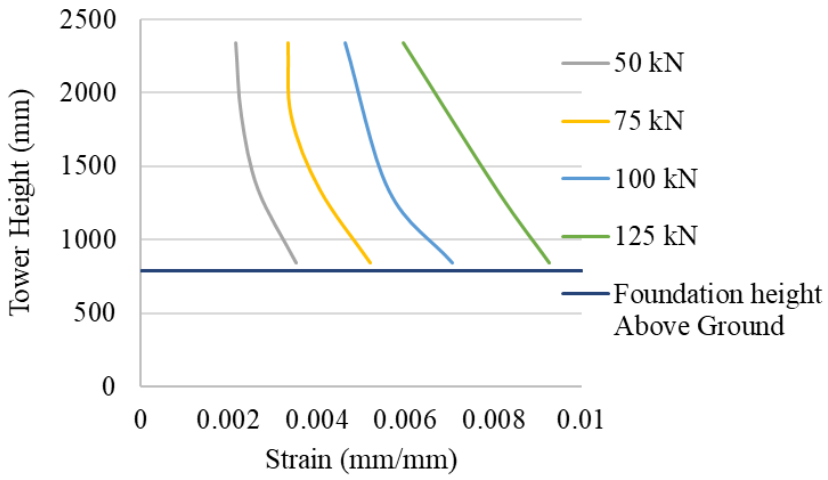

(a) GFRP tenson strain reading

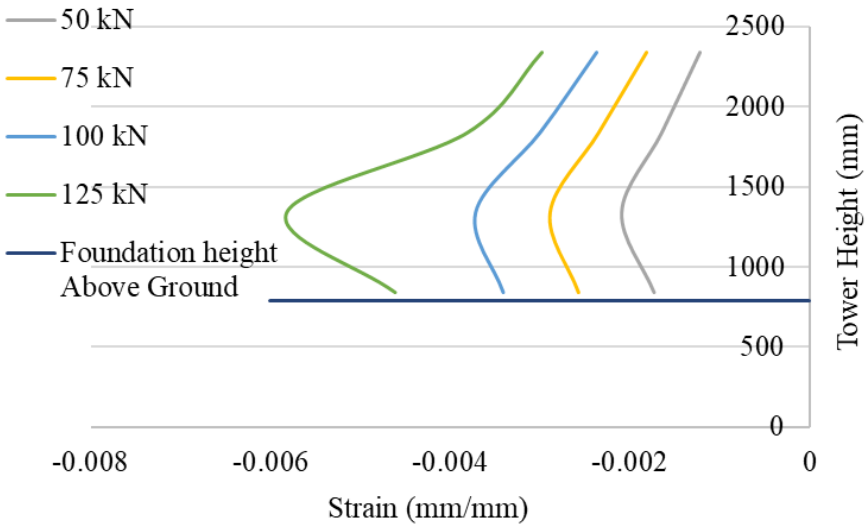

(b) GFRP compression strain reading

Figure 6.16. Comparison of GFRP strain readings at different tower heights under monotonic loading to failure.

Figure 6.17 shows the curvature distribution along the height of the tower at the peak load of 125 kN. Consistent with the discussion in Section 5.6, the GFRP tube exhibits higher curvature than the steel reinforcement due to the imperfect bonding. This behaviour explains the variations in curvature profiles along section of the tower.

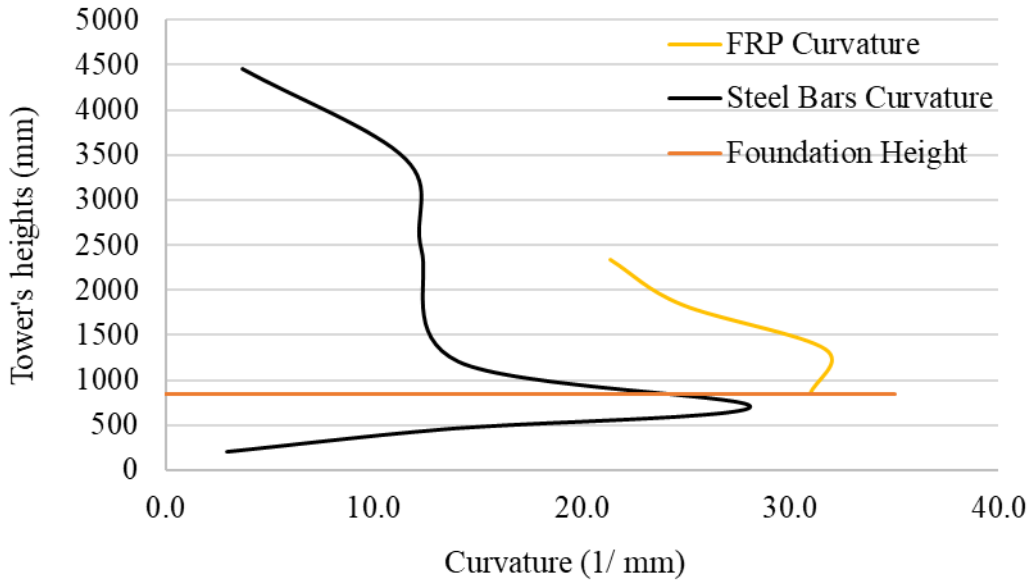

Figure 6.17. Tower's curvature vs tower's height at maximum failure load of 125 kN

The observed failure mode for the tower involved flexural rupture at a height of approximately 530 mm from the foundation. Photos of the tower after failure are shown in Figure 6.18.

(a) Tower at maximum lateral deflection

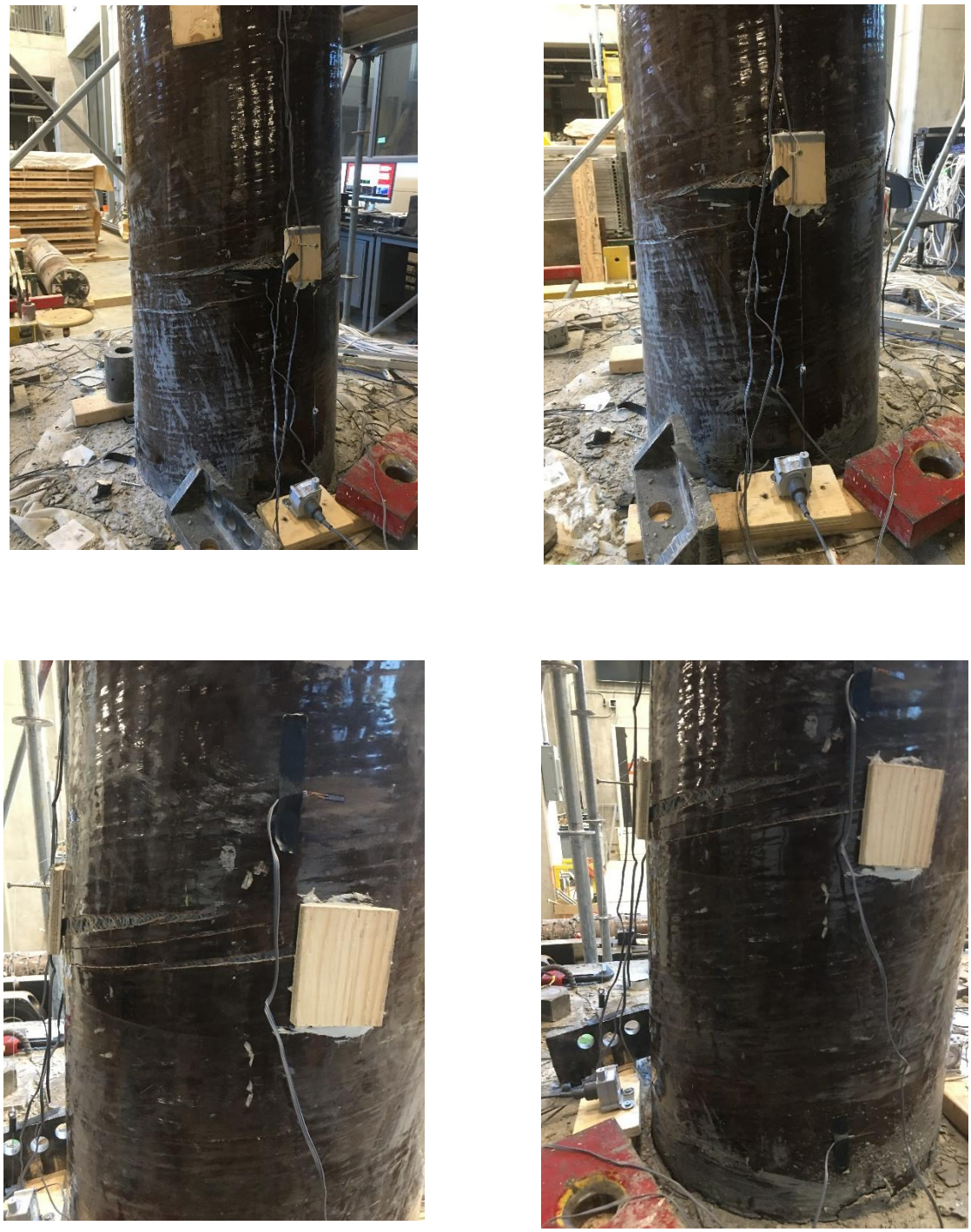

(b) GFRP rupture

Figure 6.18. Failure mode of tower specimen M4-2

Chapter 7 - Tower M5: Experimental results and analysis

7.1. Overview:

This chapter presents the detailed experimental results obtained from testing the M5 tower specimen, integrating both static and dynamic analyses. The research investigates vibration performance, centric and eccentric lateral load-deflection characteristics, and structural failure mechanisms. The results from the cyclic flexural testing under concentric loading (CL), as well as the cyclic flexural-torsional tests conducted with big left eccentricity (BLE) at 559 mm, and big right eccentricity (BRE) at 559 mm from the centroidal axis of the tower, are presented in a combined format to aid direct comparison among the three loading conditions.

Initially, the test plan included both large eccentricity cyclic loading tests (559 mm from the center) and small eccentricity cyclic tests (279 mm) on the tower. However, based on results from tower M4-1, which showed similar responses to left and right eccentric cyclic loading and identified centric loading as critical, the plan was revised. The smaller eccentric cyclic tests were omitted to focus on the large eccentricity cyclic loading. This adjustment ensured that the testing focused on more considerable eccentric loading scenarios while avoiding excessive redundancy in the test program.

The load–deflection behaviour, internal longitudinal reinforcement bar strain, and GFRP surface strain are discussed by grouping the data according to measurement height or location. This structured presentation was selected for clarity and offers a complete understanding of how varying eccentricities affect the structural response. Furthermore, the chapter includes a summary subsection that compares CL, BRE, and BLE loading scenarios for displacement behaviour, peak load capacity, steel and GFRP strain responses, and overall tower stability.

7.2. Stage 1: Free vibration test

The free vibration test aimed to evaluate the tower's dynamic characteristics, focusing on its fundamental period of vibration and damping ratio. The displacement vs time plot from the test is presented in Figure 7.1. The fundamental period of vibration (T_d), averaged over the first three

cycles, was approximately 0.176 seconds corresponding to a damped natural frequency of vibration of about 5.69 Hz for the free-standing tower (Table 7.1). Additionally, the average damping ratio ζ, determined by Equation 5.1 and 5.2 was found to be around 9%. This damping value likely results from the interaction between the concrete-filled GFRP tube, the foundation, and the prestressing system, all of which contribute to energy dissipation. Damping is important for structures because it determines how well they can absorb and dissipate energy during vibrations.

In wind turbine towers, high damping is especially crucial to reduce fatigue damage and ensure safety. The tower's vibration test results present a significant improvement in the damping ratio compared to the study conducted by Polyzois et al. (2009). This high damping ratio is a favourable characteristic because it signifies the tower's capability to effectively withstand wind-induced vibrations. The results of the vibration tests demonstrate that prestressed CFFT towers can possess good dynamic characteristics for wind turbine tower applications in remote areas. However, more research is needed to optimize the design of these towers and their dynamic characteristics to reduce the effects of wind-induced vibrations on the turbine and tower. Although the relatively high damping ratio implies good capacity to dissipate energy, reducing the risk of potential damage or failure, it is important to note that this result is for only one portion of an actual wind turbine tower and thus the overall dynamic characteristics of the installed system will be different in terms of both natural frequency and damping. Nevertheless, the relatively high damping ratio for this component bodes well for an actual CFFT wind turbine tower to have more damping than a tower constructed from components with less inherent damping.

Table 7.1. Damping values and frequency results of the tested tower

t_n #	Amplitudes x(t_n) (mm)	t_n (s)	Td (s)	Frequency (Hz)	$\zeta = (\delta/2\pi)$
0	29.9540	10.689			
1	19.0450	10.865	0.176	5.6818	0.072075
2	11.3030	11.043	0.178	5.6180	0.083037
3	5.5320	11.216	0.173	5.7803	0.113719

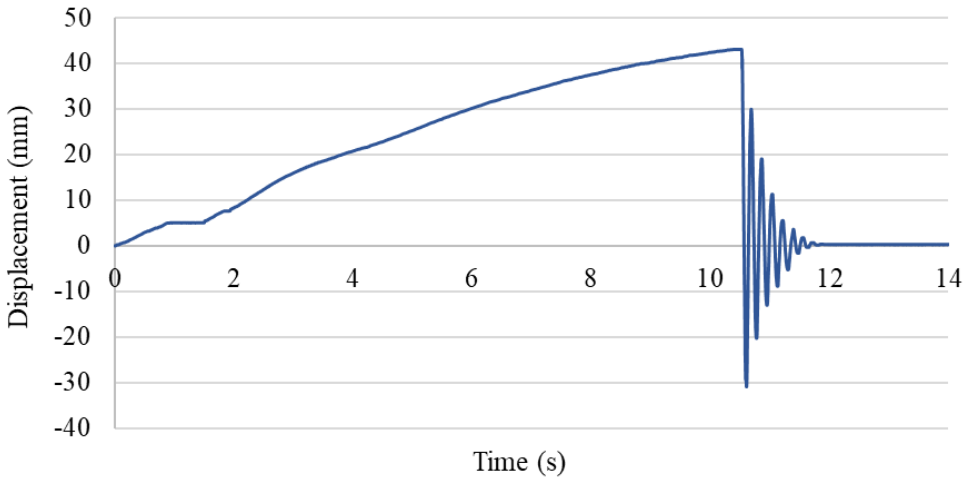

(a) Full test duration

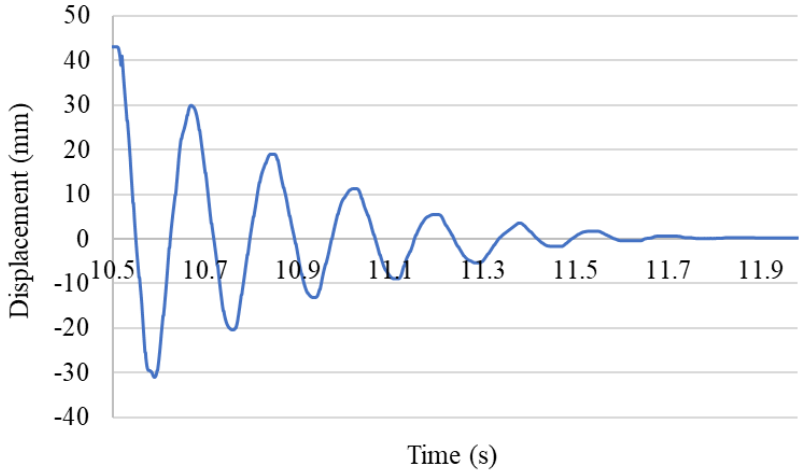

(b) Time segment from 10.5 s to 12 s

Figure 7.1. Tower M5 free vibration response

7.3. Combined load–deflection results

The load–deflection responses of the tower under all three cyclic loading configurations: CF, BRE, and BLE, are shown inFigure 7.2. The response for the CF loading was almost symmetrical under pushing (positive) loading and pulling (negative) loading, primarily displaying linear elastic behaviour with limited hysteresis at service load levels. The tower reached a maximum lateral load of 64 kN and -63 kN at approximately 82 mm in both directions, equivalent to about 1.4% of the tower height, which is close to the proposed service limit of 1.25% proposed by Nicholson (2011).

As expected, the observed response suggests that the tower maintains a stable performance and deforms elastically throughout the service range under repeated cyclic loading. The hysteresis loop formed by plotting lateral load versus lateral drift is fundamental for evaluating energy dissipation, stiffness degradation, and possible structural damage over multiple loading cycles. Importantly, the load drops in M5 were smaller than those observed in M4. This improvement can be attributed to the modified clamping system in M5, which was redesigned to match its geometry. A larger hole was cut to ensure a better fit, the epoxy likely sealed the edges more effectively, and the four bolts securing the clamp appeared to work more efficiently. These refinements contributed to help the tower sustain a more consistent slope in the load deflection curve and reduced the load drops that typically appeared when the loading direction reversed. Notably, no damage was observed during testing, confirming the tower's ability to withstand cyclic service loading without degradation.

For the BRE loading, with a 559 mm right-side eccentricity, the tower response was slightly unsymmetric under pushing (positive) loading and pulling (negative) loading, displaying mainly linear elastic behaviour with limited hysteresis. The tower reached a peak lateral cyclic load of +57 kN at a lateral displacement of 70 mm, equivalent to approximately 1.2% of its height. In comparison, a lateral load of -50 kN was recorded at a lateral displacement of -66 mm, reflecting the tower's response to loading in the opposite direction.

Generally, the response was similar to that observed under CF loading scenario. However, for similar applied lateral loads (57 kN and -50 kN), the average resulting displacements were slightly lower (70 mm vs 74 mm in CF loading, and -66 mm vs -70 mm).

When comparing the BLE and BRE cases under similar applied lateral loads (+53 kN and -50 kN), the resulting displacements were found to be comparable. For instance, under BRE loading, the tower exhibited displacements of approximately 65 mm and -66 mm, while during BLE loading, the recorded values were 68 mm and -65 mm.

The lateral load vs time response under cyclic loading conditions for all three tests is presented in Figure 7.3. Overall, the findings show that while the tower's response looks mostly elastic, the recorded strain shows that the steel reinforcement reached yielding under all cyclic loading test

scenarios. Although eccentricity caused slight changes in overall stiffness, the tower remained stable throughout testing with no visible signs of damage.

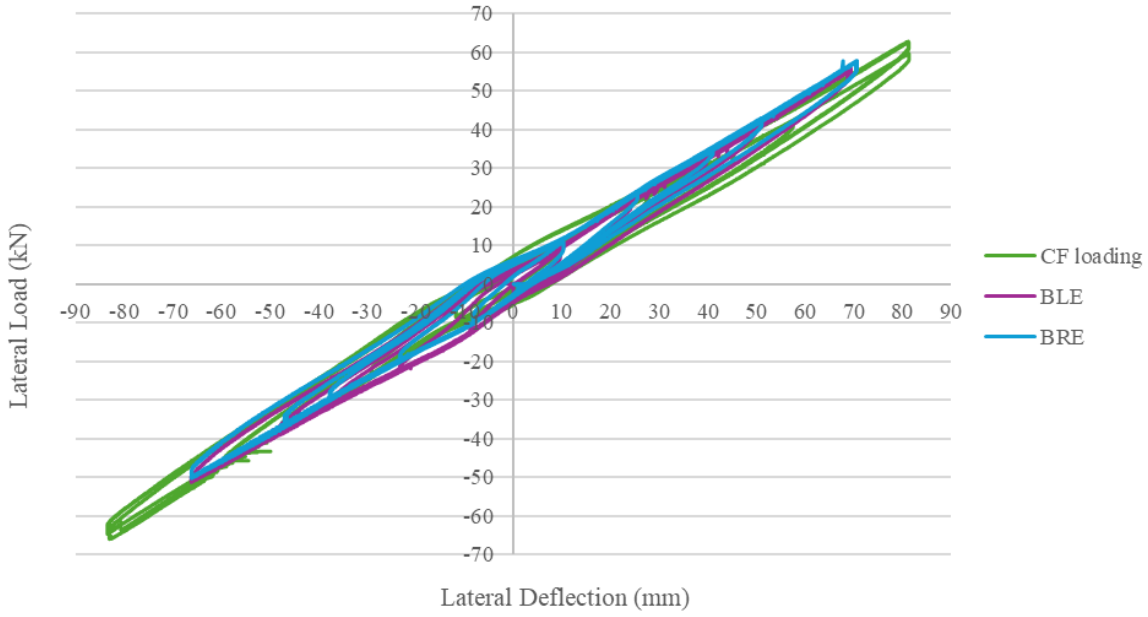

Figure 7.2. Lateral load–lateral drift response under concentric, and big right and left eccentric (± 559 mm) cyclic loading conditions

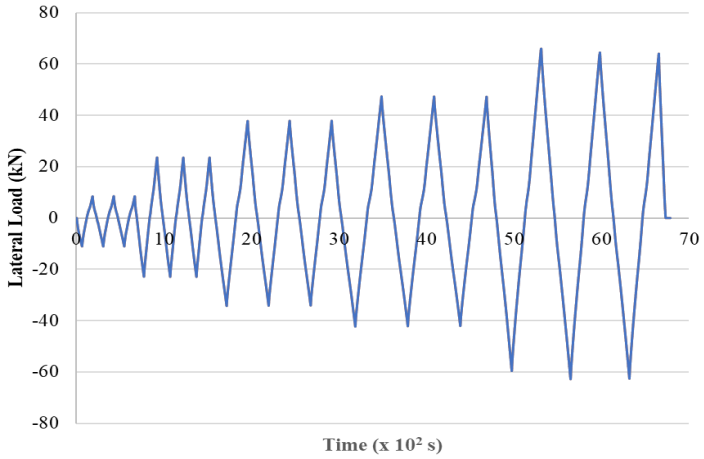

(a) CF loading

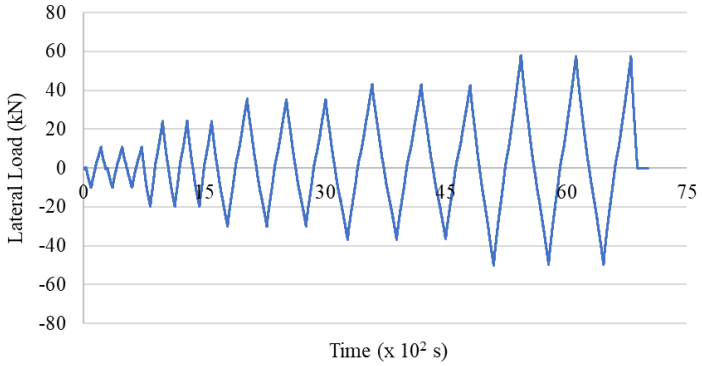

(b) BRE

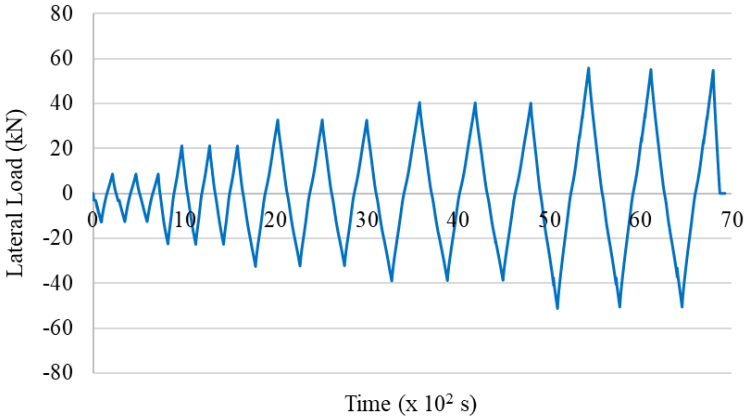

(c) BLE

Figure 7.3. Lateral load vs time response under (a) concentric, (b) big right eccentric (559 mm), and (C) big left eccentric (559 mm) cyclic loading conditions

7.4. Strain in internal longitudinal steel reinforcement bars

The strain behaviour of internal steel reinforcing bars during the final loading cycles of the tower under the three cyclic loading configurations: CF, BRE, and BLE, are shown in Figure 7.4 an Figure 7.5. The results highlight the alternating tensile and compressive strain patterns observed in reinforcing bars ‘A’ and ‘B’ under reversed loading directions. Specifically, reinforcing bar ‘A’ experienced tensile strain during pushing (positive) loading and compressive strain during pulling (negative) loading, while bar ‘B’ displayed the opposite behaviour. Importantly, reinforcing bar ‘A’ experienced tensile strains that exceeded the yield threshold across all cyclic service loading test scenarios, indicating the development of inelastic behaviour. Reinforcing bar ‘B’, however, seemed to be more localized and dependent on the load orientation and position.

7.4.1. Strain response in rebars ‘A’ and ‘B’ under concentric flexural (CF) loading

Under CF loading, the peak tensile strains occurred at 950 mm and 1200 mm above the tower base, with reinforcing bar ‘A’ reaching 3601 με and bar ‘B’ reaching 3259 με, respectively, during the final cycle. The maximum compressive strains were -738 με for bar ‘A’ at 950 mm and -863 με for bar ‘B’ at 1200 mm. These strain levels indicate that the region between 700 mm (top of foundation block) and 1450 mm experienced the most significant stress concentration, corresponding with the expected moment peak for cantilever behaviour.

Tensile strains in bars ‘A’ and ‘B’ were consistently greater than the corresponding compressive strains. This is primarily attributed to tensile cracking in the surrounding concrete, which reduces its capacity to resist tension and increases the demand on the steel reinforcement. Notably, the tensile strains in both bars exceeded the conventional yield strain of steel, with yielding observed at approximately 37 kN for bar ‘A’ and -50 kN for bar ‘B’, indicating the onset of plastic behaviour under cyclic loading.

7.4.2. Strain response in rebars ‘A’ and ‘B’ under big right eccentric (BRE) loading

The strain behaviour of the reinforcing bars under BRE loading shows a combination of flexural and torsional effects due to the imposed asymmetry. As illustrated in Figure 7.4, reinforcing bar

‘A’ experienced tensile strain during pushing (positive) loads and compressive strain under pulling (negative) loads, while reinforcing bar ‘B’ showed the inverse response, consistent with load reversal.

Throughout the test, both reinforcing bars experienced tensile strains that exceeded the yield threshold at some points under the maximum applied BRE loads, indicating the development of inelastic behaviour. The peak tensile strains were recorded at a height of 950 mm and 1200 mm near the upper edge of the foundation block, with bar ‘A’ reaching 2996 με and bar ‘B’ reaching 2308 με, respectively. In contrast, the maximum compressive strains were -616 με for bar ‘A’ at 950 mm and -649 με for bar ‘B’ at 1200 mm. These levels, although slightly lower in tension than those under CF loading, confirm the presence of inelastic deformation in both bars and demonstrate the critical interaction between flexural and torsional stress conditions. These findings suggest that the critical strain zone under BRE loading was concentrated between 700 mm and 1450 mm above the tower base, likely due to localized stress concentrations in this region.

When compared to CF loading under similar peak cyclic loading (53 kN pushing and -50 kN pulling), BRE loading induced slightly lower tensile strains in most cases, as illustrated in Figure 7.4. Reinforcing bar ‘A’, for instance, experienced lower strain at 700 mm, 950 mm, 1200 mm, and 1450 mm. Similarly, bar ‘B’ with the BRE loading recorded slightly lower tensile strains across most elevations under pulling loading, at 700 mm, 950 mm, and 1200 mm. At 1450 mm, however, the tensile strain was slightly higher in BRE (1498 με vs.1468 με in CF), suggesting localized moment redistribution due to torsion.

In terms of compressive strains, BRE loading produced more compression in lower sections of both reinforcing bars. Reinforcing bar ‘A’ experienced higher compression at 700 mm and 950 mm, while showing slightly lower values at 1200 mm and 1450 mm. Reinforcing bar ‘B’ followed a similar trend, with greater compression under BRE at 700 mm and 950 mm, and reduced values at 1200 mm and 1450 mm. The strain concentration under BRE loading was particularly concentrated between 950 mm and 1200 mm from the tower base. This region corresponds to where combined flexural and torsional moments are maximized due to the loading eccentricity. The cyclic loading likely contributed to progressive cracking and stiffness degradation in the

concrete. Although BRE loading did not produce the absolute maximum tensile strains observed in CF loading, the interaction of torsional and flexural effects along with the accumulation of damage led to more distributed strains along the tower.

7.4.3. Strain response in rebars ‘A’ and ‘B’ under big left eccentric (BLE) loading

In line with the patterns identified under BRE loading, the strain response of the reinforcement during BLE loading shows a combination of flexural and torsional effects due to the imposed asymmetry. As illustrated in Figure 7.4, reinforcing bar ‘A’ experienced tensile strain during pushing (positive) loading and compressive strain under pulling (negative) loading, while reinforcing bar ‘B’ developed the inverse behaviour, consistent with load reversal. Throughout the test, both reinforcing bars experienced tensile strains that exceeded the yield threshold at most points, revealing the development of inelastic behaviour.

The peak tensile strains were recorded at a height of 950 mm and 1200 mm near the upper surface of the foundation block, with reinforcing bar ‘A’ reaching 2953 με and reinforcing bar ‘B’ reaching 2420 με, respectively. In contrast, the maximum compressive strains were recorded as -616 με for reinforcing bar ‘A’ at 950 mm and -612 με for reinforcing bar ‘B’ at 1200 mm. These values, although slightly lower in tension than those under CF loading, confirm the inelastic deformation in both reinforcing bars.This is especially noticeable in the localized strain increase at certain heights which likely result from stress redistribution from eccentric loading. These findings suggest that the critical strain zone under BLE loading was concentrated between 700 mm and 1450 mm above the tower base (similar with what was observed in BRE loading), likely due to localized stress concentrations in this region.

Comparison between CF and BLE under equivalent peak loads (53 kN pushing and -51 kN pulling) shows perceptive trends (Figure 7.4). Compared to CF under equal peak loads, BLE loading induced slightly lower tensile strains in most cases for reinforcing bar ‘A’. However, at 1200 mm, BLE produced a slightly higher strain. For reinforcing bar ‘B’, BLE produced slightly higher tensile strains at 700 mm and 950 mm, but lower at 1200 mm and 1450 mm, again suggesting a localized redistribution of internal forces. When compared to BRE loading under the same cyclic amplitude, BLE induced slightly higher tensile strains in most locations, as illustrated in Figure

7.4. Reinforcing bar ‘A’ recorded a higher strain at 700 mm, 1200 mm, and 1450 mm. The only exception was observed at 950 mm, where BRE recorded a slightly higher value of 2996 με compared to 2953 με in BLE. Reinforcing bar ‘B’ similarly showed increased strain under BLE at 700 mm, 950 mm, and 1200 mm. BRE loading only showed a higher tensile value at 1450 mm. These differences, although relatively small, indicate that BLE loading imposed more tensile strain on reinforcement, particularly in the critical region, likely due to the effects of accumulated damage.

The compressive strain patterns give more insight into this difference in behaviour. Under BLE loading, reinforcing bar ‘A’ generally showed slightly lower compressive strains across most heights compared to CF. The only exception was at 950 mm where BLE loading recorded a slightly higher compressive strain compared to CF loading. For reinforcing bar ‘B’, BLE induced increased compression at the lower levels (700 mm and 950 mm) compared to CF loading, while at higher elevation (1200 mm and 1450 mm), compressive strains were lower compared to CF loading. The strain data suggests a redistribution of internal stresses due to the eccentric loads which caused some out-of-plane bending as well as twisting of the tower.

When compared with BRE, BLE again showed slightly lower compressive strains. Reinforcing bar ‘A’ recorded a lower strain at 700 mm, identical values at 950 mm, and slightly reduced compression at 1200 mm. Reinforcing bar ‘B’ showed very similar values at 700 mm, a slightly higher strain at 950 mm, and lower values at 1200 mm and 1450.

In summary, BLE loading generally induced a more tensile response in the reinforcement than BRE loading, which may also be related to asymmetric rigidity of the test setup caused by loose bolts in the clamping and foundation systems. The shift in peak strain locations and slight reduction in compressive strain levels show a torsional redistribution of internal forces, with the critical region for plastic hinge remaining concentrated between 700 mm and 1450 mm.

Nevertheless, comparing the strain data in Figure 7.6, the overall differences in strain behaviour were not significant.

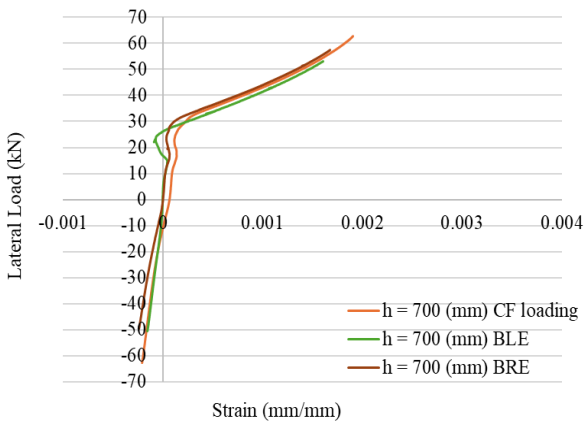

(a) Strain reading on rebar 'A' at 700 (mm)

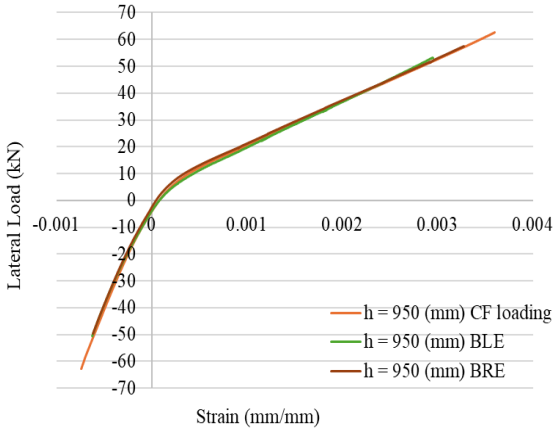

(b) Strain reading on rebar 'A' at 950 (mm)

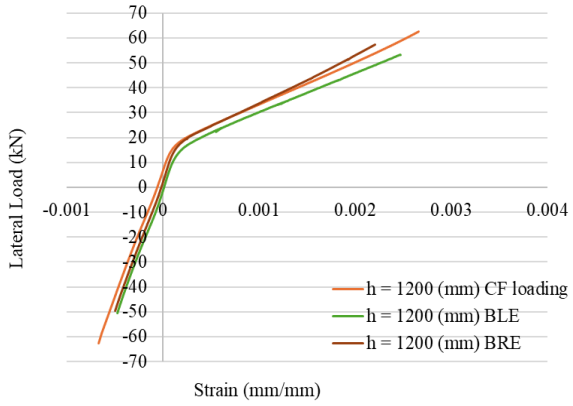

(c) Strain reading on rebar 'A' at 1200 (mm)

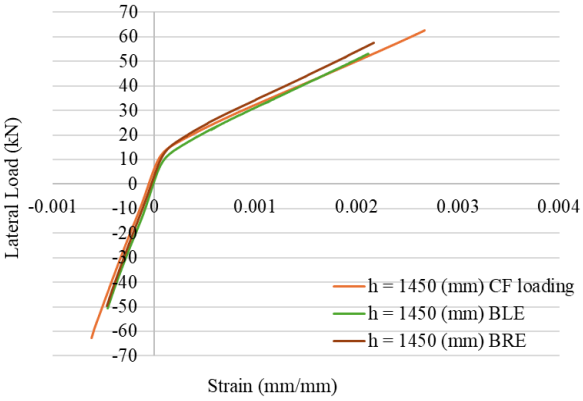

(d) Strain reading on rebar 'A' at 1450 (mm)

Figure 7.4. Strain readings recorded on reinforcing bar 'A' under both push and pull loading phases for concentric, and big left and right eccentricity (559 mm) cyclic loading conditions.

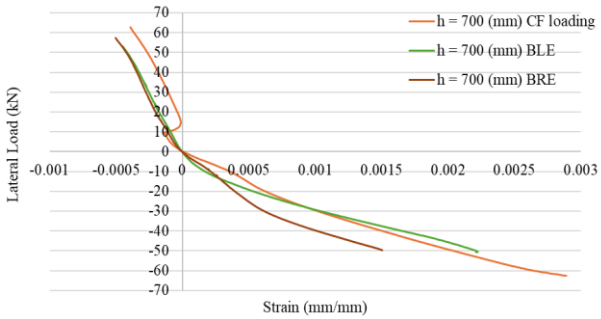

(a) Strain reading on rebar 'B' at 700 (mm)

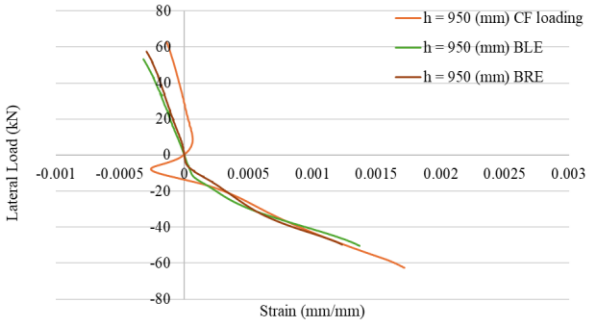

(b) Strain reading on rebar 'B' at 950 (mm)

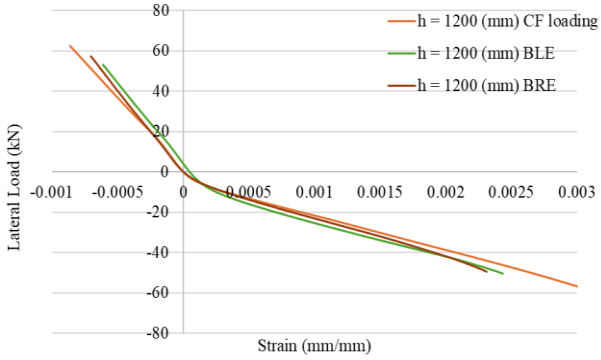

(c) Strain reading on rebar 'B' at 1200 (mm)

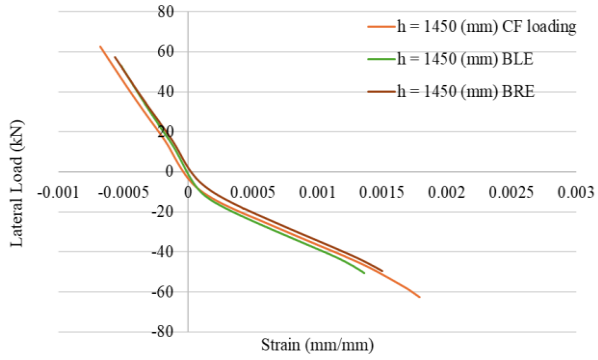

(d) Strain reading on rebar 'B' at 1450 (mm)

Figure 7.5. Strain readings recorded on reinforcing bar 'B' under both push and pull loading phases for concentric, and big left and right eccentricity (559 mm) cyclic loading conditions.

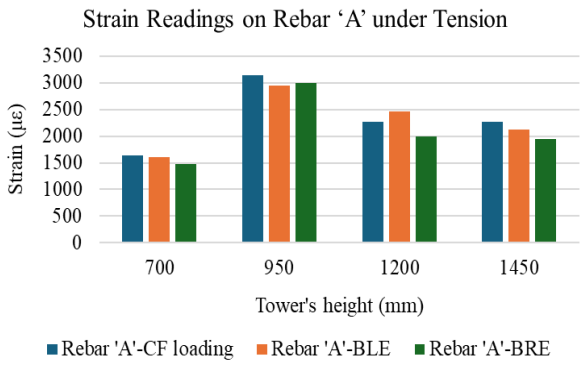

(a) Under pushing loading

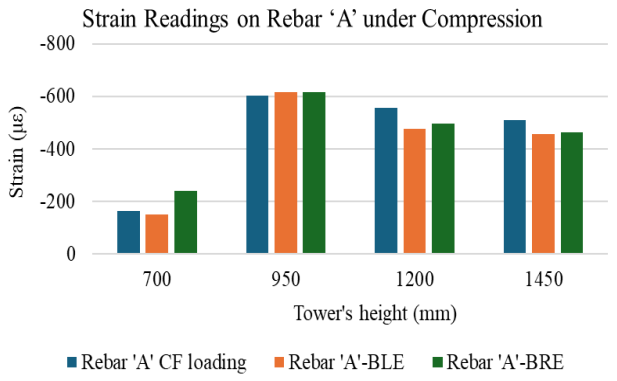

(b) Under pulling loading

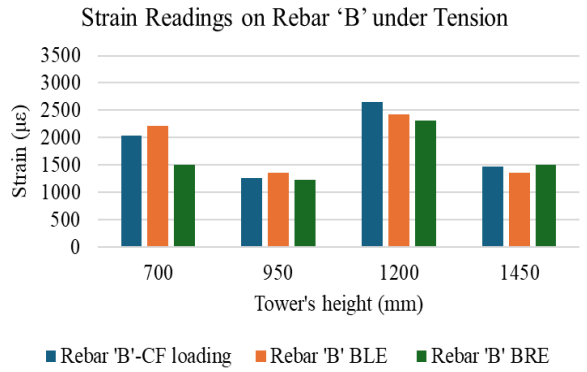

(c) Under pulling loading

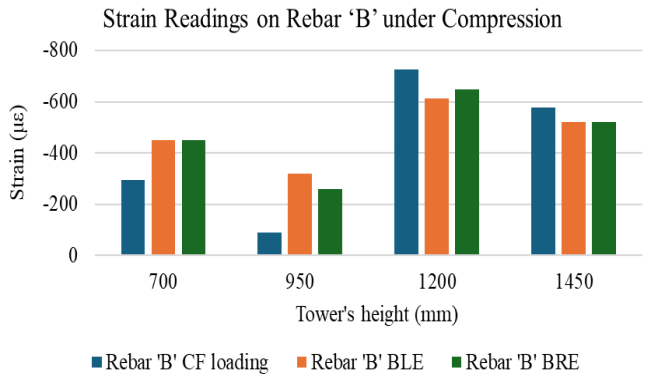

(d) Under pushing loading

Figure 7.6. Comparison of rebar strain values rebars 'A' and 'B' under CF loading, BLE, and BRE cyclic loading conditions

7.4.4. Strain response in rebars 'C' and 'D' under concentric flexural (CF) loading

Furthermore, Figure 7.7 presents the strain responses of steel reinforcing bars 'C' and 'D', where strain gauges were installed in an alternating pattern between the two neutral axis bars—bar 'C' on the left side and bar 'D' on the right side of the tower. These responses were recorded under both pushing (positive) and pulling (negative) phases of CF cyclic loading. Under pushing loading, reinforcing bar 'C' recorded strain values of 1974 με at 700 mm and 1281 με at 1200 mm, while reinforcing bar 'D' showed peak values of 1177 με at 950 mm and 667 με at 1450 mm. During the

pulling phase, bar ‘C’ measured 1553 με at 700 mm and 1070 με at 1450 mm, while bar ‘D’ recorded 2135 με at 950 mm and 1022 με at 1450 mm. Notably, throughout both loading directions, all recorded strains remained tensile (positive), which aligns with analytical predictions indicating a shift of the neutral axis due to concrete cracking and progressive stiffness degradation.

All recorded strains remained positive during the final full load cycle, indicating consistent tensile behaviour, which is expected for cracked concrete sections. This consistent tensile response can be attributed to the shift of the neutral axis caused by cracking on the tension side. Some minor asymmetries between reinforcing bars ‘C’ and ‘D’ were observed and are likely due to small differences in prestress levels of the four tendons.

During construction, prestressing losses could not be uniformly controlled across all tendons, leading to non-uniform initial stress states in individual bars. These local variations influence how forces are distributed across the section, leading to the observed strain differences. The fact that tensile strains persisted in both reinforcing bars confirms that the neutral axis was consistently nearer to the compression face of the tower. Despite these small inconsistencies, the recorded strain levels between 700 mm and 1450 mm highlight a concentration of flexural demand in this zone, reinforcing its classification as a critical flexural region in the tower.

7.4.5. Strain response in rebars ‘C’ and ‘D’ under big right eccentric (BRE) loading

Under BRE loading, the strain responses in reinforcing bars ‘C’ and ‘D’ again showed directional asymmetry due to the applied eccentricity. As shown in Figure 7.7, reinforcing bar ‘C’ recorded peak strains of 1893 με at 700 mm and 1135 με at 1200 mm during the pushing phase. Reinforcing bar ‘D’ showed lower strain values under pushing loads: 795 με at 950 mm and 446 με at 1450 mm. In contrast, under pulling conditions, bar ‘C’ displayed a reduced response, with 886 με at 700 mm and 546 με at 1200 mm, while bar ‘D’ showed higher strain values of 1635 με at 950 mm and 770 με at 1200 mm.

A comparative analysis between BRE and CF loading scenarios shows several important trends. Under pushing loads, BRE generally induced slightly higher tensile strains in reinforcing bar ‘C’, particularly at the 700 mm elevation (1694 με in BRE vs.1548 με in CF) and at 1200 mm (1012

με vs.1004 με). However, during pulling loading, the strain values in bar 'C' under BRE were notably lower: 886 με at 700 mm compared to 1313 με in CF, and 546 με vs.876 με at 1200 mm indicating an asymmetric redistribution of strain likely influenced by torsional coupling. Reinforcing bar 'D' followed a similar but inverted trend. Under pushing loads, it recorded lower strains in BRE compared to CF: 700 με vs.927 με at 950 mm, and 385 με vs.508 με at 1450 mm. During pulling, BRE again produced slightly reduced strains relative to CF at both 950 mm (1635 με vs.1766 με) and 1450 mm (770 με vs.844 με). These differences suggest that while BRE generated higher strain levels on the side of the tower subjected to eccentric flexure (reinforcing bar 'C'), the opposing side (reinforcing bar 'D') experienced reduced strain due to the different stress distribution. Overall, despite these variations, both reinforcing bars continued to experience tensile strain across all locations and phases, reinforcing the conclusion that the neutral axis stayed well above mid-height of the section during the entire load cycle.

7.4.6. Strain response in rebars 'C' and 'D' under big left eccentric (BLE) loading

Figure 7.7 illustrates the strain response of reinforcing bars 'C' and 'D' under BLE loading, where the applied torsion was in the opposite direction compared to BRE. During the pushing phase, bar 'C' showed peak strains of 1631 με at 700 mm and 1193 με at 1200 mm, while bar 'D' reached 1066 με at 950 mm and 586 με at 1450 mm. Under pulling loads, bar 'C' again showed a reduction in strain levels (1141 με at 700 mm and 829 με at 1200 mm), while bar 'D' exhibited a significant increase, peaking at 1625 με at 950 mm and 826 με at 1200 mm.

When compared with CF loading, BLE induced slightly higher tensile strains for bar 'C' during pushing: 1631 με at 700 mm and 1193 με at 1200 mm versus 1548 με and 1004 με in CF, respectively. However, under pulling, the BLE values dropped below those noted in CF: 1136 με at 700 mm and 826 με at 1200 mm versus 1313 με and 876 με, respectively. Reinforcing bar 'D' also displayed slightly lower strains in BLE compared to CF under pulling: 1617 με at 950 mm and 822 με at 1450 mm versus 1766 με and 844 με in CF. A direct comparison between BLE and BRE under identical cyclic loading levels further highlights the effect of eccentricity direction. In pushing, both reinforcing bars 'C' and 'D' recorded lower strains in BLE. Bar 'C' recorded 1631 με vs.1694 με in BRE, while bar 'D' showed a value of 1066 με vs.700 με. Under pulling, the roles

reversed, bar ‘C’ in BLE recorded slightly higher strain than in BRE (1136 με vs.886 με), while bar ‘D’ showed a near-equivalent response (1617 με in BLE vs.1635 με in BRE).

Overall, the comparative analysis confirms that both BRE and BLE produce asymmetric strain patterns due to the interaction of torsion with flexure loading. While the strain magnitudes differ slightly depending on the direction of eccentricity, the overall response in both reinforcing bars remained tensile across all measurement points. This reinforces the conclusion that the neutral axis had shifted above mid-height due to tension cracking and confirms that flexural behaviour remained the dominant response mode in the tower under cyclic eccentric loading.

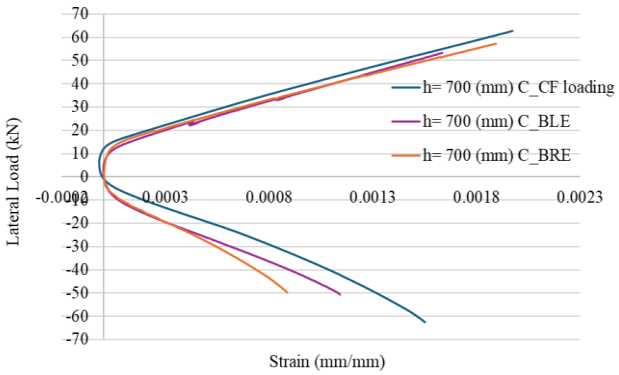

(a) Strain readings recorded on rebars 'C' at 700 (mm)

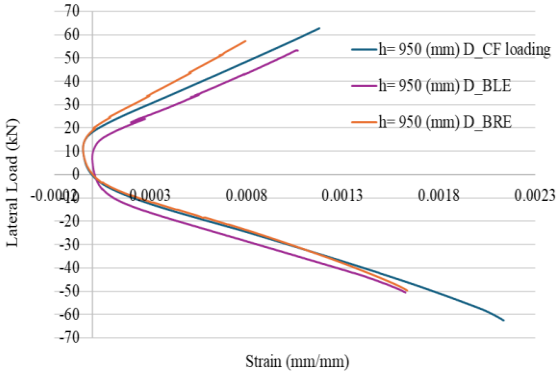

(b) Strain readings recorded on rebars ‘D’ at 950 (mm)

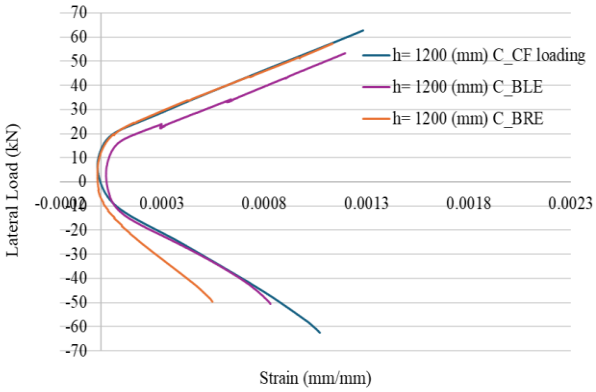

(c) Strain readings recorded on rebars 'C' at 1200 (mm)

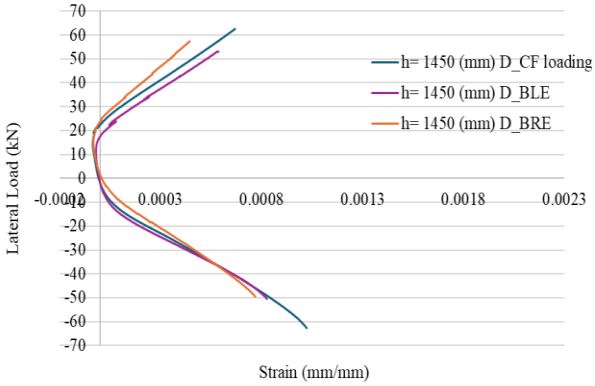

(d) Strain readings recorded on rebars ‘D’ at 1450 (mm)

Figure 7.7. Strain readings recorded on rebars 'C' and ‘D’ under both push and pull loading phases for concentric, big left and right eccentricity (559 mm) cyclic loading conditions

7.5. GFRP surface strain response under cyclic loading

This section presents the surface strain response of the GFRP during the final load cycles of all three cyclic loading cases: CF, BRE, and BLE. Figure 7.8 and Figure 7.9 display the strain data for sides ‘A’ and ‘B’, respectively, which experienced tension and compression depending on the direction of the applied load.

7.5.1. Strain response in sides ‘A’ and ‘B’ under concentric flexural (CF) loading

Under CF loading, the strain profiles indicate asymmetrical cyclic behaviour which does not fully align with the recorded load vs. top deflection response. Peak tensile strains were monitored on sides ‘A’ at a height of 840 mm and side ‘B’ at 1340 mm, measuring 1712 με and 1908 με, respectively. In contrast, maximum compressive strains were -1617 με on side ‘A’ and -1419 με on side ‘B’ both at the height of 840 mm. This behaviour confirms that the tensile strains exceeded the compressive ones, likely due to the development of cracks in the concrete core, which lowered its compressive resistance. A critical concentration of strain was consistently observed between 840 mm and 1340 mm, identifying this zone as a critical stress region in the tower. Notably, the recorded strain from the GFRP surface in this zone aligns with the peak strain zone identified in steel reinforcement strain data for reinforcing bars ‘A’ and ‘B’, even though the exact strain gauge positions differed slightly. The convergence of both GFRP and steel strain readings in this region clearly confirms the recognition of this zone as the critical region for stress development during cyclic loading. Furthermore, the strain readings in the hoop direction, measured on the GFRP surface along sides C (left side of the tower) and D (right side), remained close to zero throughout the test.

7.5.2. Strain response in sides ‘A’ and ‘B’ under big right eccentric (BRE) loading

The BRE loading configuration showed a strain response trend consistent with previous CF loading cases, but with slight differences due to the torsional component directed toward the right side of the tower cross-section. Under pushing (positive) loading, side ‘A’ experienced tensile strain while side ‘B’ was in compression. At 1340 mm, peak tensile strains were measured as 1560 με on side ‘A’ and 1461 με on side ‘B’ which aligns with the observations from the steel reinforcing

bars as the peak tensile strain on bar ‘A’ was higher than the recorded strain on bar ‘B’, while compressive strains reached -1208 με on side ‘A’ and -1323 με on side ‘B’ both at 840 mm. Just like in the CF loading test, tensile strains were consistently higher than compressive strains, and all values remained below the GFRP failure threshold of 0.016, confirming the tower adequacy of the GFRP tube even under BRE. Notably, the tensile strain on side ‘A’ was slightly higher than side ‘B’, showing a consistent pattern with previous observations.

When compared to CF loading at similar peak forces (53 kN and -50 kN), BRE loading produced very similar tensile and compressive strains along sides ‘A’ and ‘B’ from the height of 700 mm to 1450 mm (Figure 7.10). For side ‘A’ under pushing (tensile) loads, BRE showed slightly lower tensile strains, such as at 840 mm and 1840 mm, while showing a slightly higher value at 1340 mm (1360 με vs.1337 με in CF) indicating a redistribution of internal stress. Similarly, side ‘B’ produced slightly lower compressive strains under pushing (compressive) loads, such as at 840 mm, 1340 mm, and 1840 mm. Furthermore, under pulling (tensile) conditions, the strain decreased at 840 mm, 1340 mm, 1840 mm, and at 2340 mm.

Overall, these results show that while BRE loading introduced some asymmetry because of the torsional effect, the tower's strain response continued to be dominated by flexural behaviour. The shifts in strain were comparatively small and limited to specific areas, reinforcing the tower’s ability to handle complex cyclic loading without showing any major signs of distress or deterioration.

7.5.3. Strain response in sides ‘A’ and ‘B’ under big left eccentric (BLE) loading

The strain behaviour under BLE loading showed a similar trend to CF, but with minor notable differences occurring from the added torsional component. When the tower was subjected to pushing (positive) loading, side ‘A’ experienced tensile strains while side ‘B’ was in compression. Conversely, under pulling (negative) loading, side ‘A’ experienced compression and side ‘B’ experienced tension. Strain magnitudes were higher in tension than in compression, with no recording indicating strain levels approaching the failure strain observed in coupon tests (0.016). This absence of high strain magnitudes and any visible surface cracking confirm the integrity of the GFRP tube under the maximum BLE loading. Peak tensile strains were recorded with 1490 με

on side ‘A’ at 840 mm, and 1315 με on side ‘B’ at 1340 mm. The maximum compressive strains reached -1258 με on side ‘A’ and -1277 με on side ‘B’, also within the critical vertical region at 840 mm. When compared to CF loading at similar peak forces (53 kN and -50 kN), BLE loading produced slightly higher tensile strains alongside ‘A’ at the height from 700 mm to 1450 mm, while compressive strains on the same side were slightly reduced. For side ‘A’ under pushing (tensile) loads, strain values were showing higher values at 840 mm, 1340 mm, 1840 mm, and 2340 mm. During pulling (compressive) loading, side ‘A’ recorded lower value at 840 mm, 1340 mm, 1840 mm, and 2340 mm. For side ‘B’ the pattern slightly changed. During pushing (compressive) loads, the BLE test consistently produced higher compressive strains than CF, specifically at 840 mm, 1340 mm, 1840 mm, and at 2340 mm. However, under pulling (tensile) loading, side ‘B’ showed some reduction in strain recording at 840 mm, 1340 mm, 1840 mm, and 2340 mm.

In summary, the strain responses under BLE loading confirmed the flexural behaviour of the tower even with torsional effects. The slight differences in strain magnitudes between sides ‘A’ and ‘B’ highlight the sensitivity to eccentricity. Furthermore, all the measured strains remained safely below the material limits, indicating the GFRP tube’s effectiveness in maintaining structural integrity under these complex loading conditions. Furthermore, the strain readings in the hoop direction, measured on the GFRP surface along sides C and D, remained close to zero throughout the test.

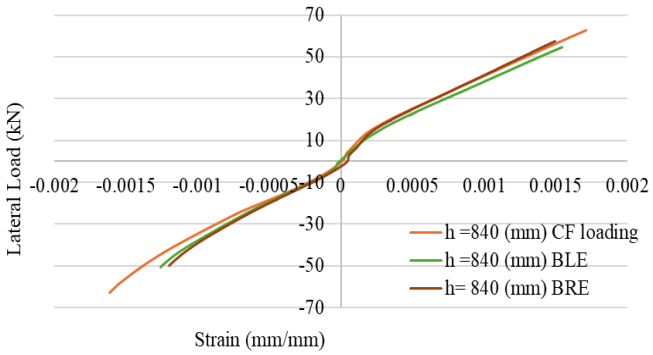

(e) Strain reading at a height of 840 (mm)

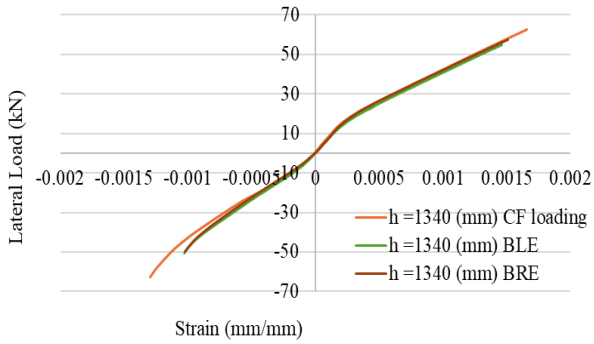

(f) Strain reading at a height of 1340 (mm)

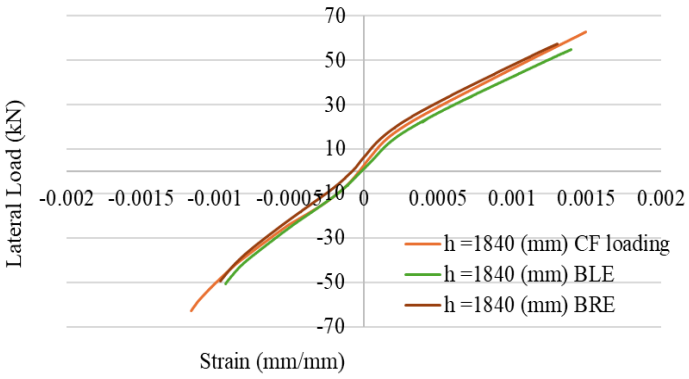

(g) Strain reading at a height of 1840 (mm)

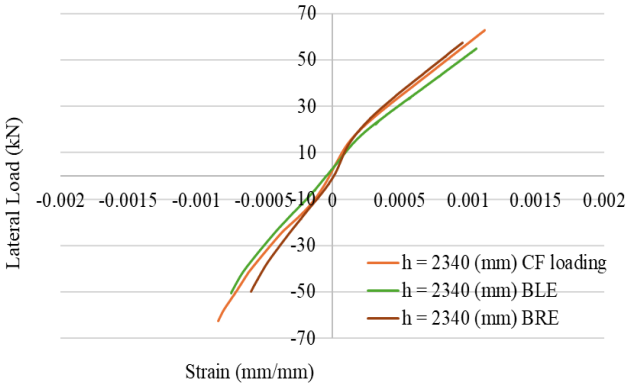

(h) Strain reading at a height of 2340 (mm)

Figure 7.8. Strain readings recorded on Side 'A' under both push and pull loading phases for concentric, big left and right eccentricity (559 mm) cyclic loading conditions.

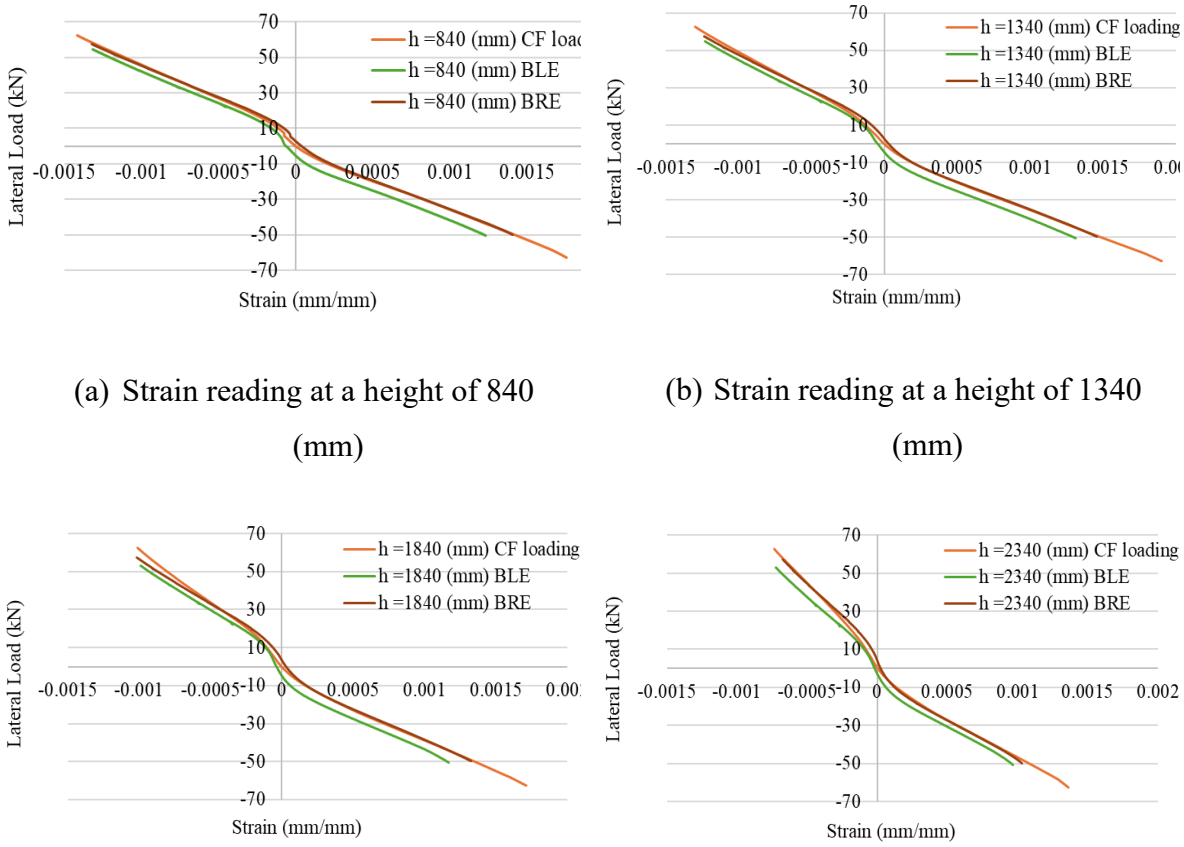

(a) Strain reading at a height of 840 (mm)

(b) Strain reading at a height of 1340 (mm)

(c) Strain reading at a height of 1840 (mm)

(d) Strain reading at a height of 2340 (mm)

Figure 7.9. Strain readings recorded on Side 'B' under both push and pull loading phases for concentric, small left eccentricity (279 mm), big left and right eccentricity (559 mm) cyclic loading conditions.

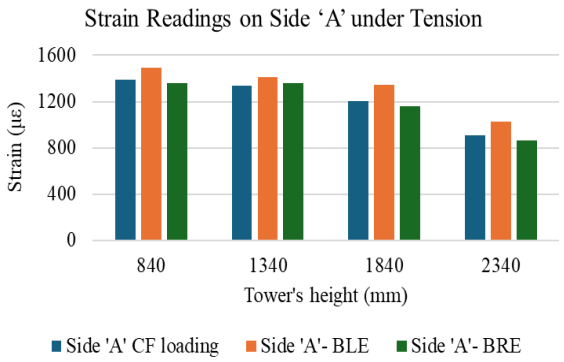

(i) Under pushing loading

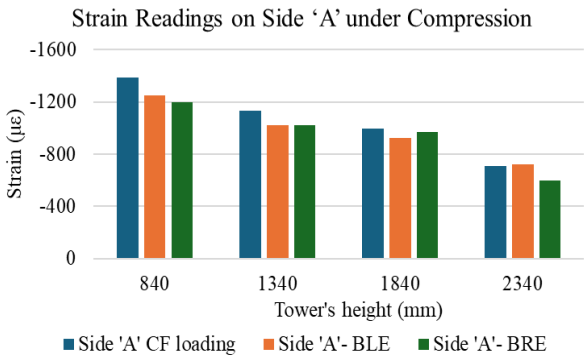

(j) Under pulling loading

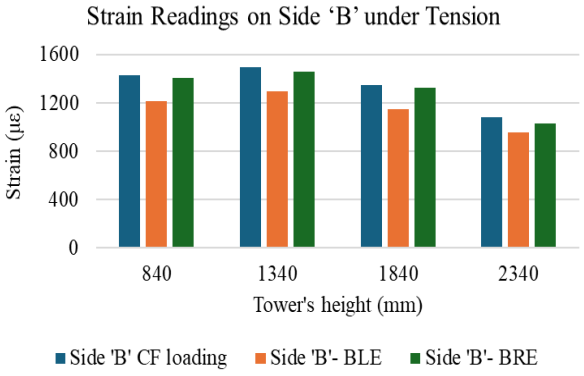

(k) Under pulling loading

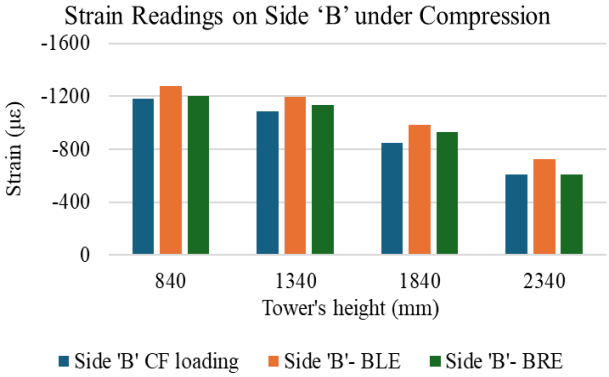

(l) Under pushing loading

Figure 7.10. Comparison of strain values on sides 'A' and 'B' under CF, BLE, and BRE cyclic loading conditions

7.6. Test to failure

The load-deflection response of the tower for Stage 4 (monotonic loading to failure) is shown in Figure 7.11. The response was fairly linear up to approximately 140 kN (240 mm), followed by a slight decrease in stiffness up to the peak load. Failure was initiated by GFRP rupture on the tension side of the tower near the top of the foundation block at an applied load of 182 kN and displacement of 361 mm. After completing the test and opening the foundation, it was observed that the GFRP rupture/crack had formed and propagated internally within the foundation, extending toward the bottom end of the tower. This finding highlights the CFFT tower's ability to withstand a substantial portion of the failure load before cracks appear. Strain gauge data suggests that the steel reinforcing bars at the tension and compression sides near the top of the foundation block yielded prior to FRP rupture. The yield load, measured at around 66 kN (Figure 7.12), represents approximately 36% of the failure load. The corresponding strain curves versus the tower height are presented in Figure 7.13. These curves highlight the difference between tensile and compressive strain behaviours, showing areas where stress concentrations were particularly evident due to concrete cracking.

The curvature vs tower height at the maximum applied load (182 kN) is illustrated in Figure 7.14. This critical zone, which extends from the foundation's base to approximately 1200 mm represents the transition from elastic to inelastic behaviour, as verified in the steel reinforcing bar strain curve. In this region, the structure experiences significant stress and deformation. Unlike the other towers, the curvature determined from the steel bar strains exceeded that of the GFRP tower at the top of the foundation block. This is likely an indication of a wide crack forming at the level of the steel strain gauge with concentrated rotation at that section.

The maximum strains measured in the FRP tube were 7083 με in compression, and 9362 με in tension, both at a height of 840 mm, as illustrated in Figure 7.15. The peak load was followed by a series of load drops as the displacement continued to increase. The test was eventually stopped after the actuator reached its maximum stroke capacity. The ultimate displacement reached during the test was 522 mm with a corresponding force of 115 kN (37% below the peak load), showing the tower's ability to sustain large deformations without catastrophic failure. Photos of the tower after failure are shown in Figure 7.16.

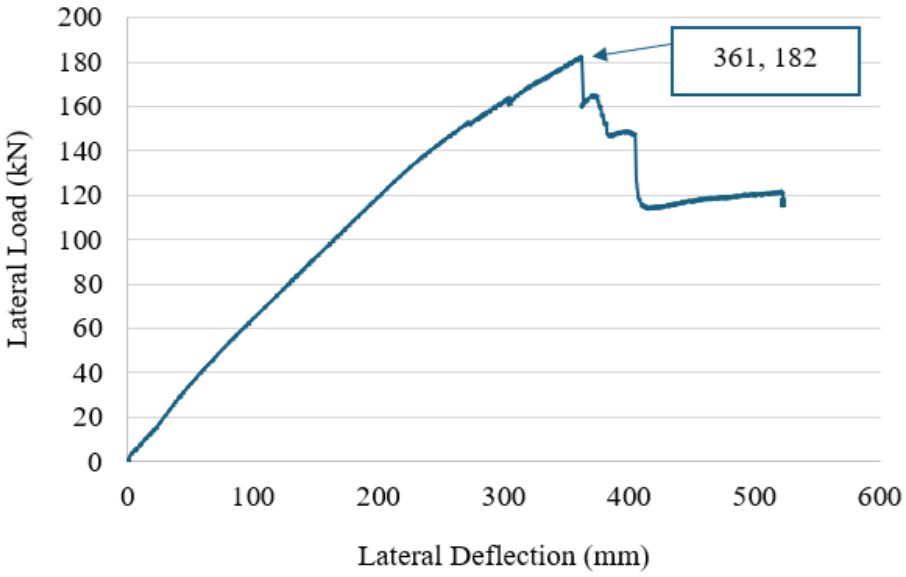

Figure 7.11. Monotonic load-deflection response

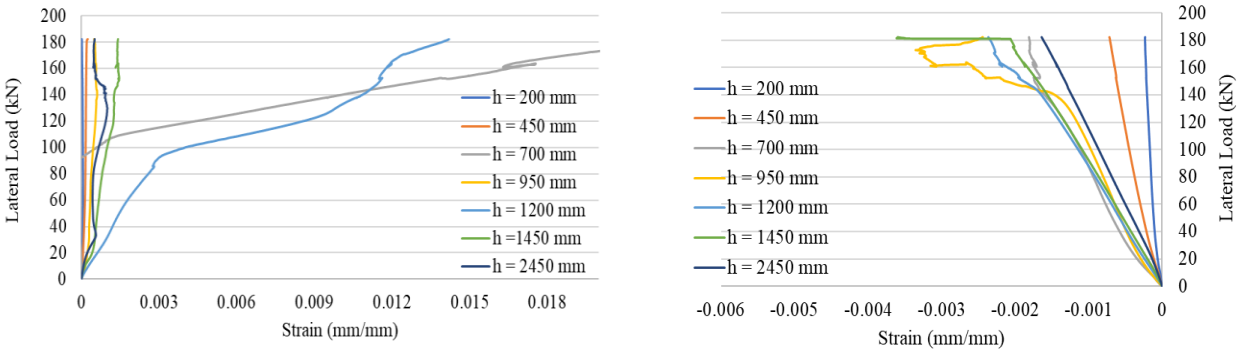

(c) Strain reading on rebar 'A'

(d) Strain reading on rebar 'B'

Figure 7.12. Lateral load vs longitudinal strain curves for tower M5

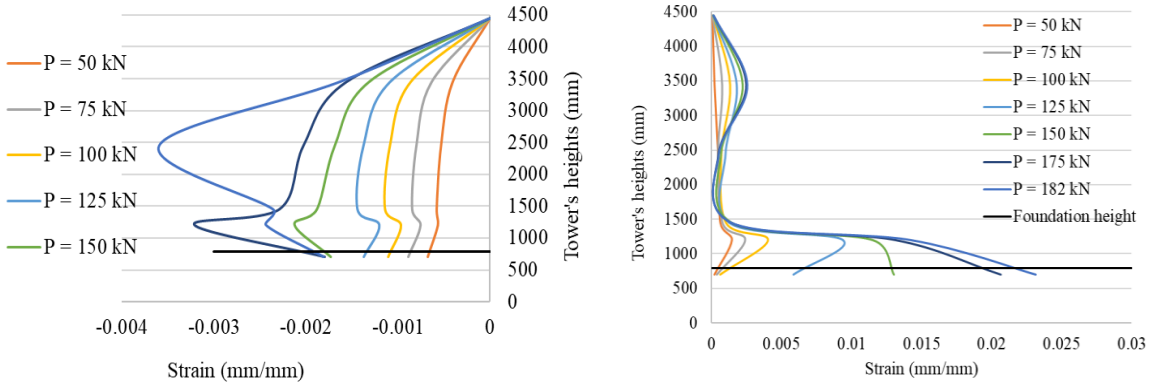

(a) Rebar 'B' under compression

(b) Rebar 'A' under tension

Figure 7.13. Tower height vs rebars 'A' and 'B' strain reading

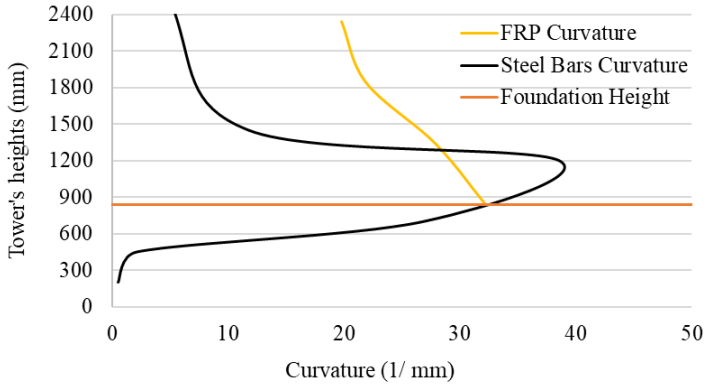

Figure 7.14. Tower's curvature vs tower's height at maximum failure load of 182 kN

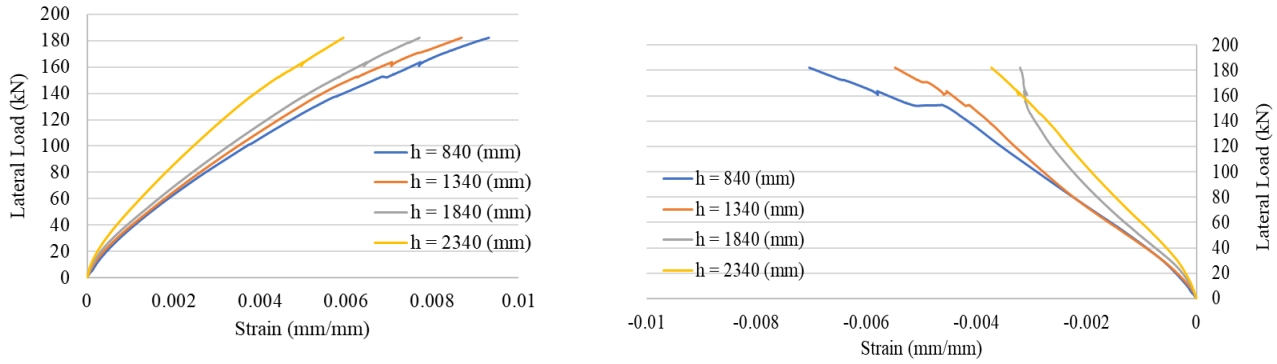

(c) Strain reading on side 'A'

(d) Strain reading on side 'B'

Figure 7.15. Strain readings recorded on the GFRP surface

(a) Tower at ultimate displacement

(b) Tower after unloading

(c) FRP tensile rupture above the foundation block

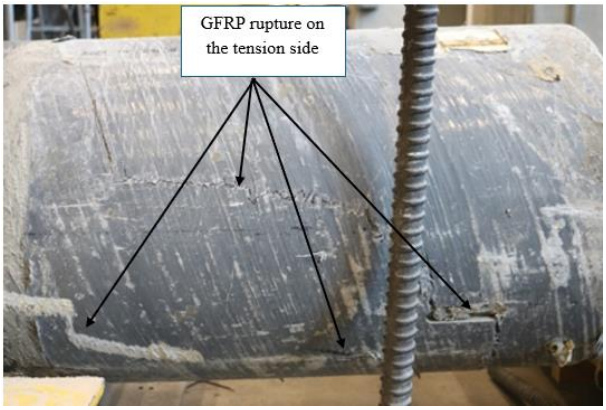

(d) Rupture surface shown after removal from foundation propagating towards tower base

Figure 7.16. Failure mode of tower specimen M5

7.7. Numerical Model Verification

7.7.1. Stage 1. Free Vibration Test

Just like Tower M4, the dynamic behaviour of Tower M5 was evaluated using a free vibration test. From the displacement-time data, M5 showed a fundamental vibration period of 0.176 seconds, which corresponds to approximately 5.7 Hz, and a damping ratio of about 9%. The FE simulation for M5 followed the same approach as with M4, where an initial lateral displacement was applied at the top of the tower and then released at the start of step number 3 in the dynamic analysis, allowing the structure to vibrate freely.

In terms of results, the first peak displacement in the FE model closely matched what was observed in the experiment, which suggests that the simulation accurately captured the tower's initial stiffness and mass properties. However, the peaks in the experimental data dissipated faster than in the simulation, as illustrated in Figure 7.17, likely due to the higher damping observed during testing (around 9%), which was not fully captured in the numerical model.

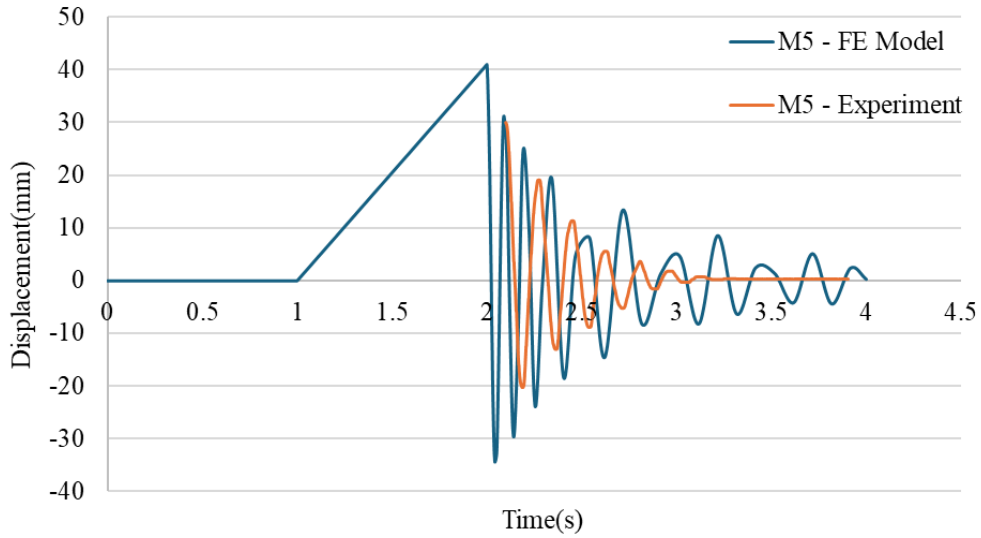

Figure 7.17. Comparison of displacement-time history for free vibration response of M5 – experimental and modeling results

7.7.2. Stage 2: Cyclic flexural testing under concentric loading (CF)

The geometry of the M5 tower differed from M4, so the M4 model was adjusted and recalibrated to better represent M5's behaviour under the applied loading protocols. Most modeling parameters from M4 were kept unchanged, but the interaction properties were adjusted: a friction coefficient of 0.6, an internal contact force of 1500 N, and a foundation rotational spring stiffness (D44) of 3.8 x 10^{10}. Importantly, the amplitude used in the M4 model for SLE and BLE was also adopted for M5 under CF loading, but with an 18.5% increase to account for both the differences in geometry and the sharp load drops that occurred at displacement reversals. With this calibration, the model was able to reproduce the experimental response with very close accuracy.

The numerical and experimental results showed close agreement up to ±50 mm displacement (Figure 7.18). At +50 mm, the experiment reached an average peak of +39 kN compared to +40 kN predicted (2.5% higher). At -50 mm, the experimental peak was -39 kN, while the model predicted -44 kN (11.4% higher). At larger negative displacements, the model slightly over-predicted load and energy absorption (19.2% at -53 mm), while the experiment exhibited a smoother reverse loading response.

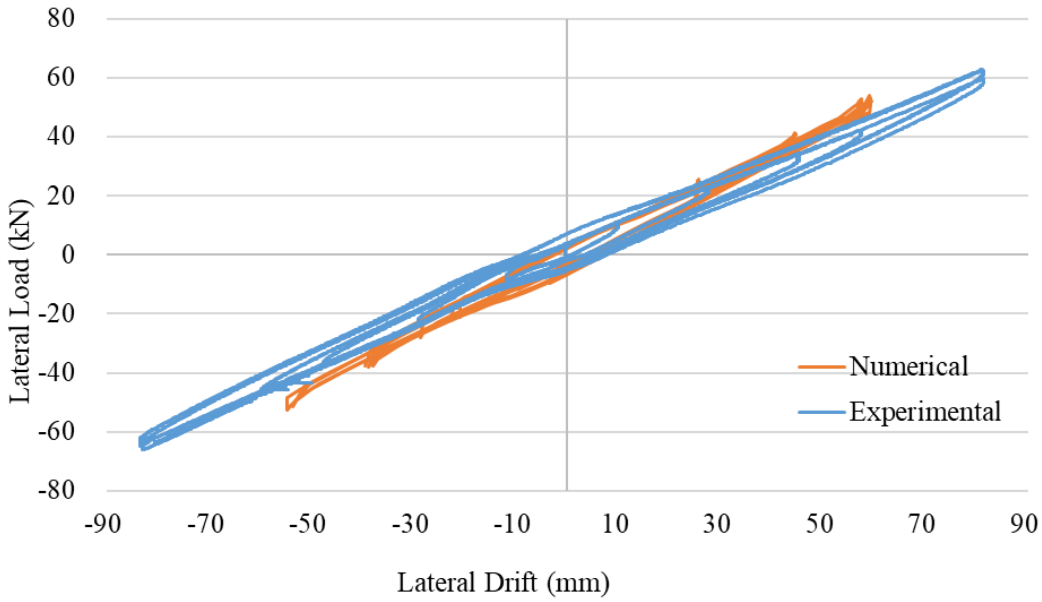

Figure 7.18. Load–Displacement Response of M5 under CF Loading: Experimental vs. Model

Figure 7.19 (a) illustrates that the earliest signs of tensile damage (red zones) developed at the tower's bottom near the foundation, where tensile stresses and bending effects are highest. Approximately 95% of the material stiffness had been degraded at that stage. The presence of such high damage, despite the use of high-strength concrete (f'c = 61 MPa), underscores the intensity of the tensile stress state and confirms that the reinforcement is actively engaged, transferring stresses through yielding.

The von Mises stress distribution in Figure 7.19 (b) illustrates how tendons on the tension side carried the primary load, while compression-side tendons also developed significant stress, providing equilibrium against the bending forces and ensuring structural stability. This response was consistent with M4, although the stresses were slightly more noticeable in M5. The concrete core (Figure 7.19 (c)) experienced only localized stresses near the foundation, with a maximum von Mises stress of 18.4 MPa, which is about 30% of the crushing capacity of the 61 MPa concrete.

Strain contours (LE11) in Figure 7.19 (d) further confirmed that bending concentrated around the tower base, aligning with the patterns observed for M4 under CF loading. Together, these observations demonstrate that the FE model successfully replicated the flexural response of the M5 tower.

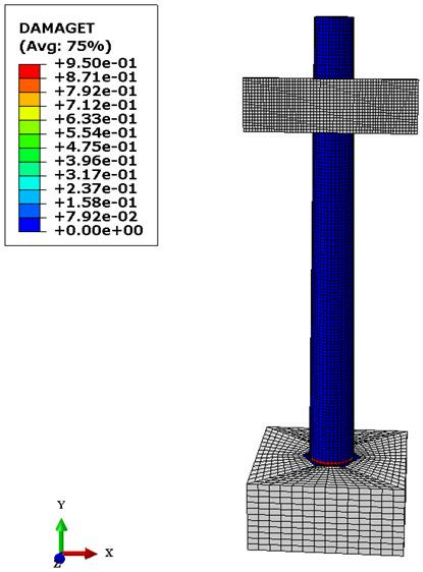

(a) Tensile damage distribution

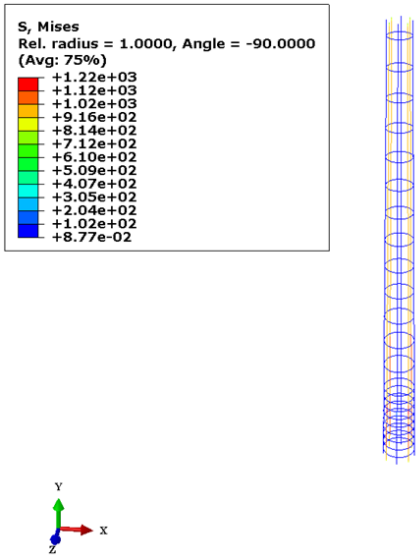

(b) Stress contours in rebars (blue) and tendons (red)

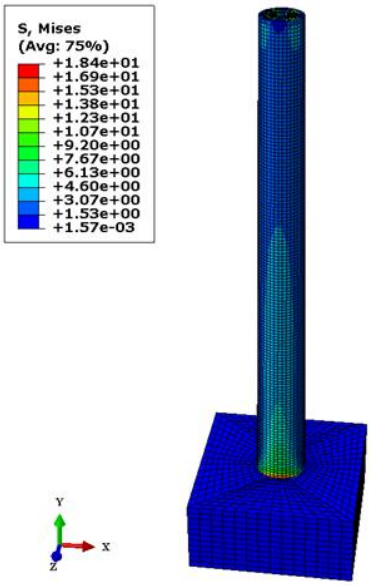

(c) Stress contours in concrete core

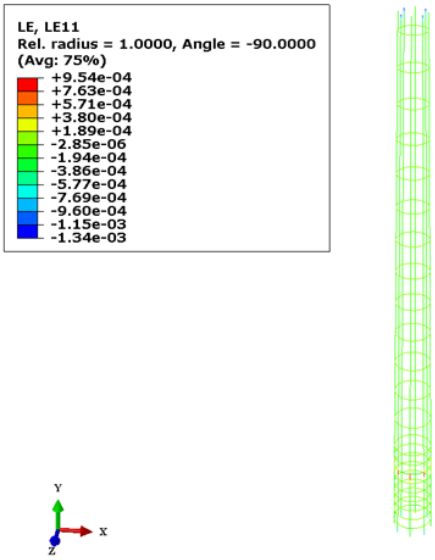

(d) logarithmic strain contours in rebars and tendons

Figure 7.19. FE simulation of the M4 tower under CF loading illustrating stress contours and damage distribution

7.7.3. Stage 3B: Big left eccentric loading at 558.8 (mm)

For the BLE loading scenario of tower M5, the finite element model was derived from the BLE model of tower M4. The control points were reassigned to RP3–5, maintaining an eccentricity of 559 mm. The same quasi-static loading procedure was applied, with tower-top displacement tracking the response and base shear recorded at RP2 and RP3-5. While most M4 parameters were retained, interaction settings were updated to reflect M5 conditions: a friction coefficient of 0.6, internal contact force of 1500, and a foundation rotational spring stiffness D44 of 3.0 x 10^{10}. The loading amplitude remained the same as in the M4 BLE tests.

The mesh was refined to preserve numerical accuracy, keeping the element size consistent with M4. As shown in Figure 7.20, the numerical results captured the main experimental trends, including initial stiffness and the load- displacement response up to +55 mm and -52 mm. At +55 mm, the experiment recorded an average peak of +44 kN, while the model predicted +45 kN (2.2% higher). At -52 mm, the experimental peak was -41 kN, compared to -43 kN predicted by the model (4.6% higher). Overall, within the applied amplitude, the model effectively simulated the experimental response up to +44 kN and -41 kN.

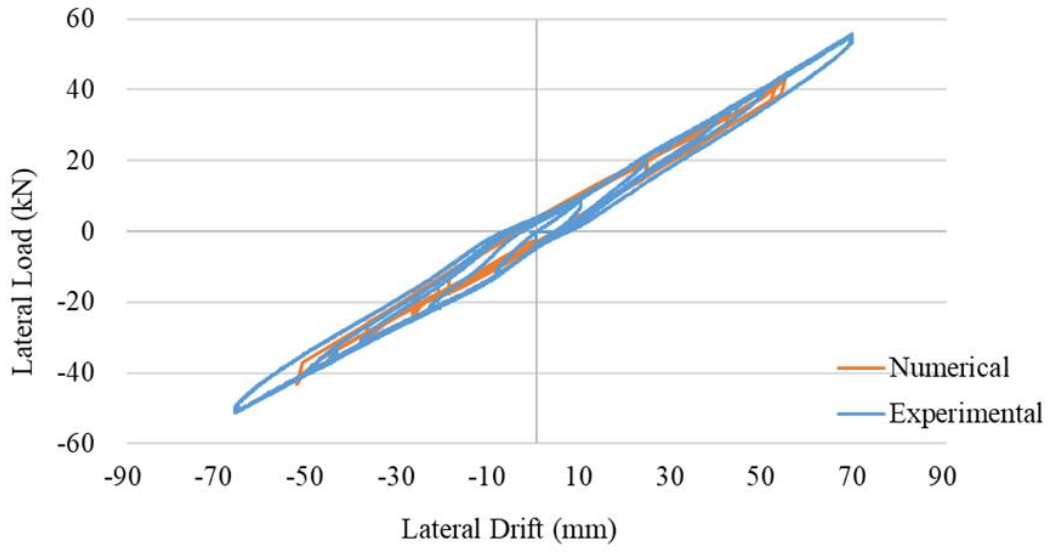

Figure 7.20. Load–Displacement Response of M5 under BLE Loading: Experimental vs. Model

Figure 7.21 (a) illustrates that the earliest signs of tensile damage (red zones) developed at the tower lower part near the foundation, where bending and tensile stresses are highest. Approximately 15% of the concrete tensile stiffness was degraded at the base due to smeared cracking, which is much less than in the CF case. The von Mises stress contours in Figure 7.21 (b) show that tendons on the tension side resisted the majority of the applied demand, while tendons on the compression side developed noticeable stresses that balanced the bending moment and maintained structural stability. Compared with CF loading case, the same pattern was observed, but stresses in CF loading were slightly higher. The concrete core (Figure 7.21 (c)) showed localized stresses near the foundation, with a maximum of 18.4 MPa around 30% of the concrete's crushing capacity and equal to the value observed under CF loading. Strain contours (LE11) in Figure 7.21 (d) confirmed bending concentrated at the base, consistent with CF loading, but slightly lower.

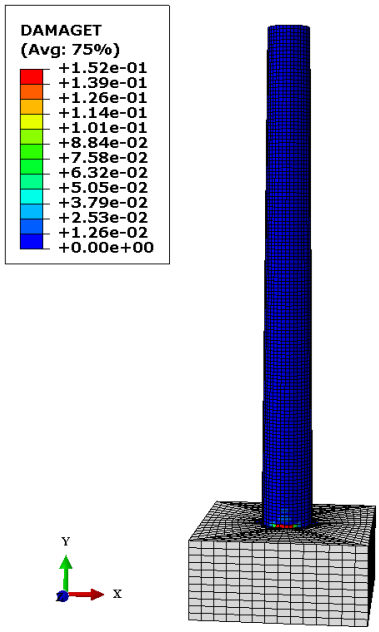

(a) Tensile damage distribution

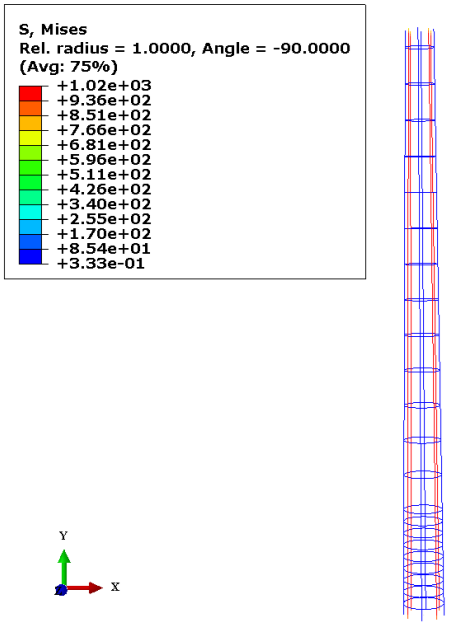

(b) Stress contours in rebars (blue) and tendons (red)

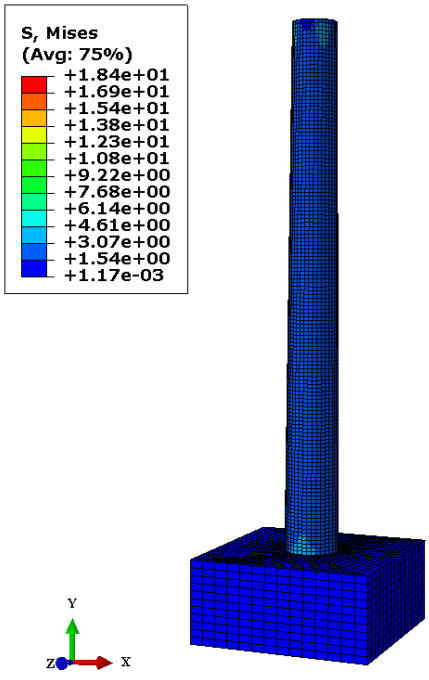

(c) Stress contours in concrete core

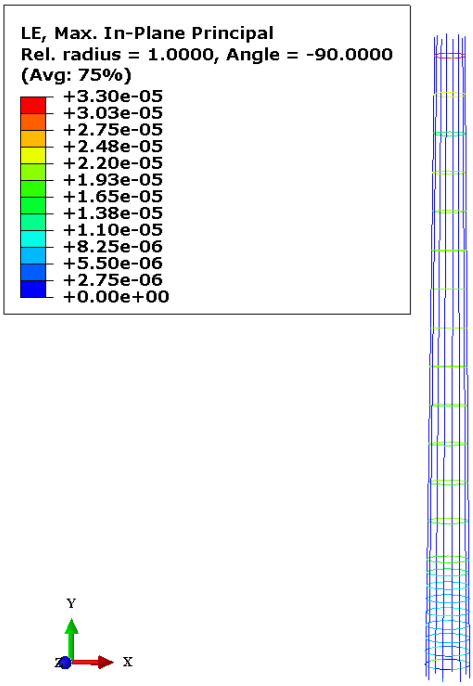

(d) logarithmic strain contours in rebars and tendons

Figure 7.21. FE simulation of the M5 tower under BLE loading illustrating stress contours and damage distribution

7.7.4. Stage 4: Test to failure

The final stage of model verification focused on evaluating the FE model's performance under monotonic lateral loading to failure, replicating the experimental test conducted on the M5 tower. As shown in Figure 7.22, both the experimental and numerical results for the tower show a mostly similar trend. However, some differences are noticeable, particularly in stiffness and the tower response after the peak load.

The numerical model displays a stiffer response and a more sudden decline after reaching the peak load of 173 kN at 311 mm. This is likely due to the use of idealized boundary conditions, simplified assumptions of full material continuity with no cracking until a defined limit is hit, and a failure criterion in the simulation that initiated a sudden loss of strength.

A possible reason for this mismatch is the absence of a coupon test to determine the specific properties of the GFRP tube used in M5. Instead, the model assumed the same GFRP properties as those used for Tower M4, which may not exactly reflect the actual material behaviour in M5. This assumption, combined with the effects of prior cyclic loading and the progressive cracking and stiffness degradation in the concrete during testing, likely contributed to the observed differences between the experimental and numerical curves.

In addition, Figure 7.23 (a) illustrates the tensile damage distribution in the concrete core of the M5 tower under monotonic lateral loading, as predicted by the Concrete Damaged Plasticity (CDP) model. Unlike Tower M4, where damage remained more concentrated near the upper interface of the foundation block, Tower M5 shows a wider spread of tensile damage extending internally within the foundation toward the bottom end of the tower. This broader crack pattern is likely due to the lower level of post-tensioning used in the M5 specimen, which resulted in reduced initial compressive stress in the concrete. As a result, flexural cracks were able to form earlier and propagate more widely under loading.

The von Mises stress distribution offers additional details about the behaviour of the tendons and reinforcement bars under flexural loading. As expected in a prestressed system, the tendons on the tension side, clearly shown in the red zones (Figure 7.23 (b)), experience high tensile stress,

confirming that they are carrying most of the applied lateral load, which aligns with the observed experiment strain response. On the compression side, the tendons also carry considerable stress, indicating their role in resisting bending forces and contributing to the structural stability of the tower.

Further supporting this, the strain contour (E11), which reflects deformation along the tower's height, shows elevated strain levels near the base. This matches well with the experimental data, where strain gauges recorded the greatest curvature in that same region. This consistency between the model and the test results strengthens confidence that the simulation accurately captures the tower's flexural response under loading.

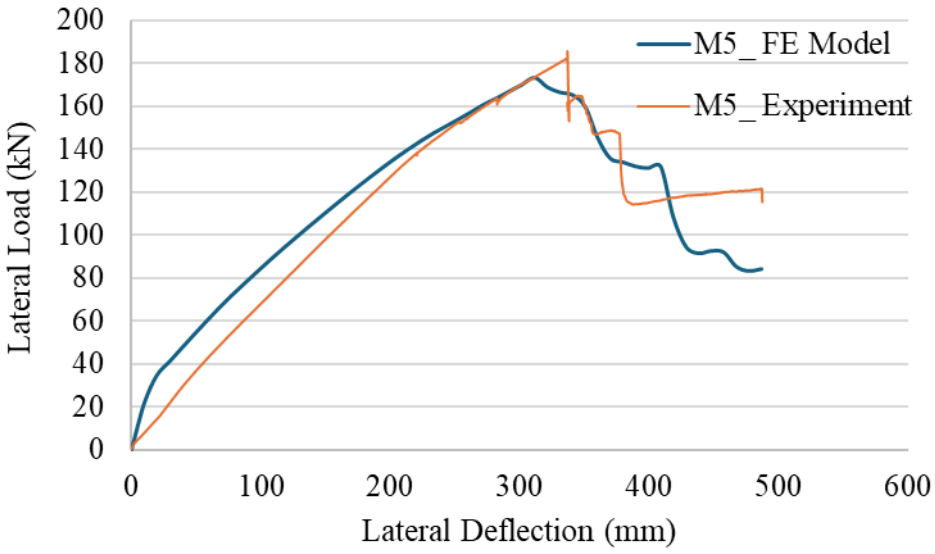

Figure 7.22. Comparison of load- displacement response of M5 – experimental and modeling results

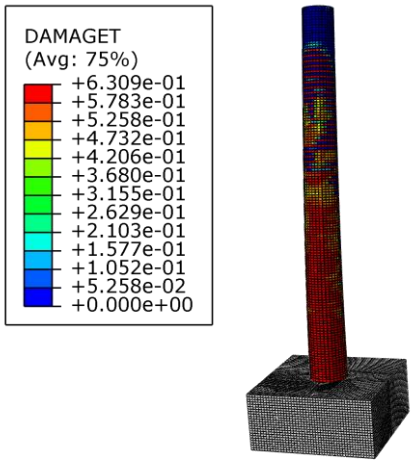

(a) Tensile Damage Distribution

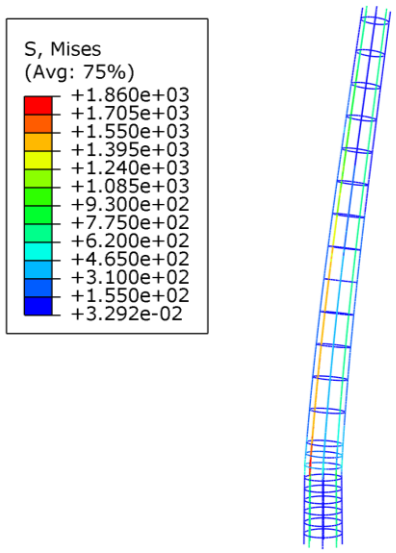

(b) Stress Contours in rebars and tendons

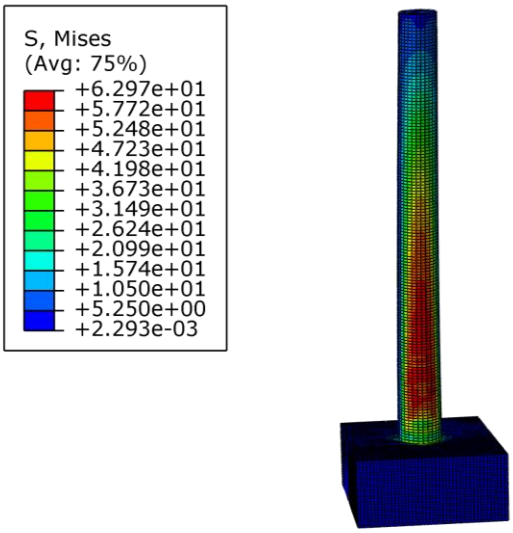

(c) Stress Contours in concrete core

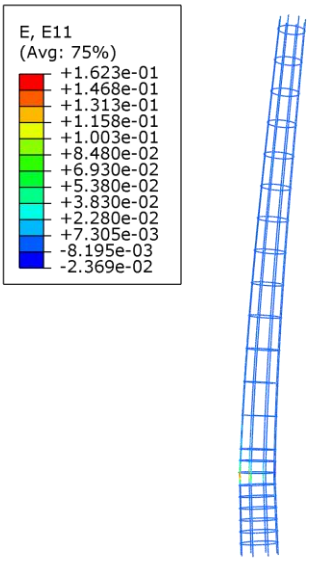

(d) Deformation pattern

Figure 7.23. FE simulation of the M5 tower illustrating stress contours and damage distribution

Chapter 8 - Discussion

8.1. Introduction

This chapter presents a comprehensive discussion of the experimental results obtained from testing the three towers (M4-1, M4-2, and M5) under dynamic and quasi-static cyclic lateral loading followed by monotonic loading to failure. The aim in this chapter is to look at the patterns across all towers, highlight the key differences in behaviour, and understand what these differences reveal about the performance of prestressed concrete-filled FRP tube (CFFT) towers when used in real-world wind energy applications.

8.2. Comparison of Tower Performance

8.2.1. Characterization of dynamic properties

Beginning with the dynamic characteristics, all three towers showed good performance during the free vibration tests. Towers M4-1 and M4-2 had nearly identical dynamic behaviour, with a fundamental period of approximately 0.152 seconds and a damped natural frequency of around 6.6 Hz. Their damping ratios were also quite similar: 4.0% for M4-1 and 4.4% for M4-2. These values fall within the expected range for FRP-concrete systems and align with previous studies on all-FRP towers conducted by Polyzois et al. (2009). Tower M5, on the other hand, had a noticeably higher damping ratio at approximately 9% and a slightly lower natural frequency of 5.7 Hz (Table 8. *1*). Although M5 has a larger diameter, the lower prestressing force (790 MPa) reduced axial stiffening compared to M4-1 (1020 MPa), and the increased mass slightly lowers the natural frequency compared to M4. At the same time, the higher damping ratio indicates that M5 is more effective at dissipating vibrational energy, likely due to the combination of geometric effects, prestressing, and potential slip between the concrete and GFRP. This increased damping observed suggests an enhanced ability to dissipate energy. Since the vibration test was carried out before the cyclic loading, no obvious signs of debonding were present. However, higher damping could indicate some energy dissipation due to potential slip between interfaces (concrete-FRP, FRP-grout, grout-foundation, etc), and as only a single tower of this size was tested, it cannot be confirmed if these observations reflect typical behaviour. Importantly, all three towers had natural

frequencies above the range where wind turbines typically operate (usually 0.3 to 2.5 Hz), meaning there is a very low risk of resonance. This is a reassuring finding for the safe long-term use of these towers in the field. However, this finding should be confirmed for towers of greater height.

Table 8. 1. Summary of the natural frequency and damping ratio for M4 and M5

	M4-1		**M4-2**		**M5**	
t_n #	**Frequency (Hz)**	**ζ =(δ/2π)**	**Frequency (Hz)**	**ζ =(δ/2π)**	**Frequency (Hz)**	**ζ =(δ/2π)**
1	6.8970	0.03391	6.8776	0.02860	5.6818	0.07207
2	6.8173	0.02958	6.7883	0.04431	5.6180	0.08304
3	6.6653	0.03590	6.6320	0.03738	5.7803	0.11372

8.2. 2. Comparative Analysis of Monotonic Load-Deflection Response

The load–deflection responses of the three tested towers (M4-1, M4-2, and M5) highlight the influence of prestress level, cross section geometry, prior damage history, and foundation boundary conditions on overall tower behaviour. The key failure loads and corresponding displacements obtained from the monotonic tests are summarized in Table 8.2. As shown in Figure 8.1, M4-2 exhibited relatively high initial slopes during early loading, indicating higher lateral stiffness. However, when comparing between the two specimens M4-1 and M4-2, M4-1 achieved a slightly higher load capacity than M4-2 (132 kN vs 125 kN), and this difference must be interpreted in the context of the applied loading sequence. Specifically, BRE loading was conducted first on M4-2 up to 143 kN, meaning that prior to the monotonic test, the tower had already undergone reinforcement yielding, cracking of the concrete core, and partial debonding between the GFRP tube and concrete, as confirmed by strain measurements in both the reinforcement and the GFRP tube. As a result, the monotonic test did not reflect the behaviour of an undamaged tower but rather the residual capacity of a specimen with existing inelastic damage (more details in Section 6.6). During monotonic reloading, GFRP strains (9956 με in tension and -5946 με in compression) remained below rupture thresholds until final failure, showing that rupture occurred only after progressive inelastic action within the steel and concrete core. This explains why M4-2, when

tested under monotonic loading, reached a lower load capacity and failed in a more abrupt and brittle manner. The slightly higher stiffness observed in M4-2 can also be attributed to its higher tendon prestress (which closed existing cracks upon unloading) and reduced foundation flexibility/rotation relative to M4-1. This highlights parameter interaction by showing how prestress and boundary conditions collectively influence stiffness. Both towers also confirmed that the most critical inelastic response zone extended from the base to approximately 1350 mm, where reinforcement yielding, concrete cracking, and FRP stresses were concentrated.

In contrast, the M5 tower demonstrated a significantly higher capacity and deformation ability under monotonic loading. The tower reached a peak lateral load of 182 kN at a displacement of 361 mm, showing the highest strength among the three tested specimens. Failure was initiated by GFRP rupture on the tension side near the foundation, similar in mode to M4-1 and M4-2, but the larger cross-sectional size allowed M5 to sustain greater load and deflection prior to rupture. Strain gauge data confirmed that reinforcement yielding occurred before FRP rupture, at around 66 kN (36% of the failure load), showing a consistent development of inelastic behaviour prior to ultimate failure.

Another important distinction was the peak behaviour of M5. Unlike the sudden drop observed in M4-2, M5 maintained load-carrying ability with large deformations. After rupture, the tower sustained displacements up to 522 mm while still carrying 115 kN (37% below the peak load). This capacity to undergo substantial deformation without catastrophic failure highlights the ductility and energy absorption of larger CFFT sections. The critical inelastic response zone in M5 was concentrated within the first 1200 mm above the foundation, similar to what was observed in M4-1 and M4-2, and again confirming the localization of damage near the base where reinforcement yielding and FRP rupture initiated. Together, these comparisons show how prestress, geometry, and loading cases interact to shape the monotonic response. M4-1 showed the baseline behaviour with minimal pre-existing damage, M4-2 revealed the effect of prior eccentric damage on residual capacity, and M5 highlights the strength and deformation advantages of larger sections, including their ability to sustain significant displacements without catastrophic failure. These findings emphasize that both section design and prestress level are critical for enhancing ductility and residual strength in CFFT wind turbine towers.

Table 8.2. Summary of Failure Loads and Corresponding Displacements of Tested Towers

Specimen ID	Failure Load (kN)	Displacement at Failure (mm)
M4-1	132	267
M4-2	125	231
M5	182	361

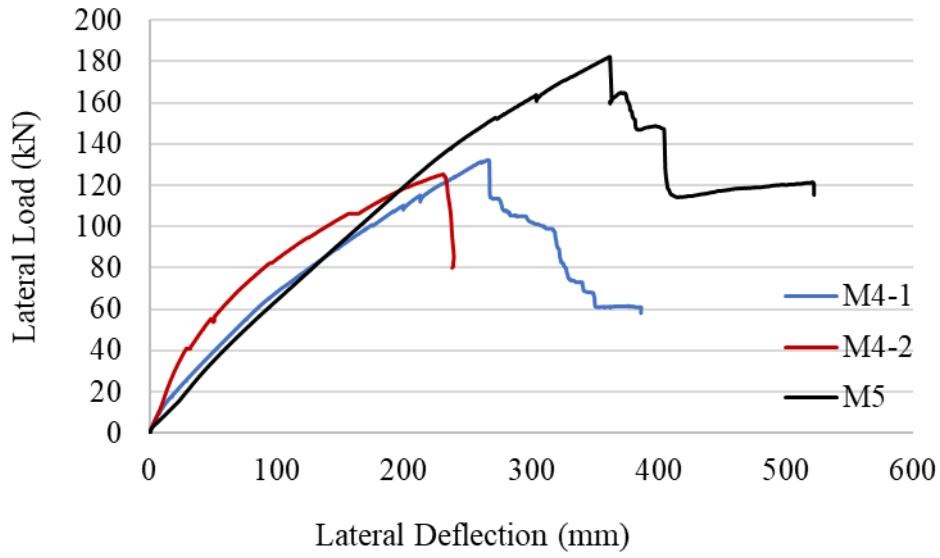

Figure 8.1. Load–deflection response under monotonic loading for specimens M4-1, M4-2, and M5

8.2.3. Influence of Prestress and Section Size on Stiffness and Strength

M5 displayed markedly different behaviour than the other two towers. Despite ultimately achieving the highest peak load (182 kN), its initial slope was noticeably lower, indicative of a lower lateral stiffness compared with both M4-1 and M4-2. This reduction in stiffness is consistent with the lower prestressing force applied in M5, which reduced the ability of the tendons to provide pre-compression and delay cracking. Prestress enhances flexural rigidity in composite sections by increasing the contribution of the concrete core and improving composite action between the GFRP

tube and concrete; therefore, its reduction in M5 directly impacted the initial stiffness response. Additionally, FE simulations indicated increased base/foundation rotation in M5 testing, further reducing effective lateral restraint and contributing to lower measured stiffness. This behaviour was primarily included to align the model with the experimental results. These factors together demonstrate that initial stiffness is governed not only by section dimensions, but by a combination of prestress effectiveness and boundary compliance.

In contrast, the larger section of M5 contributed positively to its ultimate capacity. Even with reduced prestress level and increased foundation rotation, M5 achieved greater peak load compared with M4-1 and M4-2. The FE model confirmed that the stiffness degradation in M5 was governed by reduced tendon forces (Section 8.3.1) and foundation flexibility. Therefore, the ultimate strength was mainly controlled by section geometry and confinement effects.

Overall, the comparison demonstrates that stiffness and ultimate capacity are influenced by different parameters. Initial stiffness is strongly affected by prestress level, prior damage, and boundary conditions, whereas ultimate capacity is primarily controlled by section geometry, confinement efficiency, and damage progression. The observed behaviour of M5 emphasizes this difference: its lower stiffness was offset by the benefits of a larger section, resulting in the highest load capacity. These findings align with the conclusions of Fam and Mandal (2006) regarding prestressed concrete-filled FRP tubes, where prestress enhances early stiffness, while section dimensions, confinement, and damage history dominate strength and ductility characteristics.

8.2.4. Comparative Cyclic Response under Concentric and Eccentric Loading

The effect of eccentricity on tower behaviour was further investigated through the cyclic flexural-torsional tests. Under CF cyclic loading, the three towers demonstrated variations in both initial stiffness and hysteretic response. Although M4-1 and M4-2 were nominally identical, differences were observed in stiffness and in the load drops during displacement reversals (Figure 8.2). The FE model, which employed consistent material properties, indicated that these differences occurred from the test setup rather than the towers themselves; specifically, variations in foundation rotation and friction within the clamping system due to differences in bolt tightness (Section 5.7.2). This was confirmed by the close agreement between the calibrated FE model and

the M4-1 experimental response. When M4-1 is compared with M5 under CF loading (Figure 8.3), both tests show a similar initial stiffness. However, greater foundation rotation and lower flexural stiffness in M4-1 led to a divergence that the FE model also captured (Section 5.7.2). In addition, M4-1 showed greater sharp load drops than M4-2, indicating greater energy dissipation at the interface between the clamping system and the tower surface during load reversals. The measured load levels at peak displacements were very close: 44 kN in M4-1 vs 47 kN in M5 at +60 mm (6.4% higher), and –39 kN vs -43 kN at -55 mm (9.3% higher). These results highlight the main role of boundary conditions in driving response variability.

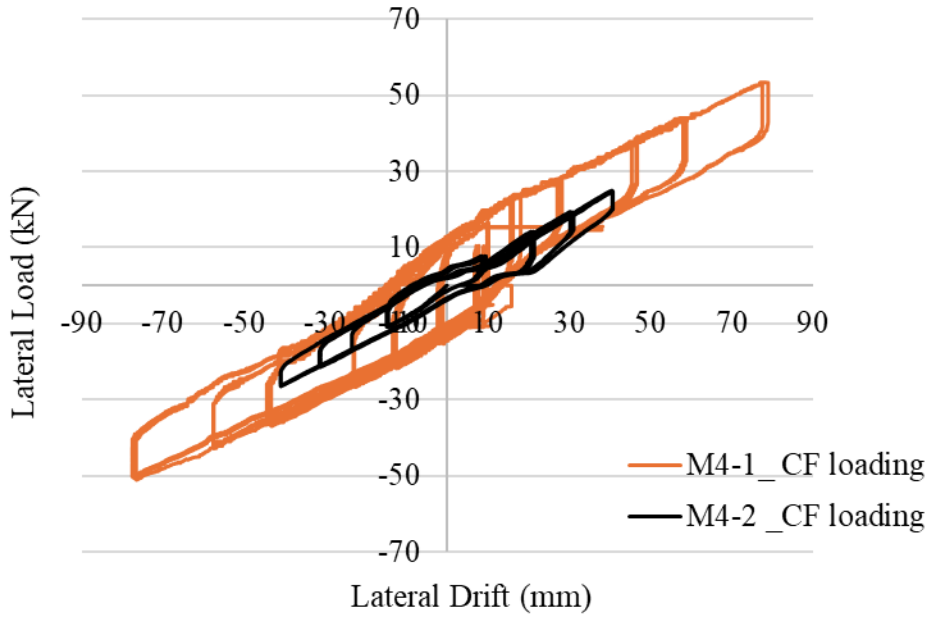

Figure 8.2. Lateral load–lateral drift response for M4-1 and M4-2 under concentric cyclic loading condition

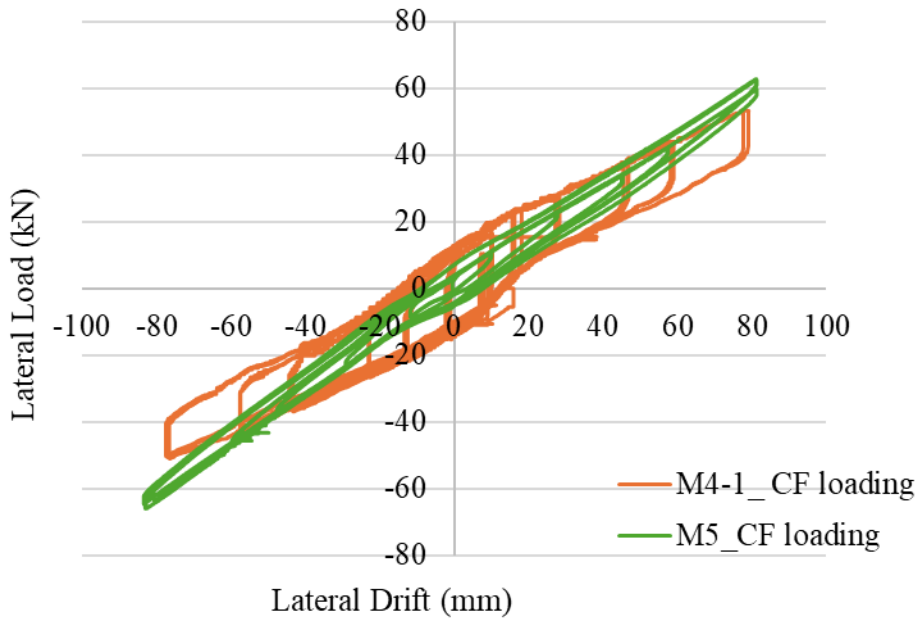

Figure 8.3. Lateral load–lateral drift response for M4-1 and M5 under concentric cyclic loading condition

Under BRE loading (Figure 8.4), M4-1 exhibited higher stiffness than M4-2, mainly due to greater foundation rotation. However, both towers showed only minor and comparable load drops during reversals, indicating limited energy dissipation at the interface between the clamping system and the tower surface.

Under BLE loading (Figure 8.5), both towers M4-1 and N4-2 showed very similar response in terms of stiffness and load drops during reversals, reflecting the consistency of their structural behaviour. However, as noted earlier in Section 6.3, M4-2 tower reached the peak displacement of -51 mm when the load was only -36 kN. This was due to the cable transducer reaching the limit of its measurement range, preventing any further displacement from being captured. The similarity in response of the two towers indicates that the foundation secured to the strong floor and the clamping system connection to the towers were highly consistent. This suggests that under BLE cyclic loading, the combination of geometric similarity, material properties, and boundary conditions resulted in closely matched structural performance, with minor differences primarily

attributable to measurement limitations rather than characteristic differences in the two towers themselves.

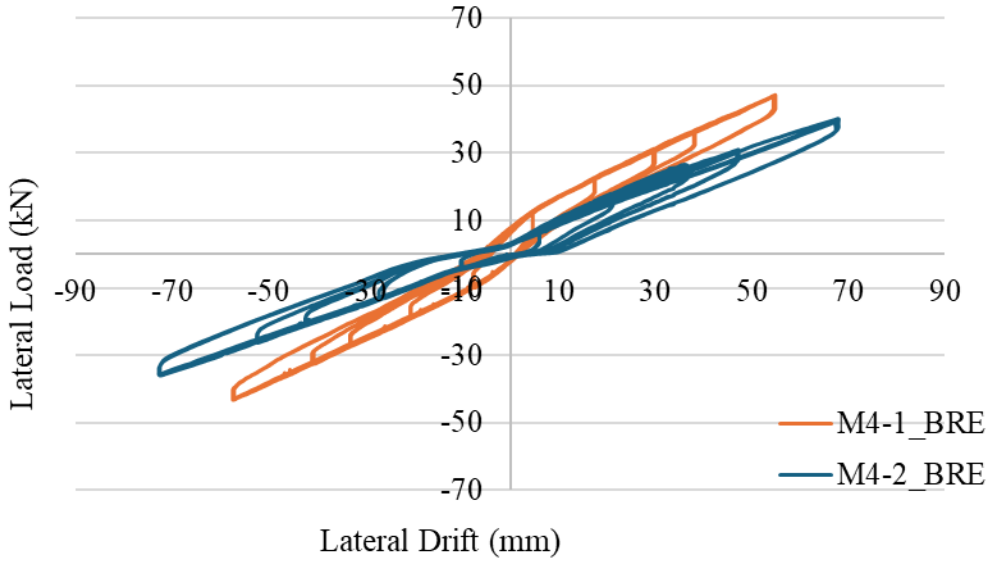

Figure 8.4. Lateral load–lateral drift response for M4-1 and M2-2 under BRE loading condition

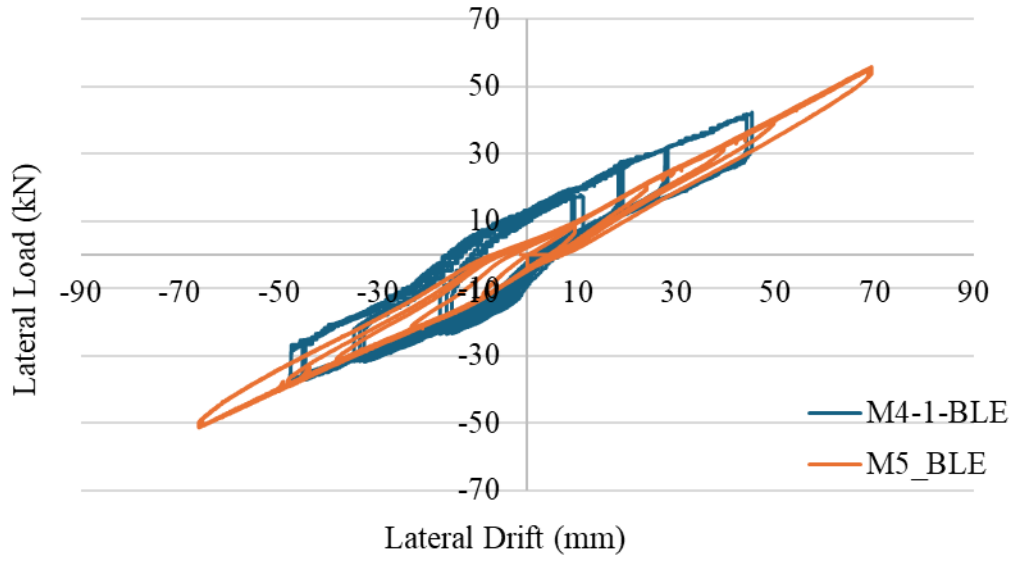

Figure 8.5. Lateral load–lateral drift response for M4-1 and M2-2 under BLE loading condition

Under BRE loading (Figure 8.6), M4-1 and M5 displayed very similar response in stiffness and load-drop during reversals. M5 showed a slight reduction in stiffness under positive (pushing) loading, likely due to its lower prestressing level. This behaviour is consistent with the FE model results presented in the parametric study on the effect of prestressing on load–deflection behaviour, which confirmed that M5 experienced stiffness degradation as a result of its reduced tendon forces. Despite this, the consistent load-drop behaviour indicates that the clamping system provided a reliable connection to both towers.

In addition, under BLE loading, M4-1 and M5 showed different response in terms of stiffness and load drops during reversals (Figure 8.7). M4-1 displayed a nonlinear slope in the load–deflection curve while M5 remained approximately linear. Strain measurements revealed that no yielding occurred in the steel reinforcement of M4-1 under BLE loading, even though its load–deflection response exhibited a nonlinear slope. This suggests that the observed nonlinearity was primarily due to cracking of the concrete core and local bond-slip at the GFRP–concrete interface, rather than reinforcement yielding. In contrast, M5 showed yielding of the steel rebars in both tension and compression under BLE loading, yet its overall response remained nearly linear. The larger section size and confinement in M5 allowed the tower to maintain a stiffer and more stable overall response. M4-1 showed greater sharp load drops than M5, indicating greater energy dissipation at the interface between the clamping system and the tower surface during load reversals. This behaviour is consistent with the FE model (Sections 5.7.3 and 5.7.4).

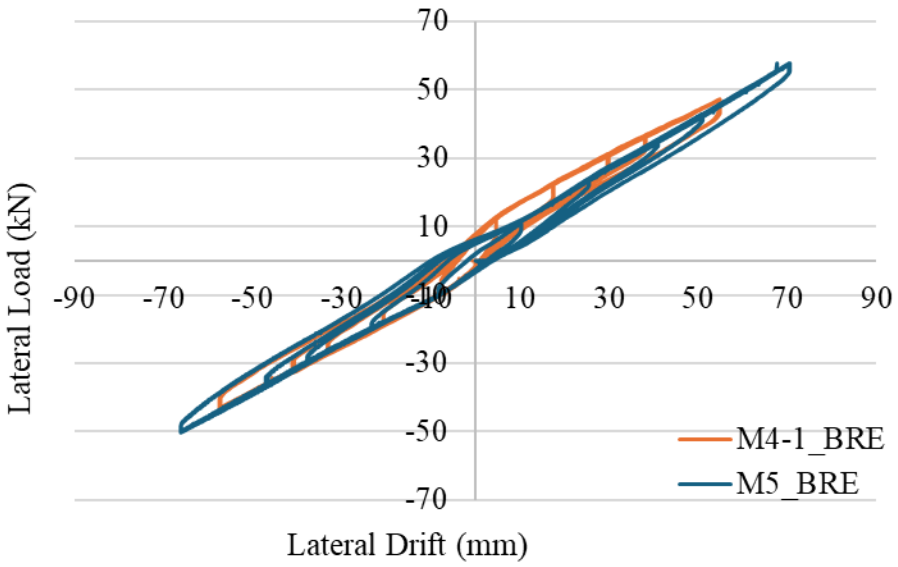

Figure 8.6. Lateral load–lateral drift response for M4-1 and M5 under BRE loading condition

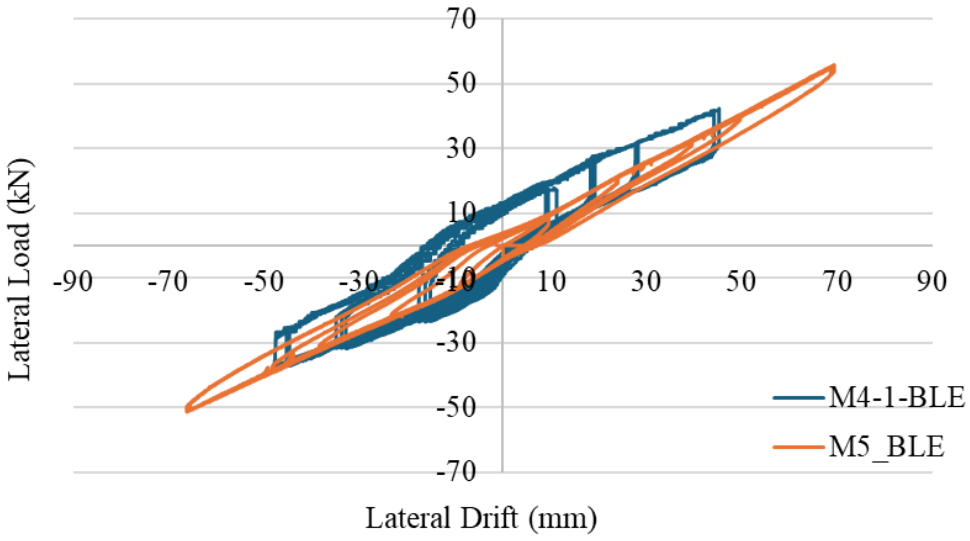

Figure 8.7. Lateral load–lateral drift response for M4-1 and M5 under BLE loading condition

Looking at strain behaviour in the longitudinal steel reinforcement bars (‘A’ and ‘B’), all towers showed consistent flexural behaviour. Reinforcing bar ‘A’ typically experienced tension during pushing (positive) loading and compression during pulling (negative) loading, while reinforcing bar ‘B’ did the opposite. The critical zone for strain, across all towers and loading types, was

consistently between 700 mm and 1200 mm from the base where the maximum bending moment occurs in a cantilevered system.

Under the same CF lateral loads (+25 kN and. -26 kN), M4-1 and M4-2 showed a similar strain pattern. Reinforcing bar 'A' in tower M4-1 reached 1475 με at 700 mm, while in tower M4-2, the highest reading was 1354 με at 950 mm.At these loads, M5 recorded 1264 με at 950 mm, indicating lower tensile demands compared to M4. This suggests that plastic deformation was developing even without visible signs of damage on the exterior.

The response of the central rebars, 'C' and 'D', was also important. These bars, located near the centroidal axis of the section, were mainly in tension, which makes sense given that concrete cracking tends to shift the neutral axis. Under eccentric loading, however, these bars occasionally switched between tension and compression, mainly during BRE loading tests. This type of variation indicates local redistribution of internal forces due to combined flexural and torsional effects. The strain response in M4-1 and M4-2 was more inconsistent, possibly influenced by uneven prestressing.

8.3. Parametric Study on the Influence of Design Variables

Once the numerical model was validated against the experimental results, a series of parametric analyses were carried out to evaluate the impact of different design parameters on the performance of post-tensioned CFFT towers. In a previous study (Gong, 2021), the effect of certain design parameters such as reinforcement ratio, tower height, concrete filling ratio, and fibre orientation on the load-deflection response of CFFT towers subjected to a concentrated lateral load at the tower top were numerically investigated. That study primarily focused on global stiffness and strength trends and did not account for concentric and eccentric cyclic loading. Adding to those findings, the main variables of interest in this section are tower diameter, prestressing level, concrete tensile strength, confinement, and GFRP properties, which are investigated using a numerical model calibrated against experimental cyclic test results. These analyses not only clarify the role of each factor in stiffness, peak load, and failure behaviour but also help to confirm the sensitivity and reliability of the developed model.

8.3.1. Effect of Prestressing on Load–Deflection Behaviour

As discussed in Section 4.2.4, prestressing was applied in a dedicated step before displacement loading, ensuring that the prestress forces were fully developed prior to applying external loads. This method effectively replicates the mechanical behaviour of prestressed concrete, resulting in improved structural stiffness and reduced deformation. For this analysis, the geometry of tower M4 was used. Three levels of prestress forces were investigated (500 MPa, 1000 MPa, and 1500 MPa). The results show that increasing prestressing force steepens the initial slope of the load–deflection curve (Figure 8.8), with limited effect on ultimate strength. This is expected since higher prestress enhances crack resistance, making the structure stiffer in the early stages of loading.

In line with this, the experimental results showed generally inelastic behaviour under monotonic loading test to failure for all three tower specimens, but their stiffnesses varied depending on the prestress level. Among the three towers in the test to failure cases, M5 with the lowest initial prestress of about 790 MPa, displayed the lowest stiffness, while M4-2 was stiffer than M4-1. These observations confirm that the level of prestressing directly governs the load–deflection performance, with higher prestressing levels producing stiffer and more resilient responses.

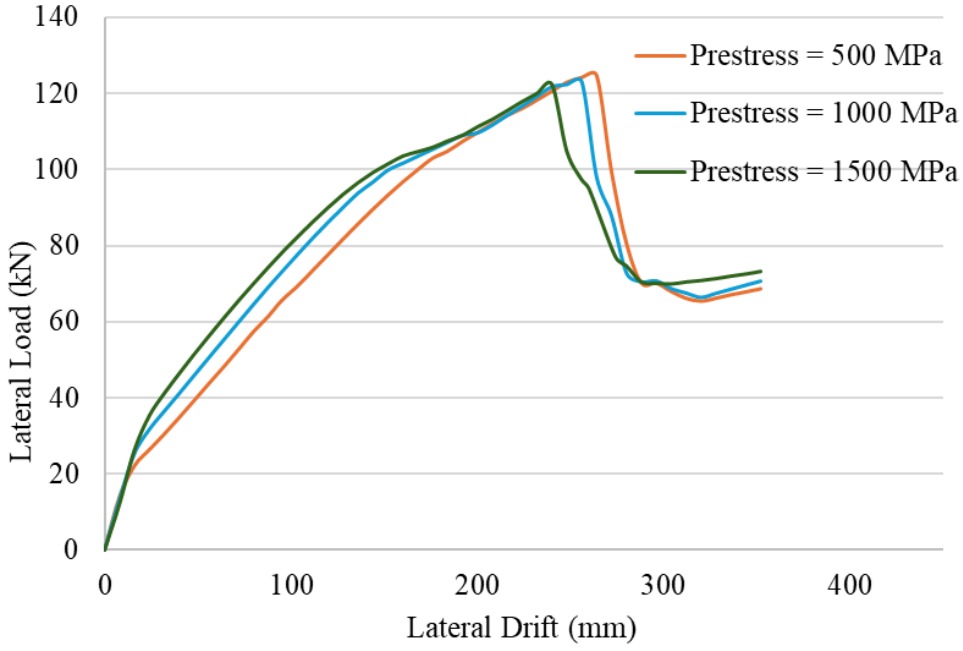

Figure 8.8. Effect of prestress force on lateral load–drift response

8.3.2. GFRP Tube Thickness

To examine the effect of GFRP tube thickness, a finite element parametric study was performed considering tube thicknesses of 10 mm, 18 mm, and 20 mm. As shown in Figure 8.9, increasing the GFRP tube thickness clearly improves both the lateral stiffness and the maximum load capacity. For this analysis, the geometry of tower M4 was used. The 20 mm tube thickness shows the highest performance, followed closely by the 18 mm section, while the 10 mm tube shows lower strength and softens earlier in the response. These trends match what was seen in the experimental program. For example, the M5 tower, which had an average tube thickness of about 10 mm, showed a noticeably lower stiffness compared to M4-1, which had a thicker tube of about 14 mm. This difference was evident even though M5 had a larger cross-section, confirming that the thinner GFRP tube reduced its flexural rigidity and provided less confinement to the concrete core. When combined with the lower prestressing level in M5, the reduced thickness explains its lower stiffness.

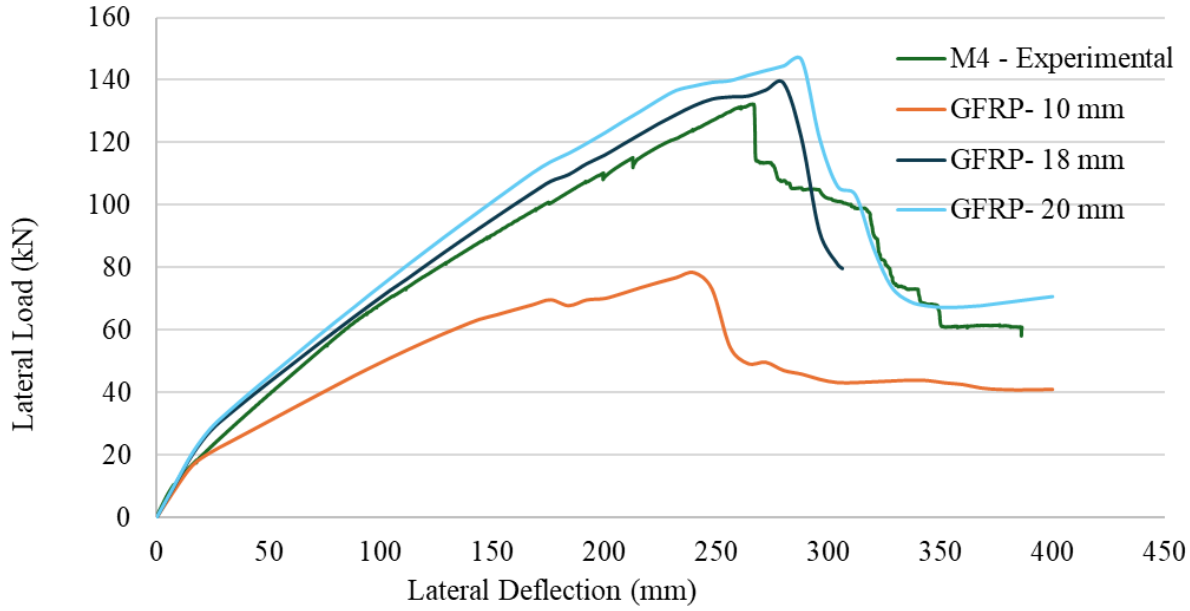

Figure 8.9. Effect of GFRP tube thickness on lateral load–drift response

8.3.3. Effect of concrete confinement

As part of the parametric investigation, the influence of concrete confinement on the lateral load–deflection response was assessed. Results indicate that unconfined concrete exhibits significantly lower stiffness, reduced peak load, and limited ductility. By contrast, modeling the concrete as confined using Lam and Teng (2003) FRP-confined stress strain relationship noticeably improves these responses. For this study, tower M4's geometry was adopted in the modeling. Both the nominal compressive strength of 50 MPa and the experimentally determined strength of 62 MPa were considered, with the latter producing the highest lateral capacity and better post-peak behaviour. Different concrete strengths were tested, and it was found that the confined concrete strength of 62 MPa provided a response that was stiffer and more representative of the experimental behaviour (Figure 8.10). These findings underscore the critical role of confinement modeling in achieving realistic simulations of FRP-confined concrete structures.

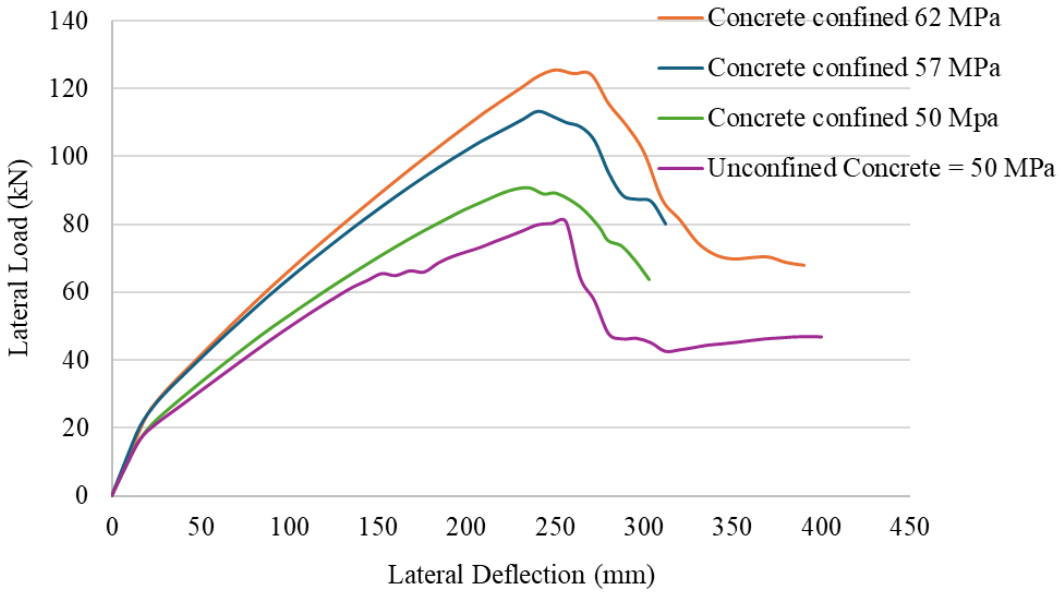

Figure 8.10. Effect of concrete confinement on the lateral load–deflection behaviour of the tower

8.3.4. Effect of elastic modulus of the GFRP tube

To understand how the GFRP tube's stiffness affects the tower's performance, a series of Abaqus simulations were performed for M5 tower with three different longitudinal elastic modulus values of 18, 21, and 26 GPa (Figure 8.11). Results indicate that increasing the modulus enhances the tower's initial stiffness and peak lateral load capacity, reflecting the greater axial and bending rigidity provided by the stiffer tube. In addition, the peak responses show more pronounced drops with higher E value (especially E26), reflecting the brittle failure of stiffer GFRP tubes. In contrast, the lowest modulus model (E18) exhibits a more gradual post-peak decline. Notably, the E18 model aligns most closely with the experimental observations, emphasizing the importance of accurately characterizing the GFRP elastic modulus in Abaqus to ensure reliable simulation outcomes. These findings highlight that the elastic modulus of the GFRP tube is a critical parameter influencing both the strength and ductility of CFFT towers.

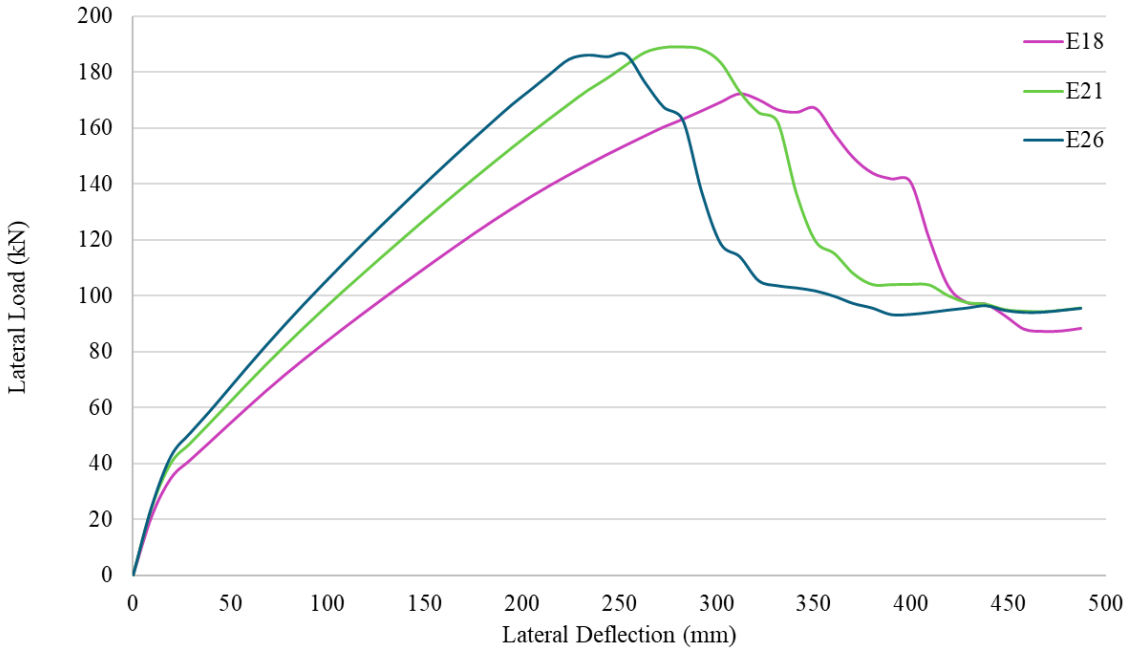

Figure 8.11. Effect of elastic moduli for the GFRP tube on the lateral load–deflection behaviour of the tower M5

8.4. Analytical Predictions

Analytical predictions were developed in this study to estimate the structural response of the post-tensioned concrete-filled GFRP tube (CFFT) towers and to provide a benchmark against experimental and numerical findings. The analyses included determination of the ultimate moment resistance for towers M4 and M5 considering both confined and unconfined concrete models, shear resistance calculations, sectional moment–curvature evaluation, and simplified deflection predictions using the moment–area method. The analytical results were then compared with the experimental observations.

- **Moment resistance and shear resistance of towers**

The analytical predictions confirmed the large benefit of FRP confinement on flexural strength. Table 8.3 presents the total calculated moment resistance at the base of each tower using confined and unconfined concrete, along with the moment obtained from the experimental test. For Tower M5, the confined model predicted 754 kN·m, which aligned closely with the experimental ultimate resistance of approximately 766 kN·m (2% lower). However, unconfined concrete model predicted 594 kN.m which is about 22% lower than the experimental ultimate moment for M5. For Tower M4, the confined concrete model predicted a base moment resistance of 651 kN·m, compared to 449 kN·m for unconfined concrete, while the experimental ultimate moment reached approximately 556 kN·m. These comparisons highlight that neglecting confinement would underestimate capacity by 20-25%, leading to nonconservative designs, while a fully confined model over-estimated the capacity in the case of the smaller tower. This suggests that the hollow core of the tube resulted in at least partial confinement, while the differences between tower sizes requires further investigation.

Shear resistance predictions show that the predicted capacities far exceeded the maximum applied shears for both towers. Specifically, the total shear resistance was approximately 799 kN, compared with maximum applied shears of 132 kN for Tower M4 and 182 kN for Tower M5 (Table 4.8), indicating a large margin of safety. While shear was not the governing mode of failure, these

results reinforce the importance of accounting for FRP confinement effects in flexural design and confirm that both towers were adequately designed to prevent shear failure.

Table 8.3. Maximum moment resistance (M_r) for each tower

Towers' Group	Mr (kN.m), unconfined concrete	Mr (kN.m), confined concrete	Mr (kN.m), experimental results
M5	594	754	766
M4	449	651	556

- **Moment- curvature evaluation**

In addition to moment resistance, the lateral deflection of the towers was predicted using the same sectional model applied for the analytical estimation of bending capacity. The curvature along the height of the towers was determined based on the neutral axis depth and the corresponding concrete compression strain for the applied moment. The resulting curvature was then used to estimate the lateral deflection (Δ) using the moment–area method. Detailed calculation steps for curvature and deflection are provided in Section 4.2.4, and Appendix D.

Figure 4.5 compares the predicted deflection profiles of Towers M4 and M5 with the experimentally measured top displacements at failure, while Figure 4.6 presents the corresponding load-deflection relationships. The analytical model captures the general trend of deflection with applied load; however, the experimental deflections were slightly higher. This divergence may be partially due to differences between the assumed and actual prestress levels, as the model assumed an ideal prestress of 1000 MPa, while the effective prestress during testing might have reduced by relaxation, friction losses, and other construction-related factors. Additional factors such as early cracking, bond slip between the GFRP tube and concrete core, and minor construction limitations also contributed to slightly larger experimental deflections.

Despite these differences, the predicted deflections provide a reliable upper-bound estimation for design purposes and clearly demonstrate the influence of prestressing and confinement effects on tower stiffness.

8.5. Critical Assumptions and Limitations

While the experimental and numerical investigations provided valuable insights into the behaviour of post-tensioned concrete-filled GFRP tube (CFFT) towers, several critical assumptions were made in the development of the analytical models, and finite element simulations. These assumptions, along with the corresponding limitations, must be acknowledged to define the scope of applicability of the findings and highlight areas for future work.

One of the primary assumptions concerned the material properties of the GFRP tube. In the numerical models, the GFRP tube was treated as an orthotropic material (Section 4.2.2). This choice allowed the directional stiffness of the composite to be represented more accurately than in isotropic models, but it did not capture the full range of degradation mechanisms such as matrix cracking, fibre pull-out, and delamination. Similarly, the concrete was represented using the Concrete Damaged Plasticity (CDP) model with confined stress–strain curves taken from established models and literature. These simplifications captured the main structural response but could not reproduce progressive cracking, creep, or other long-term effects.

The prestressing was assumed to remain fully effective, and perfect bond was taken between the concrete, steel, tendons, and GFRP tube. In practice, losses in prestress and bond-slip effects are likely, particularly under cyclic or fatigue loading.

Another major simplification was the assumption of perfect bond between the concrete, steel reinforcement, prestressing tendons, and the GFRP tube (Section 4.2.). This ensured efficient load transfer in the numerical models but neglected the possibility of bond-slip, debonding, or local interface imperfections that are likely under cyclic or fatigue loading. Such effects may contribute to stiffness degradation and energy dissipation, as suggested by the experimental results.

Finally, the environmental and long-term effects were outside the scope of this study. All tests were conducted under controlled laboratory conditions, and therefore factors such as temperature variations, freeze–thaw cycles, UV exposure, moisture entrance, and fatigue were not examined. These issues are particularly critical for remote northern areas, where extreme weather and limited maintenance could significantly impact long-term durability.

8.6. Unexpected Observations and Behaviour

During the experimental program, several behaviours were observed that deviated from the analytical predictions and numerical expectations. These outcomes provide important insights into the actual performance of post-tensioned CFFT towers and highlight where the assumptions outlined earlier in Section 8.5 may have influenced the results. Although towers M4-1 and M4-2 were designed to be nominally identical, they exhibited noticeably different stiffness and degradation behaviours (Figure 8.1). This unexpected variation is likely due to subtle differences in fabrication, variations in applied prestress forces, and slight discrepancies in foundation movement or the clamping system connection to the tower. These observations highlight the practical limitations of assuming perfect material uniformity and repeatability assumptions often made in FE models but not always achievable in experimental testing.

During the BRE loading for M4-1 and M4-2, the magnitude of sharp load drops was smaller than expected. Both M4-1 and M4-2 exhibited modest, similar drops (Figure 8.4), suggesting that foundation rotation and localized slippage at the clamping interface played a larger role in energy dissipation than the material plasticity of the steel or concrete.

Under BLE loading, specimen M4-1 exhibited a nonlinear load–deflection response, despite strain measurements indicating no yielding in the steel reinforcement (Figure 5.4). This suggests that the apparent nonlinearity typically expected at these load levels was governed primarily by concrete cracking rather than steel yielding. In contrast, specimen M5 maintained slightly higher stiffness under the same loading but displayed intermittent small load drops (Figure 8.7), indicating minor energy dissipation at the interface between the clamping system and the GFRP tube.

Strain distributions along the GFRP tube surfaces also revealed unexpected behaviour. At peak lateral loads under symmetric cyclic flexural loading, localized tension strains in the steel reinforcement sometimes exceeded the corresponding tensile strains in GFRP (Figure 5.4, Figure 5.7). Normally, higher strains would be expected in the GFRP since it lies farther from the neutral axis. This unexpected trend may indicate either incomplete composite action between the concrete core and GFRP tube, or localized strain jumps in the reinforcement at crack locations, where steel

response is more concentrated than that of the outer GFRP surface. This highlights the complex interaction and differential stiffness effects between the tube and the concrete core.

M4-2 exhibited a significantly higher lateral stiffness among the tower during the test to failure (Figure 8.1). This enhanced stiffness can be attributed to the combination of a higher tendon prestress and reduced foundation flexibility or rotation relative to M4-1. Strain measurements along the GFRP tube surfaces further revealed that the confinement did not always deform uniformly with the steel reinforcement, suggesting localized debonding or differential stiffness effects. These behaviours were not fully captured in the initial analytical predictions, highlighting the sensitivity of the structural response to prestress levels, foundation conditions, and the complex interaction between the GFRP tube and the concrete core.

Chapter 9 - Conclusions and Recommendations

9.1. Conclusions

This research has comprehensively investigated the structural performance of a novel system: post-tensioned, hollow, tapered concrete-filled FRP tubes (CFFTs) for small-scale wind turbine towers in remote areas. Through an integrated program of large-scale experimental testing and advanced numerical modeling, the study successfully addressed its primary objectives. The experimental phase involved the design, instrumentation, construction, and testing of three unique large scale tower specimens under a combination of static, cyclic, eccentric, and dynamic loading protocols. This was completed by the development and validation of a FE model capable of accurately simulating the complex composite behaviour observed in the laboratory. The findings indicate that the post-tensioned CFFT system presents a highly promising solution for wind turbine towers in remote areas. It effectively combines the corrosion resistance of GFRP with the compressive strength and durability of concrete, while the post-tensioning significantly enhances serviceability performance by reducing deflections and reducing crack widths. Moreover, the system is inherently well-suited to the logistical constraints of remote areas construction, providing a durable, low-maintenance alternative to conventional steel and concrete towers.

9.2. Summary of Conclusions

The following key conclusions are drawn:

1. Structural Performance: The post-tensioned CFFT system demonstrates excellent structural performance, combining high strength, significant deformability, and favourable dynamic characteristics. The three full-scale tower specimens (M4-1, M4-2, M5) consistently achieved high ultimate lateral loads (125 - 182 kN) with considerable deformation capacity (231 - 361 mm), confirming their suitability for resisting extreme wind loads. Among the specimens, M5 showed the highest peak load and greatest deformability, while M4-1 and M4-2 showed slightly lower ultimate loads and earlier higher stiffness due to higher prestressing level. The failure mode was consistently a flexural failure initiated by tensile rupture of the GFRP tube near the base and preceded by significant deflections. Finite element and analytical predictions

were generally conservative as peak loads and deflections were slightly underestimated likely due to simplified modeling assumptions that did not fully capture the effects of prestressing and GFRP confinement.

Challenges encountered during testing included minor variations in foundation restraint and rotation, which affected lateral response and required careful calibration of numerical models. Despite these challenges, the experimental results were robust and provided a clear benchmark for assessing the relative performance of all three towers.

2. Prestressing: The integration of post-tensioning into the CFFTs was essential to the system's success. It significantly enhanced the flexural stiffness of the towers, reducing service-level deflections under lateral load. The prestressing also kept the concrete core in compression, delaying the onset of cracking and improving long-term durability.
3. Favourable Dynamic Properties: The free vibration tests revealed that the fundamental natural frequency of the M4 tower is approximately 6.6 Hz, and 5.7 Hz for M5. These frequencies lie well above the typical operating range of small- and medium-sized wind turbines (0.3- 2.5 Hz), indicating a negligible risk of resonance. The measured damping ratios (4.0- 9.0%) are consistent with or superior to those of other composite structures and indicate an inherent ability to dissipate vibrational energy, which is beneficial for mitigating fatigue demands.
4. Validated Numerical Modeling: A finite element model was developed and validated against the experimental results. The model successfully captured the global force-displacement response, strain distributions in all components (concrete, GFRP, steel, tendons), dynamic properties, and failure modes. Importantly, the model incorporated the effects of the test setup, including base/foundation rotation and localized slippage at the clamping interface with the tower, which were found to influence lateral stiffness, deflection, and sharp load drops.

   By including these boundary conditions, the simulations successfully reproduced the asymmetric responses measured under CF loading and eccentric loading (SLE and BLE). The accuracy of the model was demonstrated through close agreement with experimental outcomes as the predicted peak lateral loads were within 5-7% of measured values across M4-1 and M5 towers, and lateral displacements at ultimate experiment load (267 mm for M4-1, and 361 mm for M5) were closely replicated (240 mm for M4-1, and 311 mm for M5), with only minor

deviations noted under eccentric loading. These results confirm that the model provides a reliable tool for both ultimate strength prediction and parametric studies. Nonetheless, such methods remain valuable for preliminary design, offering designers practical and efficient tools, while the validated FE model ensures accuracy for detailed research and advanced design applications.

9.3. Practical design recommendations

The findings of this study lead to several practical recommendations for the design and implementation of post-tensioned CFFT towers for small-scale wind turbines in remote areas. The key lesson is that the system works well, but its performance depends on careful attention to materials, prestressing, geometry, foundation details, and maintenance.

First, the choice of materials and section properties is critical. As shown in Chapter 8 (Figure 8.9), the GFRP tube plays a major role in confining the concrete core, which improves both strength and ductility. That means the tube thickness cannot be chosen just for economy as it needs to be sized properly, especially for taller or more slender towers. In some cases, when stiffness is a big concern, higher-modulus fibers like CFRP may be worth considering, though their cost is higher. Geometric parameters, including tower diameter, and concrete thickness were shown through both experimental results and analytical modeling to strongly influence lateral stiffness and ultimate capacity (Sections 8.2.2, 8.2.3, and 4.2.4)

Prestressing also proved to be extremely valuable. The tests (Section 8.2.3) showed that applying post-tensioning kept the core in compression, reduced deflections, and delayed cracking. This is especially important for durability in northern climates where freeze–thaw cycles and moisture are issues. Prestressing also makes it easier to use joined, segmental construction as the segments can be stressed together on-site to behave as one continuous tower (Section 1.1, and 1.2).

Foundation and connection details also need close attention. During testing, some slip and foundation rotation were observed, which influenced stiffness and strength (Section 5.7.2). To avoid this in the field, it is important to use proper anchorage systems such as calibrated bolt preloading, mechanical locking devices such as lock nuts or Nord-Lock washers, and torque-

verification protocols during assembly. These details may sound trivial, but they make a significant difference under repeated cyclic loading.

Serviceability and dynamic behaviour are also crucial. The free vibration results (Section 8.2.1) showed natural frequencies in the 5.7–6.6 Hz range, which is securely above the operating frequency of small turbines (0.3- 2.5 Hz). This is good result, but for taller towers or when the rotor mass is included, the frequency still needs to be checked. Deflections should also be limited to keep lateral displacement below approximately 1.25% of the tower height as a good practical limit (Section 5.2). The damping measured in these towers (4- 9%, Section 8.2.1) is higher than typical steel towers, which is an advantage against fatigue, but critical areas like splices and tendon anchorages should still be designed for cyclic demands.

Another important detail is composite action between the GFRP tube and the concrete core. Strain measurements (Section 6.6, and 8.2.) showed that the deformation was not always uniform, meaning there is a risk of partial debonding. This can be improved by surface treatments, or texturing to strengthen the bond. Ensuring good composite behaviour means the GFRP confinement effect can be fully developed.

Finally, maintenance and durability need to be considered from the start. For towers in remote areas, simple inspection routines are essential such as verifying bolt torque at foundations, and visual inspection of the GFRP tube surface for potential damage. The system should also be designed to allow easy repairs such as patching the FRP locally or replacing tendon anchors without dismantling the whole tower. These practical details will extend service life, reduce long-term costs, and enhance the viability of CFFT technology for small-scale wind energy in remote regions.

9.4. Recommendations for Future Work

Based on the findings and limitations of this study, the following avenues are proposed for future research to further advance and implement this technology:

1. Influence of Material Types: Future work should explore the impact of different material choices on system performance, and durability:

- Internal Reinforcement: A comparative study on the influence of different types of internal reinforcing bars (e.g., steel vs. GFRP vs. CFRP bars) is recommended. Their differing modulus of elasticity, tensile strength, and bond characteristics with concrete could significantly affect cracking behaviour, ductility, and ultimate flexural capacity.
- FRP Tube Material: This study focused on GFRP tubes. Future investigation should explore the use of CFRP tubes, which offer a higher modulus of elasticity and strength to weight ratio. While more expensive, CFRP could enable taller or slimmer tower designs for higher capacity turbines and deserves thorough experimental validation.

2. System Optimization and Standardization: Research is needed to transition from a prototype to a standardized solution:

- Geometric Optimization: Further investigation should focus on optimizing the tower geometry (e.g., taper ratio, diameter-to-thickness ratio, hollow core ratio) for different sizes of wind turbines and various tower heights to achieve the most efficient and economical design for a given application.
- Development of Design Guidelines: There is a pressing need to translate the complex numerical and experimental results into simplified design guidelines and analytical equations. Creating user-friendly design manuals and tools will be crucial for facilitating the widespread implementation of CFFT wind turbine towers by practicing engineers, especially in remote areas.

3. Optimization of Connection Details: Research should also address the reliability of the foundation anchorage to the strong floor and clamping system. Key recommendations include:

- Preloading and Tightening: Use calibrated hydraulic torque wrenches or bolt tensioners for large-diameter bolts to achieve consistent and precise preload.

- Mechanical Locking Devices: Employ lock nuts, Nord-Lock washers, or thread-locking compounds to prevent bolt loosening under cyclic loading.
- Inspection and Verification: Establish systematic inspection and torque-verification protocols before and during testing to ensure connections remain secure.

References

1. Abdelkarim, O. I., & ElGawady, M. A. (2015). Performance of concrete-filled fiber tubes (CFFT) polymers under axial loading using large rupture strain FRP made from plastic bottles.
2. ACCIONA Windpower. (n.d.). *ACCIONA Windpower reaches 1,000 MW of wind turbines installed with concrete towers*. Retrieved March 31, 2021, from https://www.acciona.com/updates/news/acciona-windpower-reaches-1000-mw-wind-turbines-installed-concrete-towers/?_adin=11551547647
3. Arduini, M., & Nanni, A. (1997). Behavior of precracked RC beams strengthened with carbon FRP sheets. *Journal of Composites for Construction*, *1*(2), 63–70.
4. Bonacci, J. F., & Maalej, M. (2000). Externally bonded fiber-reinforced polymer for rehabilitation of corrosion damaged concrete beams. *ACI Structural Journal*, *97*(5), 703–711.
5. Cole, B., & Fam, A. (2006). Modeling of Prestressed Concrete-Filled Circular Composite Tubes Subjected to Bending and Axial Loads. *Journal of Composites for Construction*, *10*(2), 161–171.
6. Dassault Systèmes. (2006). *Abaqus Theory Manual, Version 6.6, Section 4.1: Element Formulation and Integration*. Dassault Systèmes Simulia Corp. Retrieved from https://classes.engineering.wustl.edu/2009/spring/mase5513/abaqus/docs/v6.6/books/gsa/ch04s01.html
7. Dassault Systèmes. (2009). *Abaqus Analysis User's Manual (v6.6)*. Retrieved from https://classes.engineering.wustl.edu/2009/spring/mase5513/abaqus/docs/v6.6/books/usb/pt06ch26s01alm35.html
8. Dassault Systèmes. (2014). *Element Library: Overview (Section 23.1.1), Abaqus Analysis User's Manual, Version 6.14*. [Online]. Available: https://www.scribd.com/document/396349580/Poly-Jcc
9. Dassault Systèmes. (2024). *Abaqus Analysis User's Guide, Version 2024*. Dassault Systèmes Simulia Corp. [Online]. Available: https://docs.software.vt.edu/abaqusv2024/English/SIMACAEANLRefMap/simaanl-c-visco.htm

10. de Lana, J. A., Junior, P. A. A. M., Magalhaes, C. A., Magalhaes, A. L. M. A., de Andrade Junior, A. C., & de Barros Ribeiro, M. S. (2021). Behavior study of prestressed concrete wind-turbine tower in circular cross-section. *Engineering Structures*, *227*, 111403. https://doi.org/10.1016/j.engstruct.2020.111403
11. Fam, A., & Mandal, S. (2006). Prestressed Concrete-Filled Fiber-Reinforced Polymer Circular Tubes Tested in Flexure. *PCI Journal*, *51*(4), 42–54. https://doi.org/10.15554/pcij.07012006.42.54
12. Fam, A., Pando, M., Filz, G., & Rizkalla, S. (2003). Precast Piles for Route 40 Bridge in Virginia Using Concrete Filled FRP Tubes. *PCI Journal*, *48*(3), 32–45. https://doi.org/10.15554/pcij.05012003.32.45
13. Fam, A. Z., & Rizkalla, S. H. (2001). Behavior of axially loaded concrete-filled circular fiber-reinforced polymer tubes. *Structural Journal*, *98*(3), 280–289. https://www.concrete.org/publications/internationalconcreteabstractsportal/m/details/id/10217
14. Fam, A. Z., & Rizkalla, S. H. (2002). Composite Action of Concrete-Filled Fiber-Reinforced Polymer Tubes under Flexural Cyclic Loading. *Journal of Structural Engineering*, *128*(4), 499–508.
15. Fam, A. Z., & Rizkalla, S. H. (2002). Flexural behavior of concrete-filled fiber-reinforced polymer circular tubes. *Journal of Composites for Construction*, *6*(2), 123–132. https://doi.org/10.1061/(ASCE)1090-0268(2002)6:2(123)
16. Gong, Y. (2021). *Finite Element Modelling of CFFT Small-Scale Wind Turbine Towers* [Master's thesis, Dept. of Civil Engineering, Univ. of Ottawa, Ottawa, Canada].
17. Grunberg, J., & Gohlmann, J. (2013). *Concrete structures for wind turbines*. John Wiley & Sons. https://www.wiley.com/en-ie/Concrete+Structures+for+Wind+Turbines-p-9783433030417
18. Gwon, T. G. (2011). *Structural Analyses of Wind Turbine Tower for 3 kW Horizontal Axis Wind Turbine* [Master's thesis, California Polytechnic State University]. https://doi.org/10.15368/theses.2011.159
19. Hadi, M. N. S., Khan, Q. S., & Sheikh, M. N. (2016). Axial and flexural behavior of unreinforced and FRP bar reinforced circular concrete filled FRP tube

columns. *Construction and Building Materials*, *122*, 43–53. https://doi.org/10.1016/j.conbuildmat.2016.06.044

20. Hau, E. (2006). *Wind turbines: fundamentals, technologies, application, economics*. Springer Science & Business Media. https://link.springer.com/book/10.1007/3-540-29284-5
21. Helmi, K., Fam, A., Mutti, A., & Hall, M. (2006). Effects of Driving Forces and Bending Fatigue on Structural Performance of a Novel CFFT Flexural Pile. *Canadian Journal of Civil Engineering*, *33*(6), 683–691.
22. Howie, I., & Karbhari, V. M. (1994). Effect of materials architecture on strengthening efficiency of composite wraps for deteriorating columns in the North-East. In *Proc.3rd Materials Conf., Material Engineering Division, ASCE* (pp.199–206). New York.
23. Indiamart. (2024). Modern street light poles [Photograph]. Retrieved from https://5.imimg.com/data5/SELLER/Default/2024/1/374532852/HG/RS/YK/8725064/modern-street-light-poles-500x500.jpg
24. International Energy Agency (IEA) Wind TCP. (2021). *Task 27: Small wind turbine technical report*. https://iea-wind.org/wp-content/uploads/2021/06/IEA-Wind-TCP-Task-27-Draft-Small-Wind-Turbine-Technical-Report.pdf
25. JCSS. (2005). *Probabilistic Model Code, Part III – Resistance Models*. Joint Committee on Structural Safety.
26. Kotynia, R., Baky, H. A., Neale, K. W., & Ebead, U. A. (2008). Flexural strengthening of RC beams with externally bonded CFRP systems: test results and 3D nonlinear FE analysis. *Journal of Composites for Construction*, 190–201.
27. Lee, S., & Moy, S. (2007). A Method for Predicting the Flexural Strength of RC Beams Strengthened with Carbon Fiber Reinforced Polymer. *Journal of Reinforced Plastics and Composites*, *26*(14), 1383–1401.
28. Lian, J., Zhou, H., & Dong, X. (2022). A Theoretical Approach for Resonance Analysis of Wind Turbines under 1P/3P Loads. *Energies*, *15*(16), 5787. https://doi.org/10.3390/en15165787

29. Maalej, M., & Leong, K. S. (2005). Effect of beam size and FRP thickness on interfacial shear stress concentration and failure mode of FRP-strengthened beams. *Composites Science and Technology*, 1148–1158.
30. Mandal, S., & Fam, A. (2006). Modeling of Prestressed Concrete-Filled Circular Composite Tubes Subjected to Bending and Axial Loads. *Journal of Structural Engineering*, *132*(3), 449–459.
31. Mirmiran, A., Shahawy, M., & Samaan, M. (1999). Strength and ductility of hybrid FRP-concrete beam-columns. *Journal of Structural Engineering*, *125*(10), 1085–1093.
32. Mitchell, J., & Fam, A. (2010). Tests and analysis of cantilevered GFRP tubular poles with partial concrete filling. *Journal of Composites for Construction*, *14*(1), 115–124. https://doi.org/10.1061/(ASCE)CC.1943-5614.0000041
33. Mohamed, H. M., & Masmoudi, R. (2010). Flexural strength and behavior of steel and FRP-reinforced concrete-filled FRP tube beams. *Engineering Structures*, *32*(11), 3789–3800. https://doi.org/10.1016/j.engstruct.2010.08.023
34. Nicholson, J. C. (2011). *Design of wind turbine tower and foundation systems: optimization approach* [Master's thesis, University of Iowa]. https://doi.org/10.17077/etd.bhnu76gr
35. Ozbakkaloglu, T. (2013). Compressive behavior of concrete-filled FRP tube columns: Assessment of critical column parameters. *Engineering Structures*, *51*, 188–199. https://doi.org/10.1016/j.engstruct.2013.01.017
36. Ozbakkaloglu, T., & Vincent, T. (2014). Axial Compressive Behavior of Circular High-Strength Concrete-Filled FRP Tubes. *Journal of Composites for Construction*, *18*, 04013037. https://doi.org/10.1061/(ASCE)CC.1943-5614.0000410
37. Pan, J., Chung, T. C. F., & Leung, C. K. Y. (2009). FRP Debonding from Concrete Beams under Various Load Uniformities. *Advances in Structural Engineering*, *12*(6), 807–819.
38. Parvathaneni, H. K., Iyer, S. L., & Greenwood, M. (1996). Design construction of test mooring pile using superprestressing. In *Proc. Adv. Compos. Mater. Bridges Struct.* (pp.313–324). Montreal, Canada.

39. Pham, H. B., & Al-Mahaidi, R. (2006). Prediction Models for Debonding Failure Loads of Carbon Fiber Reinforced Polymer Retrofitted Reinforced Concrete Beams. *Journal of Composites for Construction*, *10*(1), 48–59.
40. Pham, T. M., Hadi, M. N. S., & Youssef, J. (2015). Optimized FRP wrapping schemes for circular concrete columns. *Journal of Composites for Construction*. https://doi.org/10.1061/(ASCE)CC.1943-5614.0000571
41. Pham, T. M., Youssed, J., Hadi, M. N. S., & Tran, T. M. (2016). Effect of different FRP wrapping arrangements on the confinement mechanism. *Procedia Engineering*, *142*, 306–312.
42. Polyzois, D. J., Raftoyiannis, I. G., & Ungkurapinan, N. (2009). Static and dynamic characteristics of multi-cell jointed GFRP wind turbine towers. *Composite Structures*, *90*(1), 34–42. https://doi.org/10.1016/j.compstruct.2009.01.005
43. Qasrawi, Y., Heffernan, P. J., & Fam, A. (2015). Dynamic behaviour of concrete filled FRP tubes subjected to impact loading. *Engineering Structures*, *100*, 212–225. https://doi.org/10.1016/j.engstruct.2015.06.012
44. Rahai, A. R., Sadeghian, P., & Ehsani, M. R. (2008). Experimental Behavior of Concrete Cylinders Confined with CFRP Composites. In *14th World Conf. Earthquake Eng.* (pp.1–9). Beijing, China.
45. Rhoads-Weaver, H., Schwartz, S. S., Zarowny, K., Weis, T., Whittaker, S., Gluckman, M., & French, M. (2013). *Small Wind Turbine Purchasing Guide*. Retrieved from https://web.archive.org/web/20130302211547/http://www.ontario-sea.org/Storage/39/3065_Small_Wind_Turbine_Purchasing_Guide_-_Off-grid%2C_Residential%2C_Farm_%26_Small_Business_Applications.pdf
46. Rodriguez, M. (2023). Engineering challenges in the maintenance of offshore wind farms. *Inspenet*. Retrieved from https://inspenet.com/en/articulo/offshore-wind-farm-maintenance-challenges/
47. R. S. Poles. (n.d.). Modular poles [Photograph]. Retrieved from https://www.rspoles.com/solutions/products/modular-poles
48. Sadeghian, P., & Fam, A. (2010). Bond-Slip Analytical Formulation toward Optimal Embodment of Concrete-Filled Circular FRP Tubes into Concrete Footings. *Journal of*

Engineering Mechanics, *136*(4), 524–533. https://doi.org/10.1061/(ASCE)EM.1943-7889.0000091

49. Son, J.-K., & Fam, A. (2008). Finite element modeling of hollow and concrete-filled fiber composite tubes in flexure: Model development, verification and investigation of tube parameters. *Engineering Structures*, *30*(9), 2656–2666. https://doi.org/10.1016/j.engstruct.2008.02.014
50. St. Onge, J., & Fam, A. (2021). Torsional behavior of circular concrete-filled FRP tubes. *Journal of Composites for Construction*, *25*(3), 04021013. https://doi.org/10.1061/(ASCE)CC.1943-5614.0001122
51. Taisei Techno Co., Ltd. (2025). *Airfoil 1kW vertical axis wind turbine specifications*. Retrieved from https://www.taiseix.net/en/windturbine/spec/
52. Teng, J. G., Chen, J. F., Smith, S. T., & Lam, L. (2002). *FRP Strengthened Structures*. John Wiley & Sons, Ltd.
53. Veljkovic, M., Feldmann, M., Naumes, J., Pak, D., Simoes, L., & Rebelo, C. (2011). Wind turbine tower design, erection and maintenance. In *Wind energy systems* (pp.274–300). Woodhead Publishing. https://doi.org/10.1533/9780857090638.2.274
54. Watta, A., Green, M., Fam, A., & Noel, M. (2020). Segmental Hollow Concrete Filled FRP Tubes (CFFT) for Wind Turbine Towers. In *Proceedings of the 10th International Conference on FRP Composites in Civil Engineering* (pp.472–483). https://link.springer.com/chapter/10.1007/978-3-030-88166-5_40
55. Yokoyama, T. (2023). Experimental identification of high damping ratios in single-degree-of-freedom systems. *Archive of Applied Mechanics*. Retrieved from https://www.researchgate.net/publication/370382357
56. Zhang, P., Wang, S., & He, L. (2023). Modeling and simulation of the hysteretic behaviour of concrete under cyclic tension–compression using the smeared crack approach. *Materials*, *16*(12), 4442. https://doi.org/10.3390/ma16124442

Appendix A:

Hognestad Stress–Strain model for unconfined concrete

The stress-strain relationship for unconfined concrete in compression was calculated using the Hognestad concrete model (Hognestad, 1951), as described in Figure A.1. The concrete stress can be calculated using equation Eq. A.1.

$$f_c = f'_c \left[\frac{2\varepsilon_c}{\varepsilon_o} - \left(\frac{\varepsilon_c}{\varepsilon_0}\right)^2\right] \ , \varepsilon_c < \varepsilon_o \qquad \text{Eq. A.1}$$

Where fc represents compressive stress, εc is the compressive strain, $f'c$ is the ultimate compressive stress, and ε_u is the strain at which the stress equals to $0.85fc$, which is considered to be 0.0038.

The elastic modulus, E_c, is calculated by Eq. A.2.

$$E_c = 12680 + 460\, f'_c \qquad \text{Eq. A.2}$$

The strain at maximum compressive stress (ε_0) is calculated by Equation Eq. A.3

$$\varepsilon_o = \frac{2f'_c}{E_c} \qquad \text{Eq. A.3}$$

Figure A.1 presents the stress-strain relationship for Hognestad concrete model

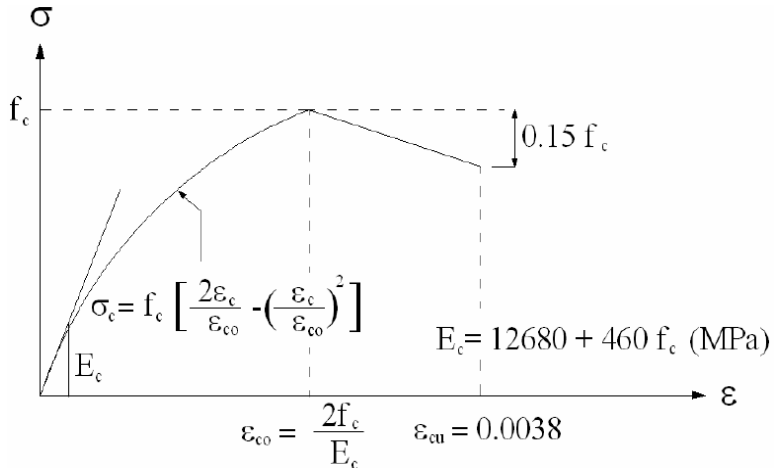

Figure A.1. Hognestad concrete model (1951)

Appendix B:

<u>Lam and Teng's Stress–Strain Model for FRP-Confined Concrete</u>

Unconfined Concrete Properties:

$f'_{c0} = 61.6\ MPa$

$\varepsilon_{C0} = 0.002$

$E_C = 4730\sqrt{f'_{C0}} = 4730\sqrt{61.6} = 37124\ MPa$

Concrete diameter, D = 535 mm

GFRP Tube Properties:

Thickness of Tube: t_{GFRP} = 10 mm

Strength of GFRP: f_{GFRP} = 92 MPa (in the hoop direction)

Ultimate Strain of GFRP: $\varepsilon_{GFRP} = 0.02$

Calculation:

The Lam and Teng's Model is defined as:

$$\sigma_C = E_C\varepsilon_C - \frac{(E_C - E_2)^2}{4f'_{C0}}\varepsilon_C^2 \ \ for\ 0 \le \varepsilon_C \le \varepsilon_t$$

$$\sigma_C = f'_{C0} + E_2\varepsilon_C \ \ for\ \varepsilon_t \le \varepsilon_C \le \varepsilon_{Cu}$$

$$f_l = \frac{2f_{GFRP}t}{D} = \frac{2(92)(10)}{535} = 3.573\ MPa$$

$$\varepsilon_{Cu} = \varepsilon_{C0}\left(1.75 + 22\frac{f_l}{f'_{c0}}\right) = 0.002\left(1.75 + 22\left(\frac{3.573}{61.6}\right)\right) = 0.00605$$

$$f'_{CC} = f'_{C0}\left(1 + 2\frac{f_l}{f'_{c0}}\right) = 61.6\left(1 + 2\left(\frac{3.573}{61.6}\right)\right) = 69\ MPa$$

The second slope of the confined model is:

$$E_2 = \frac{f'_{CC} - f_0}{\varepsilon_{Cu}} = \frac{69 - 61.6}{0.00605} = 1181\ MPa$$

$$\varepsilon_t = \frac{2f_0}{E_C - E_2} = \frac{2(61.6)}{37124 - 1181} = 0.00343$$

Appendix C:

Total Shear Strength carried by GFRP, Concrete, Steel, and Prestressing

1. Shear Strength carried by GFRP

The contribution to the shear resistance of a circular element with an external layer of GFRP with fibre orientation perpendicular to the axis of the member can be calculated using the Equation C.1 below from S806 CL 11.4.3.2

$$V_{GFRP} = \emptyset_{GFRP} E_{GFRP} \varepsilon_{GFRPe} 2 t_{GFRP} D_g \qquad \text{C.1}$$

Where,

$$\varepsilon_{GFRPe} \leq 0.75 \varepsilon_{GFRPu}$$

$$\varepsilon_{GFRPe} \leq 0.004$$

$$\varepsilon_{GFRPe} \leq K_v \varepsilon_{GFRPu}$$

And:

$$K_v = \frac{k_1 k_2 L_e}{11900 \varepsilon_{GFRPu}} \leq 0.75$$

$$k_1 = \left(\frac{f_c'}{27}\right)^{\frac{2}{3}}$$

$$k_2 = \frac{d_{GFRP} - L_e}{d_{GFRP}}$$

$$L_e = \frac{23300}{(t_{GFRP} E_{GFRP})^{0.58}}$$

<u>For the base section of the tower</u>

d_{GFRP} = 535 mm

$$V_{GFRP} = \emptyset_{GFRP} E_{GFRPe} \varepsilon_{GFRPe} 2 t_{GFRP} D_g = (1.0)(20800)(0.0023)(2)(10.0)(535)$$

$$V_{GFRP} = 512\ KN$$

2. Shear Strength carried by concrete. CSA A23.3-14, Clause 11.3.4

For members with circular solid cross sections, the circular ties or spirals used would be considered as web reinforcement and the calculation of V_C is given by Equation C.2 below.

The width 'b_w' measured as the diameter of the tower circular section and 'd' measured as the distance from the extreme compression fiber to the centroid of the longitudinal tension reinforcement. However, 'd' can be calculated as 0.8D, where D is the diameter of circular section.

$$V_C = \emptyset_c * \lambda * \beta\sqrt{f'_c} b_w d \qquad \text{C.2}$$

$$V_C = 0.65 * \lambda * \beta\sqrt{f'_{c0}}\,(0.8D^2)$$

$$= 0.65 * \lambda * \beta\sqrt{f'_{c0}}\,(0.8)\left(\frac{4A_c}{\pi}\right) \approx 0.65 * \lambda * \beta\sqrt{f'_{c0}} A_c$$

Where:

A_c is the area of hollow core concrete = $A_{con} - A_{hol}$ = (208307 mm^2- 55155 mm^2)

A_c= 153153 mm^2

β can be calculated according to Equation C.3:

$$\beta = \frac{0.4}{(1 + 1500 * \varepsilon_x)} \qquad \text{C.3}$$

Where ε_x (CL.11.3.6.4) can be determined according to Equation C.4.

$$\varepsilon_x = \frac{\frac{M_f}{d_f} + V_f - V_p + 0.5N_f - A_p f_{po}}{2\left(E_s A_s + E_p A_p\right)} \qquad \text{C.4}$$

$$\varepsilon_x = \frac{\frac{737}{0.406} + 147.4 - (0.395 * 1000)}{2 * (200000 * 0.800 + 190000 * 0.395)} = 0.00333476$$

Where $V_p = 0$ (stright tendons) , $N_f = 0$

$$\beta = \frac{0.4}{(1 + 1500 * \varepsilon_x)} = 0.6664$$

$$V_C = 1.0 * 1 * 0.6664 * \sqrt{50}\,(153153) = 72\ \text{KN}$$

3. Shear Strength carried by Steel. CSA A23.3-14 Clase **11.3.5.1**

The shear resistance of ties can be calculated as according to the V_s Equation C.5 below:

$$V_s = \frac{\varphi_s f_y A_v d_v \cot\theta}{s} \qquad \text{C.5}$$

$$= \frac{(0.85)(400)(2)(100)(412)(\cot 52)}{120} = 215\ \text{KN}$$

4. Shear Strength carried by Prestressing

The shear resistance carried by prestressing is zero because there is no vertical component from prestressing force ($V_P = 0$).

5. Total Shear Strength

The total shear strength carried by all materials is calculated according to the Equation C.6 below:

$$V_r = V_{GFRP} + V_C + V_s + V_P \qquad \text{C.6}$$

$V_r = 512 + 72 + 215 + 0 = 799\ \text{KN} > V = 151\ \text{KN}$, for the base of the tower

Appendix D:

The deflection for M5 tower with different concrete thicknesses

The deflection of the M5 tower was evaluated using a confined concrete model with GFRP controls failure mechanism as follows:

Step 1 – Basic information

- Total tower height: 5800 mm
- The height of the tower was divided to deferent intervals

Note: the towers' height is considered from the top to the bottom.

Step 2 – Properties at 5800 mm height

- Using the assumed concrete thickness and tower diameter, $Mr_{,5800}$ was calculated in the Excel spreadsheet.
- The results were:
  - $Mr_{,5800}$ = 766 (kN. m)
  - c = 124.98 (mm),
  - and ε_{cc} = -0. 003010

Step 3 – Curvature and deflection

- Curvature, $=\Phi = \frac{\varepsilon_{cc}}{c} = \frac{0.0031}{124.98} = 0.0000241$ (1/mm)
- Shaded area under the curvature diagram =

$$\Phi * L * \frac{1}{2} = 0.0000241 * 5800 * 0.5 = 0.06985$$

- Deflection, Δ= Moment of shaded area under the curvature diagram which is the total area x centroid of that area (length calculated from moment = 0)

Δ = 0.06985* 2/3* 5800 = 270 (mm)

Step 4 – Load calculation

- load applied can be calculated using Mr

$P = M_r/L = 766/ (5.8) = 132$ KN

- The M_r values gradually decrease along the tower height at set intervals and would be:
- $Mr_{,5000}$ = 132 (kN)* 5000 (mm)= 660(KN. m), where the height of 5000 (mm) measured from the top).
- Using the Excel sectional model, the neutral axis depth 'c' and concrete compression strain 'ε_{cc}' were found by adjusting the section diameter at 5000 mm height, setting the moment to 660 kN·m, and then running Solver

The results were:

c = 126.15 (mm), and

$\varepsilon_{cc} = -0.00276$

Step 6 – Curvature and deflection at 5000 mm height

- The curvature can be determined using the same equation in step 3:

$\Phi = \frac{\varepsilon_{frp}}{c} = \frac{0.00276}{126.15} = 0.00002186$ (1/mm)

- Shaded area under the curvature diagram= $\Phi * L * \frac{1}{2}$

$= 0.00002186 * 5000 * 0.5 = 0.05464$

- And the deflection can be calculated as follow:

Δ= 0.05464* 2/3* 5000 = 182 (mm)

Step 7 – Note

The same steps can be repeated for each section along both the tower M4 and M5 heights to determine the full deflection profile.

Appendix E

The input values used for the analysis.

f'c = 78 (MPa)

Tower diameter D = 535 (mm)

Mu = 766 (KN.m)

using the equation below:

$$\frac{x}{D} = \sqrt{\frac{3\pi M}{D^3 f'_c}}$$

$$x = D * \sqrt{\frac{3\pi M}{D^3 f'_c}}$$

$$x = 535 * \sqrt{\frac{3 * \pi * 766 * 10^6}{535^3 * 78}}$$

X= 416 (mm) which is the critical embedded length of the tower into the foundation

Appendix F

The calculated flexural rigidity of the tower at a height of 840 mm (strain gauge #1), where the maximum deflection occurs, is 30.22 (1/mm).
The load was applied at a height of 5000 mm.
The vertical distance from the applied load to the height of 840 mm is:

5000−840=4160 mm

The maximum applied load is **132.3 kN**.

The bending moment, M, is calculated as:

M=P×L=132.3×4160=550368 (kN·mm)

The flexural rigidity, EI, is determined by the equation

$$EI = \frac{M}{\Phi}$$

$$EI = \frac{550368}{30.22} = \ 18.2\ (N.m2)$$